Stress engineering of Friction Stir Welding: Measurement and Control of Welding Residual Stresses

A thesis submitted to the University of Manchester for the degree of
Doctor of Philosophy
in the Faculty of Engineering and Physical Science

2009

Jens Altenkirch

School of Materials

TABLE OF CONTENTS

ABSTRACT

Friction stir welding (FSW) is a maturing welding technique using a rotating tool for simultaneous heating and stir deforming the material interface to form a solid bond. Significant tensile residual stresses (RS) and component distortion may be produced even with optimized FSW parameters. Recent stress engineering techniques such as global mechanical or roller tensioning may reduce tensile RS and distortion.

This dissertation reports on the first systematic investigation into the efficiency of in-situ global mechanical tensioning (ISGMT) as well as roller tensioning applied in-situ (ISRT) and post welding (PWRT) for mitigation of tensile RS and plate distortion in high strength aluminium alloy plates joined by FSW. The techniques were evaluated by measuring the distribution of RS across the weld-line by means of neutron and synchrotron X-ray diffraction as well as the levels of plate distortion. In each case the weld microstructure and hardness distribution were characterised. The data were rationalised against the ISGMT load and roller tensioning down force respectively.

The results have shown that ISGMT and PWRT significantly mitigate longitudinal tensile RS and component distortion. ISGMT was found to decrease the tensile RS by an amount approximately equal to that of the load applied. Consequently, a stress free weld is produced with an ISGMT load equal to the magnitude of the weld-line RS in the as-welded condition. PWRT decreases the tensile RS as the rolling down force increases and significant compression may be introduced once a certain magnitude is exceeded. ISRT, at least for the range tested, was found to be less effective. The component distortion reduced along with RS mitigation. No effects on the microstructure or hardness distribution due to mechanical stress engineering were observed.

Furthermore, it was demonstrated that in order to make accurate stress measurements by diffraction, the effect of precipitation on the stress free lattice spacing must be taken into account for age hardening alloys. In order to complete this study an automated robotic sample manipulation system was developed. Finally, the degree of stress relaxation occurring on cutting down large welds was evaluated by progressively shortening test welds and determining the RS for each length. The amount of stress relaxation for each weld follows the same behaviour and appears to depend on the width of the tensile weld zone only.

DECLARATION

No portion of the work referred to in the thesis has been submitted in support of an application for another degree or qualification of this or any other University or other institute of learning.

The work presented in this dissertation is the authors work except where reference is made to others. The work in this dissertation was also reported in the following journal contributions:

- Altenkirch J., Steuwer A., Withers P. J., Buslaps T. and Berger U. (2007): *Robotic sample manipulation for stress and texture determination on neutron and synchrotron X-ray diffractometers*: Nuclear Instruments and Methods in Physics Research Section A: Accelerators, Spectrometers, Detectors and Associated Equipment, **584 (2-3)**, 248-255.
- Altenkirch J., Steuwer A., Peel M. and Withers P. J. (2009): *The extent of relaxation of weld residual stresses on cutting out cross-weld test piece:* Powder Diffraction, **24 (S1)**, 31-36.
- Altenkirch J., Steuwer A., Peel M., Richards D. G. and Withers P. J. (2008): *The effect of tensioning and sectioning on residual stresses in aluminium AA7749 friction stir welds*: Materials Science and Engineering: A, **488 (1-2)**, 16-24.
- Altenkirch J., Steuwer A., Peel M. J., Withers P. J., Williams S. W. and Poad M. (2008): *Mechanical Tensioning of High-Strength Aluminum Alloy Friction Stir Welds*: Materials Transactions: A, **39 (13)**, 3246-3259.
- Altenkirch J., Steuwer A., Withers P. J., Williams S., Poad M. and Wen S. (2009): *Residual stress engineering in friction stir welds by roller tensioning*: Science and Technology of Welding & Joining, **14 (2)**, 185-192.

A copy of each paper may be found in the appendix of this dissertation.

COPYRIGHT STATEMENT

ACKNOWLEDGEMENT

The course of the last three years in Grenoble and Manchester has certainly proven to be a long and difficult, but very interesting road for me. I would like to extend my deepest thanks to many people I met on the way for the encouragement, help and advice I received.

It is difficult to know where to begin, but probably the best to start with are my two supervisors: Phil Withers, my official supervisor at The University of Manchester and Axel Steuwer, my local supervisor in Grenoble. Both had a profound influence in guiding and shaping both my research work and this dissertation. Special thanks go to Matthew Peel and Darren Hughes in Grenoble, whose advice and valuable practical help throughout the residual stress measurements on the ID15A and SALSA beam–lines significantly improved my work. I am very grateful to David Richards from the 'Light Alloys Group' at the University of Manchester for the intensive collaboration on the finite element modeling work. Further thanks go to Phillip, Alex, Francisco and Judy for their advice and assistance during each of my visits to the School of Materials Science. I gratefully acknowledge the support from the academic and industrial members of the SEALS project. In particular, special thanks goes to Stewart Williams from the Cranfield University and Mike Poad from Airbus UK for providing the samples for this dissertation.

I would like to acknowledge the financial support received from the EPSRC Light Alloys Portfolio (UK) and the Institut Laue-Langevin as well as the beam-time provided by the European Synchrotron Radiation Facility and the Institute Laue-Langevin.

I would like to thank my parents, Christel and Wolfgang, as well as my brother Ralf and my sister Nora, who all supported me in any possible way throughout the time spent in France and the UK.

Finally, I would like to express my deepest thanks to my wife Janett, who, irrespective of the long time being separated from each other, supported me at any time and place over the past three years. I would like to dedicate this work to Janett and our little girl Lina Annabelle who was born last September of my final year. She is the greatest gift we could receive in life.

SYMBOLS AND ABBREVIATIONS

Symbol	Description	Unit
a	Unit cell parameter	(Å)
a_0	Elastically unstrained unit cell parameter	(Å)
c	Speed of light	(m/s)
d_{hkl}	Lattice spacing	(Å)
d_{0hkl}	Elastically unstrained lattice spacing	(Å)
E	Young's modulus	(GPa)
E	Energy	(keV)
F	Down force	(kN)
h	Planck's constant	
{hkl}	Miller indices	
l	Plate length	(mm)
m	Mass	(kg)
Q	Scattering vector	
S_0	Incident beam	
S_1	Diffracted beam	
T	Time	(s)
t_m	Plate thickness	(mm)
t_t	Tool tilt angle	(°)
w	Plate width	(mm)
$X_0Y_0Z_0$	Global coordinate system	
$X_SY_SZ_S$	Sample coordinate system	
$X_TY_TZ_T$	Tool coordinate system	
v	Speed	(m/s)
v_{rot}	Tool rotation speed	(rpm)
v_t	Tool traverse speed	(mm/min)
ε	Strain	($\mu\varepsilon = 10^{-6}$)
υ	Poisson's ratio	
λ	Wavelength	(Å)
σ	Stress	(MPa)
σ_{YS}	Yield strength	(MPa)
θ	Diffraction angle	(°)

Abbreviations

CMM	Coordinate measuring machine
ESRF	European Synchrotron Radiation Facility
FEM	Finite element modelling
FSW	Friction sir welding
GMT	Global mechanical tensioning
HV_{500g}	Unit for Vickers hardness with 500g test load
ILL	Institut Laue Langevin
ISGMT	In-situ global mechanical tensioning
ISRT	In-situ roller tensioning
L	Longitudinal
N	Normal
PWGMT	Post weld global mechanical tensioning
PWRT	Post weld roller tensioning
RS	Residual stress
RT	Roller tensioning
SP	Shot peening
LSP	Laser shock peening
T	Transverse

1 INTRODUCTION

In this dissertation the effectiveness of three mechanical stress engineering techniques, for the mitigation of potentially deleterious tensile welding residual stresses (RS) and the closely related component distortion, arising in welds of high strength aluminium alloy plates joined by friction stir welding (FSW), is investigated. This is an important issue as high strength aluminium alloys are primarily used in the weight sensitive aerospace industries and the relatively new solid state FSW technique allows joining these materials. As such FSW is an attractive alternative to the currently used costly and work intensive riveting technique. Even though FSW is considered as a low stress welding technique, the induced weld-line RS still may affect the component fatigue and in service life time performance. Stress engineering applied either in–situ or post welding allows the mitigation of detrimental RS and as such to improve the component performance.

In this introductory chapter the research program from which this dissertation originated and the background for this research is summarized. Further, the different research objectives, the research approach, the conventions used in this work and an outline of the work performed and reported in this dissertation is given in the final sections of this chapter.

1.1 THE SEALS PROJECT

This dissertation originated from the SEALS (Stress Engineering for Application to Large Structures) program, a research project initiated and led by Prof. S. W. Williams, Cranfield University, UK. The program involved numerous industrial companies such as AIRBUS, UK, Bombardier, UK, or BAe Systems and BAe ATC Naval Systems, UK. The aim of this program was to investigate several thermal and mechanical stress engineering techniques applied to aluminium and steel components from the aircraft as well as ship building industries joined either by tungsten inert gas welding (TIG), submerged arc welding (SAW) or FSW in order to control and minimize RS and the related distortion. It was intended to propagate the knowledge and the maturity level of the stress engineering techniques to a point allowing for their large scale industrial application.

The SEALS program was divided into two industrial areas, namely ship building and aircraft production. The aircraft production field was sub-divided into several work

packages. One these packages included the experimental determination and prediction, by means of finite element modelling (FEM), of welding induced RS in high strength aluminium alloy plates joined by FSW and mechanical stress engineering techniques applied either in-situ or after welding. It is this work package that this experimentally based dissertation originated from. In order to understand the importance of this research objective the following section will briefly introduce the reader to the background to this work.

1.2 RESEARCH BACKGROUND

Stresses can be categorized as those generated as a result of an external load (reaction stresses) and those that are internal to a body, when all external loads are removed. These internal stresses are termed residual stress (RS). RS must be in equilibrium with themselves and the resultant force and momentum produced by the RS must vanish (Masubuchi 1980). RS are caused by chemical, thermal or plastically induced volumetric material misfits in different regions within one body (Withers *et al.* 2001b) Such misfits may arise from non-uniform temperature changes leading to non-uniform local material expansion and/or contraction as it is the case during welding, where a significant non-uniform temperature profile, high temperatures at the weld-line and only slightly elevated temperatures in the far field, is introduced. The resulting elastic material misfit between these regions leads to RS.

The maximum RS within a body is limited by the local yield strength σ_{YS} of the material. RS exceeding this limit will be relaxed by plastic deformation. Depending on the material, the weld geometry and the degree of clamping during welding, distortion as a result of RS may occur along (bending or buckling) and across the weld-line (angular/butterfly) as well as rotational distortion and shrinkage may be caused (Masubuchi 1980; Masubuchi 2003; Bhide *et al.* 2006). Welding distortion due to RS can be a significant problem and may require expensive post-weld correction procedures (Williams *et al.* 2006).

High strength aluminium alloys, such as those from the AA2xxx and AA7xxx alloy groups with a high strength to weight ratio, are important structural materials for the transportation industries (Williams *et al.* 2003). Application of these materials allows for increased payloads or fuel savings and therefore better economic performance. This is

especially required in the aerospace industry. However, not just the economic performance of the aircraft is vital for the aircraft manufacture and the customer airlines competitive strength, even more important is the safety and the structural integrity of the aircraft. The optimized structural design and the selective application of high strength aluminium alloys for structural purposes allows these requirements to be fulfilled and it is therefore that the high strength aluminium alloys are of importance for the aviation industry (Williams *et al.* 2003).

High strength aluminium alloys are often considered to be non-fusion weldable due to poor post weld mechanical properties (Polmear 1995; Kou 2003; Leonard *et al.* 2003; Threadgill *et al.* 2009). An alternative recently introduced method is the solid state friction stir welding (FSW) technique. In the aviation industry, FSW is a potential replacement joining method for the time, work and cost intensive riveting technique currently used for assembling aircraft components, leading to additional weight savings as material overlaps required for riveting, can be avoided. Even though FSW is considered as a solid state welding technique with comparatively low temperatures, it may introduce significant RS and distortion in high strength aluminium alloy components, which affect the fatigue behaviour and therefore the lifetime and in service performance of these components (James *et al.* 2007b; Withers 2007).

As a result stress engineering techniques, for example the mechanical tensile loading of welds, has been suggested as a means of reducing the RS and distortion in welded structures (Yang *et al.* 1998; Staron *et al.* 2004; Xu *et al.* 2004; Price *et al.* 2007; Richards *et al.* 2008a; Williams *et al.* 2008; Wen *et al.* 2009). This mechanical loading can be performed during, or after, welding and can be categorized as *global*, where the entire component is mechanically tensioned, or *local*, where the loads are restricted to a small region. The former method applied during welding is termed in-situ global mechanical tensioning (ISGMT) and the load is introduced by direct uniaxial tensioning along the welding direction (Staron *et al.* 2004; Williams *et al.* 2006; Price *et al.* 2007). This method can also be applied after welding is completed and is then termed post weld global mechanical tensioning (PWGMT) (Williams *et al.* 2006; Price *et al.* 2007; Williams *et al.* 2008). Both techniques work by exceeding the local weld-line yield strength σ_{YS} and as such introduce plastic strain. As a result, upon load removal the remaining elastic strain hence the RS are reduced in magnitude and less component distortion arises upon removal of the weld clamping.

Local mechanical tensioning, on the other hand, can be applied using rollers that are moved along the weld-line (Williams *et al.* 2008; Wen *et al.* 2009) applying a specified down force resulting in material compression in the plate normal direction. This compression is compensated mainly by plastic elongation in the rolling direction and as a result reduces the weld-line RS and component distortion. Similar to the global tensioning technique one can differentiate between in-situ roller tensioning (ISRT) or post weld roller tensioning (PWRT).

1.3 RESEARCH OBJECTIVE

This dissertation intends to improve the understanding of the ISGMT, ISRT and PWRT techniques for mitigating RS arising from FSW high strength aluminium alloys. The aim of this research is twofold. Firstly, it is intended to increase the understanding of the correlation of the ISGMT load applied during FSW of high strength aluminium alloys and the mitigation of the final RS, as well as the achieved reduction of component distortion. Secondly, this research aims to investigate the RS and distortion mitigation effects of different ISRT and PWRT loads applied during and after FSW of high strength aluminium plates, respectively, and as such to determine the efficiency of these techniques.

In detail this research aims to investigate the precise correlation of the ISGMT load applied during FSW on the final RS distribution, while all remaining welding parameters are constant. Further, the component distortion, microstructure and post weld hardness distribution as functions of tensile loading are investigated. The idea of controlling welding RS by ISGMT is not new. Recent work (Staron *et al.* 2004; Price *et al.* 2007; Richards *et al.* 2008a; Williams *et al.* 2008) found that this technique is very powerful by means of reducing the longitudinal tensile RS. However, no general agreement on the precise tensile load necessary to produce stress free welds was found. The general target of this dissertation was to formulate a universal rule upon which an engineer can determine the ISGMT load necessary to produce a nearly stress free weld.

In comparison, the ISRT and PWRT techniques for mitigation of RS are relatively new. Even though rolling has been used previously to reduce hot cracking in aluminium welds (Yang *et al.* 1998), the application for reducing RS and distortion is relatively new. A first approach to understand the technique was made by Wen *et al*. (2009) using FEM. However, from the experimental investigation point of view no results, in terms of the RS

and distortion mitigation achieved by ISRT or PWRT, are available in the literature. Therefore, this research aims to supply experimental data as well as to improve the understanding of this technique and to give a better idea of the effectiveness of the process.

In detail this research will include the following subtasks:

- determination of the importance of the variation of the elastically unstrained unit cell parameter for the determination of RS in high strength aluminium alloys using diffraction techniques,
- an investigation of the effect of sectioning test welds on the relaxation of the RS to determine a minimum sample size that reflects real component RS,
- the investigation of the effect of different levels of ISGMT loads on the welding RS, the resulting distortion and the mechanical properties of the welded structure in high strength aluminium alloys joined by FSW,
- the investigation of the effect of ISRT and PWRT to understand the phenomenon itself as well as the effectiveness of this technique for RS reduction and
- the investigation of the effectiveness of PWRT as applied to a set of near application welds, produced in integrated stiffener panels (ISP), which are intended to be used for wing skin production,
- and finally the practical aspects of these mechanical stress engineering techniques will be discussed.

1.4 RESEARCH APPROACH

In this dissertation the effect of the above mentioned mechanical stress engineering techniques for mitigation of RS and component distortion, when applied to high strength aluminium alloy plates joined by FSW has been investigated mainly by using experimental measurements. While this approach allowed the final RS distribution to be determined as a function of the applied stress engineering technique, finite element modelling would allow monitoring of the mechanisms acting during the application of each technique and consequently to predict the RS mitigation. However, this part of the SEALS work package was undertaken by D. Richards from the University of Manchester. The actual amount of FEM work performed in this dissertation is that limited to re-designing and running an

existing model created by D. Richards, while experimental results obtained in this dissertation were feedback to evaluate and improve the FE models. The FEM results are included in this dissertation to back up and explain the experimental results.

Seven sets of welds, produced in AA2xxx and AA7xxx high strength aluminium alloys using FSW, form the basis for this research. Four sets of welds were produced with ISGMT applied while the welds in the other three sets were subject to ISRT and PWRT. While the FSW conditions within each set of test welds were constant the applied stress engineering techniques were varied within their own specific parameter range: the tensioning load in case of ISGMT and the roller down force in case of ISRT and PWRT. All welds were investigated at mid length of the weld path in terms of the reduction in RS as a function of the stress engineering technique applied. Further, the sample distortion, the post weld hardness and microstructure were investigated with the aim of determining possible secondary effects. The results from this experimental approach form a basis upon which this research aimed to formulate a general rule for the application of the ISGMT technique and enhance the industrial relevance of this technique. On the other hand, as roller tensioning is a relatively recent stress engineering technique, the effectiveness of this technique will be demonstrated and the possible acting mechanisms discussed.

1.5 CONVENTIONS AND DEFINITIONS

1.5.1 Coordinate system

All results presented in this dissertation are spatially related to the geometry of the rectangular test welds. The geometry of the test welds is defined by the plate length (l) × width (w) × plate thickness (t_m) as shown in Figure 1.1. All length scales in this dissertation are given in *mm*. A rectangular right hand side coordinate system is used for the description of spatial parameters and results in the test welds. In all cases the x-axis coincides with the welding direction and is referred to as the longitudinal direction. The in-plane y-axis, is referred to in this dissertation as the transverse direction and is perpendicular to the weld-line and parallel to the (un-deformed) plate surface. The z-axis is perpendicular to the two former axes and is referred to as the normal direction. The origin of the coordinate system is fixed at the mid length of the weld-line at the weld surface. Unless stated otherwise, the positive longitudinal axis (+x) represents the feeding direction of the FSW tool and the

positive transverse axis (+y) is towards the advancing side of the FSW process. Direction dependent parameters, or results, are indicated with a subscripted *L* for the longitudinal, *T* for the transverse and *N* for the normal directions.

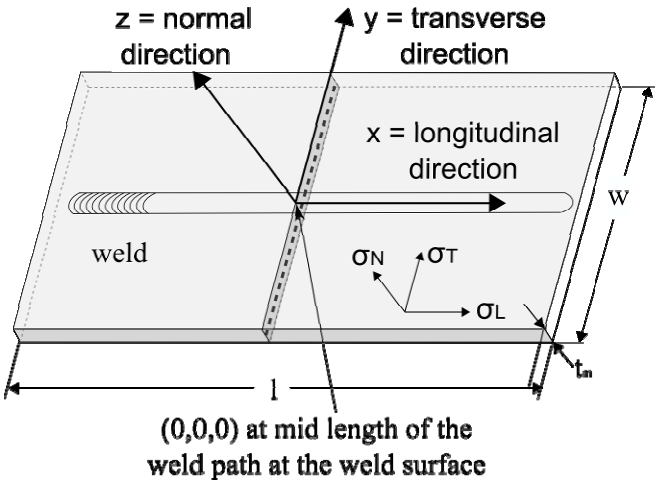

Figure 1.1: Definition of the plate geometry (length *l* × width *w* × material thickness t_m) and the coordinate system used for all spatial results throughout this dissertation. The origin of the coordinate system is placed at mid length of the weld path (=½ l) at the weld surface.

1.5.2 Units

Unless stated otherwise SI-units are used to define parameter values and constants and to present the results throughout this dissertation.

1.5.3 Strain and stress

In this dissertation compressive strains and stresses are negative, while tensile strains and stresses are positive. As indicated in Figure 1.1, the longitudinal stresses are defined as those acting along the longitudinal direction and are indicated with a subscripted *L*, while transverse stresses act in the transverse direction and are indicated with a subscripted *T*. The stresses acting in the weld normal direction are indicated with a subscripted *N*.

1.5.4 Abbreviations and sample designation

The abbreviations used in this dissertation are written out when appearing for the first time in each chapter. However, an overview of all abbreviations used in this work is given in the beginning of this dissertation. The test welds in this dissertation are grouped into four

sets (#1 to #4) of three or four test welds for investigation of the ISGMT technique, and three sets (#5 to #7) of three, five and four test welds for investigation of the ISRT and PWRT techniques. Each test weld is labelled using an X-Y-Z code, where X is the set number, Y is the material designation and Z is the varying stress engineering parameter (for ISGMT the applied tensile load in MPa and for the roller tensioning the roller down force in kN). The test weld designations are detailed in Table 3.2 and Table 3.4.

1.6 DISSERTATION OUTLINE

This dissertation is divided into seven chapters. In chapter one the reader is introduced to this dissertation. In chapter two the background information on high strength aluminium alloys, the FSW technique, the development of welding induced RS in general and with respect to FSW is given. Further, the current state of the art of existing stress engineering techniques and the determination of RS using diffraction techniques are discussed. In chapter three the experimental techniques and instrument set-ups as employed and used throughout this dissertation are detailed. The results of two initial investigations are presented in chapter four. These studies include the mapping of the variation of the elastically unstrained unit cell parameter a_0, using three techniques, and its influence on the calculated magnitude of RS. A second study was undertaken to determine the effect of stress relaxation upon sectioning of test welds. The aim was to derive an empirical rule of thumb that would allow an estimation of the minimum test weld size required to contain RS comparable in magnitude to those present in real size engineering components. In chapter five and six the experimental results on ISGMT, ISRT and PWRT obtained throughout this research are presented and discussed, as well as compared with those predicted by FEM as reported in the literature and obtained from the FEM work performed in this dissertation. However, since modelling was not a main objective of this dissertation the results will only be compared for selected sets of welds.

For clarity, detailed discussions of the results are provided on a chapter by chapter basis. However, the last chapter includes a general discussion and summary of the results from the presented work and points out goals for future work.

2 BACKGROUND

2.1 INTRODUCTION

In this chapter the author aims to review the literature required to follow through this dissertation. The first sections in this chapter address the high strength aluminium alloys and the maturing friction stir welding (FSW) technique for joining such aluminium alloys, the development of welding induced residual stress (RS) in general, as well as with respect to FSW, of high strength aluminium alloys and the RS related component distortion. Afterwards the state of the art of currently available thermal and mechanical stress engineering techniques are reviewed with special attention given to the in-situ global mechanical tensioning (ISGMT) as well as in-situ (ISRT) and post weld roller tensioning (PWRT) techniques, as these three techniques are the main subject of this dissertation. In order to evaluate the effectiveness of ISGMT, ISRT and PWRT for mitigation of RS and distortion it is necessary to determine the RS distribution as a function of relative position to the weld-line and weld-surface. In this project the non-destructive angular dispersive neutron diffraction (ADND) and energy dispersive synchrotron X-ray diffraction (EDXRD) techniques were used to determine the RS as a function of position and the applied stress engineering technique. These diffraction techniques and their related problems are discussed in the last section of this chapter.

2.2 HIGH STRENGTH ALUMINIUM ALLOYS

An evaluation of the mechanical properties of welded high strength aluminium alloys requires an understanding of the main strengthening mechanisms, as well as the effect elevated temperatures, as for example during FSW (see section 2.3), may have on the subsequent material properties. An introduction to the strengthening mechanisms in high strength aluminium alloys is given in this section.

High strength aluminium alloys from the AA2xxx and AA7xxx series develop their strength mainly by precipitation or age-hardening. Consequently, it is useful to introduce the precipitation mechanisms that occur in these aluminium alloys. The main requirement for an alloy to respond to precipitation hardening is a significant decrease in solid solubility of the alloying elements with decreasing temperature. The general procedure for

precipitation-hardening of aluminium alloys to optimise their mechanical properties (for example maximise the material strength) requires the following steps:

- Solution heating above the solvus temperature within the single phase region, so as to dissolve all alloying elements,
- Quenching the material in order to form a supersaturated solid solution (SSSS) of the alloying elements within the aluminium matrix.
- Aging by thermal treatment in order to decompose the SSSS, so as to form a fine dispersion of precipitates. This can be done at elevated temperatures (artificial aging) or at room temperature (natural aging). However, this step is very sensitive to the temperature and even slight variations may result in significant deviations in the precipitation microstructure (Polmear 1995) and mechanical properties.

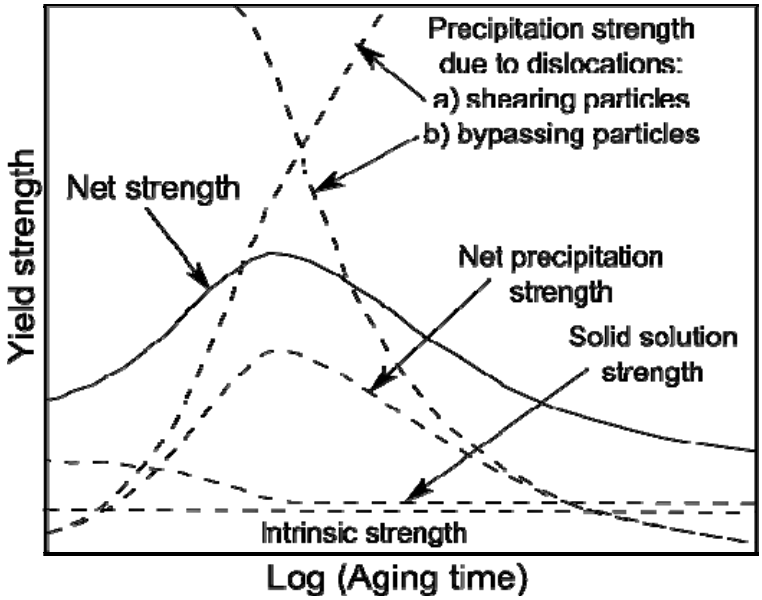

Figure 2.1: Schematic diagram showing the contribution to strength increase relative to the intrinsic material strength from solid solution strengthening and precipitation hardening (Shercliff *et al.* 1990).

The aim of age-hardening is to form finely dispersed precipitates. Once formed these precipitates cause lattice distortions thus impeding dislocation motion and as such increase the yield strength σ_{YS} and hardness of the material (Shercliff *et al.* 1990; Polmear 1995; Maloney *et al.* 1999). However, moving dislocations will cut or shear through Gunier-Preston zones (GPZ) (Polmear 1995) which range from Å to a few nm in size (Dumont *et al.* 2006) and are the coherent and closely spaced initial precipitates after solutionzing. The

cutting is indicated by the dashed line a) in Figure 2.1. In this so-called under-aged condition the peak strength is not achieved (for example T3 temper). As aging proceeds the precipitates grow and dislocations can no longer cut through them as easily which results in increased material strength. As coarsening continues the particle strength and spacing increase further until the dislocations start bypassing the precipitates by bowing around them ("Orowan bowing"). Consequently, the material strength decreases again as depicted with line b) in Figure 2.1. This is the over-aged condition (for example T8 temper). Highest strength is achieved where the contribution of cutting/shearing and bypassing intersect as shown in Figure 2.1. Material in this condition is called peak-aged and designated as T6 temper. Further strengthening of high strength aluminium alloys may arise from solid solution strengthening or any cold work applied (Shercliff *et al.* 1990) as also depicted in Figure 2.1, but in general the contribution from these mechanisms is small in comparison.

During welding of high strength aluminium alloys using FSW (see section 2.3) the material experiences a thermal cycle local to the weld-line, which is comparable in magnitude and time history to the procedure for precipitation-hardening. As the formation and structure of precipitates is extremely sensitive to the aging temperature and time, the local weld thermal cycle may result in significant changes of the local precipitate microstructure. Indeed, from previous work one can expect major variations in the distribution, size and density of precipitates and subsequently mechanical properties across a weld arising as a result of the thermal-mechanical cycle as imposed by the FSW (Peel *et al.* 2003; Su *et al.* 2003; Genevois *et al.* 2005; Jones *et al.* 2005; Dumont *et al.* 2006; Kamp *et al.* 2006). In this dissertation numerous different materials were used for the different investigations. However, the high strength aluminium alloys mainly from the lithium containing AA2xxx and AA7xxx series are of most importance for this dissertation, hence it appears useful at this point to introduce the reader to the general precipitation sequences and precipitate microstructures of these materials in the following sections

2.2.1 Precipitation in Aluminium-Lithium alloys

In this dissertation the low density AA2199-T8E74 aluminium-lithium alloy (composition see Table 3.1), as developed by Alcoa.Inc, was used for test weld production. Due to the relatively recent development of the material little is known about the precise

precipitation sequences (Khelifati *et al.* 2006). Nevertheless, similar lithium containing aluminium alloys have been examined before and the following general precipitation sequences during aging and precipitate compositions were determined (Polmear 1995; Huang *et al.* 1998):

$$\text{SSSS} \rightarrow \text{cubic or spherical } \delta' (Al_3Li) \rightarrow \text{cubic } \delta (AlLi)$$
$$\rightarrow \text{thin hexagonal platelets } T_1 (Al_2LiCu)$$

In binary Al-Li alloys the strengthening is achieved by the formation and homogeneous distribution of coherent, metastable cubic or spherical δ' (Al_3Li) precipitates. Further aging leads to the nucleation of the additional heterogeneous δ (AlLi) phase forming primarily in the grain boundaries (Polmear 1995; ASM_4 2001). The addition of Cu and Mg plays an important role on strengthening as these elements lower the solubility of lithium. Other phases have been reported to form in such kind of systems, like T_2 (Al_6CuLi_3) precipitating on grain boundaries having a major effect on the toughness. Phase such as T_B (Al_7Cu_4Li), Θ' and Θ''(Al_2Cu) depend significantly on the quenching rates in Al-Li alloys (Csontos *et al.* 2000) and are therefore difficult to adjust. Traces of Zn are added to improve the corrosion resistance and Zr and Mn to control the grain structure by the formation of fine dispersoids (Polmear 1995).

2.2.2 Precipitation in AA7xxx Aluminium Alloys

In this dissertation the high-strength AA7449-W51aluminium alloy (composition see Table 3.1) was mainly used for test weld production for this dissertation. The overall consensus for the precipitation or un-mixing sequence from the super saturated solid solution (SSSS) in high strength AA7xxx (Al-Zn-Mg) aluminium alloys can be summarized as the formation of several phases (Polmear 1995; Schmuck *et al.* 1995; Maloney *et al.* 1999; Sha *et al.* 2004; Dumont *et al.* 2006; Kamp *et al.* 2006):

$$\text{SSSS} \rightarrow \text{GP zones (GPI and GPII)}$$
$$\rightarrow \text{Metastable hexagonal } \eta' (MgZn_2) \rightarrow \text{Stable hexagonal } \eta (MgZn_2)$$
$$\rightarrow \text{Metastable cubic T'} (Mg_{32} (A1, Zn)_{49}) \rightarrow \text{Stable cubic T} (Mg_{32} (A1, Zn)_{49})$$

GPZ in AA7xxx alloys are generally described as small solute enriched spheres (Polmear 1995). GPI zones contain Zn, Mg and Al and are coherent with the matrix and form over a wide aging temperature range (room temperature to 150 ºC). GPII zones are Zn-rich plates forming after quenching from above 450 ºC and aging above 70 ºC (Sha *et al.* 2004). Nevertheless Godard *et al*. (2002) reported that formation of GPZ and subsequent precipitates may already have taken place during quenching. Either GPI or both, GPI and GPII, zones may form and act as precursors to the metastable η' phase. A substantial amount of copper (1.8 to 2.4 wt%) may be added to increase the temperature range of stable GPZ (Srivatsan *et al.* 2000; Sha *et al.* 2004) that may grow to the metastable η' phase. This phase is fully coherent with the matrix and precipitates in platelet form. The fine dispersion of η' particles is believed to be the main strengthening factor, and hence it is important to achieve this state when highest strength is desired (Sha *et al.* 2004).

The structure of the subsequent η phase is similar to the equilibrium phase $MgZn_2$ and appears in platelet, rod or sphere shapes. The occurrence and growth of this phase is associated with a decrease in hardness and strength (Polmear 1995; Schmuck *et al.* 1995; Sha *et al.* 2004). Further, the T phase (Mg_{32} (A1, $Zn)_{49}$) may be present in small quantities (Polmear 1995; ASM_4 2001).

Overall the precipitation process is a complex function of the applied temperatures and, in the case of the AA7xxx series alloys also the time of temperature exposure. The different precipitation steps may progress simultaneously and the exact type and final size of precipitates occurring depends on the amount and ratio of Mg and Zn and the time history of the quenching and aging process (Polmear 1995).

The aluminium-lithium as well as the high strength aluminium alloys are of particular interest for the aviation industry due to low density, hence weight, as well as the high strength that is achieved by precipitation hardening. However, additional weight reductions can be achieved by replacing the riveting and fastening methods currently used for joining structural aircraft components, if such aluminium alloys could be joined by welding. This would avoid material overlaps and reduce the use and weight of the fasteners. As these alloys are commonly considered as 'non-weldable' by fusion welding, the relatively new but maturing FSW technique can be considered as an attractive alternative technique for joining such difficult-to-weld aluminium alloys. This technique is detailed in the following section.

2.3 FRICTION STIR WELDING

2.3.1 Introduction

High strength aluminium alloys are mainly applied in aerospace engineering applications because of their high specific strength as well as their comparatively low density (Heinz *et al.* 2000; Lequeu *et al.* 2001; Williams *et al.* 2003). These alloys are generally classified as 'non-weldable' by fusion welding because of hot cracking upon cooling, as well as poor post weld microstructure and porosity in the weld zone (Leonard *et al.* 2003). Alternatively, the maturing solid-state Friction Stir Welding (FSW) technique can be used to join aluminium alloys, as well as other metals, that are difficult to join by conventional fusion welding. FSW was developed in 1991 at 'The Welding Institute' (TWI) in the UK (Thomas *et al.* 1991). The technique generally avoids melting the material, hence the produced welds offer several advantages, such as better preservation of baseline mechanical properties, reduced RS, less distortion and fewer weld defects (Mishra *et al.* 2005; Threadgill *et al.* 2009). In the following sections the FSW process, the process parameters and the typical FSW microstructures are detailed and some recent FSW applications are highlighted.

2.3.2 Friction Stir Welding Process: Basic Principles

The basic concept of FSW is remarkably simple, as shown in Figure 2.2a. A non-consumable rotating tool, comprising a cylindrical tool shoulder and a specially designed tool pin, is forced into the abutting edges of the components and subsequently traversed along the joint line. Interface friction increases the work pieces' temperature and the stir deformation of the softened material forms a solid state weld. No special weld seam preparation is required. In detail the FSW process comprises of the following steps (Thomas *et al.* 1991; Mishra *et al.* 2005; Threadgill *et al.* 2009):

- The components are clamped firmly to the backing plate to avoid separation of the plates by the forward moving tool and to react the welding down force.
- The rotating tool is lowered until the pin completely penetrates the material and the tool shoulder touches the plate surface and exerts a preset down force (force control mode).

- The friction in the tool shoulder-material interface generates near melting point temperatures, hence metal in this area softens, while lower temperatures and less softened material occur around the tool pin closer to the weld root as well as lateral to the FSW tool.
- After a stationary period termed the *dwell* to heat up and soften the surrounding material the rotating tool is traversed along the joint line thereby heating, softening and stir deforming the interface of the components. The soft metal in front of the tool is drawn in by the tool shoulder and pin and moved around (stirred) horizontally and vertically in a complex manner depending on the tool shoulder and pin design, before it is forged to the back of the weld tool, where it forms a coherent weld upon cooling.
- When the end of the weld path is reached the tool is simply extracted from the material leaving an *exit-hole* behind. Usually both the dwell point and the exit hole are cut off the welded structure.

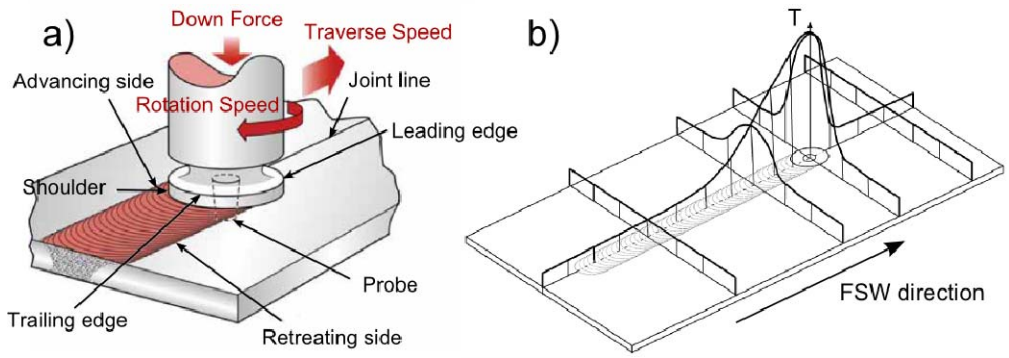

Figure 2.2: (a) Illustration of the FSW technique (Birch 2005) and (b) the typical temperature distribution as modelled for an AA2024-T3 friction stir weld (after Wen *et al.* 2009).

FSW is an asymmetric process as the two sides of the weld experience different welding conditions. On the so-called advancing side (see Figure 2.2a) the tool rotation and translation coincide resulting in greater relative tool motion. On the opposite, the retreating side, the tool rotation and translation counteract. Further, the front of the tool may be referred to as the leading edge while the back side is termed trailing edge (Thomas *et al.* 1991; Mishra *et al.* 2005; Threadgill *et al.* 2009).

The peak temperature during FSW depends on the welding parameters, but generally is below the material melting point. The typical temperature distribution is illustrated in

Figure 2.2b. In front of the moving tool a significant temperature gradient from room to peak temperature builds up (Tang *et al.* 1999). Upon cooling behind the FSW tool the temperature decreases relatively slowly while also spreading out to each side hence widening the temperature profile before decreasing back to room temperature far behind the tool (Wen *et al.* 2009).

2.3.3 Process Parameters

The efficiency of the FSW process as well as the final microstructure and hence the post weld mechanical properties of high strength aluminium plates joined by FSW are determined by a number of process parameters. Three significant parameters are the clockwise- or counter-clockwise tool rotation rate w_{rot} [rpm], the tool traverse speed v_t [mm/min] along the weld-line and the tool down force F [kN]. For the production of the test welds used in this dissertation a load controlled FSW machine was used and therefore the down force F was the parameter of interest, rather than the tool plunge depth which is the equivalent parameter for position controlled machines. Parameters such as the tool tilt angle, tool design and material, as well as the weld design and degree of clamping, are also important factors and may have significant influence on the FSW performance. However, a detailed description of these parameters is beyond the scope of this section and may be found elsewhere (Thomas *et al.* 1991; Mishra *et al.* 2005; Threadgill *et al.* 2009).

Even though much work has been done investigating the precise effect of the tool rotation rate w_{rot}, the tool traverse speed v_t and the tool down force F on the final weld properties (Tang *et al.* 1999; Sato *et al.* 2002; Peel *et al.* 2006a; Peel *et al.* 2006b; Steuwer *et al.* 2006b; Wei *et al.* 2007; Lombard *et al.* 2009), the overall interaction of these and the remaining parameters is complex and still ill understood. The following sections give a brief overview of the state of knowledge on the effects of the FSW parameters v_{rot}, v_t and F.

2.3.3.1 Tool Rotation and Tool Traverse Speed

The tool rotation speed v_{rot} as well as the tool traverse speed v_t have significant influence on the FSW process and must be chosen with care to ensure an efficient and successful welding cycle. In general a higher tool rotation rate at a constant tool traverse speed generates higher temperatures, as shown in Figure 2.3a due to increased tool-material

interface frictional heating (Tang *et al.* 1999; Sato *et al.* 2002; Peel *et al.* 2003). In turn this results in an increased amount of material around the tool being softened and hence intensifies the stirring and plastic flow of material (Tang *et al.* 1999; Thomas *et al.* 2005).

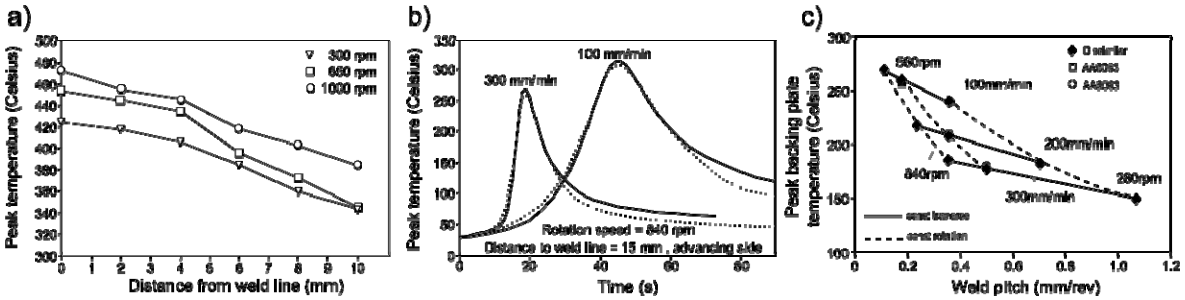

Figure 2.3: (a) The effect of the rotation speed on temperature distribution as a function of distance from weld-line in a 6.4 mm thick AA6061-T6 friction stir weld (tool shoulder Ø = 18 mm, pin Ø = 5 mm at 120 mm/min traverse speed (Tang *et al.* 1999). (b) The effect of different traverse speeds on the peak temperature as measured (solid) and predicted (dotted) 15 mm from the weld-line on the advancing side in an AA5083 FSW (Peel *et al.* 2006b). (c) Peak temperature at the weld root at below the weld-line for dissimilar and similar welds joined by FSW as a function of traverse and rotation speed (Peel *et al.* 2006b).

Melting of the material is mostly avoided as the maximum temperatures reach 80 % to 90 % of the material melting point (Tang *et al.* 1999; Zhu *et al.* 2002). Nevertheless, excessive rotation rates may be detrimental to the post weld mechanical weld properties such as the yield strength σ_{YS} or hardness as the material close to the weld-line may significantly overage (see section 2.2). On the other, hand for low tool rotation speeds the heat generation and material softening is insufficient causing a degradation of the material stirring. This may introduce weld defects such as tunnels (small, connected cavities parallel to the welding direction, mostly on the advancing weld side (Price *et al.* 2007)) or root flaws as shown in Figure 2.4 (Leonard *et al.* 2003; Wei *et al.* 2007). Further, the FSW tool may experience severe wear (Prado *et al.* 2001; Fernandez *et al.* 2004). In the worst case the tool may break due to the high reaction forces arising in the component material.

The tool traverse speed v_t has the opposite effect on the heat input compared to the rotation speed. At a constant rotation speed higher traverse speeds lead to lower temperatures as the material is exposed to frictional heating for less time as depicted in Figure 2.3b. On the other hand, very slow traverse speeds may lead to overheating of the material (Steuwer *et al.* 2006b; Lombard *et al.* 2008; Lombard *et al.* 2009).

Peel *et al.* (2006b) investigated the effect of both parameters on the weld temperature by combining the two parameters in the so-called pitch ($=v_t/ v_{rot}$). They reported results for

the peak weld-line temperature distribution at the weld root as a function of weld pitch for varying tool rotation and traverse speeds as shown in Figure 2.3c. A combination of low traverse speed and high rotation speed leads to highest weld temperatures and vice versa.

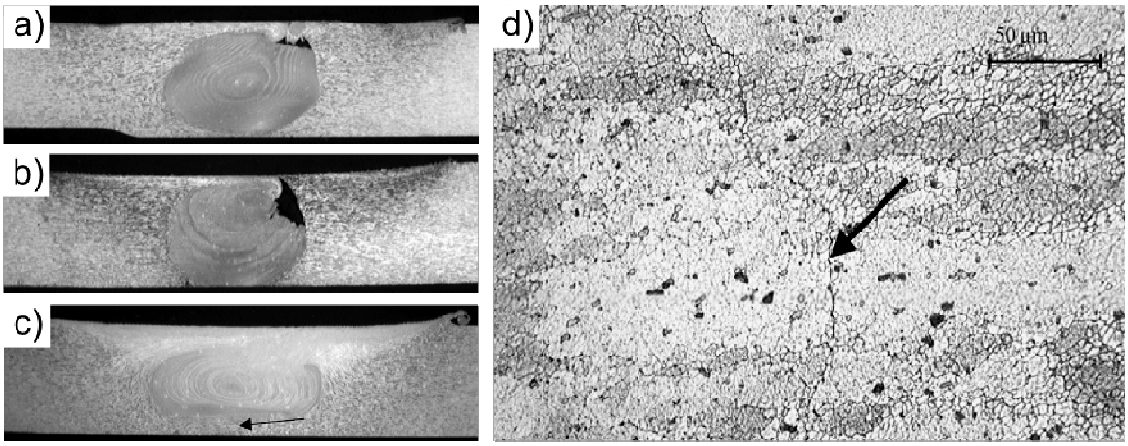

Figure 2.4: Different weld defects, which may arise from poorly adjusted welding parameters. All examples are from welds made in 6 mm AA2014; (a) tunnel defect below weld surface on advancing side, (b) surface breaking tunnel defect, (c) macrograph of a root flaw which is magnified in (d) (Leonard *et al.* 2003).

The optimum welding speeds vary for different aluminium alloys and weld geometries. While relatively thin sheet may be joined with tool rotation rates ranging from 800 to 1500 rpm, thicker material is usually joined at slower rates (Mishra *et al.* 2005; Threadgill *et al.* 2009). The tool traverse speeds may vary from 100 to 700 mm/min depending on the machine and FSW tool capabilities as well as the material response (Mishra *et al.* 2005).

2.3.3.2 Tool Down Force

Another significant parameter is the tool down force *F*. An increase in *F* has a similar effect as higher tool rotation speeds. The increased pressure leads to higher tool-material interface frictional heating resulting in increased welding temperatures (Mishra *et al.* 2005; Wei *et al.* 2007; Threadgill *et al.* 2009). However, care must be taken: On the one hand overheating is detrimental for the mechanical properties, but also the rotating tool shoulder may be pushed into the material surface producing a significant amount of flash (material that is squeezed and moved to the weld sides leading to weld path thinning as illustrated in Figure 2.5a. At the same time at the weld root the tool pin may touch the backing plate and eventually welding the work pieces to the backing plate, or the tool itself may experience

significant wear. On the other hand, an insufficient down force will not push the tool far enough into the work piece, hence the tool shoulder does not fully contact the component surface (see Figure 2.5b) resulting in insufficient or no frictional heating at all. This may result in ineffective stirring, which may cause inner and/or surface defects as illustrated in Figure 2.4. In addition as the material is insufficiently softened, the reacting forces on the welding tool may exceed the limits resulting in severe tool wear or even fracture (Prado *et al.* 2001). Nevertheless, such effects may also arise from variations in material thickness and a slow adjustment of the tool position and down force.

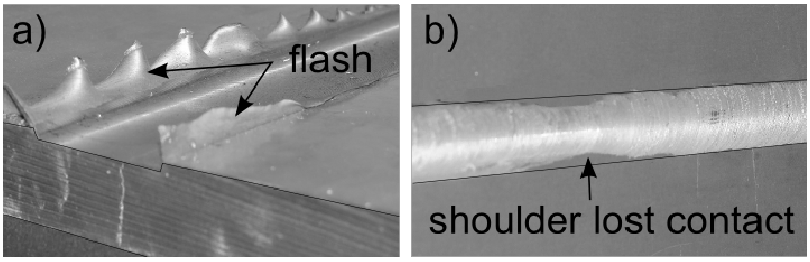

Figure 2.5: Illustration of the effect of the tool down force when it is (a) to big in a 20 mm AA7449 FSW with a down force of approximately 90 kN and (b) to low in a 5mm AA2199 FSW welded at 800 rpm, 400 mm/min and set down force of 1.5 kN (Poad 2007). In (a) also the plate thinning in the weld-line path due to the removal of material can be seen. However, such effects may also be due to variations in plate thickness.

2.3.4 Microstructure

The excessive plastic deformation of the weld-line material and the high temperatures during FSW of high strength aluminium alloys generates a highly characteristic macroscopic structure (Mishra *et al.* 2005; Dumont *et al.* 2006; Threadgill *et al.* 2009) as shown in Figure 2.6, which with increasing distance from the weld-line can be categorized into the following distinctive microstructural regions:

- the stir zone or weld nugget (*WN*) at the weld-line which is exposed to both high temperatures and severe plastic deformation due to the tool rotation,
- the thermo-mechanically affected zone (*TMAZ*) which experiences high temperatures and some plastic deformation due to stirring,
- the heat affected zone (*HAZ*) where elevated temperatures affect the microstructure, but no mechanical deformation occurs and

- the unaffected parent material (*PM*) far from the weld zone, where neither the stirring deformation in the weld zone nor the welding temperatures have any effects.

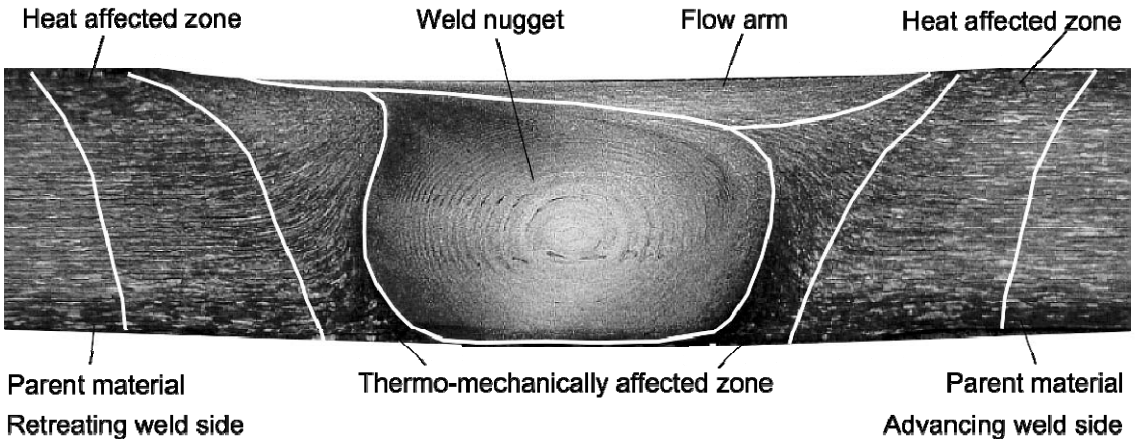

Figure 2.6: Cross-section (N-T plane) of a FSW showing the characteristic weld zones including the classical onion ring structure. This is a 10 mm AA6082 weld (Greitmann *et al.* 2005).

A detailed microstructural description of each zone is given in the following sections. As described above, the elevated temperatures during FSW of high strength aluminium alloys affect the local precipitation microstructure and it is therefore useful to review the current knowledge on the precipitation sequences during FSW at the end of this section.

2.3.4.1 The Stir Zone

FSW excessively deforms the stir zone, or WN material, and in combination with the high temperatures generates a recrystallised, equiaxed and fine-grained microstructure (Sato *et al.* 2002; Dumont *et al.* 2006; Kamp *et al.* 2006) which corresponds to the location and roughly the cross-section shape of the tool pin. Some authors distinguish between the WN and the so-called flow arm (see Figure 2.6) which consists of near surface material that is dragged from the retreating to the advancing weld side by the rotating tool shoulder (Greitmann *et al.* 2005; Peel 2005). Often reported features in FSW are the so-called 'onion rings' which may consist of alternating bands of fine and coarse grains appearing on the N-T cross-section in the WN. The formation of onion ring structures occurs as a result of geometric effects based on the extrusion of FSW tool pin shaped sheets of material during each rotation of the forward moving tool and as a result of the temperature distribution in the weld nugget (Rhodes *et al.* 1997; Krishnan 2002; Attallah *et al.* 2006).

The grain size in the WN depends on the dynamic recrystallization temperature during FSW (Mahoney *et al.* 1998; Murr *et al.* 1998; Benavides *et al.* 1999; Kamp *et al.* 2006) which is a function of the applied FSW parameters (Sato *et al.* 2002). It is often reported to be an order of magnitude smaller than the grain size in the PM (Murr *et al.* 1997). Different welding parameters (see section 2.3.3) resulting in different temperatures and hence grain sizes in the WN, but generally for FSW of high strength aluminium alloys it was found that the grain size may vary between ~1 µm to ~10 µm in the WN (Rhodes *et al.* 1997; Jata *et al.* 2000; Sato *et al.* 2002; Allehaux *et al.* 2003; Bussu *et al.* 2003; Su *et al.* 2003; Dumont *et al.* 2006; Kamp *et al.* 2006). External cooling by liquid nitrogen, water or methanol as applied by thermal tensioning (see section 2.5.2) may reduce the grain size to below 1 µm, as the dynamic recrystallization temperature and post weld grain growth is significantly reduced behind the FSW tool (Benavides *et al.* 1999; Su *et al.* 2003).

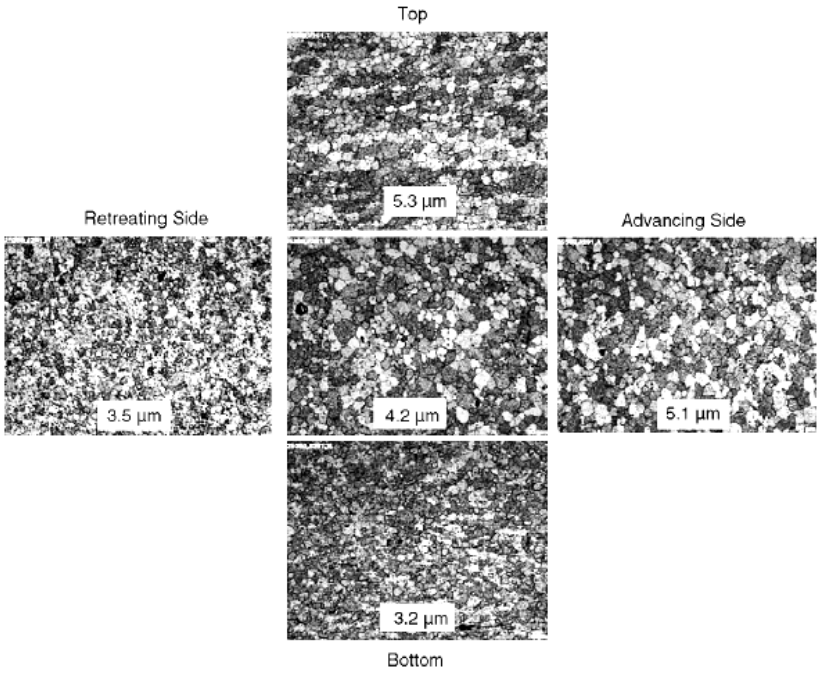

Figure 2.7: Grain size variation in the weld nugget of an AA7050 friction stir weld (Mishra *et al.* 2005).

A decrease in grain size from the weld surface to the bottom as well as from the advancing to the retreating side within the WN (see Figure 2.7) was also reported by Sato (2002) and Sutton (2002). This observation supports the assumption of through thickness as well as across weld-line temperature gradients, which affects the dynamic recrystallization during FSW. While lateral temperature gradients can be explained by the asymmetry of the

FSW process (see section 2.3.2), the through thickness temperature variation is due to the fact that significant heating is accomplished by the tool shoulder at the weld surface, but less frictional heat is produced by the tool pin (Richards *et al.* 2008a). Further, the backing plate cools the components from the weld bottom thus increasing the through thickness temperature gradient.

2.3.4.2 The Thermo-Mechanically-Affected Zone

In contrast to common fusion welding techniques FSW produces a TMAZ, a distinct zone intermediate between the WN and the HAZ (see Figure 2.6).

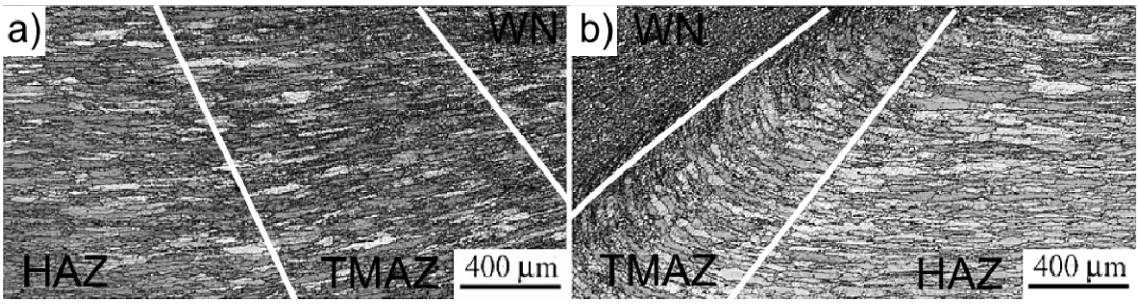

Figure 2.8: The grain structure of the TMAZ and HAZ on a) the retreating and b) the advancing side of an AA 7449 FSW (Dumont *et al.* 2006).

The TMAZ experiences high temperatures and some plastic deformation. The TMAZ microstructure consists of both grains of original size and structure and grains that are mechanically deformed by the stirring and partly recrystallised due to the elevated process temperatures. The grains are partly distorted and rotated following the tool shoulder and pin motion to varying degrees (Dumont *et al.* 2006) as shown in Figure 2.8a for the retreating and in Figure 2.8b for the advancing side of an AA7449 friction stir weld. Note that the TMAZ boarder is more distinct and narrow on the advancing side, while on the opposite weld side it is wider and some what indistinct (James *et al.* 1999; Dumont *et al.* 2006).

2.3.4.3 The Heat Affected Zone

The zone adjoining the TMAZ with increasing distance from the weld-line is the HAZ. The grain structure in this zone experiences no plastic deformation but is still affected by a

thermal cycle. As a result grain growth may occur, but in general the PM grain structure remains (Mahoney *et al.* 1998; Mishra *et al.* 2005) as depicted in Figure 2.8.

2.3.4.4 The Variation of the Precipitation Microstructure

With respect to the solid state character of FSW of high strength aluminium alloys the temperatures locally induced are below the material melting point (Tang *et al.* 1999): yet they may be sufficient to induce local changes in the precipitate microstructure around the weld-line (Sha et al. 2004; Dumont et al. 2006; Kamp et al. 2007; Sullivan et al. 2008). As a result, the weld-line mechanical properties may alter significantly. The prediction of these effects is difficult as the influence of the thermal excursion on the precipitates depends strongly on their initial structure, coherency, size and volume fraction (Kamp *et al.* 2006; Kamp *et al.* 2007). As indicated in section 2.2 at any given time and temperature the following may occur: complete dissolution of existing precipitates; partial dissolution and/or coarsening of existing precipitates; or nucleation and growth of new precipitates (Dumont et al. 2006). These mechanisms may continue even after the weld thermal cycle is complete: the remaining solute may form new precipitates, which subsequently may grow by natural ageing.

These effects have been discussed numerously (Rhodes *et al.* 1997; Maloney *et al.* 1999; Jata *et al.* 2000; Su *et al.* 2005; Kamp *et al.* 2006) and in detail for the AA7xxx series as used in this dissertation (Robson *et al.* 2001; Robson 2004b; Robson 2004a; Dumont *et al.* 2006; Kamp *et al.* 2007; Sullivan *et al.* 2008). In the following paragraph a brief summary of the precipitation variation in the AA7xxx series alloy used here, due to the local thermal exposure during FSW in the various weld zones, is given.

Dumont *et al.* (2006) performed an exhaustive experimental study on the precipitate and micro-hardness distribution across the weld zone in a high (350 mm/min) and low (175 mm/min) traverse speed friction stir weld in 6.5 mm thick AA7449-T3 (under-aged) and -T79 (over-aged) material produced with a constant rotation speed (350 rpm). They reported that the various weld zones experience different precipitation behaviour as a result of the initial temper and the varying thermal field during welding. As a consequence of such changes in the precipitation microstructure, the mechanical properties, such as the hardness, may vary. In detail they reported (Dumont *et al.* 2006):

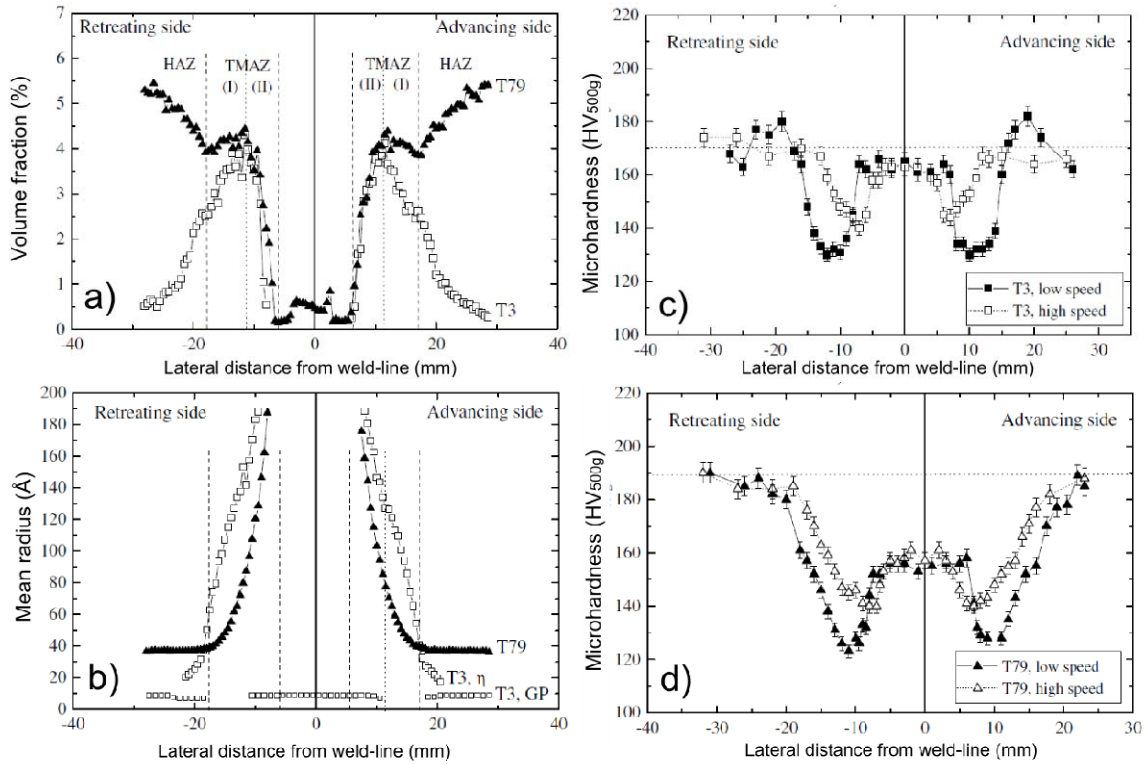

Figure 2.9: Comparison of (a) the volume fraction and (b) the mean radius of strengthening precipitates (GP zones and η-precipitates) as a function of lateral distance from the weld-line in a 6.5 mm thick AA7449-T3 and –T79 friction stir weld. In (c) and (d) the hardness distribution as a result of the precipitation variations is depicted for varying traverse speeds (Dumont *et al.* 2006).

- Due to dissolution of smaller η-precipitates in the T79 temper the precipitate volume fraction in the HAZ decreased compared to that in the PM (compare Figure 2.9a and Figure 2.9b with the remaining precipitates attaining a constant mean radius. Once a critical number of solute atoms dissolved into solution, competing particle coarsening may start, but the remaining time at high temperatures is too short for this to have a significant effect. As a result the hardness decreases slightly in the HAZ as depicted in Figure 2.9d. In the under-aged condition (T3 temper) the initial small GP zones may dissolve and upon cooling re-precipitate, while the initial small η-precipitates may grow slightly leading to a possible increase in volume fraction and possibly in hardness (Figure 2.9c).
- The TMAZ displays two regions of different behaviour, as depicted in Figure 2.9a. In the outer zone of the TMAZ a constant (T79 starting temper) and an increasing (T3 starting temper) volume fraction of η-precipitates can be observed. In the second region closer to the WN the volume fraction decreases

for both initial tempers. The mean radius of the precipitates steadily increases in both zones as can be seen in Figure 2.9b. In the T79 weld this behaviour is attributed to growth and coarsening of pre-existing precipitates, while in the under-aged condition, first the GP zones dissolve before re-precipitating and coarsening to new stable η-precipitates. The coarsening leads to a reduction in hardness over the entire TMAZ, independent of the initial temper and welding speed.

- The WN is marked by a complete disappearance of coarse η-precipitates and a significant drop in the volume fraction to a level similar to that of the T3 starting level. The formation of new small GP zones in the recrystallised region upon cooling leads to an increase in hardness to a level similar to the under-aged condition. For the T79 temper this results in lower hardness compared to the initial PM hardness. Both conditions are depicted in Figure 2.9c and Figure 2.9d.
- A decrease in traverse speed at constant rotation speed leads to a widening of the hardness profile, indicating a higher heat input resulting in higher temperatures for a longer time per unit volume at the weld-line.

While Dumont *et al.* (2006) determined the precipitation sequences during FSW from the post weld precipitation microstructure, Kamp *et al.* (2006; 2007) investigated the precipitation sequences, using a FE model which considers the metastable η'-phase along with its equilibrium η-phase during discrete time steps and evaluated the predictions based on experimental work by Robson *et al.* (2004).

Kamp *et al.* (2006) applied a typical thermal cycle for FSW as depicted in Figure 2.10a and differentiated between the different weld zones. They predicted the mean radius (see Figure 2.10b) and volume fraction (see Figure 2.10c) of the stable and meta-stable η- and η'-precipitate distribution for the different weld zones of a 20 mm thick AA7449 friction stir weld. Complete dissolution of small η'-particles and the transformation of coarse η'- to η-precipitates with increasing temperature was observed in all weld zones. As the peak temperature is approached, small η-particles dissolve and their volume fraction decreases again. The additional solute now available enables further coarsening of the remaining η-particles, as depicted in Figure 2.10b. Upon cooling, further coarsening of surviving stable

η-particles occurs, leading to an increase in both particle radius and volume fraction. Further, new small metastable η' re-precipitate and the volume fraction increases. The final precipitate distribution as predicted by Kamp *et al.* (2006) is to some extent in good agreement with the experimental results for the overaged AA7449-T79 material as obtained by Dumont *et al.* (2006).

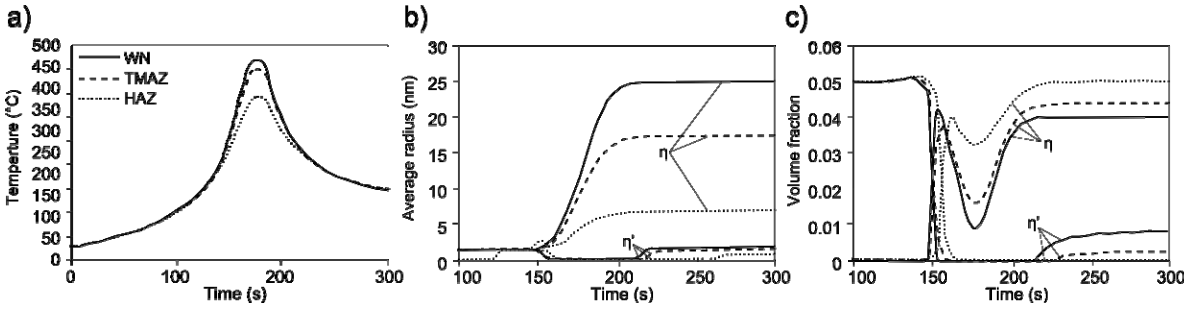

Figure 2.10: The modelled thermal cycle (a) during FSW of 20 mm thick under-aged AA7449 and the resulting changes of the average size (b) and (c) volume fraction of stable and meta-stable η- and η'-precipitates (after Kamp *et al.* (2006)).

The post weld spatial variation of the precipitation microstructure across a high strength aluminium friction stir weld due to the local thermal cycle, not only affects the mechanical weld-line properties, it also affects the local amount of alloying elements in solution, which results in a variation of the unstrained unit cell parameter a_0. This is of significant importance for the determination of RS using synchrotron X-ray and neutron diffraction and is discussed in more detail in section 2.6.6.3.

2.3.5 Applications

FSW is not fully understood at present, but many potential applications, especially in the aerospace sector are considered or already applied. Commercial application of high strength aluminium alloys may primarily be found in the safety critical aerospace industry, which relies on these alloys mostly for structural components and fuselage skin applications. The aerospace industry is very cautious when implementing new and relatively unverified techniques such as FSW. Nevertheless some "flying" applications where FSW of high strength aluminium alloys was used to join aircraft components were reported in the literature.

FSW of high strength aluminium alloys is of significant importance for the EADS Company for reduction of manufacturing costs and time as well as weight of the aircraft

structures. One test application is the manufacturing of an upper panel of a central wing box for airplanes, as shown in Figure 2.11a and Figure 2.11b, where FSW is used for joining integrated stiffener panels. Successful trial welds have been carried out in AA7075-T77511 and AA7349-T6511 on 1500 x 480 mm self stiffened 10 mm thick extruded panels, as shown in Figure 2.11c (Marie 2001). Many more FSW applications in aircraft structures (wing components, fuselage skin) are possible and under investigation at EADS.

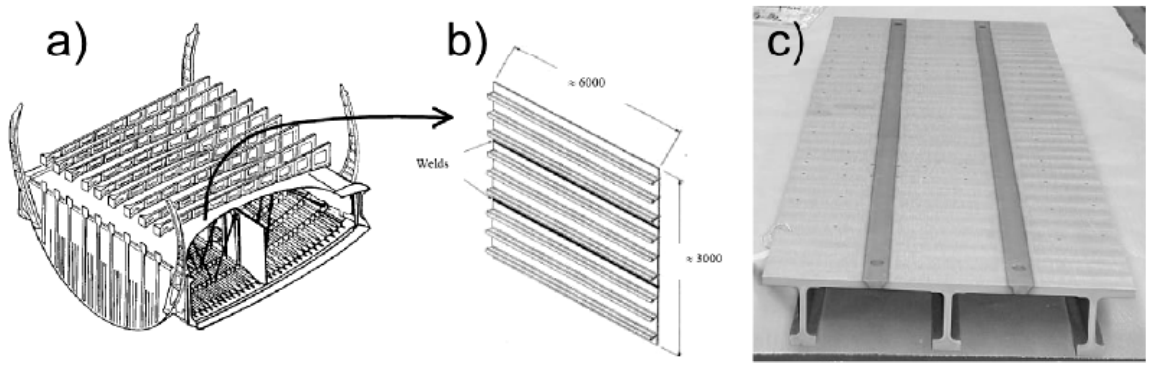

Figure 2.11: (a) Illustration of an Airbus central wing box. (b) Illustration of the upper panel of the wing box. (c) Test friction stir welded upper wing box panel, note the single extruded panels and the typical near trapezoid shape of the weld region (Marie 2001).

Other companies such as the Eclipse Aviation Corporation use FSW extensively for the production of the twin-engine Eclipse 500 aircraft cabin structure (see Figure 2.12a) made from the AA2xxx and AA7xxx alloys (Christner *et al.* 2003). The joining speed was up to 6 times faster than for the previously used riveting technique and superior lap joining properties with a considerable reduction in component weight were achieved.

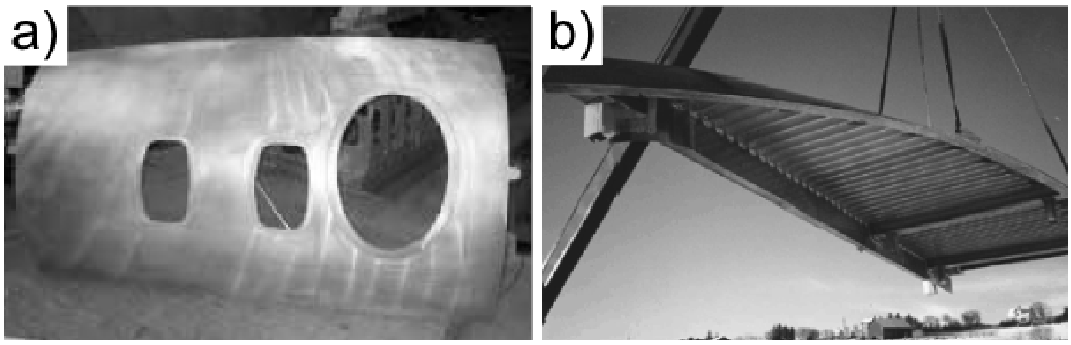

Figure 2.12: (a) Part of Eclipse 500 cabin assembly manufactured using FSW high strength aluminium alloys (Christner *et al.* 2003) and (b) finished friction stir welded panel of half the width of the superstructure of a cruise liner (Midling *et al.* 1999).

In ship building FSW of medium strength AA5xxx and AA6xxx alloys has been reported for the production of large panelled components. Figure 2.12b illustrates a prefabricated panel produced from smaller extruded sections joined by FSW, to decrease the amount of manual welding work required during the assembly at the shipyards (Midling *et al.* 1999).

FSW has high potential to be used in fabrication production for applications, where straight as well as curved weld-lines are required and where a solid support from underneath the weld-line can be ensured in order to counteract the welding forces.

2.3.6 Conclusions

FSW is a maturing joining technique well suited for materials otherwise considered as 'non-weldable'. FSW is a remarkably simple technique for joining materials. A non-consuming rotating tool comprising a tool shoulder and pin is moved along the weld-line. It softens the material by frictional heating and deforms and mixes the plate interfaces to form a solid joint. The advantages of this FSW are:

- the solid state character allowing to weld all common aluminium alloys and avoids problems of hot cracking, porosity, element loss etc common to the aluminium fusion welding processes ,
- high weld quality and good mechanical properties (Dawes *et al.* 2000; Magnusson *et al.* 2000; Sato *et al.* 2001; Bussu *et al.* 2003; Peel *et al.* 2003; Mishra *et al.* 2005; Cavaliere *et al.* 2006; Threadgill *et al.* 2009),
- the technique is simple to control by the speed and force parameters and therefore highly repeatable (Thomas *et al.* 1991; Mishra *et al.* 2005),
- no special weld preparation is required,
- no shielding gas or filler wire are required for aluminium alloys (Thomas *et al.* 1991; Mishra *et al.* 2005; Threadgill *et al.* 2009),
- the absence of fusion removes much of the thermal contraction associated with solidification and cooling, leading to significant reductions in distortion (Price *et al.* 2007),
- the process can be scaled to produce single pass welds in materials ranging from 0.5 -75 mm (Ahmed *et al.* 2008).

FSW creates a characteristic weld microstructure comprising the weld nugget, a thermo-mechanically affect zone and a heat affected zone. The geometric dimensions of each zone depend on the FSW conditions and as such can easily be changed. FSW is increasingly applied in the transportation industries, such as the aviation sector. Nevertheless, even though FSW is a solid state welding technique it may introduce near melting point temperatures local to the weld-line and lead to non-uniform material expansion and contraction. This may result in significant RS within the welded structure. It is the development, magnitude and distribution of RS and the related component distortion that is of interest in this dissertation and therefore is addressed in the next section.

2.4 RESIDUAL STRESS AND DISTORTION IN FRICTION STIR WELDS

2.4.1 Introduction

Before introducing the reader to the typical residual stress (RS) distribution produced by FSW high strength aluminium alloys and the related weld distortion, it is worth looking into the fundamentals of the generation of RS during welding, as well as the correlation between RS and distortion. It is important to understand the development of RS for the investigation of the mechanisms of the stress engineering techniques (see section 2.5). This is especially the case for techniques applied during welding as these methods affect the RS development rather than the final RS state. On the other hand, it is necessary to know the RS typically introduced by FSW in order to determine the efficacy of in-situ, as well as post welding, applied stress engineering techniques. The following sections will introduce the reader to RS and the development of RS during welding before reviewing the available literature on RS in high strength aluminium plates, joined by FSW. Afterwards the correlation between RS and distortion is discussed.

2.4.2 Residual Stress

RS, as defined in section 1.2, are those stresses acting internally to a body without any external load applied. RS are caused by chemical, thermal or plastically induced volumetric material misfits in different regions within a body (Withers *et al.* 2001b). Considerable thermal gradients occur during welding and these may result in the development of significant RS. Depending on the amplitude and orientation of the RS, noteworthy effects

on the mechanical properties such as the fatigue and fracture behaviour or stress corrosion response (Masubuchi 1980; James *et al.* 2007b; Withers 2007), may occur resulting in the degradation of its lifetime performance. Further, in service loads may superimpose onto the RS and if both are of the same sign may exceed the local yield strength σ_{YS} leading to deformation of the component. In some applications this may require the replacement of the part (for example bent structural aircraft components) or may cause severe damage (for example deformation of rotating parts (turbine blades) leading to imbalance). In the worst case RS exceeding the yield strength σ_{YS} may assist in premature failure by fracture during service of the component resulting in catastrophic damage. On the other hand, differently orientated RS and service loads may cancel each other out and as a result increase the maximum bearable in-service load as well as improve the life time performance. Consequently, RS can be detrimental or beneficial depending on the character of the RS and the in-service conditions. Therefore RS may be taken as a design feature for mechanical engineering. However, this requires precise knowledge of the present RS and appropriate techniques for stress adjustment.

Type	Scale	Description
Type I	Macroscopic	Type I RS affect and equilibrate within a volume comparable in scale to that of the component itself. They are most important to engineers because type I RS have significant impact on the component performance.
Type II	Microscopic	Type II RS affect a volume comprising a few grains in a polycrystalline or multiphase material and may arise from misfit strains between differently orientated grains or different phases due to thermal or mechanical property variations.
Type III	Intragranular	Type III RS act over a very short range within a single grain and may be attributed to misfit strains around dislocations, precipitates and solute atoms.

Table 2.1: Classification and description of RS types (Masubuchi 1980; Withers *et al.* 2001b).

RS may be classified according to the length scale over which they act and self-equilibrate, as shown in Table 2.1. The overall RS state within a component is determined by the sum of all three types, the macroscopic, the microscopic and the intragranular type of RS. However, this dissertation is primarily concerned with type I, or macroscopic RS, because these have a significant impact on the in service life time performance of a component as these superimpose with the in-service loads. Yet, the RS of type II and III are just as important, as these may cause micro cracks which in combination with the macroscopic residual and in-service stresses may lead to premature component failure by fracture.

2.4.3 Origin of Residual Welding Stress

RS in welds are due to a large temperature variation experienced by the different regions of the material during the welding process resulting in irregular material expansion and shrinkage (Masubuchi 1980). The general formation of RS and the temperature across a fusion weld-line as a function of position relative to the weld pool as stated by Masubuchi (1980) is illustrated in Figure 2.13.

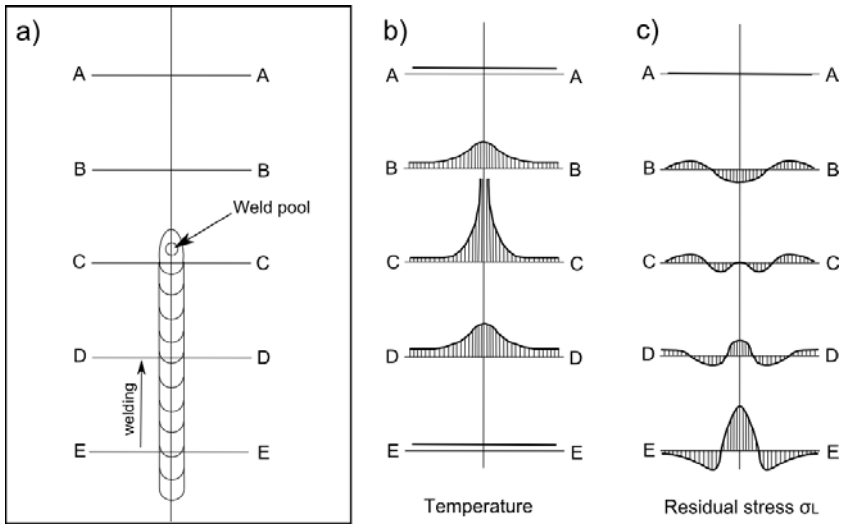

Figure 2.13: Development of longitudinal RS during welding: (a) Schematic snap-shot of the moving weld tool and cross trajectories as a function of distance from the weld tool representing different welding states, (b) Schematic of the welding temperature and (c) the current RS distribution for each state of welding (after Masubuchi 1980).

While the material far in front of the welding tool (line A-A) is not affected by the weld thermal cycle, the metal closer to it (line B-B) experiences a heat input resulting in local expansion. This expansion is constrained by the cold surrounding material, hence the weld zone is subject to a compressive strain and hence compressive RS balanced by small tensile RS in the cold PM. Due to intense temperatures below the weld tool (line C-C) the material yield strength σ_{YS} will decrease simultaneously and further thermal expansion is accommodated by plastic flow rather than elastic strain. The RS directly below the weld tool is nearly zero as the highly softened material can not support any load. During FSW the material around and below the tool is soft, but still solid and likely to support some load, but being exposed to near melting point temperatures these loads are negligible. Behind the welding tool the material starts cooling (see Figure 2.13 section D-D and E-E) as heat conducts into the surrounding material and the environment. The weld material starts to contract initially which is accommodated by plastic flow in the reverse direction

resulting in elastic tensile strain in the cold weld. The overall plastic deformation upon heating and cooling leaves a misfit between the yielded weld zone and the non-yielded PM resulting in a new equilibrium forcing the weld zone into tension balanced by compressive RS in the PM (Kou 2003). This is shown schematically by line E-E in Figure 2.13.

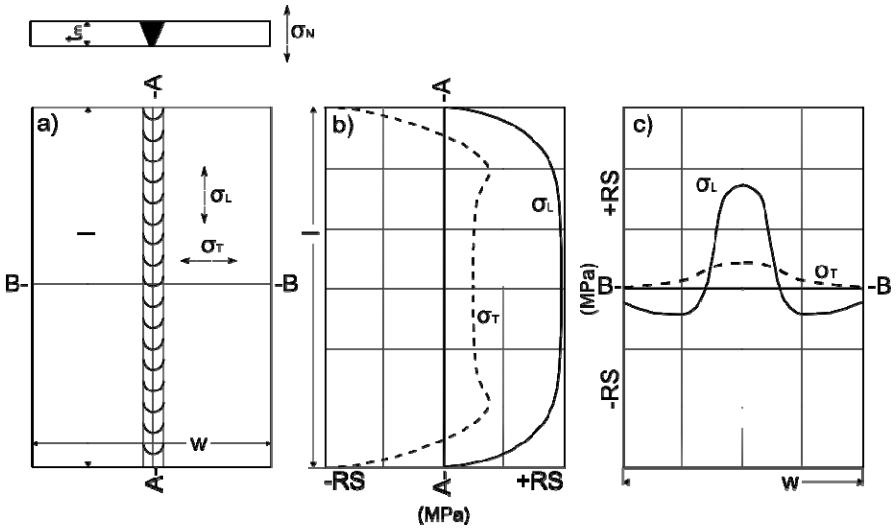

Figure 2.14: Schematic of the typical RS distribution in a flat plate joined in the butt weld configuration: (a) Schematic of the plate dimensions and the RS directions, (b) σ_L and σ_T distribution along the weld-line, (c) σ_L and σ_T distribution across the weld-line (after Masucbuchi 1980).

After Masubuchi (1980) the general RS distribution in a flat plate (length l × width w × thickness t_m) joined in the butt weld configuration can be assumed to be as illustrated in Figure 2.14. The longitudinal and transverse RS along the weld-line (line A-A in Figure 2.14b) tend to be invariant over the distance of steady state welding conditions. In this area the longitudinal RS σ_L are tensile and comparatively high, while decreasing to zero at the plate edges. The transverse RS σ_T are tensile, but much lower and towards the plate edges equilibrate themselves by turning into compression. Across the weld (line B-B in Figure 2.14c) the longitudinal RS σ_L follow a peak shaped stress profile being tensile in the weld-line and balanced by lower compressive RS towards the plate edges to be in equilibrium. The transverse RS σ_T are low and zero at the plate edge.

2.4.4 Residual Stress in Friction Stir Welds

Numerous investigations of RS in high strength aluminium alloy plates joined by FSW have been reported in the literature (James *et al.* 1999; Wang *et al.* 2000; Donne *et al.*

2001; Sutton *et al.* 2002; Peel *et al.* 2003; Staron *et al.* 2004; Peel 2005; Prime *et al.* 2006; Price *et al.* 2007) from which the following observations may be extracted.

In general the longitudinal RS across the weld-line follow an M-shape distribution, as illustrated in Figure 2.15 being tensile in the weld zone and balance as compressive RS in the PM. Transverse RS may follow a similar shape, but are significantly smaller. As illustrated in Figure 2.15 Staron *et al*. (2004) reported longitudinal peak RS of ~140 MPa (~0.38 σ_{YS} of the PM (Genevois *et al.* 2006)) in 6.3 mm thick (v_{rot} = 350 rpm, v_t = 95 mm/min) and in 3.2 mm thick (v_{rot} = 574 rpm, v_t = 195 mm/min) friction stir welded AA2024-T351 plates. In each case the weld-line RS were significantly lower resulting in the typical M-shaped distribution. No significant transverse RS were reported as shown in Figure 2.15.

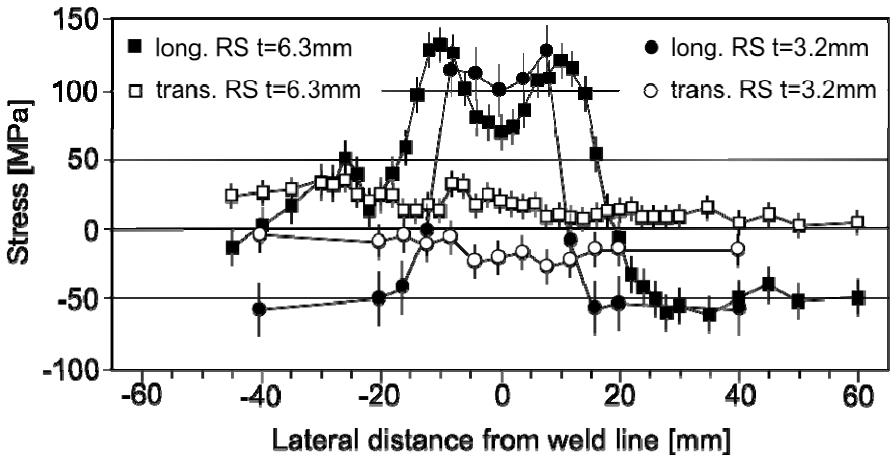

Figure 2.15: Longitudinal and transverse RS distribution as function of distance from weld-line in 125 × 380 × 6.3 mm^3 (v_{rot} = 350 rpm, v_t = 95 mm/min) and 125 × 380 × 3.2 mm^3 (v_{rot} = 574 rpm, v_t = 195 mm/min) thick AA2024-T351 friction stir welds as determined at the ARES neutron diffractometer at the Geesthacht Neutron Facility, Germany (Staron *et al.* 2004).

Wang *et al*. (2000) reported peak RS rising from ~160 MPa (~0.50 σ_{YS} of PM (ASM_2 2001)) in a 6mm thick AA6061-T6 friction stir weld (v_t = 279 mm/min) to ~200 MPa (~0.64 σ_{YS} of PM (ASM_2 2001)) by increasing v_t to 787 mm/min at constant tool rotation rate. At the same time the lateral distance between the stress peaks decreased. A similar trend was reported by Peel *et al*. (2003) in an AA5083-H19 friction stir welded sample (150 ×200 ×4 mm^3), but with lower longitudinal peak RS increasing from 40 MPa (~0.10 σ_{YS} of PM) to 60 MPa (~0.16 σ_{YS} of PM) by doubling v_t to 200 mm/min. Others also found comparatively small RS in specimens, which were cut down to a small size compared to the original weld dimensions. There is a tendency of decreased RS as the specimen size

decreases, which may be explained by stress relaxation during specimen cutting (Masubuchi 1980; Peel 2005; Prime *et al.* 2006). However, this is discussed in detail in section 2.6.6.4 and 4.3.

While the reported stress magnitudes vary significantly from case to case, some general features for the RS distribution in friction stir welds were reported. At the weld surface the longitudinal RS peaks are usually located slightly outside the tool shoulder edge in the TMAZ and shift towards the weld-line with increasing depth (Mishra *et al.* 2005; Threadgill *et al.* 2009). This may be attributed to the shape of the FSW tool and the surrounding temperature field. Variations of the position of the RS peak were observed as FSW parameters vary (compare Figure 2.15). The M-shaped RS distribution widens for higher tool rotation rates at constant tool traverse speed (Donne *et al.* 2001; Staron *et al.* 2004) which may be associated with an increased heat input. The higher temperatures subsequently spread out further into the PM, hence the zone of plastic misfit arising from the temperature cycle reaches further out and therefore widens the RS distribution shape. Further, widening of the M-shaped RS profile occurs for increased tool shoulder diameter (Donne *et al.* 2001; Peel 2005). On the other hand, the M-shape is narrower for increased tool traverse speed at constant tool rotation rate (Wang *et al.* 2000; Peel 2005; Threadgill *et al.* 2009). A slight asymmetry of the M-shaped RS distribution was observed which may be explained by the asymmetric nature of the FSW process (see section 2.3.2). The RS can be higher on the advancing than on the retreating side which is believed to be due to higher temperature during welding caused by the superimposed rotation and traverse speed on this side of the FSW tool (Sutton *et al.* 2002; Peel *et al.* 2003; Threadgill *et al.* 2009).

Price *et al.* (2007) explained the formation of the M-shaped stress profile based on experimental observations, while Richards *et al.* (2008a) used a FEM approach to explore the mechanisms acting during the build up of this particular stress profile. However, both descriptions are complementary to each other as shown in the following.

Price *et al*. (2007) provided a graphical illustration of the development of the typical M-shaped RS distribution in high strength aluminium alloy plates joined by FSW as shown in Figure 2.16. Graph a and b depict the temperature and the temperature dependent material yield strength σ_{YS} as a function of lateral distance from the weld-line for three different positions (1-3) behind the FSW tool. Graph c depicts the arising longitudinal tensile RS due to the material shrinkage in the weld zone upon cooling as described in

section 2.4.3. The RS_1 at position 1 and temperature 1 is too low to exceed the local σ_{YS1} (graph d) but at position 2 (graph e) and 3 (graph f) the trajectories of the arising RS_2 and RS_3 and the σ_{YS2} and σ_{YS3} overlap as the RS develop quicker than the local σ_{YS} recovers upon cooling. However, this overlap leads to relaxation of the RS by plastic elongation of the weld zone material thus forming the typical M-shaped RS distribution as displayed in graph f) by the solid line in the final condition (position 3 far behind the FSW tool). From this graphical explanation one can conclude that the M-shaped RS distribution around the weld-line can be taken as a direct footprint of the temporary local yield strength σ_{YS}. However, this would mean that the amount of bearable in-service loads reduces to zero as any applied load superimposes on the RS and initially leads to plastic deformation as the local yield strength σ_{YS} is overcome immediately. As this is not the case the local yield strength σ_{YS} must recover to even higher values by post weld natural aging.

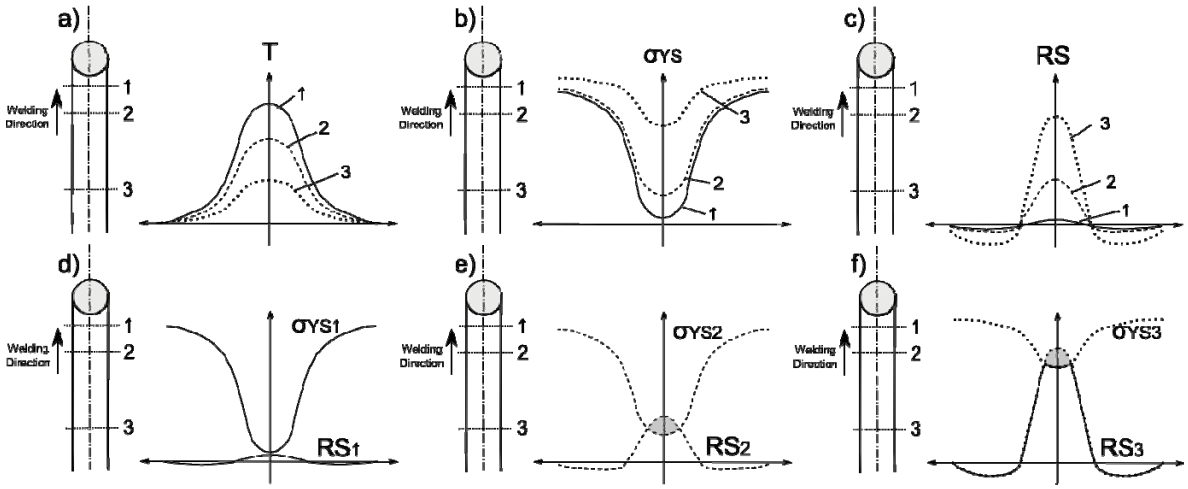

Figure 2.16: Schematic illustration of the development of the typical M-shaped RS profile in plates joined by FSW (after Price *et al.* 2007): (a) the temperature distribution, (b) the local yield strength, (c) the developing RS, (d-f) the local yield strength and RS for each position, where the curves overlap plastic deformation occurs.

Richards *et al.* (2008a), who performed FEM work on high strength aluminium alloy plates joined by FSW, partly confirmed and extended this description of the development of the M-shaped RS distribution. They determined that a combination of compressive plastic straining ahead of the FSW tool and the limitation of the arising longitudinal tensile RS by the low yield strength σ_{YS} behind the tool leads to tensile plastic straining hence a drop in weld-line RS. In contrast to Price *et al.* (2007), Richards *et al.* (2008a) stated the final M-shaped RS profile is formed right at the beginning of the cooling and that the RS built up

slower than the recovering yield strength σ_{YS} during the initial natural aging and so the final peak RS are significantly lower than the local yield strength σ_{YS}. This explanation is more likely to mirror the real process as the weld-line yield strength is higher than the local RS and so additional load can be applied without causing local plastic deformation.

2.4.5 Distortion of Weldments

Service loads may superimpose on RS and lead to deformation as the local yield strength σ_{YS} is exceeded. However, in case RS reach the local yield strength without an external load being applied, as may be the case for welding RS, they relax by plastic or elastic deformation of the material within the affected region. It is these deformations that are called distortion. Tensile as well as compressive RS, forming in the weld area, due to uneven heating and cooling cycles, may result in different kinds of distortion as illustrated in Figure 2.17 (Masubuchi 1980; Bhide *et al.* 2006). These are classified into angular and bending (mainly a result of tensile RS) as well as buckling (due to compressive RS) distortion and transverse and longitudinal shrinkage as well as rotational distortion (Masubuchi 1980). According to Masubuchi (1980) buckling distortion is defined as numerous bending distortion bows in one plate, while Bhide *et al.* (2006) defined buckling distortion as a combination of angular and bending distortion, which depending on the degree of freedom and the potential energy stored within the welded plate may result in different degrees of buckling modes.

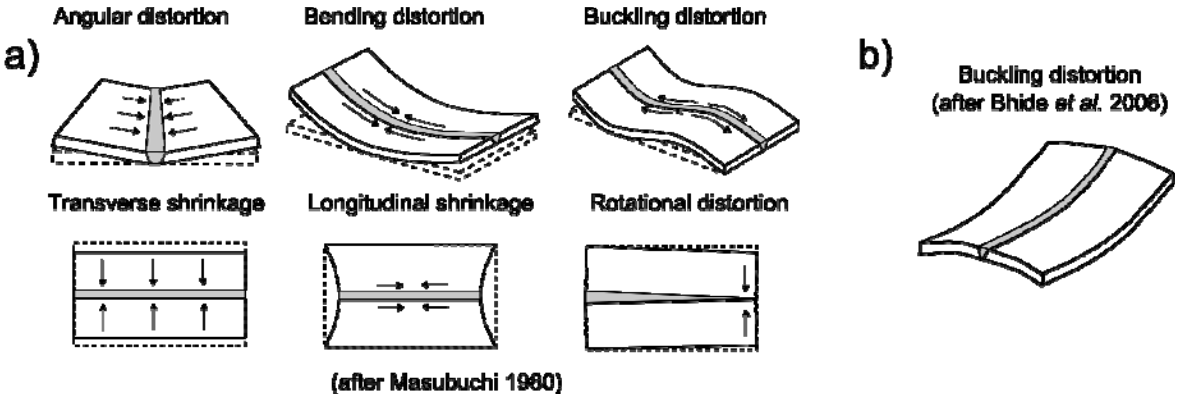

Figure 2.17: (a) Types of distortion in welded plates (after Masubuchi 1980), the arrows indicate the direction of shrinkage of the weld metal that may cause the deformation of the welds, each view shows the weld surface. While angular distortion may be plastic, the bending and buckling distortion are almost always elastically distorted (Bhide *et al.* 2006). Bhide *et al.* (2006) defined buckling distortion as a combination of both, angular and bending distortion as depicted in (b).

In this dissertation the angular and bending distortion of plates joined by FSW are of main interest. The lateral and through thickness asymmetry of the FSW technique leads to temperature gradients across the weld as well as through thickness. Consequently the amount of volumetric misfit of the material differs as a function of position. The material near the weld surface is plastically compressed due to expansion upon heating, while during cooling, the material shrinkage introduces tensile loads pulling the weld-line material in both the longitudinal and the transverse directions (Richards *et al.* 2008a). This effect is less near the weld bottom, presumably due to the lower temperatures, thus resulting in a through thickness mismatch, which may result in angular and/or bending distortion. Price *et al.* (2007) reported significant convex bending distortion of 21.6 mm and concave angular distortion with respect to the weld surface in an $1135 \times 250 \times 3.2\,\text{mm}^3$ AA2024-T351 friction stir weld. Wen *et al.* (2009) predicted the distortion of friction stir welded integrated stiffener panels (material data from AA2024-T3) being $3667 \times 500\,\text{mm}^2$ in size and the cross-section as depicted in Figure 3.2. They reported the same types of distortion with an out-off plane off-set of ~10 mm in the final weld as depicted in Figure 2.18a.

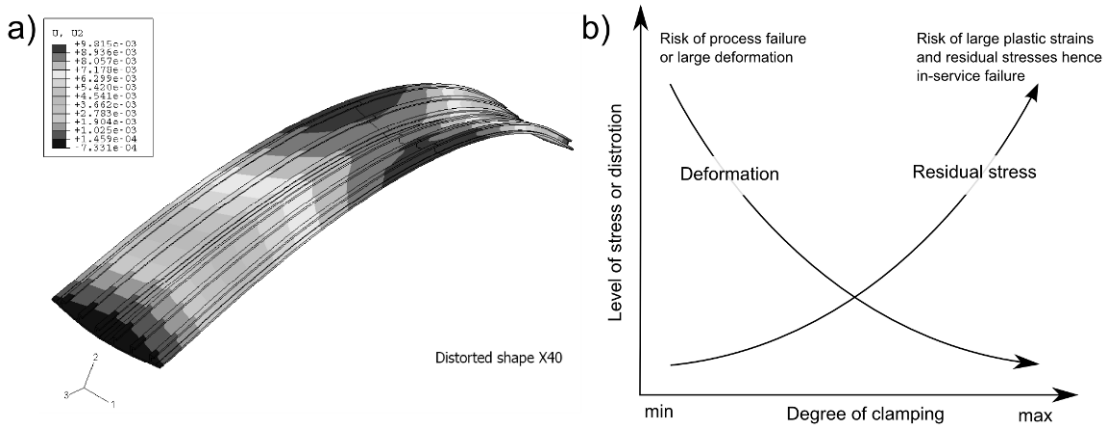

Figure 2.18: (a) Bending and angular distortion of an integrated stiffener panel joined by FSW as predicted by Wen *et al.* (2009) and (b) the effect of the degree of applied clamping during welding and cooling on the formation of distortion and the level of RS (van der Aa 2007).

In practice several types of distortion can occur at the same time making it difficult to distinguish between the different forms. For example the bending distortion of a plate may also be considered as mode I buckling (after Masubuchi 1980), where just one bow appears. On the other hand, bending and angular distortion may occur at the same time in a plate, which can then be considered as buckling distortion after Bhide *et al.* (2006).

Depending on the plate and weld dimensions the level of transverse and bending distortion may vary. Masubuchi (1980) stated that generally in thin material the thermal differences and hence the arising plastic misfits are less significant thus reducing the amount of deformation. On the other hand, thicker material is rigid enough to withstand the arising RS that lead to distortion of the welded component. However, as reported by Michaleris *et al.* (2006) thicker welds are less sensitive to buckling and usually deform by bending and angular distortion, while thinner welds are prone to buckling.

Another important factor for weld distortion is the degree of clamping applied during welding and cooling as depicted in Figure 2.18. While welding a structure without any clamping may lead to significant deformation, but low RS as a result of the plastic straining, rigid clamping may cause the opposite to occur. The optimum degree of clamping is at the intersection of both trajectories depicted in Figure 2.18b.

Within this dissertation the arising distortion of the welded plates as a function of the applied stress engineering techniques is determined. The aim of stress engineering is to control and mitigate RS, especially those in the welding direction. As the distortion appears to be closely related to the RS occurring in weldments (Masubuchi 1980; Masubuchi 2003; Price *et al.* 2007), applying stress engineering techniques successfully should also reduce the component distortion.

2.4.6 Conclusions

RS in welds arise from the material misfit developing during the thermal cycle. The local heating causes the material in front of the welding tool to expand which is constrained by the surrounding colder material hence compressive RS may arise leading to plastic straining once the local yield strength σ_{YS} is reached. The intense temperatures below the FSW tool soften the material such that only small loads can be supported. Upon cooling the material starts contracting initially resulting in elastic tensile straining eventually causing plastic straining as the arising stresses exceed the current local yield strength σ_{YS}. The overall plastic deformation upon heating and cooling leaves a misfit between the strained weld zone and the non-affected PM forming a new equilibrium forcing the weld zone material into tension balanced by compressive RS in the PM.

The RS found in high strength aluminium alloys joined by FSW may reach up to 60 % of the PM room temperature yield strength σ_{YS} (James *et al.* 1999; Wang *et al.* 2000; Donne

et al. 2001; Sutton *et al.* 2002; Peel *et al.* 2003; Staron *et al.* 2004; Peel 2005; Prime *et al.* 2006; Price *et al.* 2007). Usually the RS follow an M-shape distribution with the stress peaks close to the FSW tool shoulder edge, while the stress in the WN may be significantly lower as depicted in Figure 2.15. Closely related to RS is the distortion of welded components. Significant bending distortion was reported (Price *et al.* 2007; Williams *et al.* 2008) in friction stir welds containing high tensile RS, while lower RS resulted in reduced distortion. A tool to control and therefore minimize RS and the related distortion are stress engineering techniques, either applied by thermal or mechanical methods. The following section will detail these stress engineering techniques.

2.5 CONTROL OF WELDING RESIDUAL STRESS: STATE OF THE ART

The main emphasis of this dissertation is to improve our understanding of three mechanical stress engineering techniques as well as to determine the correlations between the individual stress engineering technique parameters and the achieved mitigation of RS, and related component distortion, in high strength aluminium welds joined by FSW. Even though this dissertation concentrates on the mechanical stress engineering techniques ISGMT, ISRT and PWRT, it is useful to briefly introduce the reader to the current state of the art of existing stress mitigation techniques. This allows for evaluation and comparison of the investigated techniques within the field of existing stress engineering methods. The following sections will introduce the reader to the existing stress engineering techniques.

2.5.1 Introduction

The typical distribution of RS in welded structures has been described in section 2.4.3 and is depicted in Figure 2.14. Across the weld-line high longitudinal tensile RS act which are balanced by low compressive stresses over the remaining plate width. Along the weld-line the longitudinal tensile stresses are constant and decrease to zero at the free end surface. The transverse RS are in low tension compared to those acting parallel to the welding direction. Given the problematic nature of welding induced tensile RS and the related distortion, scientists as well as engineers are searching for methods to control and reduce the level of longitudinal tensile RS. Numerous stress engineering techniques were developed and received an increased amount of attention in the recent past (Staron *et al.*

2004; van der Aa *et al.* 2006; Williams *et al.* 2006; Price *et al.* 2007; Richards *et al.* 2008a; Richards *et al.* 2008b; Williams *et al.* 2008; Wen *et al.* 2009). While some techniques appear to be well understood, for other techniques the knowledge of the mechanisms acting is limited and a lack of experimental as well as FEM work exists in order to fully understand the mechanisms acting. The following sections will briefly overview the current state of the art on the available stress engineering techniques.

An intuitive method to reduce the RS and distortion is to optimize the welding technique itself (Masubuchi 1980). Reducing the heat introduced to the components (Steuwer *et al.* 2006b; Lombard *et al.* 2008) or by improving the welding process the arising plastic misfit can be reduced resulting in less RS and distortion. This can be achieved for example by minimizing the size of the heat affected zone, or reducing the number of weld passes. Another option is to weld the components from both sides which will reduce the through thickness variation of plastic misfit (Masubuchi 1980) and as a result the bending and the angular plate distortion. However, in practice parameter optimization is limited by design requirements, as well as such issues as avoiding the introduction of flaws or voids and the drive to maintain economic production rates.

As a result, several stress engineering techniques, which can be applied either during welding or after the process is complete have been developed. These may be divided into thermal and mechanical methods. Also, combinations of both techniques are possible. The most important techniques are:

- thermal methods:
    - the application of a leading and/or trailing cold and/or hot spot (Guan *et al.* 1994; Michaleris *et al.* 1997; van der Aa *et al.* 2006; van der Aa 2007; Richards *et al.* 2008b; Williams *et al.* 2008),
    - global and local preheating (Michaleris *et al.* 1997; Williams *et al.* 2008) and
    - post weld heat treatment (Williams *et al.* 2008) as well as
- mechanical methods:
    - surface peening (Hammersley *et al.* 2000; Rankin *et al.* 2003; Evans *et al.* 2005; Ali *et al.* 2007; Hatamleh *et al.* 2007),
    - vibratory methods (Masubuchi 1980),

- global tensioning (Staron *et al.* 2004; Williams *et al.* 2006; Richards *et al.* 2008a) and
- roller tensioning (Liu *et al.* 1996; Yang *et al.* 1998; Wen *et al.* 2009).

As stress engineering techniques are applied differently, their basic principal mechanisms for the reduction of the RS hence the distortion tend to fall into two groups. Firstly, methods that are applied during welding that tend to reduce the compressive yielding in front of the welding tool upon heating (see section 2.4.3). Secondly, methods that are applied either during, or after welding, that increase the tensile yielding behind the welding tool to compensate for the material shrinkage immediately in the hot weld, or if applied after welding, to overcome the local weld-line yield strength σ_{YS} and plastically deform the material by elongation (Richards *et al.* 2008a).

The achieved reduction of tensile RS by means of thermal or mechanical techniques depends on the amount of the reduction of compressive plastic deformation ahead and the amount of increased tensile plastic yielding achieved behind the welding tool (Richards *et al.* 2008a). In general, less compressive yielding in front of and increased tensile yielding behind the weld tool results in higher reduction of tensile RS. If the stress engineering techniques are applied excessively compressive RS may be introduced (Michaleris *et al.* 1999; van der Aa *et al.* 2006; Price *et al.* 2007; Richards *et al.* 2008a; Wen *et al.* 2009).

2.5.2 Thermal Stress Engineering Methods

Thermal tensioning methods can work by both above mentioned mechanisms, namely reducing the amount of compressive yielding ahead and increasing the tensile yielding behind the welding tool. Thermal stress engineering methods may be divided into static thermal tensioning and temporary or dynamic thermal tensioning techniques for both, in-situ and post weld applications. Static thermal tensioning affects welding RS and subsequently the component distortion by generating tensile stresses in the weld zone prior to, during and after welding by imposing a predetermined steady state temperature gradient to the components. One example is preheating the entire component, or selected areas, to decrease the temperature gradients across the weld-line during welding and to induce tensile strains near the weld-line as the heated areas of the components are expanding (Michaleris *et al.* 1997).

Post weld heat treatment is applied to the entire component after welding is complete. It results in thermal expansion of the entire component leading to elongation of the weld-line material and plastic deformation once the local yield strength σ_{YS} is overcome. In addition the RS reduce due to creep occurring at elevated temperatures. However, care must be taken as these global heat treatments may significantly affect the mechanical properties of the base material. This is especially the case for heat treatable alloys. As a result these methods should preferably be applied to materials with a stable high temperature microstructure.

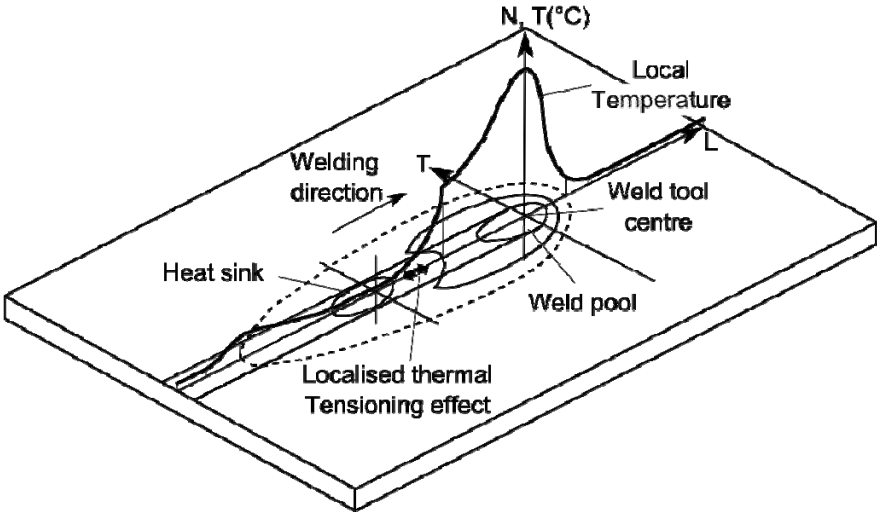

Figure 2.19: Schematic of the trailing cold spot stress engineering technique. The trailing heat sink behind the welding tool leads to increased material contraction upon cooling causing the intermediate material to plastically elongate, thus reducing the final RS and distortion level (after van der Aa *et al* 2006).

Transient thermal tensioning techniques utilize dynamic temperature differentials. These may be produced by two heating bands travelling behind and to both sides of the welding hot spot (Michaleris *et al.* 1999) leading to local material expansion causing the contracting material behind the welding tool to plastically elongate. Another method as shown by Guan *et al.* (1994), van der Aa *et al.* (2006), Gabzdyl *et al*. (2001) and Richards *et al*. (2008b) is to apply local cooling to the weld-line ahead and/or behind the welding tool using CO_2 or water spray. The leading cold spot leads to material shrinkage allowing for more elastic material expansion upon heating as the welding tool approaches and as a result less plastic misfit. On the other hand, the trailing cold spot, a typical thermal weld profile is depicted in Figure 2.19, has the same effect. Cooling the weld-line material at a constant distance behind the moving welding tool leads to increased material contraction causing the material between the welding tool and the cold spot to plastically elongate thus

reducing the final RS and plate distortion. FEM work by Richards *et al.* (2008b) and experimental investigations performed by van der Aa *et al.* (2006) showed that the leading and trailing cold spot methods respectively are effective techniques for RS and distortion mitigation in butt welds as shown in Figure 2.20.

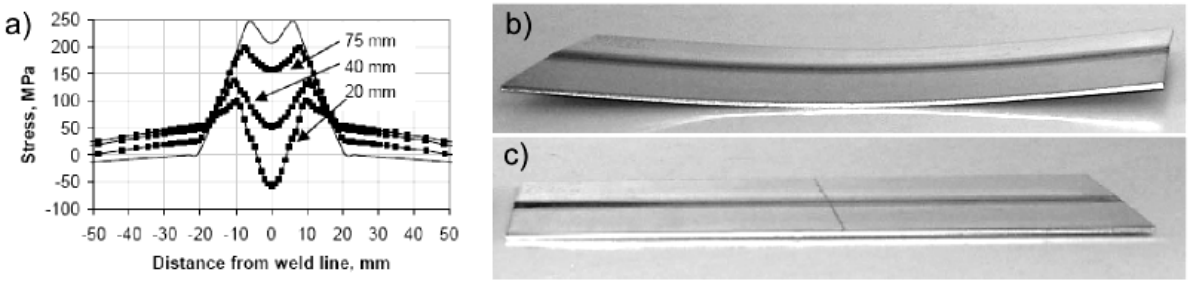

Figure 2.20: (a) The FE simulated longitudinal RS distribution across the weld-line at mid thickness halfway along the welded AA2024-T3 sheets without cooling (line), and with cooling applied at distances of 20, 40 and 75 mm (line and markers) behind the tool (Richards *et al.* 2008b). While (b) shows a conventionally welded plate (c) depicts the effect of a trailing heat sink on the weld distortion (van der Aa *et al.* 2006).

Despite the effectiveness of static and especially dynamic thermal tensioning, not only the precise determination of the appropriate heating or cooling intensity, size and position of the heat sources and sinks is required to optimise the process (Richards *et al.* 2008b), but also the environmental conditions need to be considered carefully as for example heat convection from the component to the weld backing table may vary for different material combinations. Further, even for simplified geometries, a conventional parametric experimental study for determination of the appropriate process parameters appears impractical as the number of process configurations is prohibitively large (Michaleris *et al.* 1999). Nevertheless, if applied properly significant reductions in welding RS and subsequently sample distortion as shown in Figure 2.20 may be achieved (Michaleris *et al.* 1997; Michaleris *et al.* 1999; van der Aa *et al.* 2006; Richards *et al.* 2008b).

2.5.3 Mechanical Stress Engineering Methods

Similar to thermal tensioning a number of different mechanical tensioning methods to mitigate welding RS have been developed and may be categorized into static and dynamic methods, depending on whether they are applied in-situ or post welding. The mechanical stress engineering techniques include surface peening based on shot peening (SP) (Evans *et al.* 2005; Ali *et al.* 2007) or laser shock peening (LSP) (Hammersley *et al.* 2000; Zhang *et*

al. 2005; Hatamleh *et al.* 2007), vibration techniques (Masubuchi 1980), in-situ global mechanical tensioning (ISGMT) (Staron *et al.* 2004; Williams *et al.* 2006; Price *et al.* 2007; Richards *et al.* 2008a) or post weld global mechanical tensioning (PWGMT) (Williams *et al.* 2006; Price *et al.* 2007) as well as roller tensioning (Williams *et al.* 2008; Wen *et al.* 2009) which may be applied in-situ (ISRT) as well as post welding (PWRT). Similar to thermal tensioning, the mechanical tensioning methods also aim to reduce the compressive yielding ahead and increase the tensile yielding behind the welding tool. The following sections detail the current state of the art of the mechanical methods briefly, while special attention is given to the ISGMT as well as the ISRT and PWRT techniques as these methods are of interest for this dissertation.

2.5.3.1 Surface Peening

Surface peening in general is a surface treatment used to enhance predominantly the fatigue and stress corrosion behaviour and damage tolerance of a component by introducing a layer of compressive stresses at the component surface leading to a redistribution of the welding RS. One way to apply a mechanical surface treatment is the bombardment of the surface with a stream of small spherical media called shots. These shots indent and plastically deform the surface generating a work hardened surface layer of typically a few hundred micrometres in depth (Evans *et al.* 2005; Zhang *et al.* 2005; Ali *et al.* 2007; James *et al.* 2007b) as is illustrated in Figure 2.21a. This technique is called shot peening (SP).

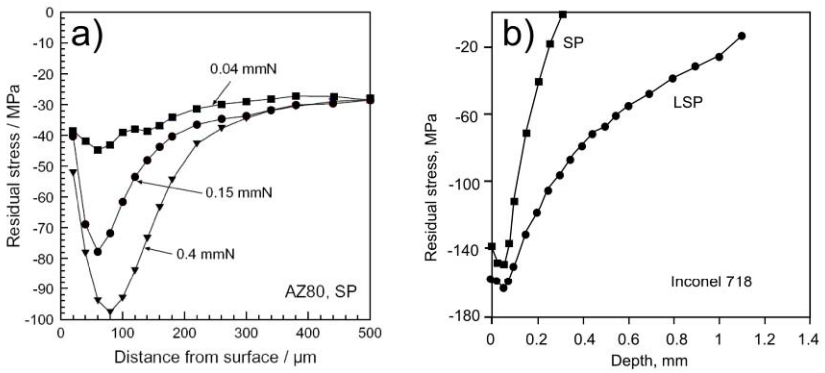

Figure 2.21: (a) Increased SP intensity leads to higher magnitudes of the compressive RS, while the affected surface layer thickness remains constant (in the current case ~300 µm as applied to wrought magnesium AZ80 alloy (Zhang *et al.* 2005)). (b) The LSP technique introduces compression to greater depths compared to SP in the same material as shown for Inconel 718 material (Hammersley *et al.* 2000).

The more recent laser shock peening (LSP) method uses a pulsed laser beam that activates an ablative surface layer (for example black paint) underneath a transparent cover layer (for example water) causing the ablative layer to vaporize. The constrained thermal expansion of the vaporized layer causes shockwaves to be sent into the material, leading to plastic deformation over a few hundred micrometer from the surface depending on the material and laser shock peening intensity (Hammersley *et al.* 2000; Zhang *et al.* 2005; Hatamleh *et al.* 2007). A RS depth profile comparing the effect of SP and LSP applied to the same material (Inconel 718) is shown in Figure 2.21b. While similar magnitudes of compression are introduced, the LSP affects a bigger volume. The layer of compressive RS produced by these two techniques is beneficial for delayed crack initiation and crack growth hence extending the component life cycle (Evans *et al.* 2005; James *et al.* 2007b). However, the compressive layer is balanced by tensile stresses deeper in the material which will superimpose onto the existing tensile welding RS. This may result in decreased component life cycle performance. The application of SP or LSP for stress engineering requires care in terms of where at the component surface and to what extent near surface compressive stresses should be introduced, in order to affect the welding RS in a beneficial way.

2.5.3.2 Vibratory Stress Relief

The vibratory stress relief technique was introduced in the 1970s and to date is a very ill understood technique for mitigating RS and distortion in welded structures (Masubuchi 1980; Walker *et al.* 1995; Aoki *et al.* 2003). The amount of literature is limited and the reported results vary significantly. Basically, the technique works by vibrating the component at a fixed frequency at stresses below the material yield strength σ_{YS} for a certain number of cycles (Walker *et al.* 1995). The mechanisms believed to act during vibratory stress relief include local plastic deformation, for example in the low yield strength σ_{YS} weld metal (Aoki *et al.* 2003) or micro structural rearrangement or 'energy' absorption as summarised by Withers (2007). However, to date the technique itself is neither well understood nor optimum parameters have been reported, but the technique itself has been shown to work in some cases (Masubuchi 1980; Walker *et al.* 1995; Aoki *et al.* 2003).

2.5.3.3 Global Mechanical Tensioning

Global mechanical tensioning can be applied either in-situ (ISGMT) or post welding (PWGMT). The plates are mechanically tensile loaded along the welding direction using a tensioning rig as shown in Figure 2.22. This device typically consists of serrated and hardened jaws with hydraulic rams attached to one end to apply the tensile load to the plates (Williams *et al.* 2006; Price *et al.* 2007). Slipping can further be restricted by pins or bolts in each grip passing through pre-machined holes in the plates. Both, ISGMT and PWGMT, significantly mitigate the developing RS during welding, or reduce the RS in the cold weld respectively, and subsequently the plate distortion (Masubuchi 1980; Staron *et al.* 2004; Williams *et al.* 2006; Price *et al.* 2007; Richards *et al.* 2008a; Williams *et al.* 2008). While the idea of tensile loading a structure to reduce the welding RS and subsequently distortion around the weld-line is rather old, the amount of work available on the effectiveness or establishing the basic principles of the mechanical tensioning technique is limited and does not allow for firm conclusions (Masubuchi 1980; Pilipenko 2001; Staron *et al.* 2004; Price *et al.* 2007; Williams *et al.* 2008).

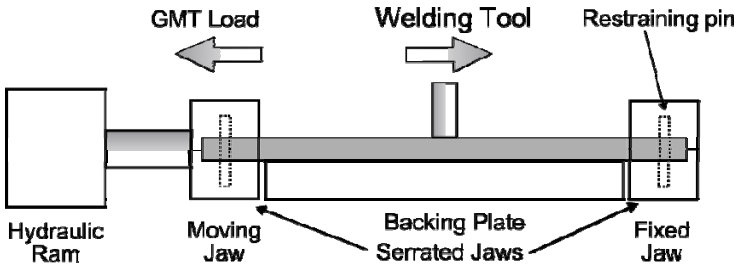

Figure 2.22: Schematic illustration of a global mechanical tensioning rig to apply tensile loads to the plates either during welding (SGMT) or after welding is complete (PWGMT). The plates are mounted in serrated and hardened jaws with hydraulic rams attached to one jaw to apply a tensile load. Slipping is further restricted by pins/bolts in each grip passing through pre-machined holes in the plates (after Price 2007).

Masubuchi (1980) reported the successful application of 2-dimensional in-plane stretching during fusion welding thin sheets onto a frame producing completely flat panels. However, this investigation was performed with a view of mitigating the distortion of the welded structure and no results on the effects of tensile loading on the RS reduction were reported.

Recent experimental, as well as FEM, work provides some fundamental knowledge of the ISGMT and PWGMT as well as the mechanisms acting during the application of these techniques. While Pilipenko (2001) theoretically explored the PWGMT technique to

explain the effect of the tensile loading on the longitudinal welding RS, Price *et al.* (2007) conducted experimental work comparing PWGMT and ISGMT applied to AA2024-T3, joined by FSW and TIG welding respectively. However, the first experimental work on the effect of ISGMT on the RS distribution was performed by Staron *et al.* (2004) who reported results for AA2024-T351 plates joined by and tensioned during FSW. Richards *et al.* (2008a) investigated the mechanisms acting during ISGMT by means of FEM using a linked thermal and mechanical model for the FSW process of different high strength aluminium alloys and different ISGMT loads. In detail these investigation revealed the following details.

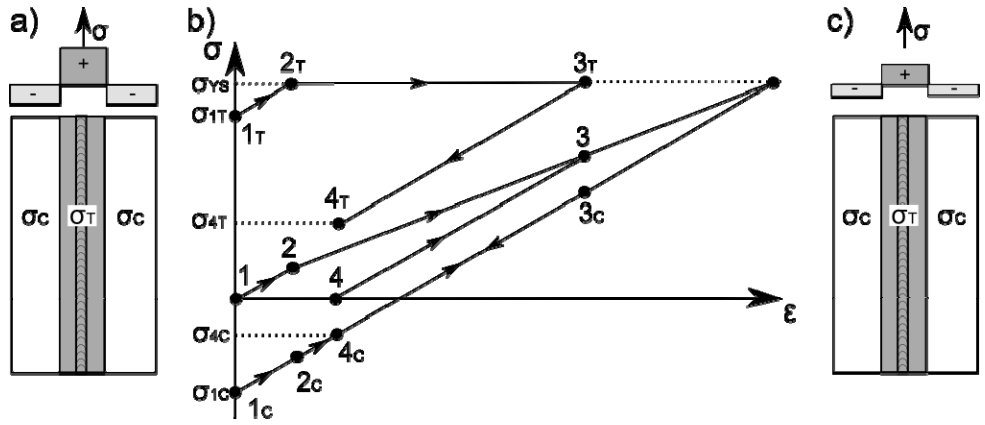

Figure 2.23: Schematic illustration of (a) a butt welded plate and its longitudinal RS distribution prior to applying PWGMT, (b) the welded plates elastic and plastic elongation as a function of the tensile PWGMT loading and unloading (the number are referred to in the text) and (c) the same plate with the mitigated RS after applying PWGMT (after Pilipenko 2001).

Pilipenko (2001) considered a fusion butt welded steel plate as schematically illustrated in Figure 2.23a with tensile RS σ_T in the weld zone balanced by compressive RS σ_C ($-\sigma_C=½\sigma_T$) further away in the PM. To model the PWGMT effect, as illustrated in Figure 2.23b, an external tensile load σ was applied to the ends of the welded plates, thus elongating the welded structure. This is represented by the linear increase from point *1* to *2* and the corresponding stresses from 1_T to 2_T and 1_C to 2_C. Loading the plate within the elastic region (to point *2*) means that the structure returns to its initial state if the external load was released and no RS mitigation would occur. However, exceeding point *2* by increasing the external load σ overcomes the tensile yield strength σ_{YS} as the external load superimposes onto the tensile RS σ_T and the weld zone plastically deforms. Consequently, less load increase as represented by a decrease of the slope of the trajectory of the external load σ (between point *2* and *3*) is required to achieve further elongation. Releasing the

loaded structure after increasing the external load to an arbitrary value, for example point *3* below the yield strength σ_{YS}, causes the elastic deformation to vanish while the plastic elongation remains. As a result of the plastic deformation of the weld-line material the elastic misfit between weld zone and PM is reduced. Consequently, the RS redistribute to ensure equilibrium and as a result the tensile weld zone and compressive PM stresses reduce in magnitude as shown schematically in Figure 2.23c. Pilipenko's model gives a first insight into the way that PWGMT affects the RS distribution, however, it does not account for possible differences of the material yield strength σ_{YS} between the weld zone and the PM as is the case for welds in high strength aluminium alloys (Allehaux *et al.* 2003; Dumont *et al.* 2006).

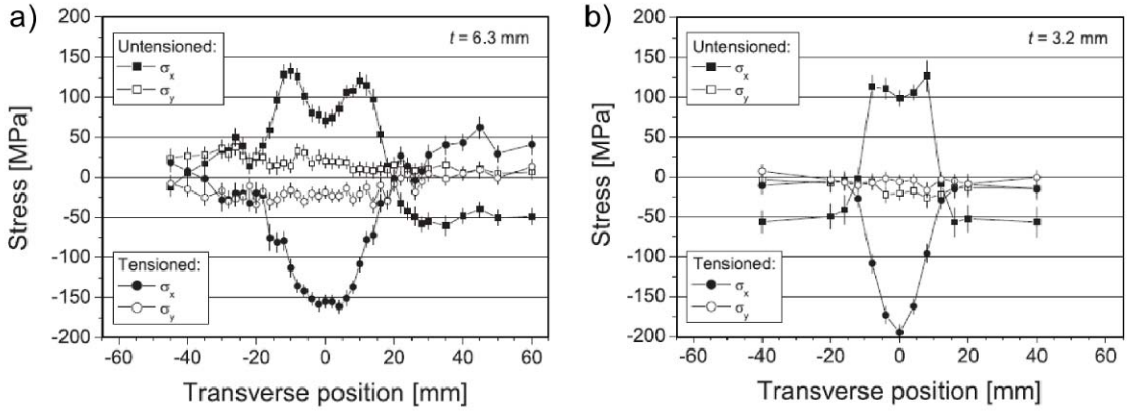

Figure 2.24: Longitudinal and transverse RS distribution in the as welded and to 0.70 σ_{YS} (~228 MPa) tensioned friction stir welds in 6.3 mm (a) and 3.2 mm (b) thick AA2024-T351 plates (Staron *et al.* 2004). The 6.3 mm welds were produced with 348 rpm, 96 mm/min and a M8 tool while the 3.2 mm welds were produced with 576 rpm, 198 mm/min and a M5 tool.

Staron *et al.* (2004) reported RS measurements, using neutron diffraction on the ARES instrument at the Geestacht Neutron Facility at GKKS, Germany, of the effect of ISGMT on the RS mitigation in 6.3 mm and 3.2 mm thick AA2024-T351 aluminium sheets joined by FSW and tensioned to 0.7 σ_{YS} (~228 MPa). The ISGMT load was applied using a rig, as illustrated in Figure 2.22, producing an evenly spread tensile loading condition along the ends of the plates and creating a uniform longitudinal tensile stress parallel to the weld-line. The tensioning loads were released after the FSW tool had traversed along the weld-line and the plates had cooled down.

As shown in Figure 2.24a and Figure 2.24b as a result of the ISGMT, the typical M-shaped RS distribution with tensile longitudinal RS peaks of ~140 MPa in the 6.3 mm (a) and 3.2 mm (b), disappears and significant compressive RS of approximately -150 MPa and

-200 MPa respectively are introduced to the weld-line. Staron *et al.* (2004) therefore concluded that ISGMT is a very effective technique to mitigate longitudinal tensile RS as long as the ISGMT load is chosen carefully. Significant compressive RS may be introduced if excessive loading is applied. No effect on the transverse RS due to the ISGMT was observed.

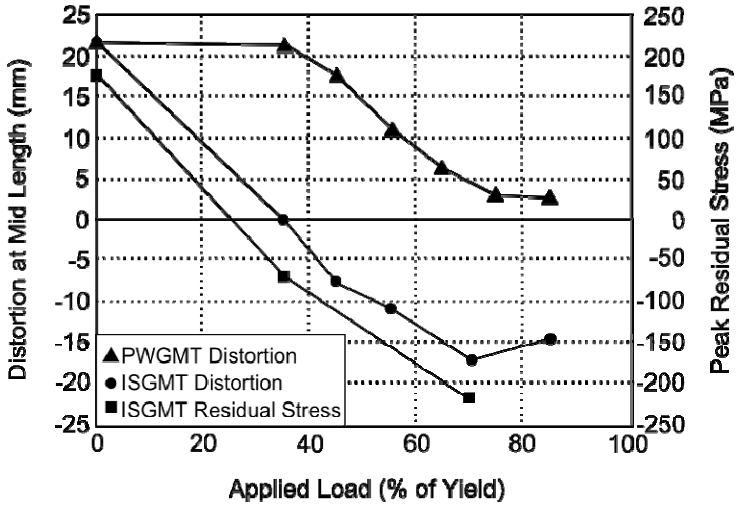

Figure 2.25: The plate bending distortion and the longitudinal peak welding RS at mid length of a 3.2 mm thin AA2024-T3 plate joined by FSW in the butt weld configuration as a function of applied ISGMT and PWGMT load (after Price *et al.* 2007).

Based on the work of Staron *et al.* (2004), Price *et al.* (2007) experimentally compared the effect of PWGMT and ISGMT on the mitigation of the welding RS and the resulting bending distortion as a function of the applied ISGMT load in 3.2 mm AA2024-T3 plates joined by FSW, as well as in TIG welding, using energy dispersive X-ray diffraction at the ID15A beam-line at the European Synchrotron Radiation Facility in Grenoble, France. They reported that the required tensile PWGMT load to overcome the weld-line material yield strength σ_{YS} in a cold weld is comparatively high. It requires approximately $0.7\,\sigma_{YS}$ (~228 MPa) of the PM to exceed the weld-line material yield strength in order to minimise the plate bending distortion (Figure 2.25), which is believed to be closely related to the longitudinal RS distribution (Price *et al.* 2007). However, such high loads are difficult to apply and require very strong and cumbersome tensioning machinery with increasing size of the engineering components; hence the PWGMT can be considered as an industrial relevant technique for a small number of applications.

Alternatively, Price *et al.* (2007) reported that significantly smaller loads are required to reduce longitudinal RS and subsequently the bending distortion when ISGMT is applied for FSW and TIG welding when the yield strength σ_{YS} of weld-line material is low due to

the elevated temperatures during welding. They stated that an ISGMT load of 0.35 σ_{YS} of PM (~114 MPa) already leads to low longitudinal compressive RS and minimises the plate bending distortion, as shown in Figure 2.25. Even higher loads lead to significant compressive weld-line RS in the longitudinal direction, while the transverse RS again are not affected by the ISGMT. The change in the sign of the longitudinal RS is accompanied by a switch in the plate distortion from concave to convex relative to the weld surface as shown in Figure 2.25. Further, a linear correlation between the applied ISGMT load and the reduction in longitudinal RS was observed. Price *et al.* (2007) predicted that a RS free weld may be produced if the ISGMT load is ~0.25 σ_{YS} of PM for the applied FSW parameter settings in this aluminium alloy. In addition, they presumed that ISGMT with increased loading is required to minimise distortion in welds produced with higher heat input during FSW, as increased temperatures are believed to cause higher RS and more plate distortion.

Further, Price *et al.* (2007) reported an effect of ISGMT on weld defects such as pores or tunnels defects (see section 2.3.3.1) occurring in the weld zone of friction stir welds. They found that welds produced with welding parameters outside the optimum process window (energy input above or below optimum level) for FSW in 6.3 mm thick AA2024-T3 material displayed severe tunnel defects and pores especially at the beginning of the weld. The application of an ISGMT load of 0.7 σ_{YS} of PM reduced the amount of pores and the tunnel defects nearly vanished. When the same ISGMT load was applied to a weld produced with optimized FSW parameter no defects were observed and they concluded that ISGMT increases the plasticity in the weld zone and in combination with optimized FSW parameters reduces defect formation (Price *et al.* 2007).

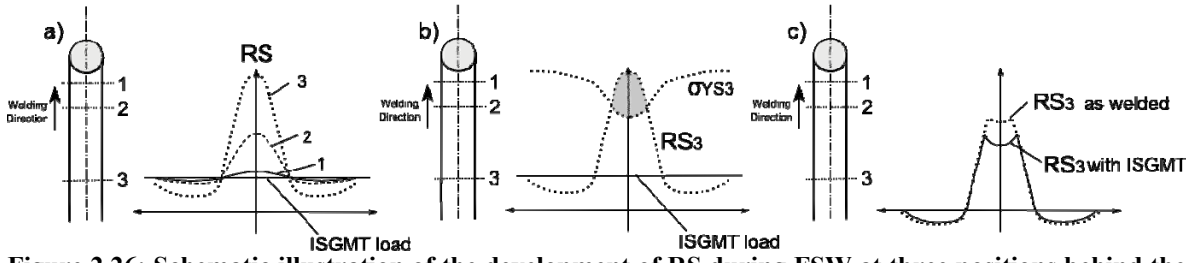

Figure 2.26: Schematic illustration of the development of RS during FSW at three positions behind the FSW tool: (a) the increased RS profile due to the superimposed ISGMT load, (b) more plastic deformation occurs as the yield strength and RS distribution overlap more and (c) comparison of the final RS distribution for as welded and welded with ISGMT applied (after Price 2007).

Finally, Price *et al.* (2007) provided a graphical illustration of the development of the typical longitudinal RS distribution in plates joined by FSW with an applied ISGMT load,

as shown in Figure 2.26. Based on Figure 2.16, graph a in Figure 2.26 depicts the arising longitudinal tensile RS for the three positions (1-3) behind the weld tool, superimposed with the stress introduced by ISGMT. This increases the resulting overlap between the trajectories of the arising RS and the local yield strength σ_{YS}, thus increasing the amount of RS that relaxes by plastic elongation of the material as shown in graph b) for position 3. The increased overlap, hence plastic deformation, leads to a reduction of the volumetric misfit between the weld zone and the PM and consequently to reduced longitudinal RS. This is depicted in graph c), where the RS for an as-welded (see Figure 2.16 f) and an in-situ global mechanical tensioned plate joined by FSW are compared.

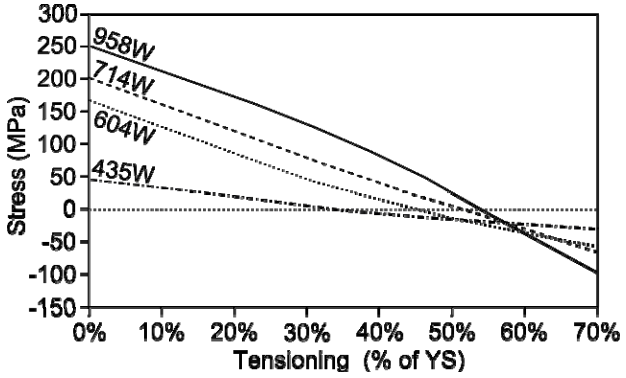

Figure 2.27: Predicted maximum longitudinal RS as a function of the applied tensioning load as a fraction of the material yield strength. The stress mitigation is shown for different power inputs during welding (Richards *et al.* 2008a).

Richards *et al.* (2008a) investigated the mechanisms acting during and the effect of ISGMT by means of FEM and confirmed the above discussed results by Staron *et al.* (2004) and Price *et al.* (2007). Richards *et al.* (2008) used a sequential thermal and mechanical model (see section 3.5) for simulating the FSW process of different high strength aluminium alloys and the effect of varying tensioning loads applied during the FSW process. They concluded that the RS reduction and the ISGMT loads correlate reciprocally proportional, and that for the investigated cases the optimum tensioning level is around 0.40 σ_{ys} of PM. In Figure 2.27 the predicted maximum RS as a function of the applied ISGMT load as a fraction of the material yield strength σ_{YS} is shown for friction stir welds joined with different power inputs.

Within this dissertation ISGMT was applied to test welds in high strength aluminium alloys joined by FSW and the RS distribution has been determined. The results of these experiments are presented in chapter 5.

2.5.3.4 Roller Tensioning

Roller tensioning by guiding rollers along the weld-line can be considered as the locally applied version of global mechanical tensioning. Similar to ISGMT and PWGMT, roller tensioning is not a new invention and has been used on fusion welds before to reduce hot cracking, RS and distortion, as well as to improve the mechanical properties of welded joints. Liu *et al.* (1996) reported the use of synchronous rolling during fusion welding of AA2024-T4 to prevent the hot weld material from cracking upon cooling. Two rollers alongside the weld-line trailing the weld tool exert a down force in order to introduce a compressive strain in the transverse direction to counteract the crack initiating transverse tensile RS forming during cooling. Yang *et al.* (1998) performed FE simulation as well as experimental work on a similar system with the aim to mechanically compress the weld-line material in order to reduce both transverse RS and the buckling distortion in TIG welded AA2024 aluminium alloy. They stated that larger roller pressure increases the reduction of transverse RS and also reduces the hot cracking. Xu *et al.* (2004), on the other hand, used a single trailing roller positioned directly on the TIG weld-line to produce compression in the weld normal direction in order to elongate the material in the welding direction to reduce hot cracking.

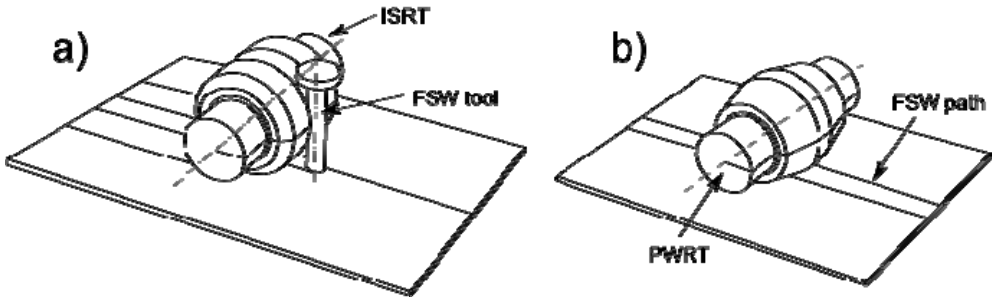

Figure 2.28: Schematic illustration of the ISRT double roller (a) and (b) the single roller applied for PWRT (after Wen *et al.* 2009).

Wen *et al.* (2009) summarised that until recently roller tensioning has only been applied to fusion welds but no work has been reported on the application of this technique for FSW. Therefore, they conducted initial research using a FEM approach to investigate the effect of roller tensioning along the welding direction to mitigate longitudinal RS and the bending and angular distortion in FSW of the high strength aluminium alloy AA2024-T3. They investigated both in-situ roller tensioning (ISRT) and post weld roller tensioning (PWRT). The simulated ISRT was applied with a double roller as depicted in Figure 2.28a,

with a transverse roller gap slightly greater than the diameter of FSW tool shaft thus allowing the ISRT rollers to follow the welding tool closely. The PWRT methods were categorised into PWRT applied dynamically directly trailing the FSW tool, so as to affect the hot material, and PWRT applied after welding to the cold weld. Both methods are applied using a single PWRT roller positioned directly on the weld seam as shown in Figure 2.28b.

The FEM predictions indicate that if applied properly roller tensioning can generate sufficient compressive plastic deformation in the plate normal direction, which is equilibrated by material elongation in the rolling or longitudinal direction and, as such, counteracts the longitudinal tensile welding RS. Wen *et al.* (2009) summarized the effect of rolling down force, the roller width and diameter and, therefore, the subsequent reduction in plate thickness for roller tensioning and the distance between the welding tool and the trailing roller for ISRT to be the main influencing parameter for the mitigation of RS and distortion.

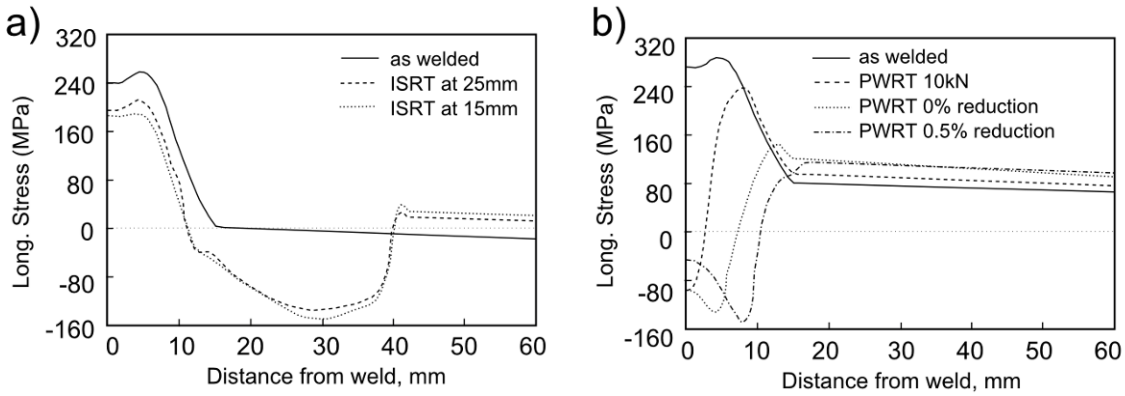

Figure 2.29: The predicted effect of (a) ISRT (Ø=100 mm, 2×29 mm wide and 20 mm gap) and (b) PWRT (Ø=100 mm and 20 mm wide) applied to the cold weld on the longitudinal RS distribution in an AA2024-T3 plate (500 ×250 ×3.2 mm^3) joined by FSW as predicted using ABACUS FEM software.

As depicted in Figure 2.29a, Wen *et al.* (2009) found that ISRT at distances of 15 and 25 mm behind the FSW tool with a double roller (Ø=100 mm, 2×29 mm and 20 mm gap) significantly affects the final longitudinal RS distribution profile. The FE model predicted that ISRT introduces elastic and plastic material elongation next to the weld path, thus eventually causing the weld-line material to overcome the local yield strength σ_{YS} leading to plastic elongation and thereby reducing the RS. They found that ISRT trailing at a short distance leads to more plastic material elongation in the weld-line due to higher temperatures, and hence a lower yield strength σ_{YS}. Consequently, the mitigation of the

longitudinal RS is slightly higher than for ISRT applied at greater distances. On the other hand, ISRT introduces significant compressive RS next to the weld zone as illustrated in Figure 2.29a (Wen *et al.* 2009).

PWRT applied to the cold weld using a roller of 100 mm in diameter and 20 mm width was found to turn the tensile into compressive RS even when only a small down force was applied. In this case, PWRT introduces plastic compression directly to the weld-line material in the plate normal direction causing significant plastic elongation in the rolling or longitudinal direction and to some extent in the transverse direction (Wen *et al.* 2009). A rather small down force of 10 kN is sufficient to turn tensile weld-line RS of ~250 MPa into compressive RS of nearly the same magnitude. However, the effect is restricted to the RS occurring at the weld-line, leaving significant tensile RS peaks at the weld seam edge. By increasing the reduction in material thickness achieved by the PWRT, or increasing the roller width those remaining tensile RS peaks can be mitigated and a wide zone of compressive RS following a W-shaped distribution can be introduced. The model showed that PWRT applied to the warm weld with a lower local yield strength σ_{YS} by running the roller directly behind the FSW tool, has less effect than when applied to the cold weld. While the RS decreased by nearly 500 MPa by PWRT the cold weld the in-situ PWRT only achieved a reduction of ~200 MPa.

Finally, Wen *et al.* (2009) concluded that PWRT, if applied excessively with high down forces, small roller diameters and significant thickness reduction, can turn tensile RS into high compressive RS, while ISRT was said to be less effective. As no experimental data were available to validate the FE model, it was recommended to produce test friction stir welds with ISRT and PWRT applied to investigate experimentally the effect on the RS as well as the post weld mechanical properties.

Within this dissertation ISRT and PWRT was applied to test welds in high strength aluminium alloys joined by FSW and the RS distribution has been determined. The results of these experiments are presented in chapter 6.

2.5.4 Conclusions

In this section several thermal and mechanical stress engineering techniques for mitigation of welding induced RS and the related distortion were reviewed, whereby

special attention was given to the global mechanical tensioning applied during welding (ISGMT) and the roller tensioning applied during (ISRT) as well as after welding (PWRT).

A substantial amount of work, based on experimental (Staron *et al.* 2004; Williams *et al.* 2006; Price *et al.* 2007) and FEM (Richards *et al.* 2008a) approaches, has been performed in order to understand the mechanisms acting during ISGMT applied to FSW. While it is clear that ISGMT along the FSW direction leads to reductions of the longitudinal tensile RS by decreasing the compressive yielding in front of and increasing the tensile yielding behind the welding tool, no general conclusion regarding the level of ISGMT load required to produce stress free welds was made. It is this question that this dissertation addresses by investigating systematic sets of test welds in high strength aluminium alloys joined by FSW and subject to varying ISGMT loads.

On the other hand, ISRT and PWRT are relatively new techniques with respect to the application to FSW (Williams *et al.* 2008; Wen *et al.* 2009). While a FEM approach to explore the effectiveness of the technique for reduction of longitudinal tensile RS and the related distortion has been reported, no experimental data exists to evaluate these FEM results. In this dissertation several sets of friction stir welds in high strength aluminium alloys with ISRT and PWRT applied are investigated in terms of the RS mitigation.

In order to evaluate the effectiveness of any stress engineering technique with respect to the RS mitigation, it is important to determine the RS as a function of the applied stress engineering method. The techniques used for RS determination in the test welds investigated in this dissertation are addressed in the following section.

2.6 DETERMINATION OF RESIDUAL STRESS

It is impossible to measure RS directly. Instead one can determine RS from measured changes of material properties that are altered by the RS. A variety of techniques exist that can be differentiated into destructive and non-destructive (Hauk 1997; Withers *et al.* 2001a).

Destructive techniques for example the hole drilling (Macherauch 1992; Withers *et al.* 2001a) or the contour method (Prime *et al.* 2000; Withers *et al.* 2001a), are based on the measurement of the material deformation as a result of the redistribution of internal stresses as material is removed from the component (Withers *et al.* 2001a). From the amount of deformation one can back-calculate the RS present in the component prior to removing

material. These methods are not used in this dissertation; hence a detailed discussion is beyond the scope of this section.

Non-destructive techniques do not require damaging the component of interest. Non-destructive techniques, such as the ultrasonic or the magnetic method, determine the change of speed of sound travelling through the material, or the change of a magnetic field response of the material due to RS (Withers *et al.* 2001a). However, these techniques are limited as RS gradients along the propagation direction of the sound or magnetic waves can not be detected.

As an alternative, non-destructive diffraction based techniques, using neutron or synchrotron X-ray radiation, allow the determination of RS with high spatial resolution (Webster *et al.* 1996; Hauk 1997; Withers *et al.* 2001a). Even though many different variations of diffraction based methods exist, within this dissertation only two, namely the angular dispersive neutron diffraction (ADND) as well as the energy dispersive synchrotron X-ray diffraction (EDXRD) were used for determination of the RS in the test welds, to evaluate the effects of the applied stress engineering techniques for mitigation of RS (see section 2.5).

A detailed discussion of the diffraction techniques used in this dissertation and the subsequent calculation of the RS from the obtained diffraction data is useful at this point. Further, possible problems arising during diffraction measurements, which can either be technique or sample related, with respect to the determination of RS, will also be addressed.

2.6.1 Introduction

In this dissertation the RS distribution across the weld-line in high strength aluminium alloys joined by FSW and subject to different stress engineering techniques is evaluated using ADND and EDXRD. The determination of RS using these two techniques generally requires three steps (Holden *et al.* 1995; Webster *et al.* 1996; Hauk 1997; Withers *et al.* 2001d):

- The measurement of the lattice spacing d_{hkl} of one particular family *{hkl}* of crystallographic lattice planes within a defined region in the component.
- The calculation of the lattice strain ε of the plane sampled, by relating the measured lattice spacing d to the locally corresponding value for the unstrained lattice spacing d_0 for the elastically strain free state.

- The calculation of the RS is based on the calculated strain tensor ε. This is an important point – the RS are not directly measured and the accuracy of the inferred RS values depends on the validity of the assumptions made in its determination.

The following sections detail each of these three steps.

2.6.2 Bragg Diffraction and Strain

The measurement of the lattice plane spacing d_{hkl} of a certain family of crystallographic lattice planes indicated with the Miller indices *{hkl}* is based on Bragg's law as illustrated in Figure 2.30a. Bragg's law states that for a given lattice spacing d_{hkl} constructive interference of scattered waves of the incident beam S_0 occurs only at certain Bragg diffraction angles $2\Theta_{hkl}$, leading to intensity peaks in the diffracted beam S_1. Each Bragg diffraction angle (angle 2Θ between transmitted beam S_0 and diffracted beam S_1) corresponds to one particular family of *{hkl}* lattice planes. The scattering vector Q is the bisecting vector between incident beam S_0 and diffracted beam S_1, is normal to the lattice planes sampled and represents the direction in which the strain hence the RS is determined. The mathematical relationship between the crystal lattice spacing d_{hkl} and diffraction angle Θ_{hkl} is expressed in Bragg's law (Hauk 1997):

$$n\lambda = 2d_{hkl}\sin\Theta_{hkl} \qquad \textbf{Equation 2.1}$$

where n is the order of reflection and λ the wavelength of the radiation in use. This equation can be used to determine the lattice specific strain on a set of *{hkl}* lattice planes by using the crystal lattice as a kind of internal strain gauge. When a stress is acting on the sample the *{hkl}* lattice spacing will be altered compared to the unstrained state. The strain ε_{hkl} on a set of lattice planes *{hkl}* is given by (Cullity 1978; Hauk 1997):

$$\varepsilon_{hkl} = \frac{(d_{hkl} - d_{hkl\,0})}{d_{hkl0}} = \frac{\Delta d_{hkl}}{d_{hkl0}} \qquad \textbf{Equation 2.2}$$

where d_{hkl0} is the unstrained lattice spacing for the crystallographic planes in question and d_{hkl} is the strained condition. Within an isotropic material, the *{hkl}* lattice planes normal to a uniaxial tensile stress increase the lattice spacing d_{hkl} by elastic deformation causing the diffraction angle $2\Theta_{hkl}$ to shift to lower values. On the other hand, due to

Poisson's contraction the lattice spacing decreases for planes parallel to the direction of loading. This results in a shift to higher diffraction angles. Both cases are illustrated in Figure 2.30b and Figure 2.30c. In polycrystalline materials, where a random distribution of grains is given, only those grains that fulfil the Bragg condition will contribute to the diffraction pattern.

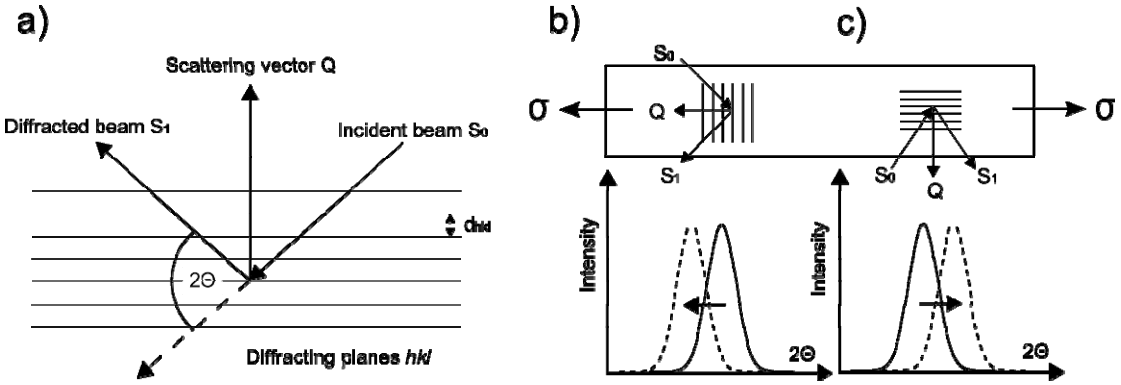

Figure 2.30: Illustration of Bragg's law: (a) the incident beam S_0 is diffracted on a set of lattice planes *{hkl}* and at certain diffraction angles 2Θ constructive interference occurs leading to intensity peaks in the diffracted beam S_1. The effect of a tensile load on crystal lattice planes orientated normal (b) and parallel (c) to the loading direction leading to increased (b) or decreased (c) lattice spacing. This results in shifts of the diffraction angle to lower angles (b) and higher angles (c) respectively.

Several techniques based on variations of Bragg's law exist to measure the lattice spacing *d*. However, in this dissertation the conventional ADND, as well as the EDXRD techniques, were employed and are detailed in the following sections.

2.6.3 Angular Dispersive Neutron Diffraction

Neutrons: Neutrons are sub-atomic particles with the mass of a proton but no electric charge. Neutrons scatter at atomic nuclei that are periodically arranged within the grains of such materials. The wavelength of a non-relativistic (thermal) neutron is given by:

$$\lambda = \frac{h}{m_n v} \qquad \textbf{Equation 2.3}$$

where h is Planck's constant, m_n is the mass and v the velocity of the neutron. Thermal neutrons are produced at neutron reactor sources. From the reactor core emitted neutrons are moderated in heavy water until they have an appropriate wavelength, similar in

magnitude to the lattice spacing of typical engineering materials. They are directed to the instruments using neutron guides.

In practice Bragg's law (see equation 2.1) applies directly for monochromatic (single wavelength) angular dispersive neutron diffraction (ADND) at neutron reactor sources. A monochromatic neutron beam is produced by selecting one wavelength from the white main beam (a range of wavelengths) using a single crystal (for example Si{111}), generally referred to as a monochromator. Based on Bragg's law the desired wavelength is selected by altering the diffraction angle of the crystal.

Angular dispersive neutron diffraction: A schematic of a monochromatic neutron beam diffraction instrument set-up for a neutron reactor source is shown in Figure 2.31a. The primary and secondary slits define the cross-section of the monochromatic neutron beam prior (S_0) and after (S_1) irradiating the sample and thereby define the nominal gauge volume size and shape. The combination of the chosen wavelength and the *{hkl}* lattice spacing measured allow using diffraction angles of $2\Theta \approx 90°$ thus producing a nearly cubical nominal gauge volume shape. The incident monochromatic neutron beam S_0 enters the sample and according to Bragg's law, is diffracted on the lattice planes *{hkl}* normal to the bisecting scattering vector *Q*. Measurement of the intensity of the diffracted beam S_1 by moving a neutron sensitive detector as a function of angular position around the gauge volume centre gives the {*hkl*} lattice plane Bragg angle. The distribution of intensity of the diffracted beam around these Bragg angles (see Figure 2.31b) often follows a Gaussian or Lorentzian type distribution hence allows using such functions to fit to the diffraction pattern in order to determine the angular position of the peak centre (Webster *et al.* 2002). Using equation 2.1 then allows for calculation of the specific lattice spacing d_{hkl}.

In Figure 2.31a the sample orientation (1) for measurement of the lattice spacing in the plate normal direction is illustrated. The depicted sample represents a cross-section of a friction stir weld with the light grey area being the weld-line. The sample is orientated such that the plate normal direction is parallel to the scattering vector Q. The set-up is termed reflection mode. On the other hand, to measure the *d*-spacing in the transverse plate direction the sample is rotated by 90° around the longitudinal plate axis of the weld as shown in orientation (2) in Figure 2.31a. This is termed transmission mode. In order to measure the lattice spacing in the longitudinal plate direction the sample is rotated around the plate normal axes, thus keeping the transmission mode set-up (not shown in the Figure).

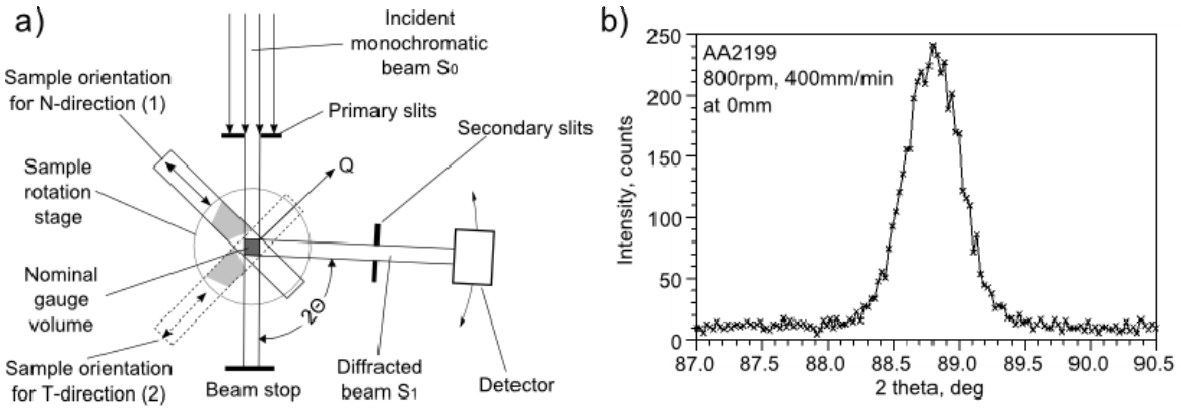

Figure 2.31: (a) Set-up for ADND on a neutron reactor source (top-view), the illustrated sample shows the N-T cross-section of a friction stir weld, in configuration (1) the lattice spacing is measured in the normal direction (see *Q*-vector orientation) and if rotated by 90° around the longitudinal axis of the welded plate the transverse direction is measured (2). Graph (b) shows a typical diffraction peak profile of a *{311}* aluminium peak as recorded on the SALSA beam-line (see chapter 3).

By rotating the detector for determination of the angular position of the diffracted beam S_1, the effective gauge volume shape and, therefore, the sampled material changes, because the secondary slits move along with the detector ensuring a constant beam size for S_1. On the other hand, the angular width of the diffraction peak is comparatively small; hence this requires little angular movement of the detector, thus minimizing the effects of the altering gauge volume. To overcome this problem, 2-dimensional area detectors can be used to measure the intensity of the diffracted peak over an angular range, which is determined by the size of the detector window.

In this dissertation the ADND was used on the dedicated SALSA neutron diffractometer at the Institut Laue-Langevin (ILL) in Grenoble, France (Pirling *et al.* 2006). Instrument details and the exact set-up for the ADND to measure the lattice spacing is given in section 3.3.2.

2.6.4 Energy Dispersive Synchrotron X-ray Diffraction

The second method to measure the lattice spacing *d* used in this dissertation is the energy dispersive synchrotron X-ray diffraction (EDXRD) technique.

Synchrotron X-rays: Synchrotron X-ray photons are produced at electron accelerator rings, usually consisting of a series of straight vacuum pipes forming an n-sided polygon, also referred to as storage ring. In the case of the European Synchrotron Radiation Source (ESRF) in Grenoble, France, the electrons are initially produced and accelerated in a linear booster (linac) before accelerated even more in a circular booster ring (circumference =

300 m, 6 GeV, 10 Hz). Finally, the electrons are injected into the storage ring (circumference = 844 m), where they circulate. Naturally, electrons at high energy move linearly, however in order to circulate the electrons pass through 64 single pairs of magnets (bending magnets) where they are accelerated radially towards the next section pipe, as illustrated in Figure 2.32. The radial acceleration results in the emission of X-ray photons travelling approximately tangentially to the curved electron path. At straight sections the electrons may pass through multiple pairs of dipole magnets, so-called wigglers or undulators, where the electrons are "wiggled" from side to side without actually changing the original propagation direction. However, each time they oscillate they emit X-ray photons resulting in an X-ray photon beam of higher intensity than produced at a single bending magnet.

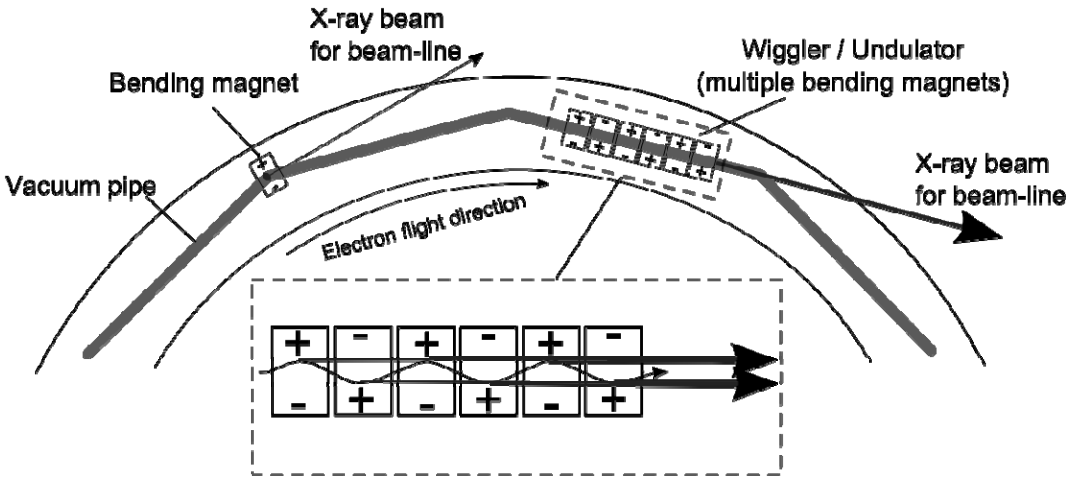

Figure 2.32: Schematic of the production of synchrotron X-ray radiation at an electron accelerator. At bending magnets the electron beam is redirected towards the next vacuum pipe section whereby X-ray radiation is emitted, higher intensity X-ray radiation is produced using wigglers or undulators consisting of a series of dipole magnets.

The intensity and energy hence wavelength spectrum of the emitted synchrotron X-ray beam depend on the amount and the speed of the electrons circulating in the storage ring. The wavelength λ in Å of an emitted photon is related to its energy by:

$$\lambda = \frac{hc}{E_{hkl}} = \frac{12.39842}{E} \qquad \textbf{Equation 2.4}$$

where c is the speed of light in vacuum and E the energy of the photon in keV. The wavelength spectrum varies from infra-red (~0.1 keV) to hard X-rays (>20 keV). While neutrons interact with atomic nuclei, X-ray photons are scattered by atomic electron clouds

and therefore are well suited for the measurement of lattice plane distances by Bragg diffraction.

Energy dispersive synchrotron X-ray diffraction: In contrast to ADND a white synchrotron X-ray beam is used for EDXRD based on the following modified version of Bragg's law (Hauk 1997):

$$\frac{hc}{E_{hkl}} = 2d_{hkl}\sin\Theta \qquad \textbf{Equation 2.5}$$

A schematic illustration of a typical EDXRD beam-line set-up is shown in Figure 2.33a. The EDXRD technique is based on a "white" (all wavelengths) incident beam S_0. This allows Bragg diffraction to occur on several lattice plane families *{hkl}* at a single scattering angle, 2Θ, hence several *{hkl}* diffraction peaks contribute to the energy spectrum of the diffracted beam S_1 as depicted in Figure 2.33b. Using an energy sensitive Ge-detector this energy spectrum is measured (Hauk 1997; Reimers *et al.* 1999; Steuwer *et al.* 2004).

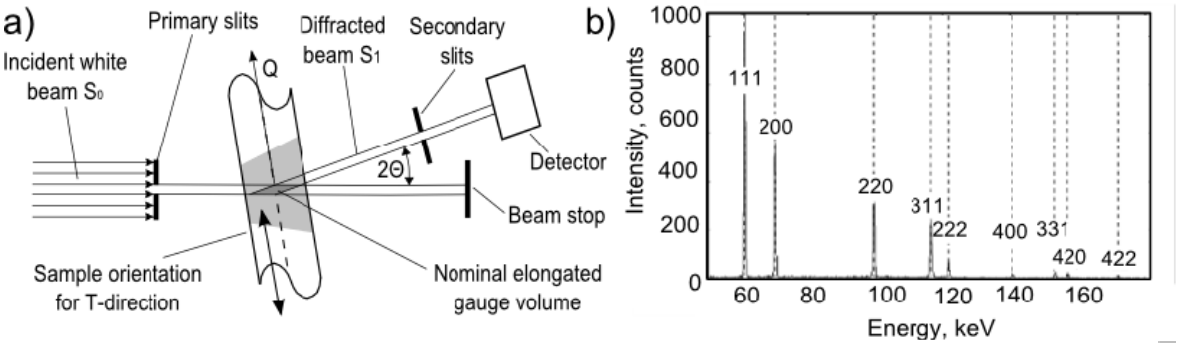

Figure 2.33: (a) EDXRD set-up (top-view), the illustrated sample shows the N-T cross-section of a friction stir weld. In the depicted orientation the lattice spacing *d* of several *{hkl}* lattice planes in the transverse direction is measured in the weld nugget (after Reimers *et. al.* 1999). A typical diffraction pattern as obtained using EDXRD on an aluminium powder with a 0.1×0.1×2.3 mm^3 gauge volume, 2Θ = 5° and 35 sec counting time is shown in (b).

Primary and secondary slits determine the cross-section of the incident and diffracted beam S_0 and S_1, respectively, and as a function of the diffraction angle 2Θ define the dimensions and shape of the gauge volume. Compared to the nearly cubical gauge volume shape for ADND instruments, the low diffraction angles normally used for EDXRD lead to an elongated diamond shaped gauge volume as is depicted in Figure 2.33 a.

In this dissertation the high energy beam-line ID15A at the European Synchrotron Radiation Facility (ESRF) in Grenoble, France was used for the EDXRD based RS determination. The instrument and set-up details are given in section 3.3.3.

An advantage of EDXRD is that several *{hkl}* lattice plane families contribute to the diffraction energy profile at the same time. This tends to reduce spurious results introduced by texture and elastic and plastic anisotropy (Hutchings *et al.* 1992; Daymond *et al.* 1997). In addition, the range of wavelengths means more differently orientated grains within the gauge volume contribute to the diffracted signal, thus to some extent reducing problems attributed to a large grain size (see section 2.6.6.2). Using appropriate full-pattern refinement, based on fitting Gaussian, Lorentzian or combinations of both types of functions (Voigt) to each peak allow for determination of the unit cell parameter, which for fcc materials such as aluminium, is designated a. As a result to calculate the average strain ε based on equation 2.2 one replaces the d-values with the unit cell parameters for the strained (a) and unstrained (a_0) condition (Cullity 1978; Hauk 1997):

$$\varepsilon = \frac{(a - a_0)}{a_0} = \frac{\Delta a}{a_0} \qquad \textbf{Equation 2.6}$$

The unit cell parameter a for materials with cubic unit cell structures is representative for the crystal strain, as it represents an average value of lattice specific d-spacings. The correlation between the specific lattice plane spacing d_{hkl} and the unit cell parameter a for cubic unit cell structures is expressed in the following equation (Barret *et al.* 1980; Hauk 1997):

$$d_{hkl} = \frac{a}{\sqrt{(h^2 + k^2 + l^2)}} \qquad \textbf{Equation 2.7}$$

where h, k and l are the Miller indices. This equation allows for conversion of data obtained using one diffraction method to be implemented with data derived using another one. Within this dissertation, the aluminium d_{311} data as obtained using ADND on the SALSA beam-line were converted into unit cell parameter a values in order to allow for combination with EDXRD unit cell parameter values. This is possible as the *{311}* lattice plane mirrors the average strain of the unit cell most accurately (Clausen *et al.* 1998) as is discussed in section 2.6.5. In this dissertation for simplicity it is refereed to the unit cell

parameter a as well as the unstrained unit cell parameter a_0, even when the data are based on the specific lattice planes spacing d_{hkl} or d_{hkl0}.

ADND and EDXRD enable determination of the residual strain. In both cases the shift of the strain due to RS acting in welded plates as a function of lateral position from the weld-line can be determined by moving the test welds along the transverse plate direction (as indicated with the arrows in Figure 2.31 and Figure 2.33), such that the gauge volume samples the material in the desired region. Using computer controlled translation stages in combination with user written macros this means that the strain as a function of distance from the weld-line and/or the weld surface can be mapped automatically.

Having calculated the residual strain ε in several directions using equation 2.6, one can now calculate the RS. The relations between strain and stress, as well as the equations necessary to calculated RS from strain as used for this dissertation are detailed in the following section.

2.6.5 Calculation of Residual Stress

The determination of the RS in welded structures using diffraction techniques requires the measurement of the unit cell parameter a and the corresponding value for the unstrained condition a_0 respectively. After calculation of the strain ε using equation 2.6, one can derive the RS. However, prior to the introduction of the RS calculation it is useful to briefly introduce the very basic concept of residual strain and stress and their correlation.

The stress acting on an elastically isotropic cube of material may be represented by the components illustrated in Figure 2.34, where the face normal stresses σ_{ij} ($i = j$, solid lines) act perpendicular and shear stresses σ_{ij} ($i \neq j$, dotted lines) act parallel to the cube faces. If no rotational force is acting on the cube the shear stresses along opposite surfaces are equal but contrarily directed and so they cancel out each other. Therefore, only six out of the nine components are independent. In case the stress in one direction is zero or sufficiently small it can be neglected and the triaxial state converts into a biaxial or in-plane stress state. This condition occurs at free surfaces, where the out-of-plane stress must be zero. This stress condition allows the application of laboratory X-ray diffraction measurements with penetration depths of a few micrometer, in order to determine the near surface in-plane RS.

On the other hand, using synchrotron X-rays or neutrons enables penetrating much further into the bulk material of the component hence a 3-dimensional stress state should be assumed, when using such methods. In samples where one dimension is much smaller than the other two, as is the case for sheet or plate material, with the internal loading mainly in-plane, often little or no stresses are acting normal to the plate surface. Hence, a 2-dimensional stress state as illustrated in Figure 2.34b may be assumed. This assumption is commonly employed in the RS analysis of thin welded structures.

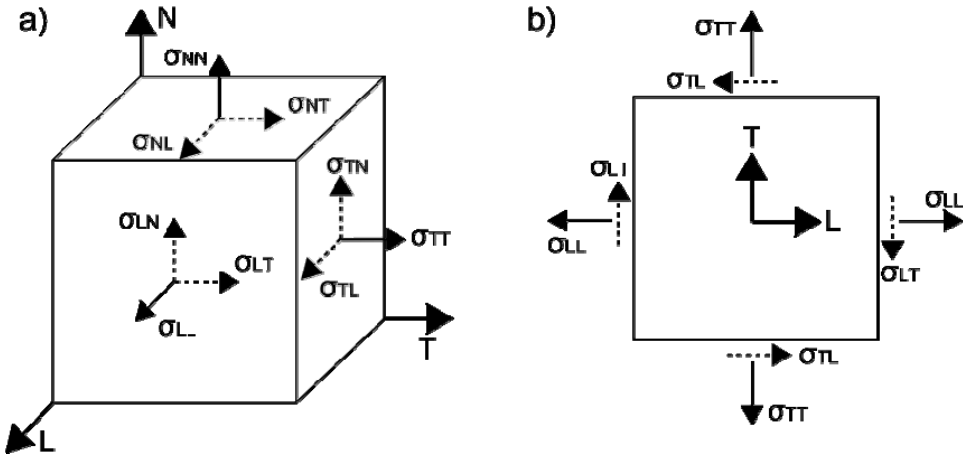

Figure 2.34: (a) Unit cube with nine components of stress and (b) reduction to in-plane stress condition (Hauk 1997), the solid lines represent stresses normal to the cube faces whereas the dotted lines illustrate the shear stresses.

The fundamental relationship between strain ε and stress σ is described in Hooke's law in scalar form for the one-dimensional (equation 2.9) and for the three-dimensional case in tensor form (equation 2.10) (Hauk 1997):

$$\sigma = E\varepsilon \qquad \textbf{Equation 2.8}$$

$$\sigma_{ij} = \sum_{kl} C_{ijkl}\varepsilon_{kl} \qquad \textbf{Equation 2.9}$$

where E is Young's modulus and C the stiffness tensor of fourth rank. The acting stress σ along mutually orthogonal coordinate axes L, T and N at a point can be determined from the strain measurements made along these axes (scattering vector Q is aligned). In this case the stresses in the three directions are calculated by (Hauk 1997; ISO/TTA3 2001):

$$\sigma_{LL} = \frac{E}{(1+\upsilon)(1-2\upsilon)}\left\{(1-\upsilon)\varepsilon_{LL} + \upsilon(\varepsilon_{TT} + \varepsilon_{NN})\right\} \qquad \textbf{Equation 2.10}$$

$$\sigma_{TT} = \frac{E}{(1+\upsilon)(1-2\upsilon)}\left\{(1-\upsilon)\varepsilon_{TT} + \upsilon(\varepsilon_{LL} + \varepsilon_{NN})\right\} \qquad \textbf{Equation 2.11}$$

$$\sigma_{NN} = \frac{E}{(1+\upsilon)(1-2\upsilon)}\left\{(1-\upsilon)\varepsilon_{NN} + \upsilon\,(\varepsilon_{LL} + \varepsilon_{TT})\right\} \qquad \textbf{Equation 2.12}$$

where υ is Poisson's ratio. In case of an in-plane stress, where the out-of-plane stress (for example σ_{NN}) is close to zero and may be neglected, equations equation 2.11 to 2.13 reduce to (ISO/TTA3 2001):

$$\sigma_{LL} = \frac{E}{(1-\upsilon^2)}(\varepsilon_{LL} + \upsilon\,\varepsilon_{TT}) \qquad \textbf{Equation 2.13}$$

$$\sigma_{TT} = \frac{E}{(1-\upsilon^2)}(\varepsilon_{TT} + \upsilon\,\varepsilon_{LL}) \qquad \textbf{Equation 2.14}$$

When the directions of the strain measurements coincide with the principal directions of deformation of the component, the calculated stresses are the principal RS .

The values for the Young's modulus and the Poison's ratio differ significantly for the different lattice plane families *{hkl}* in anisotropic materials such as steel or copper, whereas in isotropic or quasi isotropic materials like aluminium these values experience only slight changes for the different reflections. Clausen *et al*. (1998) calculated the various values of the Young's modulus with respect to different sets of lattice planes for different material, which are shown in Table 2.2.

	{111}	**{200}**	**{220}**	**{311}**	**{331}**	**{531}**
aluminium	73.3	67.8	71.8	70.2	72.3	71.2
Stainless steel	246.2	149.8	212.0	183.2	220.9	199.2
Copper	158.0	101.5	138.7	121.8	143.8	131.2

Table 2.2: Calculated Young's modulus for several sets of lattice planes in aluminium, stainless steel and copper (Clausen *et al.* 1998).

In case of aluminium and many aluminium alloys a quasi isotropic condition may be assumed and a global Young's modulus of ~71 GPa (an average of the crystal lattice specific Young's modulus) as well as a global Poisson's ratio of υ=~0.33 are well accepted values for the calculation of RS. As a result, these values were used for the calculation of RS in this dissertation. Further, the assumption that the *{311}* lattice plane spacing, as measured on the SALSA beam-line (see section 3.3.2), is representative for the overall average response of the material to an applied stress allows for the conversion from d_{311} into the unit cell parameter *a* using equation 2.7.

During the determination of residual strain and stress using diffraction, one may encounter significant difficulties. Those that may primarily arise in this dissertation are addressed in the following sections.

2.6.6 Problems Associated with Diffraction based RS Determination

Many problems affecting the results of diffraction experiments may occur and require special attention. These problems may be categorized into those relating to the sample positioning with respect to the gauge volume location and those that are related to material properties and sample dimensions. In this section the surface effect; a problem due to inaccurate sample positioning, the material related texture and grain size problem, as well as the attenuation problem, are addressed and possible solutions to minimize their erroneous effects are detailed.

A further very important issue using diffraction for the determination of RS in welds made from high strength aluminium alloys is the variation of the elastically unstrained unit cell parameter a_0, as a function of lateral distance across the weld-line and through weld thickness. This variation may occur as a result of changes in precipitation due to the thermal cycle experienced during FSW (see section 2.2 and 2.3.4). If not accounted for, this shift may significantly alter the calculated residual strains and stresses and therefore requires special attention. The variation of the unstrained unit cell parameter is discussed in detail in section 2.6.6.3. A comparative study of different methods to obtain the variation of the unstrained unit cell parameter and its effect on the magnitude of the RS was performed in this dissertation. The results are presented in section 4.2.

Finally, the size of the measured sample plays an important role as the RS relax upon material removal. With respect to the diffraction based determination of RS in engineering components it is interesting to know in how far the RS determined in the test welds mirror those that are present in real size components. The problematic nature of stress relaxation in a weld upon cutting to produce smaller and easier to handle samples is addressed in section 2.6.6.4. Within this dissertation a study on the effect of material removal on the stress relaxation was performed and the results are presented in section 4.3.

2.6.6.1 The Surface Effect

Surface effects arise when the gauge volume, as defined by the incident and diffracted beams S_0 and S_1 respectively, is only partly immersed in the sample, as depicted in Figure 2.35. This leads to systematic shifts of the diffraction peak (Webster *et al.* 1996), which subsequently may be interpreted as real shifts of the measured unit cell parameter. These shifts occur due to the so-called 'geometric effect' resulting from the angular difference between the diffraction angle θ implied by the beam set-up and the actual diffraction angle θ' due to a shift of the centre of gravity of the partially filled gauge volume. While the graph in Figure 2.35a depicts the surface effect for measurements in reflection mode graph b) shows the same effect for the transmission mode set-up.

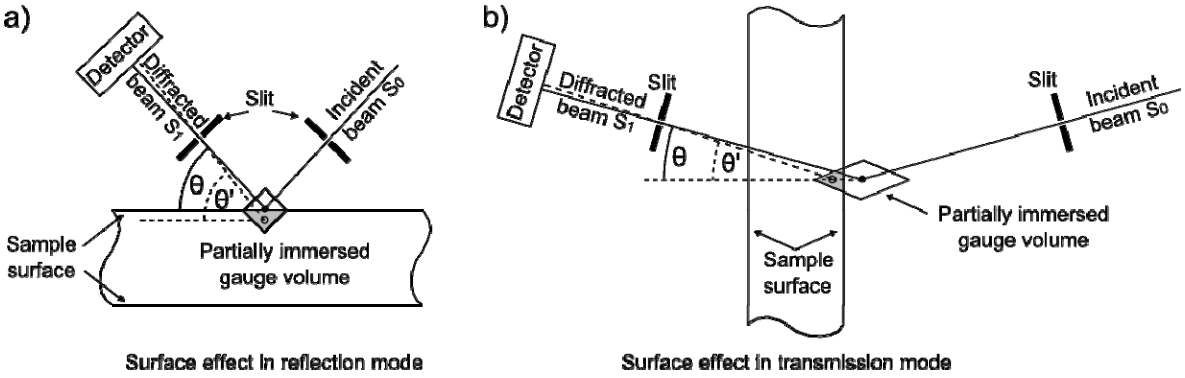

Figure 2.35: Schematic illustration of the geometric effect causing the so-called surface effect, a systematic shift in the measured d-spacing. The effect for measurement in reflection mode is shown in (a) while (b) illustrates the phenomenon for the transmission mode. In both cases the solid line represents the intended orientation of the diffracted beam, while the dotted line shows the actual orientation and the angular offset determined by the detector.

In order to avoid surface effects special care must be taken whilst positioning the sample with respect to the gauge volume location. So called 'wall-scans', where the sample is moved such that the gauge volume moves from being completely outside the sample to entirely penetrating the sample, whilst recording the intensity of the diffracted beam of the sample position in the requested direction can be used. From the sample position vs. intensity plot one can then determine the exact position of the sample surface, with respect to the gauge volume location, and as a result one can position the sample such that the gauge volume is always fully within the material and avoid the surface effect.

More advanced techniques for precise sample manipulation based on re-engineering methods using 3-dimensional models of the sample in question exist. James *et al.* (2004; 2007a) introduced a method based on the determination of the location of distinctive

fiducial points (for example spheres) mounted onto the sample surface to determine the arbitrary sample location in the instrument coordinate system, with respect to the gauge volume. A 3-dimensional virtual model of the sample is used to represent this location in the simulated instrument environment. Once the sample location is determined in the model, each sample movement can be planned and simulated and the required coordinates for the motorized sample stages can be calculated in order to allow for moving the sample. Depending on the accuracy of the sample positioning procedure, surface effects can be avoided and measurements close to the surface with a fully emerged gauge volume are possible.

2.6.6.2 Texture and Grain Size Effects

An important material related diffraction problem can be attributed to the texture (grain orientation) and the grain size distribution of the material sampled by the gauge volume (Hauk 1997).

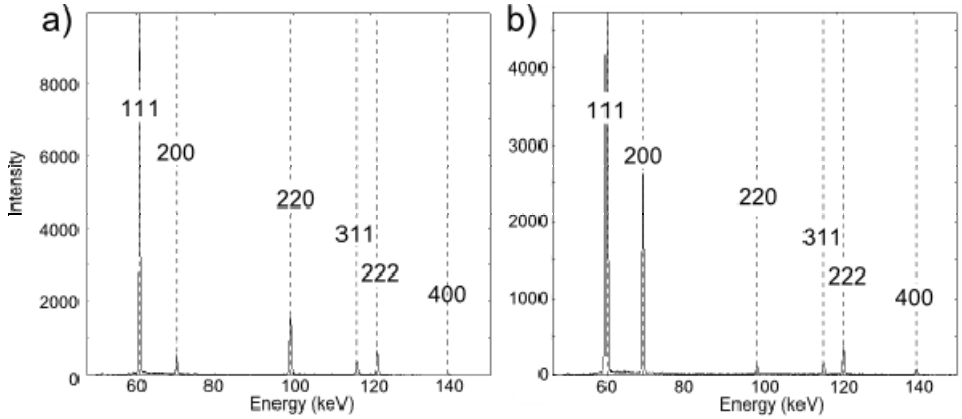

Figure 2.36: EDXRD diffraction patterns (0.1 × 0.1 × 2.3 mm gauge, 2Θ = 5° and 60 sec counting time) for two measurement points separated by 5 mm in an AA2199-T831 5 mm thick plate (original work from this dissertation). The {200} peak intensity is small in (a) it is significant in (b) and vice versa for the {220} peak. The {111} reflection occurs in both profiles, but varies significantly in intensity. This variation indicates textured material and/or grain size variations. Note the different scales on both graphs .

A material is texture free when it has a perfectly random orientation of polycrystalline grains. As a result the gauge volume always samples a similar number of grains that fulfil the Bragg condition, thus leading to well defined diffraction peaks, such as depicted in Figure 2.33, for a reference aluminium powder, which are of similar intensity at different measurement points. On the other hand, when a material has a strong or a significantly

varying texture, the number of grains contributing to the diffraction pattern varies significantly for different locations in such a material. This may result in peaks missing out or changing significantly in intensity, as depicted in Figure 2.36 for an AA2199 aluminium alloy plate in two points being 5 mm apart. This complicates the data fitting and may increase the measurement uncertainty and point to point scatter of the final data.

A similar effect may occur as a result of variations of the size of the grains irradiated in the gauge volume. In case the grains are significantly small a statistically meaningful number is sampled thus contributing to the diffraction profile. With increasing grain size the number of grains irradiated decreases, hence fewer grains can contribute to the diffraction profile. This may result in decreasing diffraction intensities as the probability of grains contributing to the diffraction pattern reduces. On the other hand, in case a few big grains are orientated such to contribute the peak intensity may be increased significantly. In order to mitigate these sources of error, several methods exist. One can oscillate the sample to increase the number of grains being sampled by the gauge volume. However, this should only be done in a direction normal to that of the measurement, as otherwise the spatial resolution of the measurement technique decreases. Another method is to increase the size of the gauge volume, as this also increases the amount of grains contributing to the diffraction profile. Again this may reduce the spatial resolution depending on the direction of measurement. In case of the EDXRD set-up, as described in section 2.6.4, a slight increase of the cross-section dimensions of the primary and secondary beam leads to a significant elongation of the gauge volume especially for low diffraction angles, thus increasing the danger of surface effect problems (see section 2.6.6.1). Finally, by increasing the counting time per measurement point one can also improve the quality of the diffraction patterns. Even though only few neutrons or photons may be diffracted by the sampled material per time interval in a small gauge volume, over a long time this may still produce a meaningful diffraction profile. However, this is a time and therefore cost intensive method and should be avoided if possible.

2.6.6.3 The Unstrained Lattice Parameter

A critical aspect of the residual strain, hence stress, determination using diffraction techniques as described in section 2.6.3and 2.6.4 is the precise knowledge of the unstrained unit cell parameter a_0 (Steuwer *et al.* 2007). The precise strain determination in most

engineering components requires a and a_0 to be known to a greater accuracy than 10^{-4}Å (Hauk 1997). The situation is even more complicated when a sample displays a spatial variation of a_0 as a result of a thermal exposure for example as during welding. In high strength aluminium alloys the variation of a_0 is due to a varying solute content as illustrated in Figure 2.37 (Barret *et al.* 1980; Hutchings *et al.* 1992) which is a function of the thermal history dependent local precipitation behaviour (section 2.2 and 2.3.4.4).

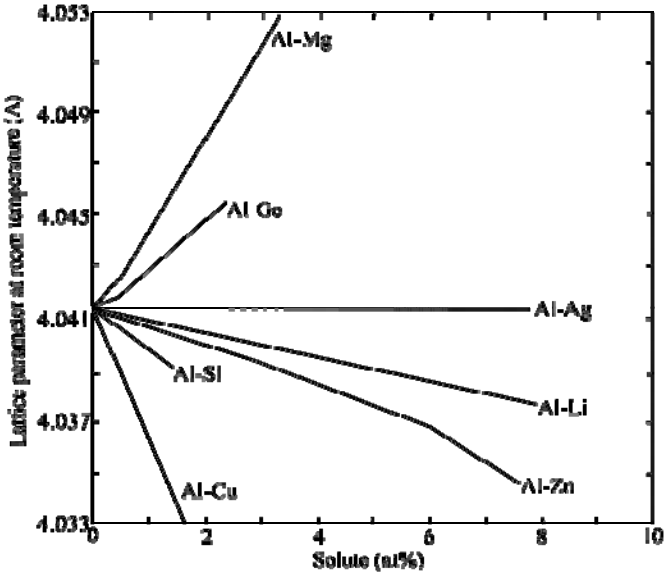

Figure 2.37: Variation of the unstrained lattice spacing in aluminium based solid solutions as a function alloying elements (after Barret *et al.* 1980; Hutchings *et al.* 1992).

If these changes are not taken into account significant errors may be introduced in the determination of the subsequent residual strain and stress (Steuwer *et al.* 2007; Withers *et al.* 2007). Several methods exist to determine the shift of a_0 as a function of position throughout the sample (Santisteban *et al.* 2002; Withers *et al.* 2007). Those of interest for this dissertation are the plane stress assumption, the $\sin^2\psi$, and the relaxed comb methods and are summarized in the following.

Plane Stress Assumption Method: This method assumes that the RS in the plate normal (σ_N, out-of-plane) direction is zero (i.e. a plane stress condition) and so the normal strain is due solely to the Poisson contractions arising from the RS in the other two in-plane directions. In this situation it is possible to calculate a_0 based on the redundant information

obtained by measuring the strain in all three principal stress directions, assuming that they coincide with the main sample directions (Allen *et al.* 1985):

$$a_0 = \left(\frac{1-\nu}{1+\nu}\right)a_N + \left(\frac{\nu}{1+\nu}\right)(a_L + a_T) \qquad \textbf{Equation 2.15}$$

where a_L, a_T and a_N are the measured unit cell parameters in three orthogonal directions. This technique has previously been used to determine the RS in thin sheet welded aluminium alloys (Staron *et al.* 2004). Although this method can be readily applied to welds in thin sheets, it is not clear at what thickness this assumption is no longer valid.

The $sin^2\psi$ Method: This method is well-established for the measurement of RS using laboratory X-rays (Cullity 1978; Hauk 1997), but can also be applied to determine the unstrained unit cell parameter a_0 (Santisteban *et al.* 2002). In the conventional technique a series of lattice parameter measurements is made with the scattering vector oriented at several increments of the angle-ψ between the in-plane direction and the normal direction as depicted in Figure 2.38. The RS is determined from the slope of the resulting unit cell parameter a vs. $sin^2\psi$ plot and does not require the knowledge of a_0 - so long as the stress field is biaxial (Peel *et al.* 2003).

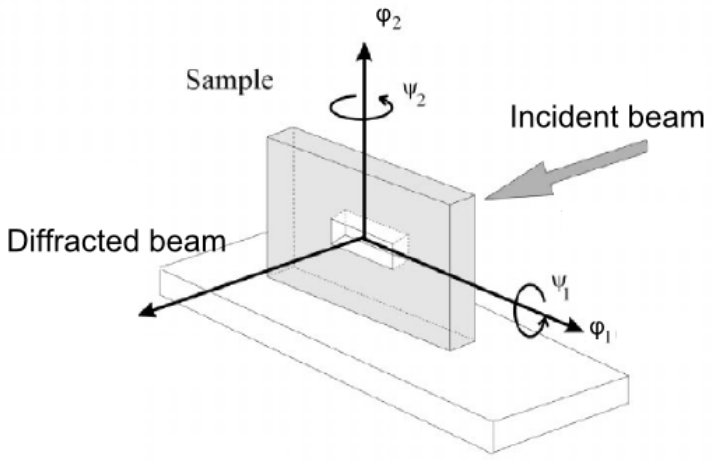

Figure 2.38: Schematic illustration of the rotation axes for inclination of the test specimen for the $sin^2\psi$ method.

Performing this technique on a small sample removed from the original weld to produce a biaxial stress state allows for determination of a_0. Naturally, the measured RS are

not representative of those in the complete weld, but it is possible to use this data to derive a_0, by performing inclinations in two orthogonal directions (Santisteban *et al.* 2002; Steuwer *et al.* 2007; Withers *et al.* 2007) as depicted in Figure 2.38. The sample is inclined to different angles ψ around the two in-plane axes φ_1 and φ_2. A linear regression of a vs. $sin^2\psi$ is performed for the data set of each axes and the linear functions gradient m_i and intercept a_{ni} used to calculate a_0 using (Santisteban *et al.* 2002):

$$a_0 = (a_{n\varphi=0^\circ} + a_{n\varphi=90^\circ})/2 + \left(\frac{\nu}{1+\nu}\right)(m_{\varphi=0^\circ} + m_{\varphi=90^\circ}) \qquad \textbf{Equation 2.16}$$

The quality of the linear fit acts as a measure of the validity of the measurement since shear stresses, grain size or texture result in deviations from the expected linear behaviour (Cullity 1978).

Stress Relaxed Comb Method: This method, to determine the spatial variation of a_0, involves cutting a 'comb' shaped specimen. The small dimensions of the test piece itself and the teeth cut into it allow for relaxation of the macroscopic RS to the greatest extent possible. Measurement in the stress relaxed directions within each tooth gives an average value that represents the local unstrained unit cell parameter a_0 (Hughes *et al.* 2003). If all RS were to relax due to the cutting, the values for the two measured directions should be equal, or at least very similar.

Using the $\sin^2\psi$ as well as the comb methods for determination of the unstrained unit cell parameter a_0 forcedly leads to the question of stress relaxation upon material removal. While the comb method intends to remove all macroscopic RS in order to measure a_0, it is vital to know what size test welds should be in order to retain the original RS representing those present in real size engineering components. This is discussed in the following section.

2.6.6.4 The Effect of the Sample Size on Relaxation of Residual Stress

In many cases welded structures, within which the RS are of interest for engineers and scientists, are too large or cumbersome to be investigated in their entirety using diffraction techniques. Even though recent instrument developments allow for large scale test samples

(for example the SALSA instrument, see section 3.3.2), often smaller cross-weld test-pieces are cut out to determine the RS. According to its size the RS will be partially relaxed in the removed test-piece (Masubuchi 1980), hence the RS determined will be less than those in the original component. As a result, the effect of RS on the component life cycle performance may be seriously underestimated. Alternatively, failure to take account of the retained RS when undertaking cross-weld performance testing may result in a misleading impression of the weld properties.

The typical RS distribution in butt welds is illustrated in Figure 2.14. Removing material from such a weld leads to partial relaxation of the RS requiring a redistribution of stress to maintain self-equilibrium. The amount of relaxation and redistribution in a single point will depend on its distance from the cutting region. It will tend to zero at large separations, as described qualitatively in St. Venant's Principle for a static load on the free end of a beam (Timoshenko *et al.* 1987). The RS in a given location are unaffected by changes in loading (for example by cutting a plate) if such changes occur sufficiently far away from the area of interest. St. Venant referred to the extent upon which notable relaxation of the load occurs as the '*characteristic distance*' (Timoshenko *et al.* 1987). However, it remains unclear what determines this characteristic distance and even more what this distance could be in case of butt welded structures. As a result, it is important to consider the sample size for the determination of RS. In order to determine RS comparable to those present in real size engineering components, the test welds have to remain a certain size. In practise using diffraction techniques several authors reported RS in friction stir welds that are substantially lower than the yield point of the material (Donne *et al.* 2001; Webster *et al.* 2001b; Sutton *et al.* 2002). However, in these cases the samples were cut from larger plates to facilitate handling or for mechanical testing, but the extent of relaxation of the RS was not quantified.

To date no systematic work has been carried out on the effect of the relaxation of RS upon sectioning butt welded structures, either looking at the relaxation of the longitudinal or transverse RS upon weld shortening, or reducing the width of the welded plate, respectively. Therefore, it appears vital to investigate the effect of material removal from welded structures in terms of RS relaxation. In this dissertation this has been done in order to determine a minimum test weld size that contains RS still representative of those present in real size component. The results of this study are presented in section 4.3.

2.6.7 Conclusions

From this section the following conclusions may be drawn:

- RS can be determined by measuring the specific lattice spacing d_{hkl} using for example angular dispersive neutron diffraction (ADND) or the unit cell parameter a using for example energy dispersive synchrotron X-ray diffraction (EDXRD).
- The specific lattice spacing d_{hkl} can be converted into unit cell parameter a using appropriate equations.
- By correlating a to the unstrained condition a_0 one can derive the residual strain hence stress. When significant variations of a_0 are likely it is vital to determine this parameter, as it has significant influence on the strain and stress results.
- ADND and EDXRD may encounter detrimental problems, such as the surface effect or texture and grain size effects, which may be reduced by sample oscillation or increasing the size of the gauge volume.
- In friction stir welds of high strength aluminium alloys a significant variation of the unstrained unit cell parameter a_0 due to changes in solute in solution may occur and require special attention as the RS may be significantly over- or underestimated if the applied a_0 is false.
- Even though diffraction techniques themselves are non-destructive, in certain situations it is necessary to damage the test sample in its entirety.
- Due to RS relaxation it is vital to account for the test weld size, as in samples that are too small, the remaining RS are not representative of those present in the original size weld.

2.7 SUMMARY

In this chapter the background information required to follow through this dissertation is discussed. The general precipitation behaviour of high strength aluminium alloys was reviewed. It can be stated that these alloys are very sensitive to thermal exposure resulting in significant variations in the structure and distribution of the strengthening particles hence mechanical properties. This may occur as a result of the thermal cycle experienced during welding, for example friction stir welding (FSW).

FSW is a maturing welding technique for materials otherwise considered as non-fusion weldable, such as high strength aluminium alloys. The thermal cycle in combination with the stirring action during FSW produces a characteristic microstructure consisting of the weld nugget (WN), a thermo mechanically affected zone (TMAZ) and the heat affected zone (HAZ). The microstructural distribution in combination with the precipitation variation, which is due to the weld thermal cycle, results in significant variations of the mechanical properties across the weld-line.

In common with other welding techniques FSW introduces thermal residual stresses (RS) and component distortion. RS are stresses that remain within a component even when all external loads are removed. The longitudinal stress distribution in FSW in high strength aluminium alloys follows an M-shaped distribution. Peak tensile stresses of up to 60 % of the base material room temperature yield strength σ_{YS} occur in the HAZ. The transverse RS are usually low. Bending distortion may arise with concave and convex orientation, while the angular distortion is usually concave. Buckling distortion usually occurs, if at all, in thin plates joined by FSW. Distortion can be assumed to be partly related to RS present in the component.

RS can be reduced to some extent by optimizing the welding parameters. Additionally applied stress engineering techniques based on thermal or mechanical treatment during or after welding can further minimize tensile stresses or even introduce compressive RS to the weld-line. While thermal techniques are complex and rather difficult to adjust, mechanical stress engineering techniques such as global mechanical tensioning or roller tensioning are relatively simple to apply. The current literature suggests that in-situ global mechanical tensioning (ISGMT) with the load being applied to each end of the plates along the welding direction before welding and released once the weld has cooled down, can mitigate tensile RS if the load is 20 – 40 % of the parent material yield strength σ_{YS}. The mechanisms acting decrease the compressive yielding in front of the approaching and increase the tensile yielding behind the FSW tool resulting in less volumetric misfit between parent and weld-line material in the cold weld and as such RS. However, the given tensioning rate is an approximation and to date no systematic investigation has been performed. On the other hand, roller tensioning, applied either in-situ (ISRT) or post welding (PWRT) is a new technique with respect to mitigation of welding RS. While the mechanism for ISRT is similar to that of ISGMT, the PWRT simply elongates the cold tensile weld-line material by compressing the material in the plate normal direction. A first approach understanding

these techniques was performed using FEM, showing that especially the PWRT technique is very effective for stress mitigation. However, no experimental study has been performed to date.

Experimental investigation of the effectiveness of stress engineering can be performed by non-destructive determination of the RS as a function of the applied technique using neutron and synchrotron X-ray diffraction. The crystal structure of the irradiated material is used as an internal strain gauge: the radiation is diffracted on the crystal lattice planes according to BRAGG's law and the diffraction angle changes as a function of the lattice plane spacing which is altered according to the stress acting on the crystal. Comparison to the unstrained condition allows determination of the residual strain and hence stress. One critical point when using diffraction techniques for stress determination in welds made in high strength aluminium alloys is the variation of the unstrained unit cell parameter, which is altered by the amount and distribution of precipitates. This parameter requires special attention and must be determined properly for determination of the real stresses present in the component. Further, the size of the investigated sample may affect the magnitude of the RS remaining in it. If the sample is cut to a small size, the RS may relax resulting in significant underestimation of the stresses present in real size components.

The review of the current state of the art of stress engineering techniques has identified the following tasks for this dissertation:

- Determination of the precise relation between the ISGMT load and the resulting mitigation of the longitudinal tensile RS and component distortion in high strength aluminium alloy friction stir welds by systematic experimental investigations using diffraction techniques.
- Investigation of possible effects of ISGMT on the mechanical properties of these welds (for example hardness).
- Determination of the effectiveness of the ISRT and PWRT techniques for mitigation of the longitudinal tensile RS and distortion in high strength aluminium alloy friction stir welds in a systematic experimental study using diffraction techniques.

- Comparative investigation of different methods for obtaining the elastically unstrained unit cell parameter a_0 in order to define the method best suited for the above mentioned studies.
- Investigation into the effect of the test weld size on the magnitude of RS in order to ensure a minimum test weld size that contains RS representative of those present in real size components. This is especially important as the results from this study allow evaluating the representative character in terms of RS of the test welds investigated in this dissertation.

In the following chapters the experimental techniques to perform and the results obtained from the above mentioned studies are presented.

3 EXPERIMENTAL TECHNIQUES AND METHODS

3.1 INTRODUCTION

In this dissertation the residual stress (RS) distribution in high strength aluminium alloy plates joined by friction stir welding (FSW) were investigated, in order to increase the understanding of mechanical stress engineering techniques, applied either during or after welding. The stress engineering techniques of interest for this dissertation were the in-situ global mechanical tensioning (ISGMT) as well as the in-situ roller tensioning (ISRT) and post weld roller tensioning (PWRT) and are described in detail in section 2.5.

In this chapter an overview of the high strength aluminium alloy test welds produced under varying FSW and stress engineering conditions is given. Further, the experimental techniques used to investigate these test welds are detailed. In outline, the first section of this chapter provides an overview of the test welds produced for this dissertation, addressing the material conditions, the sample dimensions, the FSW conditions and tool details as well as the applied stress engineering technique and its parameters. Also the machinery used to apply the respective stress engineering technique is detailed.

In the second section of this chapter the general diffraction instrument set-up used for stress determination, as well as the exact experimental conditions, are described in detail. In addition, in the third section a new robotic sample manipulation system, as developed and tested throughout this dissertation, is introduced. This was applied for complex sample manipulation with respect to the diffraction experiments.

Finite element modelling (FEM) predictions, partly based on work by D. Richards from the University of Manchester and partly as original work, was performed in this dissertation. The model design and details are described in the fourth section of this chapter.

In the final sections of this chapter the technique to determine the weld distortion as a function of the applied stress engineering technique is introduced. As stress engineering techniques can be applied during welding, they may affect the microstructure or post weld mechanical properties, such as hardness. Therefore, these properties were investigated using the appropriate methods, which are detailed in the end of this chapter.

3.2 SAMPLE PREPARATION

For the investigation of the RS mitigation effects of ISGMT, ISRT and PWRT, seven sets of test friction stir welds, in different high strength aluminium alloys, namely AA7449, AA2199, AA2024 and AA7136 were produced. For ISGMT 14 welds in four sets and for the ISRT and PWRT 13 welds in three sets were produced. The FSW of all test welds were produced by Airbus UK in Filton Bristol, UK, on a *Crawford Swift Powerstir 360*® machine with a 4×2 m translation table. The maximum spindle down force was 100 kN and the spindle was directly driven by a 6kW motor.

3.2.1 In-situ Global Mechanical Tensioning

The investigation of the effect of ISGMT on the RS distribution and the related component distortion was performed on the basis of four sets of test welds. The materials studied are the emerging high-strength, low-density aluminium-lithium alloy AA2199-T8E74 and the high-strength aluminium alloy AA7449-W51, two materials of special interest for the aerospace industry (Khelifati *et al.* 2006).

Material	Cu	Mg	Mn	Fe	Si	Ti	Li	Zn	Cr	Zr	Al
AA2199-T8E74	2.63	0.17	0.31	0.04	0.20	0.02	1.56	0.62	-	-	balance
AA7449-W51	1.8-2.4	1.8–2.7	0.20	-	-	0.25	-	7.5–8.7	-	0.25	balance

Table 3.1: Chemical composition of AA2199-T8E74 and AA7449-W51 in weight percent (ASM_2 2001; Khelifati *et al.* 2006).

The AA2199-T8E74 alloy has a nominal composition as shown in Table 3.1. The comparatively increased weight percentage of lithium reduces the material density to ~2.64 g/cm^3 (at 20 °C) compared to ~2.82 g/cm^3 (at 20 °C) for AA7049 or 2.77 g/cm^3 for AA2024 (at 20 °C) alloys being equal to a ~5 % weight reduction. Zn is added to improve the corrosion resistance, compared to previous generation of aluminium-lithium alloys such as AA2091 (Khelifati *et al.* 2006). The 5 mm thick AA2199 plates were supplied in the T8E74 temper, i.e. solution heat-treated, cold worked and artificially aged resulting in yield strength σ_{ys} = ~400 MPa (Khelifati *et al.* 2006). This alloy is intended to be used for fuselage applications (stretch formed panels around the nose of the Airbus A380) as it allows a reduction in the overall weight of aircraft structures (Khelifati *et al.* 2006).

The AA7449-W51 material had a nominal composition as shown in Table 3.1. The plates were supplied in 5 mm, 12.2 mm and 20 mm thickness in a W51 temper, i.e. solution heat-treated and stress relieved by stretching the material to 0.5-3 %. No elevated-temperature ageing treatment was applied. In this condition, the material has a yield strength σ_{YS} = ~583 MPa (Poad 2006). Due to its comparatively high strength this aluminium alloy is used for the application in structural aircraft components, such as wing ribs or lower wing skin (Williams *et al.* 2003).

Material		FSW conditions					Applied GMT		Label (set, material, load)
Set Alloy	σ_{ys} /UTS (MPa)	Plate size (mm)	v_{rot} (rpm)	v_t (mm/min)	F (kN)	Tool	% σ_{ys} of parent	in MPa	
Set #1 AA2199-T8E74 (bead on plate)	400/452 (Khelifati *et al.* 2006)	1000 ×400 ×5	800	400	1.5	MX-Trivex™, shoulder Ø 13 mm, threaded pin Ø 5 mm and 4.35 mm long, Ni/Co alloy MP159	0	0	1A0
							17	68	1A68
							34	136	1A136
							52	208	1A208
Set #2 AA7449-W51 (bead on plate)	583/636 (Poad 2006)	515 ×150 ×5	800	400	1.5	MX-Trivex™ , shoulder Ø 13 mm, threaded pin Ø 5 mm and 4.35 mm long, Ni/Co alloy MP159	0	0	2B0
							17	99	2B99
							30	175	2B175
Set #3 AA7449-W51 (real weld)	583/636 (Poad 2006)	1000 ×400 ×12.2	225	250	80	MX-Triflat™, shoulder Ø 30 mm, threaded pin Ø 17 mm and 11.7 mm long, Ni/Co alloy MP159	5	29	3B29
							10	58	3B58
							20	117	3B117
							30	175	3B175
Set #4 AA7449-W51 (real weld)	583/636 (Poad 2006)	450 ×200 ×20	150	140	84	MX-Trivex™, shoulder Ø 34 mm, threaded pin Ø 17 mm and 20 mm , Ni/Co Alloy MP159l	0	0	4B0
							17	99	4B99
							34	198	4B198

Table 3.2: Material details and plate dimensions ($l \times w \times t_m$), FSW parameters and tool details as well as applied ISGMT loads expressed as percentage of σ_{ys} and in MPa. The welds are labelled according to the set number, material (A – AA2199, B – AA7449) and ISGMT load in MPa.

Two different materials were used for this research in order to allow for comparison of the effect of ISGMT in different alloys joined otherwise under identical FSW conditions. On the other hand, using one material with different plate dimensions and varying FSW conditions one can extract general conclusions about the ISGMT technique. A detailed overview of the weld dimensions, the FSW conditions and the ISGMT loads is given in Table 3.2. General illustrations of the FSW tools are depicted in Figure 3.1a and Figure 3.1b; however, note these are not the tools actually used. Each weld is labelled with a set number (#1-#4), the material used (A – AA2199, B – AA7449) and the ISGMT load

applied (in MPa). While the welds in set #1 and #2 are bead on plate welds, those in set #3 and #4 are real welds.

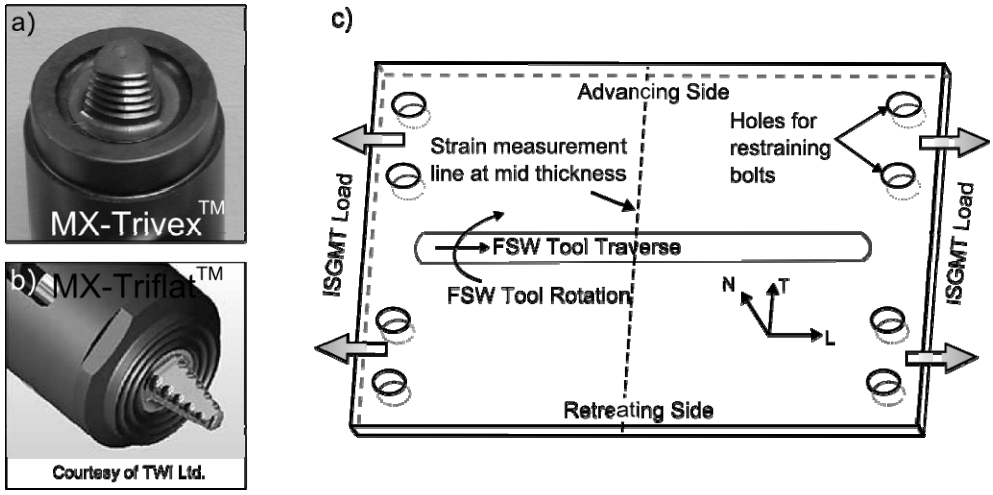

Figure 3.1: (a) General illustration of the MX-Trivex™ FSW tool as used for set #1, #2 and #4 (Colegrove *et al.* 2003) and (b) the MX-Triflat™ FSW tool used for set #3 (Perrett *et al.* 2007). In (c) a schematic showing the strain measurement line and the holes for the tensioning device as well as the principle plate directions (L-longitudinal, T-transverse and N-normal) are depicted.

Within each set of tensioned test welds an as-welded sample (except for set #3) was produced to allow for comparison with the stress engineered welds. Different tensioning loads expressed as a fraction of the room temperature parent metal yield strength σ_{ys} or directly in MPa (see Table 3.2) parallel to the welding direction were applied during FSW as schematically illustrated in Figure 3.1c, while keeping all other welding parameters constant for each individual set of welds. The ISGMT load was applied using a device consisting of hydraulic rams with serrated and hardened jaws attached to each end of the plate, as illustrated in Figure 2.22. Slipping was further restricted by bolts in each grip passing through pre-machined holes in the plates. After tensioning the plates to the appropriate level they were friction stir welded. After cooling to room temperature, the loading was removed.

3.2.2 In-situ and Post Weld Roller Tensioning

The ISRT and PWRT stress engineering techniques for application to friction stir welds in high strength aluminium alloys plates were introduced only recently (Williams *et al.* 2008; Wen *et al.* 2009). Therefore the time available to conduct extensive research within

this dissertation was limited and as such this research aims to show the effectiveness of both techniques for mitigation of the RS rather than exploring the mechanisms acting. Three sets of test welds were investigated: two sets in 5 mm thick AA2024-T3 and AA2199-T8E74 plates with differing ISRT and PWRT loads respectively using flat rollers. A third set of samples with PWRT applied using a flat as well as a corrugated (a gear-wheel shaped, see Figure 3.3d) roller was produced as a near application test series in so called integrated stiffener panels (ISP). Such panels are a recent approach for stiffener integrated wing skin production for Bombardier aircraft. The cross-section of two ISP plates joined by FSW is schematically depicted in Figure 3.2.

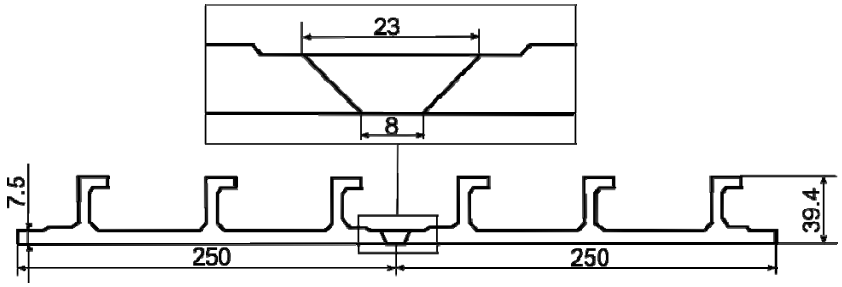

Figure 3.2: Cross-section of the ISP plates as used in this dissertation.

While the composition for the AA2199-T8E74 material, as used in test welds in set #6 is shown in Table 3.1, Table 3.3 displays the details for AA2024-T3 and AA7136-T6, two additional materials, which were used for set #5 and #7 respectively. The AA2024-T3 material was naturally aged resulting in a yield strength σ_{YS} = ~345 MPa (ASM_2 2001) and is mainly used in applications requiring high strength to weight ratios, as well as good fatigue resistance. On the other hand, the AA7136-T6 material is artificially aged at elevated temperature resulting in a yield strength σ_{YS} =~628 MPa (Poad 2006). This alloy is used for similar structural purposes as the AA7449-W51 alloy.

Material	Cu	Mg	Mn	Fe	Si	Ti	Zn	Cr	Zr	Al
AA2024-T3	3.8-4.9	1.2-1.8	0.3-0.9	0.5	0.5	0.15	-	0.1	0.18	balance
AA7136-T6	2.15	1.93	-	0.07	0.03	-	8.54	-	0.13	balance

Table 3.3: Chemical composition of AA2024-T3 and AA7136-T6 in weight percent (ASM_2 2001; Maniruzzaman *et al.* 2007).

Three different alloys were used for this investigation for several reasons: firstly, the AA2024-T3 was not available for the production of the PWRT samples at the time.

Secondly, while AA2199-T8E74 is to be used for fuselage applications, the intended structural application of the ISP plates as wing panels in aircrafts requires a high strength aluminium alloy, such as the AA7136-T6. However, the stress mitigation effects of each roller tensioning technique are of significant interest regardless of the alloy investigated. Indeed, this variation of materials serves to highlight the applicability of the technique across the alloy spectrum.

Material		**FSW**					**Applied rolling strategies & roller profile / down force (kN)**		**Label (set, material, load**
Set Alloy	YS/UTS (MPa)	Plate size (mm)	v_{rot} (rpm)	v_t (mm/ min)	F (kN)	Tool			
Set #5 AA2024 - T3	345/483 (ASM_2 2001)	500× 350 × 5	800	200	1.3	MX-Trivex™, shoulder Ø 13 mm, threaded pin Ø 5 mm and 4.35 mm long, Ni/Co alloy MP159	ISRT (flat)	0	5C0
								50	5C50
								75	5C75
Set #6 AA2199-T8E74	400/452 (Khelifati *et al.* 2006)	500× 200 × 5	800	400	1.3	MX-Trivex™, shoulder Ø 13 mm, threaded pin Ø 5 mm and 4.35 mm long, Ni/Co alloy MP159	PWRT (flat)	0	6A0
								10	6A10
								20	6A20
								30	6A30
								40	6A40
Set #7 AA7136-T6	628/668 (Poad 2006)	1000 × 500× 8	400	400	55	MX-Trivex™, shoulder Ø 23 mm, threaded pin Ø 10 mm and 7.5 mm long, Ni/Co alloy MP159	PWRT (flat / corrugated)	0	7D0
								25	7D25
								40	7D40
								50	7D50*

Table 3.4: Material details and plate dimensions ($l \times w \times t_m$), FSW conditions as well as applied roller tensioning methods and down force in kN. The welds are labelled according to: set number, material (A – AA2199, C – AA2024, D - AA7136) and roller tensioning down force in kN. The roller dimensions are given in Figure 3.3. Test weld #7D50* was rolled with a corrugated roller.

The ISRT double roll, as illustrated in Figure 3.3a was designed such that the roller load was applied on both sides of the weld-line trailing the FSW tool at ~40 mm distance as depicted in Figure 3.4a. Indeed, the gap between the rollers allowed the FSW tool shaft to pass through permitting the rollers to be placed close to the hot zone. In this way the material local to the weld can be plastically deformed by the rollers while it is still hot and soft. The flat faced double roller has a diameter of 100 mm, an effective width of 2 × 29 mm with a gap of 20 mm between. PWRT on set #6 (AA2199-T8E74) was applied using a single roll (see Figure 3.3b) with a diameter of 100 mm and an effective width of 20 mm. It should be noted that the PWRT was applied to the weld ~30 min after welding had finished and directly along the weld-line in the welding direction as shown in Figure 3.4b.

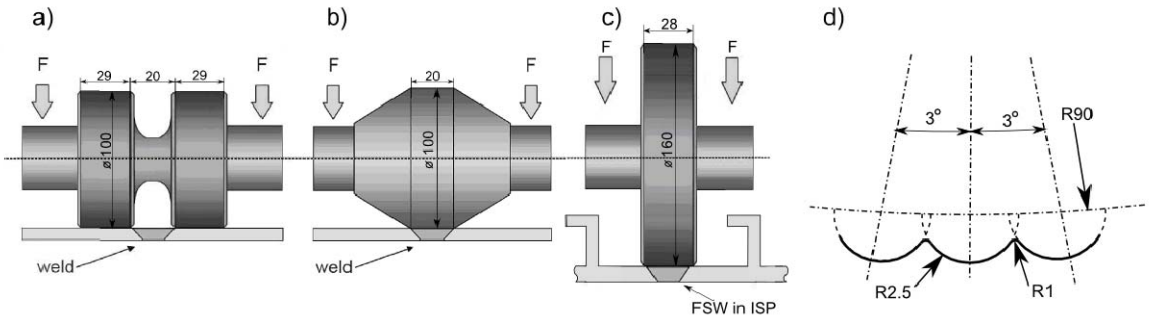

Figure 3.3: Schematic showing (a) the double and (b) the single roller and geometric dimensions for ISRT and PWRT respectively. In (c) the flat roller design for PWRT of the ISP material and in (d) the geometry of the corrugated roller are depicted. Note the greater diameter of the rollers for the ISP plates.

PWRT the friction stir welded ISP material was done with a flat faced single roller as depicted in Figure 3.3c with 160 mm diameter and 28 mm effective width. The greater diameter was necessary as the stiffeners protruded out of the panels on the weld surface where the PWRT is applied.

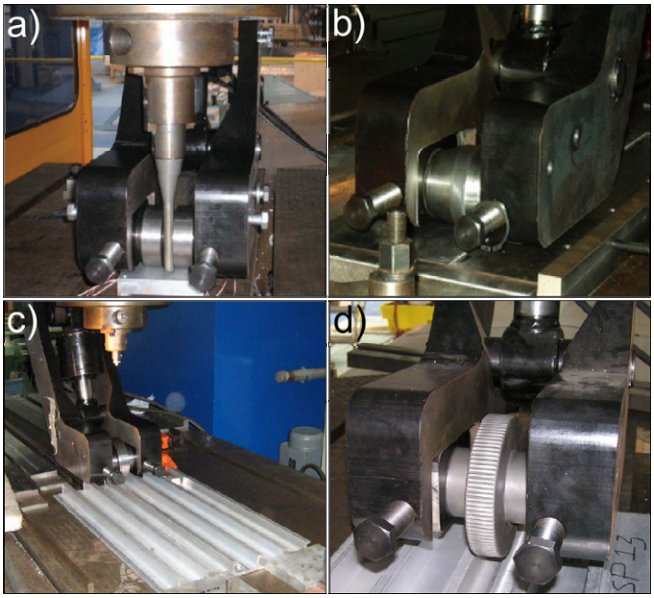

Figure 3.4: Illustration of the varying roller tensioning set-ups with (a) the double roller following the FSW tool closely as to roller deform the hot material (ISRT), (b) the single roll for PWRT flat sheet, (c) the single roll for PWRT ISP material and (d) the corrugated roller for PWRT the ISP material.

In addition to PWRT with a flat roller surface, one ISP test weld (#7D50) was produced to explore the effect of a different roller profile. A corrugated roller surface profile as depicted in Figure 3.3d and Figure 3.4d with a nominal diameter of 180 mm and 28 mm width. The 'teeth' reached out an additional 2.5 mm and being 2.5 mm in radius and 3 °

apart resulted in a lateral distance of 5 mm from tooth to tooth. The application of a corrugated roller was expected to increase the local pressure in the plate normal direction as the contact area is reduced. This should increase the RS mitigation effect of the PWRT. Again, PWRT was applied ~30 min after FSW had finished. All material, welding and rolling parameters for the investigated test welds are summarised in Table 3.4.

3.3 RESIDUAL STRESS DETERMINATION

3.3.1 Introduction

The distribution of RS in the test welds was determined as a function of the applied stress engineering technique using non-destructive angular dispersive neutron diffraction (ADND) at the SALSA (Strain Analyser for Large Scale Applications) beam-line at the Institut Laue-Langevin (ILL) and energy dispersive synchrotron X-ray diffraction (EDXRD) at the high energy beam-line ID15A at the European Synchrotron Radiation Facility (ESRF).

Set #	Long.	Trans.	Norm.	A_0
1	SALSA	SALSA	SALSA	Plane Stress
2	ID15A	ID15A		Comb
3	ID15A	ID15A		Comb, $Sin^2\psi$, Plane Stress
4	ID15A	ID15A	SALSA	Comb
5	ID15A	ID15A		Comb
6	ID15A	ID15A	SALSA	Comb, Plane Stress
7	ID15A	ID15A		Comb

Table 3.5: Overview of the different instruments used to determine the unit cell parameter *a* and the unstrained unit cell parameter a_0. Note, the values as measured on SALSA are crystallographic plane specific lattice spacings d_{hkl} which can be converted to *a*-values using equation 2.7.

In the following two sections the two instruments are described. While the general instrument set-ups for these specific diffraction techniques are detailed in the first part of each section, experimental details for the determination of RS in this dissertation are described in the second part of each section.

An overview of the instruments used for determination of the unit cell parameter, a, as well as the technique to measure the variation of the unstrained unit cell parameter, a_0, in each set of test welds is given in Table 3.5. Note, using ADND on SALSA allows to measure a specific lattice spacing d_{hkl} only. However, as discussed in section 2.6 one can convert the results into unit cell parameter values using equation 2.7 and consequently

combine the data with those obtained using EDXRD. Unless stated otherwise the RS distribution in each test weld was determined at mid material thickness as a function of lateral distance from the weld-line along a line parallel to the transverse direction at mid length of the weld path as shown in Figure 1.1. In thicker material, where a variation of the RS as a function of distance from the weld surface is likely, additional line scans were performed at different depths.

3.3.2 The SALSA beam-line

Angular dispersive neutron diffraction (ADND) measurements were carried out on the dedicated SALSA beam-line, an angular-dispersive diffractometer at the neutron reactor source at the ILL (Pirling *et al.* 2006). This beam-line is mainly used for strain measurements in metallic materials and allows performing such measurements under a wide range of conditions (cyclic loading and/or heating). For this dissertation the SALSA beam-line was used to map the residual strain, and hence RS distribution in the test welds as, a function of position and of the applied stress engineering technique.

3.3.2.1 General beam-line set-up

A plan-view schematic of the SALSA beam-line is shown in Figure 3.5a. Using a double-focusing bent Si-crystal monochromator mounted on the so-called carousel a single wavelength is selected from the white neutron beam by rotating the monochromator to the required BRAGG angle. Depending upon this angle the wavelength may range from 1.23Å to 3Å. With the change of the wavelength also the take-off angle is modified and requires rotation of the down stream instrument set-up by rotating the so-called delta table around the monochromator centre thus allowing re-alignment with the incident monochromatic beam as illustrated in Figure 3.5a.

The nominal gauge volume shape is defined by the primary and secondary slits made from BN (boron nitride) and Cd (cadmium) masks for the horizontal and vertical definition respectively. In addition rubber curtains containing B_4C (boron carbide) are placed along the incident and diffracted beam to reduce background noise.

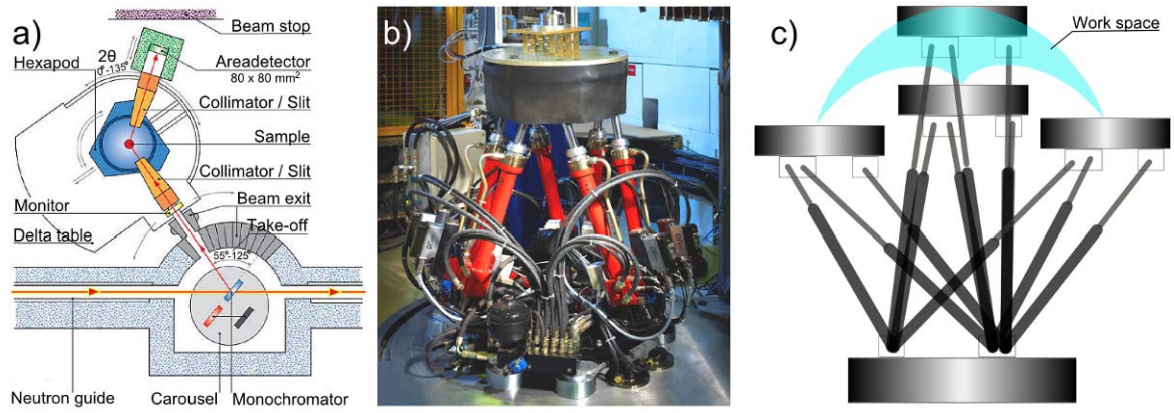

Figure 3.5: Illustration of (a) the SALSA beam-line set-up, (b) the Stewart-plate form as used on the SALSA for sample manipulation and (c) the umbrella shaped work space of the Stewart-plate form.

The SALSA beam-line had a computer controlled Stewart-platform driven by six hydraulic cylinders for translational and rotational sample manipulation as depicted in Figure 3.5b. This device offered an umbrella shaped work space (Figure 3.5c) with maximum translational movements of ±300 mm (horizontal) and 150 mm in the vertical direction (Pirling *et al.* 2006). Further, the hexapod can tilt to ±30 ° and vertically rotate the sample ±45 ° with respect to the hexapod base. The aluminium sample mounting plate of the hexapod has a 25×25 mm M10 hole grid, thus allowing using the VAMAS mounting set, which is a standardised system for fixation of test specimens (ISO/VAMAS/TWA20 2001). A few gold coloured VAMAS sample holders, fixing test welds in different orientations on the SALSA , are shown in Figure 3.7a-c.

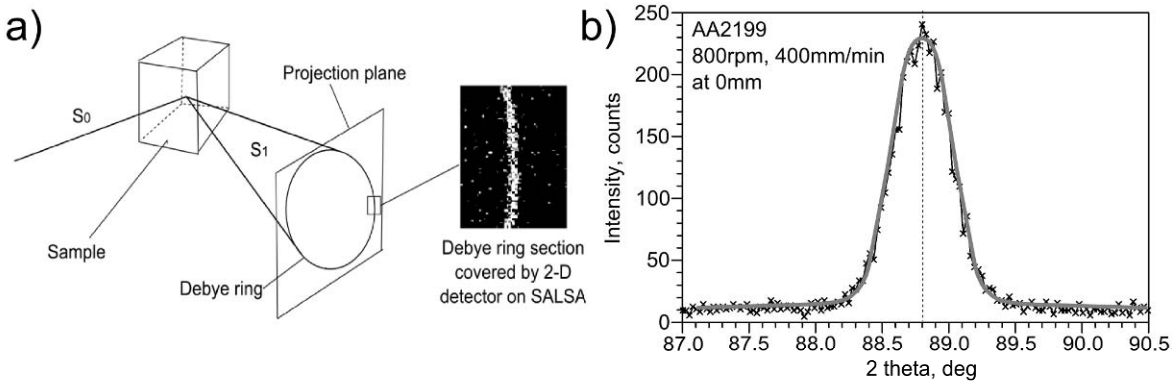

Figure 3.6: Schematic illustration of the formation of a Debye diffraction ring and how a section of this ring is covered by the 2-dimensional position sensitive detector on SALSA (a) and (b) a single peak (grey line is the fitted peak) as obtained after azimuthal integration and fitting with a Gaussian function.

The SALSA beam-line was equipped with an 80×80 mm^2 He^3 position sensitive area detector (PSD) used to determine the angular position of the intensity peak of the diffracted beam. Rather than scanning the angular position of the *{hkl}* diffraction peak by rotating the detector around the centre of the gauge volume, the PSD was fixed at the approximate 2θ diffraction angle and collects the diffracted neutrons over an angular range of ~±2.5 °. As diffraction in a crystalline material is 3-dimensional, the incident monochromatic beam diffracts for each lattice plane family into a cone shaped shell, which if projected onto a plane normal to the propagation direction forms a Debye diffraction ring as illustrated in Figure 3.6. The PSD on the SALSA beam-line covers a finite section of this Debye ring. This part of the Debye ring requires correction by azimuthal integration prior to fitting with a Gaussian profile to the single peak, though allowing extracting the angular peak position 2θ, as is illustrated in Figure 3.6b. Both, the azimuthal integration as well as the Gaussian fitting are performed with the ILL LAMP (Large Area Manipulation Program) software developed by ILL (ILL).

3.3.2.2 Experimental details

Using the standardized VAMAS sample mounting system (ISO/VAMAS/TWA20 2001) the welds investigated in this dissertation were mounted on the hexapod in three different orientations with respect to the scattering vector as depicted in Figure 3.7a-c. In this way the strain in the three different plate directions could be measured. A schematic of the incident and diffracted beam for measurement of the normal (out-of-plane) direction in reflection mode is shown in Figure 3.7d.

For all strain measurements performed on this instrument throughout this dissertation the incident monochromatic neutron beam was selected using the {400} reflexion of the Si-monochromator and was set to a wavelength of λ≈1.694 Å (take-off angle ≈ 75˚) resulting in a diffraction angle of $2\theta \approx 88.5^{\circ}$ for the *{311}* aluminium lattice plane. This plane is known to be most representative for the average strain present in the cubic cell structure of aluminium (Clausen *et al.* 2003).

As 2θ is ~90 ° the gauge volume had a nearly cuboidal shape and using the slits it was set to ~1.25×1.25×0.9 mm^3 for measurements in the longitudinal and ~1×1×10 mm^3 for the transverse and normal directions. The former smaller gauge volume is necessary to achieve the spatial resolution required for the measurement of the longitudinal direction; however,

this significantly reduces the intensity hence requires longer counting times per point. In addition, texture and grain size effects may have detrimental effects (see section 2.6.6), as the sampled material volume is smaller. On the other hand, an elongated gauge volume was used for the two remaining directions to reduce the counting time and to minimize texture and grain size effects. As an alternative one could oscillate the sample. However, at the time these measurements were performed this rocking-function was not available at the SALSA beam-line.

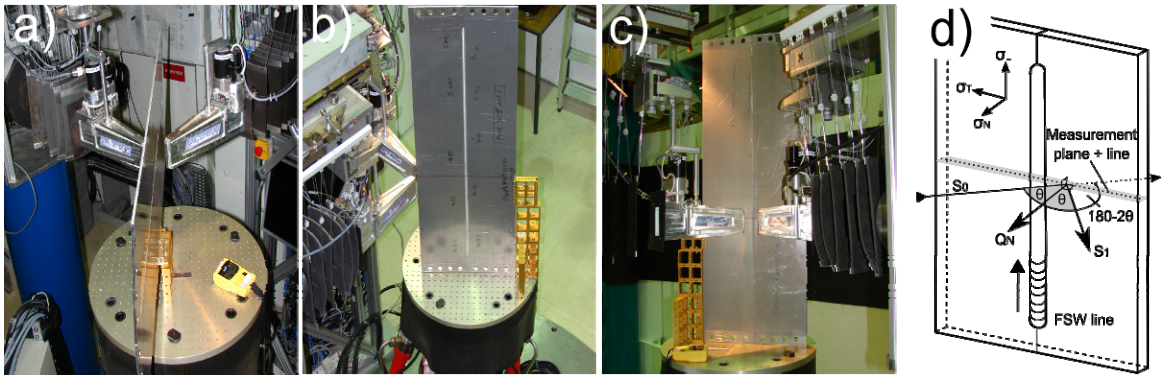

Figure 3.7: Illustration of the weld orientations for measurement of the lattice spacing in (a) the longitudinal, (b) the transverse and (c) the normal direction. A schematic illustration of the incident and diffracted beam and the sample set-up for measurement in the normal direction in reflection mode is shown in (d).

In addition to texture and grain size effects, beam divergence effects were encountered. This means that the gauge volume is always greater in dimension than the slit settings suggest and the shape varies from the theoretical form. In order to minimize divergence the vertically orientated slits were moved as close to the gauge volume as possible. Depending on the plate thickness this varied from ~25 mm for thinner plates to ~40 mm for the thicker plates thus minimizing horizontal divergence effects. However, in the vertical direction the set gauge volume height linearly increases by a factor of ~1.5 for the given gauge volume-slit distance (Hughes 2008) thus restricting the spatial resolution to ~1.35 mm when set to 0.9 mm for measurements in the longitudinal direction. This may lead to RS peak smoothing as the strain is averaged over this distance or in the worst case sharp strain peaks within this distance may be missed out or reduced in magnitude. For measurement in the transverse and normal direction the increased height of the gauge volume is acceptable as it has no effect on the spatial resolution across the weld-line. In fact it is beneficial to increase the gauge volume height as this leads to an increase in the amount of diffracted neutrons

and therefore allows for reduced counting times. Assuming that the FSW process was at steady-state at the measurement line no variation in lattice spacing hence residual strain and stress along the weld direction or direction of height of the gauge volume should be present (Steuwer *et al.* 2006b; Richards *et al.* 2008a). Therefore no erroneous results should be obtained due to the elongated gauge volume.

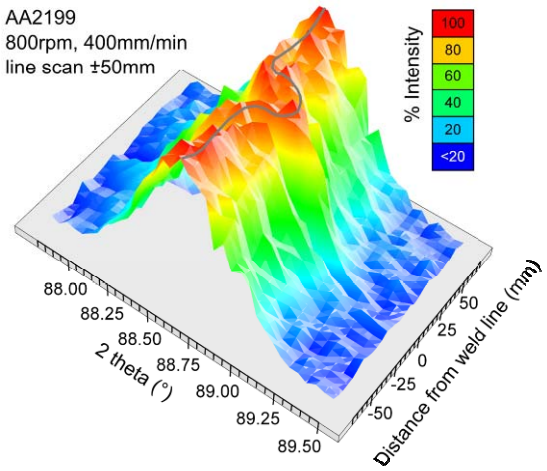

Figure 3.8: Series of *{311}* diffraction peaks after azimutal integration showing the peak shift as obtained from measuring several points along a line across a 5 mm thin AA2199 friction stir weld. For better visualisation the diffraction peak intensity is normalized and the approximate shift of the peak position is marked with the grey line (gauge volume 1×1×10 mm^3, 5 min, transverse direction).

The counting time necessary to achieve good diffraction peak quality varies due to attenuation depending on beam path length within the sample, but also texture and grain size of the sampled material may affect the counting statistics. However, unless stated otherwise the counting time was 15 min per measurement location, for the longitudinal, and 5 min per point for measurements in the transverse and normal directions.

Using the computer controlled hexapod and user written macros, the samples were moved such that relative gauge volume travel occurred across the weld-line, along the measurement line. In this way the strain profile as a function of distance from the weld-line was collected. If RS leading to strain shifts or shifts of the unstrained lattice parameter are present in the welded structure, then a shift of the diffraction peak, as shown in Figure 3.8 for a 5 mm AA2199-T8E74 plate joined by FSW, occurs. In the depicted case the 2Θ value shifts to higher angles in the wed-line, indicating either compressive stresses, a shift of the unstrained unit cell parameter, or a combination of both. Note, the diffraction peak intensity was normalized in order to simplify visualisation of the peak shift.

3.3.3 The ID15A beam-line

Energy dispersive synchrotron X-ray diffraction (EDXRD) measurements were performed on the ID15A high energy beam-line at the ESRF, France. The following sections specify the instrument set-up for the performed strain measurements in this dissertation.

3.3.3.1 General EDXRD beam-line set-up

The ID15 straight insertion section holds a 7 pole 1.84 Tesla asymmetric multipole wiggler. The X-ray beam received from the wiggler has a critical energy of 44 keV and the useful spectrum extends up to 500 keV; however, usually the beam-line operates between 70 and 400 keV for EDXRD experiments in the ID15A hutch. The initial cross-section of the incident beam, as received directly from the wiggler, is defined by a pair of vertical and horizontal, motorized slits made from W (tungsten) or WC (tungsten-carbide). The slits are placed ~60 m behind the wiggler and as a result of the long distance the X-ray beam is highly parallel. The instrument set-up from the primary slits to the sample and subsequently the secondary slits is less than ~2 m and so beam divergence is reduced even more. The diffracted beam is shaped by two sets of horizontal motorized slits, one close to the sample and the second one close to the detector. The vertical gap is defined using thin foil as slit separators. Further, the diffracted beam travels through a lead shielded copper tube that is installed between the secondary slits in order to reduce background noise. Additional slabs of lead are fixed around the detector window to prevent the entry of background radiation.

The energy spectrum of the diffracted beam was detected by a stationary liquid-nitrogen-cooled energy sensitive Ge (germanium) single-crystal detector attached to an analogue data acquisition system. However, both were recently replaced by a modernized Ge-detector and a digital electronic data read out system, allowing higher count-rates and better thermal stability of the electronic equipment.

For sample manipulation translation stages capable to move loads up to 400 kg at high positioning accuracy of the order of a few micrometers, as well Euler cradles for sample rotation are available. However, these are usually serial arrangements, requiring adjustment for each new sample manipulation problem, hence complex sample positing usually requires long instrument set-up times. Nevertheless, all translational and rotational devices,

as well as the motorized beam defining slits are computer controlled and so allow for relatively fast alignment procedures and automated strain scans.

On ID15A it is comparatively simple to use two stationary Ge-detectors (Steuwer *et al.* 2006a). Mounting one detector with a horizontal offset of 2θ and the second detector with the identical offset but in the vertical direction as it is illustrated in Figure 3.9a allows measurement of two perpendicular strain directions at the same time. By calibrating the two detectors using a reference powder one can compare the absolute values measured with the two different detectors.

3.3.3.2 Experimental details

For measurements performed in this dissertation the instrument set-up was as described above. In order to penetrate plate thicknesses of up to 20 mm of aluminium (for example set #4), high X-ray energies of 60-150 keV at a low scattering angle of $2\theta = 5°$ were used for all measurements performed on ID15A. As described in section 2.6.4 a low 2θ value tends to elongate the nominal gauge volume and so a small beam size of $100 \times 100\ \mu m^2$ for both, the incident and diffracted beam was used to restrict the maximum gauge volume length to ~2.3 mm. However, this limits the through thickness resolution of the EDXRD technique, but enables high resolution measurements in the two in-plane directions of the welded plate as long as it is mounted as depicted in Figure 3.9.

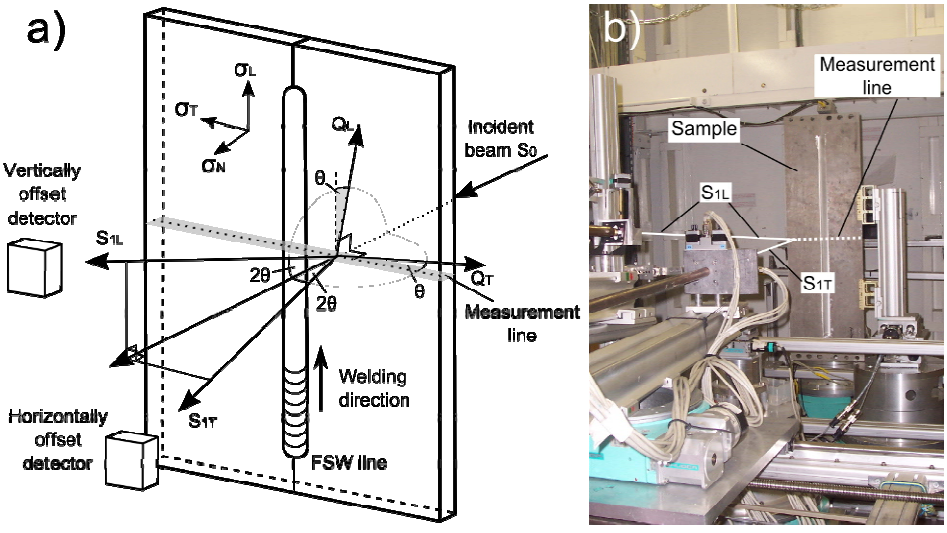

Figure 3.9: (a) Illustration of the sample set-up on the ID15A beam-line, the horizontal and vertical offset detectors and the scattering vectors. An illustration of a test weld mounted in the typical orientation on ID15A for strain measurement in the longitudinal (S_{1L}) and transverse (S_{1T}) direction is shown in (b).

By mounting the test welds using the VAMAS sample mounting system (ISO/VAMAS/TWA20 2001) as shown in Figure 3.9b, the unit cell parameter in the longitudinal and transverse plate directions are measured simultaneously. However, the welds were mounted normal to the incident beam and so the scattering vectors Q_L and Q_T are actually out of the in-plane direction by an angle of θ. Yet, as long as the 2θ value is small, the difference in the unit cell parameter between the actually measured directions and the in-plane directions is negligible (Hauk 1997). Similar to the SALSA beam-line user-written macros were applied in order to automate the sample manipulation and the measurements. Unless stated otherwise the counting time per measurement point was 1 min for each point.

The EDXRD technique produces a diffraction profile comprising several diffraction peaks as shown in Figure 2.31b, which can be fitted using the GSAS (General Structure Analysis System) profile refinement software with the diffraction intensity being determined using the LeBail method (Larson *et al.* 1994). This allows not only the determination of the lattice spacing d_{hkl} for each *{hkl}* lattice plane family sampled in the gauge volume, but one can extract the unit cell parameter a hence calculate the average strain present in the cubic unit cell. This software was used for data analysis in this dissertation.

As shown in Figure 3.8, using diffraction one can measure the shift of the lattice plane distances or the unit cell parameter (depending on the diffraction method used) as a function of lateral position in welded structures. This shift may be due to RS present in the component, due to local variations in the precipitation microstructure or such shifts may arise from a combination of both. Therefore it is vital for the RS determination in this dissertation to resolve possible shifts of the unstrained unit cell parameter a_0 as a function of position for each welding condition and set of test welds. While the background of the different methods used in this dissertation is detailed in section 2.6.6.3, the following section will give the experimental details for the measurement of the unstrained unit cell parameter using these methods.

3.3.4 Determination of the Unstrained Unit Cell Parameter

Depending on the diffraction technique used one can either determine the {*hkl*} specific elastically unstrained lattice parameter d_0 (for example ADND on SALSA) or the value for

the elastically unstrained unit cell parameter a_0 (for example EDXRD on ID15A). As mentioned before, for simplicity in this dissertation it is a_0 rather d_0 that it is referred to when referring to the unstrained condition. The *{311}* aluminium d and d_0 values as determined on the SALSA beam-line were converted into unit cell parameter values using equation 2.7.

As detailed in section 2.6.6.3, the unstrained, or stress free, unit cell parameter a_0 varies with the solute content in high strength aluminium alloys. Due to the thermal cycle during FSW, the material in the weld region may undergo changes in solute concentration as precipitates may dissolve and/or re-precipitate and grow, which in turn may result in a variation of the elastically unstrained unit cell parameter a_0. This variation as a function of position within the test weld must be determined in order to allow for an accurate residual strain, hence stress, calculation (Steuwer *et al.* 2007; Withers *et al.* 2007).

In this dissertation three methods were used to determine the variation of a_0, namely the plane stress assumption, the relaxed comb and the $\sin^2\psi$ methods. While the theoretical background of each technique is discussed in section 2.6.6.3, this section aims to outline the experimental measurement of a_0. From each set the as-welded test weld was used for determination of a_0.

3.3.4.1 Plane stress assumption technique

This technique is based on the assumption of in-plane stresses only and may be applied to welds in thin sheet. The technique requires strain measurement in all three principal directions. When this method was used, the normal direction was usually measured on the SALSA beam-line, while the value for the longitudinal and transverse directions may have been measured either on the SALSA or the ID15A beam-line (see Table 3.5). When different instruments were used an aluminium reference powder was applied to allow for correction of calibration differences between the instruments, in order to obtain comparable absolute unit cell parameter results. No special sample preparation is required for the plane stress assumption method. The value of a_0 was calculated using equation 2.15.

3.3.4.2 Comb method

The comb method is based on relaxing the macro RS. Using a *Buehler Isomet 4000* linear precision saw a thin bar from the N-T cross-section of the test weld at mid-length of the weld path covering the weld-line and PM on the advancing side as depicted in Figure 3.10a and Figure 3.10b was produced. The bars were ground and mechanically polished on the cutting surfaces to remove stresses possibly induced by the cutting process. Subsequently, teeth were cut using an oscillating diamond wire precision saw with sufficient cooling and a low feed rate. The teeth centres were approximately 1 mm apart in the region around the weld-line and additional teeth were cut in the PM in order to determine the original value for a_0 before welding. This material is assumed to be unaffected by the welding cycle. The comb sample produced from the test weld #3B29 is shown in Figure 3.10d. In this case, only half the WN is covered and the tooth to the very right sample the weld-line position (y=0).

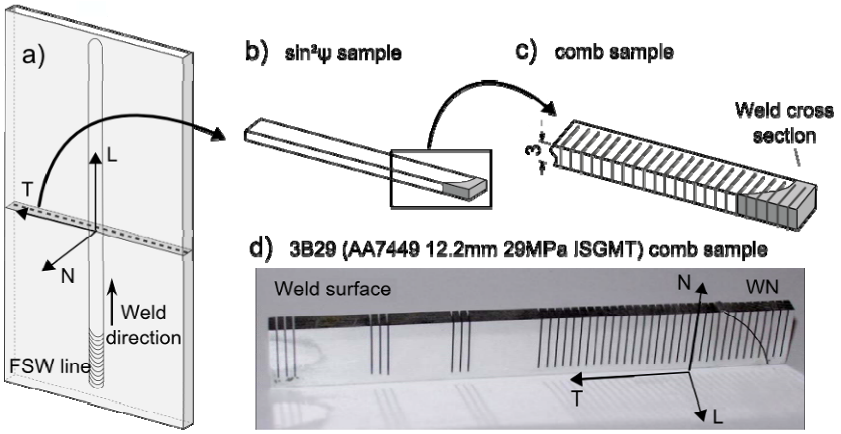

Figure 3.10: Schematic illustration of a test weld (a) and the approximate position and the orientation from where sin²ψ (b) and comb (c) reference samples where removed. In (d) the comb produced from test weld #3B29 for measurement of a_0 on ID15A is shown; within a 50 mm wide region from the weld-line covering the WN, the TMAZ the HAZ the teeth are 1mm apart, further to the left additional teeth were cut to obtain a_0 data in the unaffected PM.

Using a *Mitutoyo Euro C A 776* coordinate measuring machine (CMM) equipped with a *Renishaw* touch probe the position of the centre of each tooth, with respect to the specimen edges, were scanned. From these data the coordinates for measurement points (centre of tooth) were generated to measure the a_0 variation across the weld. In thicker material (set #3, #4 and #7) additional line scans were performed in order to account for through thickness variations.

3.3.4.3 $Sin^2\psi$ method

Producing a sample for the sin²ψ method was identical to the procedure described for the comb method except for cutting the teeth. An illustration of the mounted sin²ψ sample is given in Figure 3.10 b. The sin²ψ method is based on the assumption of a plane stress situation and as material in the longitudinal direction is removed, it can be assumed that no macro stresses are left in this direction. Therefore any remaining RS field is essentially limited to the transverse and normal directions, where stresses are generally very small. This should be apparent in very low gradients in the *a vs.* $sin^2\psi$ plots.

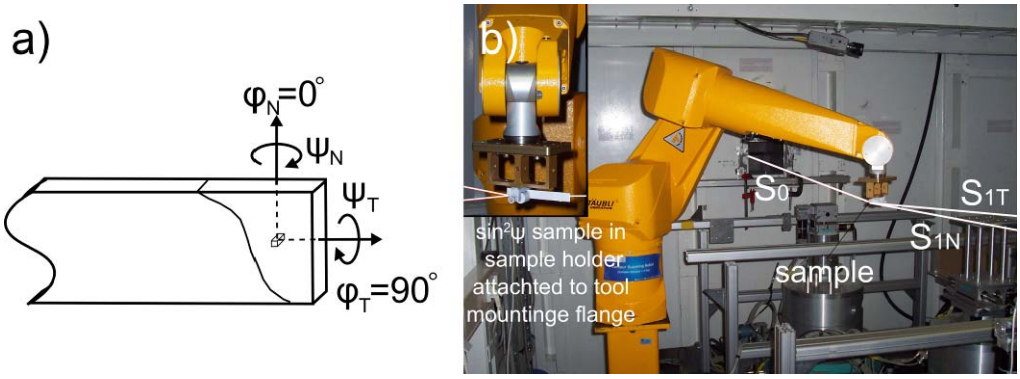

Figure 3.11: The required rotations of a thin cross-section of a friction stir weld around the two in-plane axes φ_N=0° and φ_T=90° (a) and (b) the application of an advanced serial robotic arm sample manipulation system for positioning the sample for determination of the unstrained unit cell parameter a_0 using the sin²ψ method. The inlay shows the sample being rotated to 64° around φ_N=0° with respect to the incident beam. A detailed discussion of this system is given in section 3.4.

The sin²ψ method requires complex sample manipulation. Not only translational movements from the current to the next measurement point are required, but also rotational movements of the specimen around the currently sampled material volume at the axes φ_N=0 ° and φ_T=90 ° as depicted in Figure 3.11a. Within the framework of this dissertation an advanced robotic arm sample manipulation system was developed to a prototype level for both manipulation of complex shaped samples and complex sample positioning procedures. As shown in Figure 3.11b, this system was applied for positioning the sample for determination of the unstrained unit cell parameter a_0 using the sin²ψ method. A comprehensive introduction to this robotic based system is given in section 3.4. Once, each value for *a* for the differing orientations has been determined, one can calculate the local unstrained unit cell parameter a_0 using equation 2.16.

Finally, after measurement of the local unit cell parameter a for the different plate directions and the corresponding value for the unstrained condition, the residual strain and stress can be calculated as described in the following section.

3.3.5 Calculation of RS

The strain for each measured direction was calculated using equation 2.6 and, depending on whether a tri-axial or bi-axial stress condition was assumed, the RS can be derived using equations 2.10 to 2.12 or 2.13 and 2.14, respectively.

As it was not possible to measure all sets of test welds at once, using an identical instrument set-up, the necessity of machining the a_0 reference samples from the test welds meant that the experiments were performed over some time. Naturally, each time the instrument set-up is slightly different resulting in global offsets between the absolute unit cell parameters measured on the different occasions. As a result it is not possible to apply the absolute measured stress-free unit cell parameters a_0 to determine the strain and stress directly. Instead, at each point the spatial variation in the unstressed unit cell parameter measured in the reference sample was used as a local perturbation Δa_0 to a global unstressed reference value a_{ref} used for each detector. These global a_{ref} values were chosen to ensure stress equilibrium conditions; i.e. the longitudinal RS balanced across the normal-transverse cross-section (presuming that the longitudinal stresses do not vary significantly through-thickness (all sets except set #4) and the transverse RS was zero at the edge of the plate (Masubuchi 1980; Hauk 1997; Withers *et al.* 2001c). A least-squares approach was used to modify the global average a_{ref} values in order to fulfil these stress balancing and boundary conditions. Since modifying the a_{ref} parameter (and hence strain) in one direction alters the stress in the other direction, they were solved iteratively until the solution converged. The shift in the global unstrained unit cell parameter due to this procedure varies between the different experiments, but was usually of the order of ~400 to ~600 με for the longitudinal and ~50 to ~150 με for the transverse direction. This corresponds to a global shift of the longitudinal RS distribution of around 30 to 40 MPa.

3.4 ADVANCED ROBOTIC SAMPLE MANIPULATION SYSTEM

3.4.1 Introduction

As described in section 2.6, strain measurements by diffraction for determination of RS in engineering components require flexible, precise and fast sample manipulation with respect to the gauge volume location (position and orientation). The determination of the strain tensor is based on the measurement of lattice spacing in several orientations with the gauge volume centred in the point of interest (Hutchings *et al.* 2005). Similarly, the determination of the unstrained unit cell parameter a_0 using the $\sin^2\psi$ technique (see section 3.3.4.3) requires the inclination of the sample to many different angles (Noyan *et al.* 1987; Peel *et al.* 2003) with respect to the scattering vector while maintaining the position of the sampled material. Within this dissertation a serial robotic arm sample manipulation system was developed to prototype level with the aim to allow for such complex sample manipulation procedures. This system was used for the complex sample manipulation for the $\sin^2\psi$ method for determination of the variation of the unstrained unit cell parameter (see section 3.3.4.3) and is described in the following section.

3.4.2 Sample Manipulation Techniques

Current sample manipulation methods rely mainly on combinations of linear translation devices with Eulerian-type cradles attached for rotation purposes (for example ID15A). Conventional linear translation tables are capable of precisely moving samples of a wide range of weights. Eulerian cradles are limited in rotational range for big and heavy samples, but on the other hand, when a high degree of freedom is required can only carry small and light samples. A recent approach to overcome sample manipulation limits was made on the SALSA beam-line using a Stewart-platform (see section 3.3.2) that allows translational and rotational movements within one device. However, for some applications the conventional systems and even the hexapod device may not be sufficient. On complex samples, such as turbine blades, strain measurements in several orientations may require intermediate changes of the sample mounting thus prohibiting the automation of complete measurement cycles. In some cases, additional rotational axis (for example Euler-cradles) may be added on top of the manipulation devices hence increasing the degree of freedom and lessening the required times of intermediate changes of the sample mounting. However, additional

axes increase the complexity of controlling the sample movements due to the serialisation of the axes. Further, these set-ups are often special arrangements devised for a particular experimental purpose and therefore require significant time for precise alignment. Nevertheless, there is a strong drive towards measuring RS in real engineering components with complex geometries, such as turbine blades, crank shafts, and gears etc, which pose considerable challenges to conventional sample manipulation methods.

As brought up in section 2.6.6.1 the idea of capturing the geometrical 3D outline of a component digitally using a CMM for subsequent precise sample positioning and manipulation on neutron strain diffractometers was initially proposed by Withers in 2001 (2001e), and was first incorporated within a sample scanning software environment by James *et al.* (2004).

3.4.3 Serial Robotic Arm based Sample Manipulation System

In this dissertation, the desire for less restricted movement as well as automated sample manipulation for strain measurements in distorted friction stir welds as well as for the $\sin^2\psi$ method for determination of a_0 has led to the development of a novel approach based on serial robotic arms. What makes robotic arms attractive for complex sample manipulation is the fact that six degrees of freedom are fully available (±360º rotations around and linear translations along three sample axes) within a nearly spherical work space. Both, rotation and translation are accessible at each step with a high absolute and reproducible accuracy of the order of tens of microns depending on the robotic arm in use.

This is of particular interest for neutron instruments where the required positioning accuracy in strain measurements rarely exceeds hundreds of microns. Furthermore robotic arms offer ease of use as all axes are controlled by the system control unit. In principle only the final location coordinates of the working point of the tool, or in this application the sample measurement location within the tool coordinate system ($X_TY_TZ_T$) and the gauge volume location within the robotic arm global coordinate system ($X_0Y_0Z_0$) (both coordinate systems are depicted in Figure 3.12a are required. The algebraic coordinate manipulations to direct the robotic arm motors are performed by the control unit. In order to make best use of the advantages offered by robotic arms reverse-engineering techniques to create 3-dimensional models of the sample within which the measurement locations may be

specified were used. Off-line preparation and simulation ensures safe operation of the system on the beam-line and the optimal use of the allocated beam time.

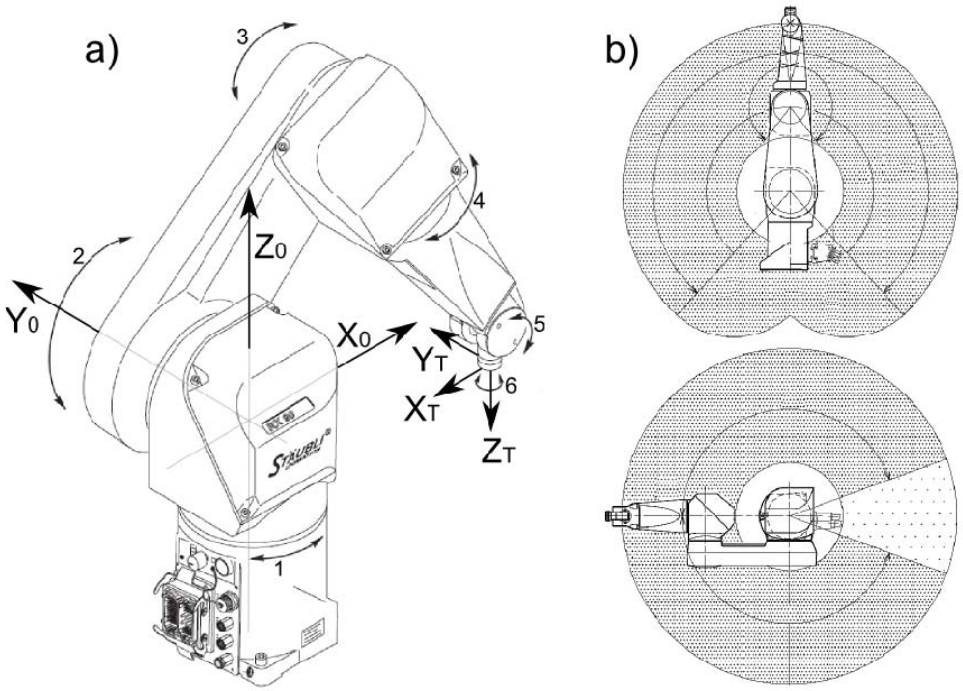

Figure 3.12: Illustration of the STAUBLI RX90L robotic arm and the internal coordinate systems: $X_0Y_0Z_0$ is the global and $X_TY_TZ_T$ is the tool coordinate system(a) and (b) illustration of the work space of the RX90L as seen from the side (top) and from the top (bottom).

Within this dissertation this system was used to measure the lateral and through plate thickness variation of the elastically unstrained unit cell parameter a_0 in test weld #3B29 using the $\sin^2\psi$ method (see section 3.3.4.3). The detailed system set-up and the sample manipulation procedure are described below.

3.4.4 The System Set-up and Functionality

The prototype system to manipulate test samples for diffraction measurements implements a *STAUBLI RX90L* high precision serial six-axis robotic arm equipped with a CS7M control unit enabling manipulation of samples of up to 9 kg weight with the full six degrees of freedom within a 2000 mm in diameter nearly spherical work envelope as illustrated in Figure 3.12b. The robotic arm can manipulate samples with a specified positioning accuracy of ±25 µm at 10 % of the nominal speed and 6 kg pay-load (STAUBLI 2001), while higher pay-loads result in less accuracy.

In the current set-up, the *RX90L* is equipped with a 125×75×12 mm VAMAS base plate (ISO/VAMAS/TWA20 2001) attached to the tool mounting flange such that the tool coordinate system $X_TY_TZ_T$ is located in the centre of the bottom surface of the VAMAS base plate as depicted in Figure 3.13d. Using the standard VAMAS sample mounting system enables fast and repeatable precision mounting of samples. The CS7M control unit, operated and programmed via TCP/IP (Ethernet) by an external PC, controls the robotic arm axes and allows communication to other systems such as the beam-line control via 16 digital input/output signal channels.

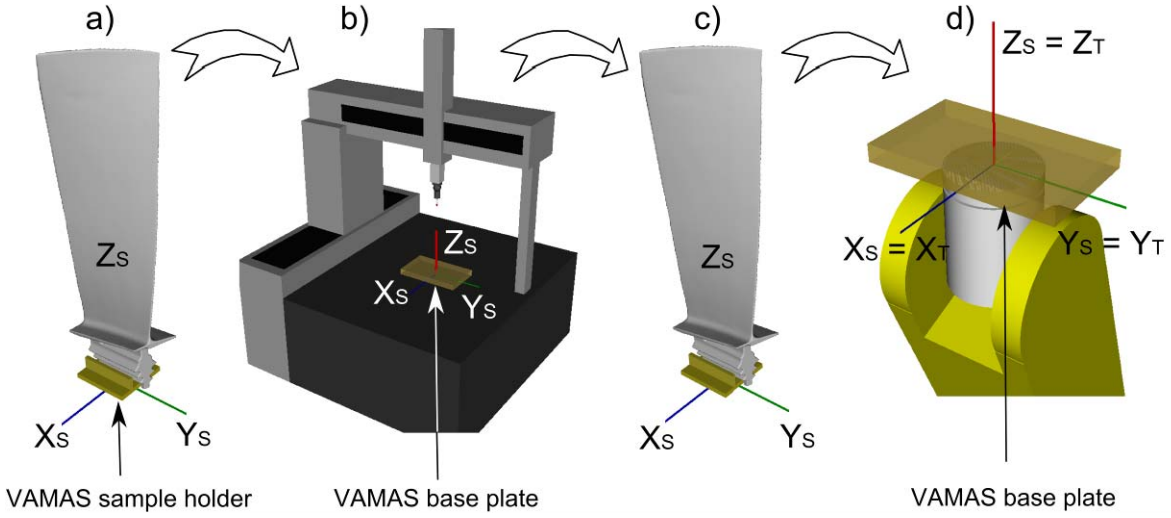

Figure 3.13: Schematic illustration of the sample manipulation procedure: in this case for a turbine blade. In (a) the sample is mounted in a VAMAS sample holder, (b) the sample holder and sample are mounted on the CMM in $X_SY_SZ_S$ and the surface geometry is scanned. In, (c) and (d) the sample holder with the sample is transferred to the robotic arm VAMAS base plate, such that $X_SY_SZ_S$ and $X_TY_TZ_T$ coincide.

The typical working procedure to prepare and perform for example a strain scanning experiment is as follows:

i. Mounting the sample in a standard VAMAS sample holder before attaching it to a VAMAS base plate on the CMM (see Figure 3.13a and Figure 3.13b).
ii. Scanning the sample surface in the coordinate system $X_SY_SZ_S$ located in the centre of the bottom surface of the VAMAS base plate using the CMM with a touch probe or laser scanner to produce a point cloud representing the sample surface.
iii. Development of the sample CAD model to reduce point-cloud data volume.

iv. Specification of the measurement grid within the CAD model and calculation of the measurement location coordinates (x_S,y_S,z_S,rx_S,ry_S,rz_S), where x_S,y_S,z_S are translation coordinates and rx_S,ry_S,rz_S are rotation coordinates for each axis.

v. Creating a simple text file containing (x_S,y_S,z_S,rx_S,ry_S,rz_S).

vi. Automatic creation of the sample manipulation script for the robotic arm control during the experiment (reading the coordinate file).

vii. Mounting the VAMAS sample holder with the sample onto the VAMAS base plate attached to the robot tool mounting flange, such that the two coordinate systems $X_SY_SZ_S$ and $X_TY_TZ_T$ coincide (see Figure 3.13 c and Figure 3.13d).

viii. During strain measurement each measurement location (x_S,y_S,z_S,rx_S,ry_S,rz_S) is successively defined as the current robot tool tip point in $X_TY_TZ_T$ (this may be done, because the sample coordinate system $X_SY_SZ_S$ and the tool coordinate system $X_TY_TZ_T$ coincide).

ix. At each location, once the acquisition period for the current point is complete, a digital signal is sent from the beam-line control to the control unit to initiate the robotic arm to move the next defined robotic tool tip point (or sample measurement location) into the work point location, which in this case is the location of the gauge volume represented in $X_0Y_0Z_0$ (see Figure 3.12a).

x. Once the movement is complete the control unit returns a signal to the beam-line control to commence strain measurement.

Procedures ix) and x) are repeated automatically until all programmed sample measurement locations have been measured.

The digitisation of the sample surface allows the virtual visualisation of the specimen. Following work by James *et. al.* (2004) this allows for preparation and simulation of the complete sample manipulation procedure offline and prior to the experiment, hence saving a substantial amount of beam time whilst ensuring safe operation of the robotic arm. Further, the digital interfacing of the control unit with the beam-line control system allows to ensure each measurement location receives sufficient illumination with the beam before movement of the specimen to the next measurement location. This system exploits the significant advantage of robotic arms, namely that any programmed measurement location can be moved directly into the gauge volume and oriented correctly for measurement. This means, for example, that the complete strain tensor can be determined for large arrays of

measurement points without having to remount and realign the sample to re-orientate, as would be necessary on simpler XYZ translation systems.

3.4.5 Positioning Alignment and Accuracy

The precise determination of the position of the gauge volume within the robotic arm global $X_0Y_0Z_0$ system can be undertaken using established methods (Hutchings *et al.* 2005). For example, a small metal pin having a known location within $X_TY_TZ_T$ can be scanned through the gauge volume with the incoming and diffracting beam correctly oriented to collect a relevant diffraction peak (*hkl*). The position of highest intensity of the diffracted signal defines the position of the gauge volume in $X_0Y_0Z_0$ in the direction of the axis scanned. Nevertheless, other techniques (for example mounting a CCD (charge coupled device) camera) are also applicable.

Within this dissertation the positioning accuracy of the *RX90L* was investigated according to ISO 9283:1998 by installing it in front of the CMM equipped with a touch probe. A 5 kg steel sphere was attached to the robotic arm tool mounting flange, such that the centre of the sphere was at (0,0,100,0,0,0) in $X_TY_TZ_T$. Subsequently an arbitrary location within the workspace of the CMM was repeatedly approached (50×) by the robotic arm at 10 % of nominal speed and each time the sphere centre position was determined by the CMM. Essentially the same measurement locations on the sphere surface were assessed by the CMM to determine the centre of the sphere. This process was insensitive to errors in the roundness of the test sphere. This procedure was repeated for six significantly differing locations of the sphere within the CMM workspace to provide a good statistical basis upon which it was concluded that the RX90L robotic arm in use has a repeatable positioning accuracy of ±21 μm for the specified set-up (Altenkirch 2005). Further details of the ISO 9283:1998 testing procedure and the results can be found elsewhere (Altenkirch 2005).

3.4.6 Conclusions

Using this advanced serial robotic arm sample manipulation system allows for precise sample manipulation in terms of position and orientation with respect to the gauge volume location of complex samples or for complex sample movements. Within this dissertation this system was used to perform the complex sample manipulation required for the $\sin^2\psi$

method for determination of the unstrained unit cell parameter a_0. More details about this system as well as other applications the system has been used for may be found in the appendix.

3.5 FINITE ELEMENT MODELING

3.5.1 Introduction

Production of trial welds and measurement of the residual strain, and hence the RS in such welds, may be both time consuming and expensive. As a result, it is desirable to be able to predict the post weld stress distribution and especially the location and magnitude of the peak RS. In addition the stress development during welding under varying conditions is of interest. Therefore finite element modelling (FEM) is an ideal tool to reduce time and expenses necessary to obtain RS data using diffraction techniques and, provided a model is validated against experimental data, it may predict experimental results with an impressive accuracy (Richards *et al.* 2008a).

Within this dissertation FEM results are presented that were partly produced by D. Richards from the University of Manchester, UK as part of the SEALS project (see section 1.1). He used an FE-model comprising a sequentially linked heat transfer model and a mechanical stress model, both created and implemented in ABAQUS/Standard software. This model was applied by D. Richards from the University of Manchester, UK for simulation of the FSW process under varying ISGMT loads for the test welds from set #3 (Richards *et al.* 2008a). In collaboration with D. Richards, the original FE model was adjusted for the test welds in set #2 and used to predict the final RS distribution as a function of the varying applied ISGMT loads. The results for set #2 are original work, while those obtained for set #3 were produced by D. Richards. It should be noted, that the experimental data obtained for the as welded test welds (#2B0 and #3B29) investigated in this dissertation (see chapter 5) were used to evaluate and improve the precision of both FE models. In this section the thermal and the mechanical models as used for simulation of the FSW with ISGMT in test welds from set #2 and #3 are briefly summarized.

3.5.2 The Thermal Model

In the thermal model the effect of the FSW tool was modelled as a composite heat source comprising a surface heat source for the FSW tool shoulder and a cylindrical volume source for the tool pin, while features such as shoulder scrolls or pin threads as depicted in Figure 3.1a and Figure 3.1b were neglected. The geometrical dimensions of the heat source were adjusted to the size of the FSW tool used to produce the real test welds. Based on work by Chao *et. al* (2003) the heat flux of this composite heat source was assumed to vary for the different tool dimensions and relatively with respect to the relative size of tool shoulder and pin. For simulation of the 12.2 mm thick AA7449-W51 test welds from set #3 (see section 3.2.1) the flux being distributed by the tool shoulder was set to 40 % and the tool pin assumed to provide the remaining 60 % (Richards *et al.* 2008a). For the 5 mm thin AA7449-W51 test welds from set #2 (see section 3.2.1) these parameters were set to 90 % and 10 % respectively. The allocation of the tool shoulder and pin powers in both cases were based on calibration studies by Richards *et. al* (2008a) and the use of a computational fluid dynamics model, incorporating the material flow (Colegrove 2000; 2005). Since the FSW tool was not explicitly included in the model, the material in the tool region has the thermo-mechanical properties of aluminium rather than steel.

The distribution of heat at each time step for the rotating and traversing FSW tool was determined by the user subroutine DFLUX which calculates the flux at each integration point under the tool and in the remaining plate volume. To capture the large thermal gradients in the thermal model, DC3D8 brick elements in a fine $1\times1\times3$ mm^3 (four layers set #3, 12.2 mm thick) and $1\times1\times2.5$ mm^3 (two layers for set #2, 5 mm thick) mesh were used around the weld-line (±20 mm for set #3 and ±10 mm wide for set #2). In both models these elements were replaced by DC3D6 wedge elements in a much coarser mesh further out in order to reduce the computational requirements. The heat transfer elements were then substituted by their direct equivalent brick and wedge elements in the mechanical stress model to facilitate the transfer of the generated thermal profile as well as to allow for capturing the RS gradients around the weld-line.

Even though slightly different from the real welding conditions where a steel backing plate covering the entire plate back surfaces was used, in the model a combination of a steel backing plate (similar in width to the weld zone) and an aluminium support structure to both sides of the backing plate were modelled by surfaces with specific heat transfer

coefficients. Heat transfer coefficients into the steel and aluminium parts were set to 200 and 150 $W K^{-1}m^{-2}$ respectively (Richards *et al.* 2008a). Any remaining free surfaces had a convection coefficient of 3 $W K^{-1}m^{-2}$. Possible heat transfer from the test welds into the tensioning grips themselves was not modelled.

3.5.3 The Mechanical Model

In the mechanical model, the material response to the thermal cycle as a function of temperature and time was simulated using a kinetically dependent softening model which allows interpolation of the material yield strength σ_{YS} as a function of the temperature. The typical yield strength σ_{YS} behaviour during a weld cycle for the aluminium alloy AA2024-T6 is depicted in Figure 3.14a for two extremes; namely, the material behaviour in its initial condition from room to near melting point temperatures of approximately 500 °C (black solid line) and the resulting yield strength σ_{YS} after cooling to reach the fully softened condition (black dashed line) (Richards *et al.* 2008a). An intermediate behaviour can be observed for smaller peak temperatures, which correspond to different lateral locations to the weld-line. Figure 3.14b depicts the same evidence, but as a function of time and local temperature for two different lateral locations, hence two different peak temperatures and consequently intermediate final yield strength of the material.

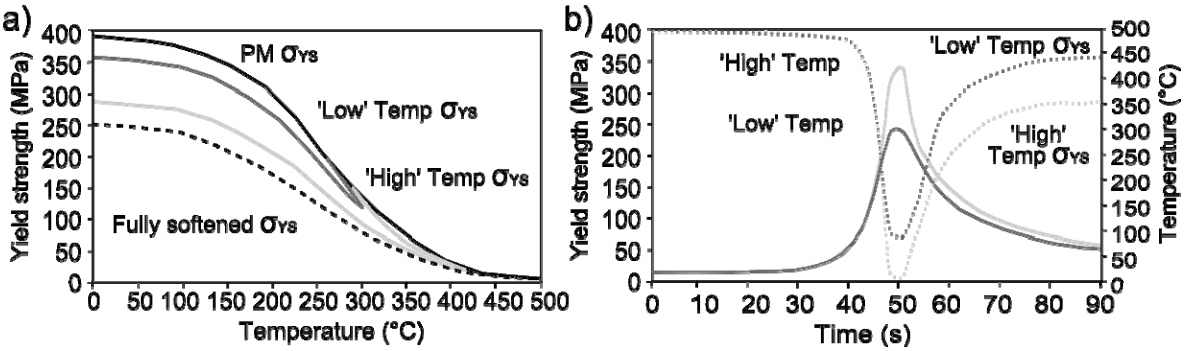

Figure 3.14: The typical material yield strength distribution as a function of high and low welding temperatures (a) and time (b) for the aluminium alloy AA2024-T6 during FSW. A similar model was used to predict the material strength response to the elevated temperatures for modelling the stress development in friction stir welds in AA7449-W51 aluminium alloy (after Richards *et al.* (2008a).

In order to simulate the clamping conditions during FSW the surfaces were fixed by limiting their degrees of freedom in the plate normal direction, thus allowing movement in the longitudinal and transverse direction when the simulated varying ISGMT loads were

applied homogeneously to the ends of the plates. The mechanical model was further divided into five time sequences, namely tensioning, clamping, welding and cooling (both based on the results of the thermal model) and finally removal of clamping and tensioning loads. The RS distribution at the mid-length of each simulated test weld was interpolated on the basis of the stress values for each element node along a line across the weld-line at mid material thickness as depicted in Figure 3.15. In this figure the temperature distribution (T) as obtained from the thermal model and the longitudinal RS distribution (σ_L) as obtained from the mechanical model for 30 and 55 sec into the FSW process of 5 mm thin AA7449-W51 without ISGMT applied (test weld #2B0) are depicted.

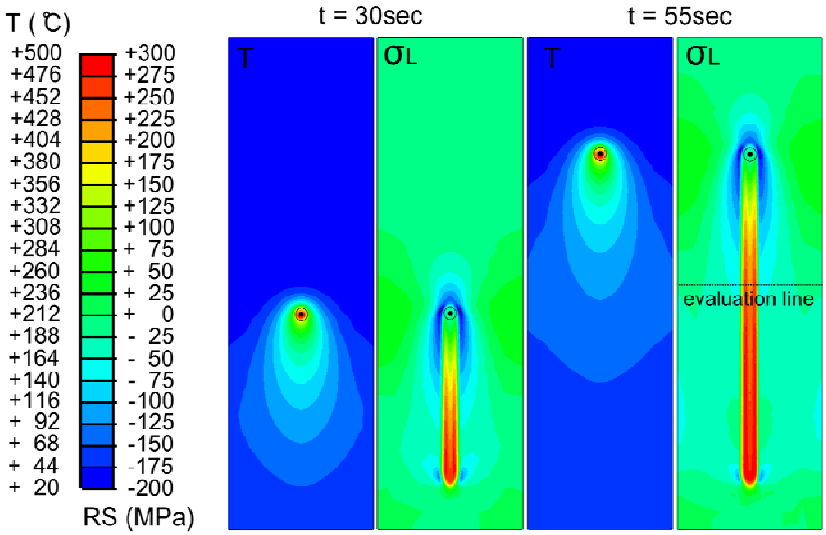

Figure 3.15: Graphical illustration of the FE model for 5 mm thick AA7449-W51 test weld (#2B0, 551 × 150 mm^2). The thermal field (T) and the longitudinal stress field (σ_L) at the weld surface at 30 and 55 sec into the FSW cycle. The tool outline is included in each graph. The mesh in both models is not depicted for clarity.

The development of the FE model for simulation of the effect of ISGMT on the final RS distribution for the test welds in set #3 was performed by D. Richards and the results obtained from this work are presented within this dissertation to complement the experimental results. By contrast, the FE model for the test welds in set #2 and the RS results obtained from this model are original work and constitute part of this dissertation.

3.6 WELD DISTORTION

RS in welded structures may cause component distortion in several directions depending on the plate and weld geometry as well as the RS distribution (see section 2.4.5).

The magnitude and direction of the RS may lead to several kinds of distortion as described in section 2.4.5. Within this project the bending distortion (deformation along the welding direction) and the angular or butterfly distortion across the weld-line (transverse direction), were of primary interest as those may directly be related to the RS in the corresponding directions.

The distortion in these two directions was determined using a coordinate measuring machine (CMM) with either a *Renishaw*™ touch probe or a *Metris LC50*™ laser scanner attached, thus allowing to scan the sample surface along (bending distortion) and across the weld-line (angular distortion). The measured data were manipulated such that the plate ends (end of scan line for each direction) were set to zero allowing to read the maximum displacement for the bending or angular distortion directly from the plotted data.

3.7 METALLURGICAL INVESTIGATION

FSW has a significant effect on the local microstructure as discussed in section 2.3.4. As a result it is important to investigate the microstructural distribution and subsequently the post weld mechanical properties across the weld-line as these are a result of the local microstructure. Further, it is of significant interest for this dissertation whether the stress engineering techniques applied during or after FSW have any influence on microstructural evolution hence the mechanical properties. In the following sections the different techniques used to explore the post weld microstructure and the hardness variation are addressed in detail.

3.7.1 Microstructure

The microstructure of the test welds has been evaluated on the normal-transverse weld cross-section. Unless stated otherwise, an image should always be considered to be on this plane and the advancing weld side is on the right hand side. Examinations of the weld macrostructure, grain and partly the precipitation microstructure have been performed.

Small specimens were removed from the test welds using a *Buehler Isomet 4000*™ linear precision saw as illustrated in Figure 3.10a and Figure 3.10b. The cutting was performed at low cutting speeds with excessive coolant to avoid microstructural changes due to elevated temperatures. The specimens were removed from the middle of the weld

path length where steady state welding conditions may be assumed. However, in cases where additional samples were removed (for example for a_0 examination) the precise position may vary slightly.

For metallurgical examination the samples were prepared using SiC (silicon carbide) grinding followed by progressively finer diamond polishing down to 1 µm using a *Buehler Phoenix 4000*™ rotary polishing machine. The process was completed by colloidal silica polishing the surfaces for approximately 10 min. In order to make the microstructure visible several chemical etching steps were performed as detailed in the following sections.

3.7.1.1 Optical microscopy

The macrostructure was revealed by etching the sample surface using Weck's reagent (Attallah et al. 2007), a two stage etchant, consisting of solution A (2 g NaOH (sodium hydroxide), 100 ml H_2O and solution B (100 ml H_2O, 4 g $KMnO_4$ (potassium permanganate), 1 g NaOH)) in which the sample is immersed for approximately 20-50 sec and 10-15 sec respectively. Applying Weck's reagent reveals the weld macro structure and grain structure by attacking the grain boundaries in the first stage, while the second stage colours the etched material. Macrographs of the specimens were taken by high resolution photography, while optical microscopy using a *Leica 4000DM*™ microscope was performed to examine the macrostructure as well as the grain size (to the extent possible) and microstructure respectively at selected points within the WN, the TMAZ, HAZ and PM.

3.7.1.2 Scanning electron microscopy

Keller's reagent (ASM_9 2001), consisting of 2 ml HF (hydrogen fluoride, 48 %), 3ml HCl (hydrogen chloride, conc.), 5 ml HNO_3 (nitric acid, conc.) and 190 ml H_2O, was used to reveal the microstructure for scanning electron microscopy (SEM). SEM observations using a Philips XL30 field emission gun-scanning electron microscope (FEG-SEM) in backscatter mode at 20 kV and a working distance of 10 mm were made on selected samples covering the weld region to observe the precipitate microstructure in the WN of welds that were as welded and stress engineered.

3.7.2 Hardness

Test samples for hardness investigations were extracted in the N-T plane from approximately the mid-length of the original weld covering the cross weld region to both sides of the weld into the neighbouring PM. The specimens were prepared in a similar manner as for the microstructural investigations. The specimens were cut using a *Buehler Isomet 4000*™ linear precision saw at low cutting speeds with excessive cooling to avoid changes in the microstructure and therefore hardness profile due to elevated temperatures.

Hardness measurements were performed as a function of distance from the weld-line as well as from the weld surface, whereby the spatial resolution was increased around the weld area (unless stated otherwise the typical step size was 1 mm) to precisely determine the gradients in the hardness profile. The Vickers micro-hardness was measured with a *Buehler MicroMet® 5101*™ hardness tester applying a test load of 4.55 N (500 g) and an indentation time of 10 sec. The resulting indents were ~70 μm^2 (180 HV_{500g}) to 100 μm^2 (80 HV_{500g}) in size.

3.8 SUMMARY

In this chapter the experimental details regarding the test weld production with the applied stress engineering techniques, the general and detailed diffraction instrument set-ups as used for ADND and EDXRD for determination of RS are described. Further, practical approaches for the determination of the unstrained unit cell parameter a_0 are detailed and along with that, a new serial robotic arm based sample manipulation system as developed for the $\sin^2\psi$ method is introduced. Finally, the techniques used to determine the weld distortion, microstructure and post weld hardness distribution are described in detail.

The results obtained using these techniques and methods for determination of the effect of ISGMT as well as ISRT and PWRT are presented in the following chapters.

4 ASPECTS FOR THE DETERMINATION OF RESIDUAL STRESS

4.1 INTRODUCTION

In this dissertation the effects of three mechanical stress engineering techniques for mitigation of tensile welding residual stress (RS) and component distortion in friction stir welds, namely in-situ global mechanical tensioning (ISGMT), in-situ roller tensioning (ISRT) and post weld roller tensioning (PWRT) have been investigated. In this dissertation these techniques are applied to high strength aluminium alloy plates joined by friction stir welding (FSW). Determination of the RS and distortion as a function of the applied stress engineering technique allows for evaluation of each technique and to determine the assets and drawbacks. However, the assessment of RS is not trivial. While the application of non-destructive diffraction methods using neutron or synchrotron X-ray radiation is well established, several difficulties may arise during the determination of RS based on these methods.

Using non-destructive diffraction techniques (see section 3.3) it is vital not only to determine the strained unit cell parameter a, but also the local elastically unstrained unit cell parameter a_0, in order to allow for the calculation of the actual residual strain and hence stress present in the component. This is especially the case in weldments made in high strength aluminium alloys. Here a significant variation of the unstrained unit cell parameter a_0 as a function of relative position to the weld-line occurs as a result of the varying precipitation microstructure due to the experienced thermal cycle during FSW (Leonard 2000; Dumont *et al.* 2006; Kamp *et al.* 2006; Steuwer *et al.* 2007). As reviewed in section 2.6.6.3, several techniques exist for the determination of the a_0 distribution (Hauk 1997; Santisteban *et al.* 2002; Withers *et al.* 2007). However, to the authors' knowledge to date no comparative study of these methods in a single test piece has been reported.

As a result, in this dissertation an investigation evaluating three methods was performed with the aim to identify the method best suited for the determination of the RS in the test welds subject to this dissertation. In the first section of this chapter the experimental details and results of this investigation are presented and discussed along with their relative merits.

A further unknown quantity when using non-destructive diffraction methods is the extent of stress relaxation, as a function of the component size. In order to obtain stress

results that are representative of RS present in real size welded structures, it is necessary to use test welds of a certain minimum size. In test welds that are too small the RS may not develop to their full magnitude. On the other hand, in test welds that are reduced in size for for example better handling, the RS may relax (Masubuchi 1980). As a result it is essential to investigate the effect of the test weld size on the RS magnitude in order evaluate to what extent the RS determined in the test welds are representative of those that are present in full size welded structures. Subsequently, this allows estimating the reasonable industrial applicability of each stress engineering technique. In this dissertation the effect of the test weld size on the longitudinal RS distribution has been determined in five test welds. The experimental details and the RS results of this fundamental study are presented in the second section of this chapter and discussed in the light of their relevance for the research performed in this dissertation.

4.2 MAPPING THE ELASTICALLY UNSTRAINED UNIT CELL PARAMETER

4.2.1 Introduction

Energy dispersive synchrotron X-ray diffraction (EDXRD) and angular dispersive neutron diffraction (ADND) as discussed in section 2.6.3 and 2.6.4 are powerful tools for non-destructive determination of residual strains and stresses in bulk engineering components. The techniques have been used for investigations into many engineering problems for example the determination of RS in high strength aluminium alloys joined by FSW (Webster *et al.* 2001a; Sutton *et al.* 2002; Withers *et al.* 2002; Peel *et al.* 2003; Reynolds *et al.* 2003; Staron *et al.* 2004; Mishra *et al.* 2005; Threadgill *et al.* 2009). Fundamental to these techniques is the accurate determination of the unit cell parameter a within a defined gauge volume and the locally corresponding value for the unstrained condition, the elastically unstrained unit cell parameter a_0. Based on knowledge of these two parameters, the strain is calculated using equation 2.6.

In high strength aluminium alloys, which obtain much of their strength by a fine dispersion of precipitates forming during a highly controlled heat treatment (see section 2.2) a sudden local heat input for example by FSW will modify the precipitation in a complex way. As discussed in section 2.6.6.3, this can be accompanied by an inhomogeneous change in the solute concentration, resulting in a significant local variation

of the elastically unstrained unit cell parameter a_0 (compare Figure 2.37) as a function of position relative to the weld-line (Barret *et al.* 1980; Leonard 2000; Dumont *et al.* 2006; Kamp *et al.* 2006; Steuwer *et al.* 2007; Withers *et al.* 2007). Consequently, in weldments in high strength aluminium alloys it is important to determine the local value for a_0 in order to allow for determination of the RS present in the component.

Several diffraction based techniques are available to determine the elastically unstrained unit cell parameter a_0 (Hauk 1997; Santisteban *et al.* 2002; Withers *et al.* 2007); each with its own benefits and difficulties as discussed in section 2.6.6.3. Although these techniques have all been used before, to the authors' knowledge no direct comparison of the techniques in a systematic manner has been reported in the literature. In this section the results of a series of investigations into the spatial variation of a_0 across the weld-line in two test welds using the plane-stress assumption, the comb and the $\sin^2\psi$ methods (see section 2.6.6.3) are presented. The advantage of using more than one method allows determination of a_0 more accurately, but may also help identifying advantages and disadvantages of each technique. The experimentally obtained results are compared and the different methods evaluated and discussed along with their relative merits for this dissertation. Further, the observations are complemented by hardness profiles measured in the N-T plane across the weld-line. This is a useful tool as the unstrained unit cell parameter a_0 as well as the hardness are affected by the size and distribution of strengthening precipitate and may be assumed to correlate with respect to spatial variations (Dumont *et al.* 2006; Steuwer *et al.* 2007).

4.2.2 Experimental details

For the comparative evaluation of the plane-stress assumption, the comb and the $\sin^2\psi$ methods for the determination of a_0, two test welds, namely #3B29 and #2B0 (see section 3.2.1) produced in the age-hardening high strength aluminium alloy AA7449-W51 were used. The former test weld was comparatively thick (12.2 mm) and as a result in this case the assumption of a plane-stress situation may be in-valid, but for comparison in this investigation this method is taken into consideration. The comb and the $\sin^2\psi$ methods were also applied to this weld. All measurements in this weld were performed 8 to 12 months after production. In the second test weld the plane-stress assumption is more likely to be

valid as this weld was only 5 mm thick. For comparison the comb method was applied. Measurements in this weld were performed approximately 2 months after production.

While the theoretical background of each method is described in section 2.6.6.3, the practical application using EDXRD on ID15A and ADND on SALSA is addressed in section 3.3.4. Table 4.1 provides an overview of the instruments and hence techniques used for each method in this comparative study.

Method / Sample	plane-stress assumption			comb	$\sin^2\psi$
	longitudinal	transverse	normal		
#3B29	ID15A	ID15A	ID15A	ID15A	ID15A
#2B0	ID15A	ID15A	SALSA	ID15A	-

Table 4.1: Overview of the instruments used for determination of the variation of the unstrained unit cell parameter a_0. On ID15A EDXRD and on SALSA ADND was used.

The *plane-stress assumption method,* as detailed in section 2.6.6.3, requires knowledge of the unit cell parameter a in three plate directions. For this method in both test welds the longitudinal, a_L, and the transverse unit cell parameter, a_T, were measured directly on the ID15A beam-line with the test welds orientated to the incident (S_0) and diffracted beam (S_1) as depicted in Figure 4.1a.

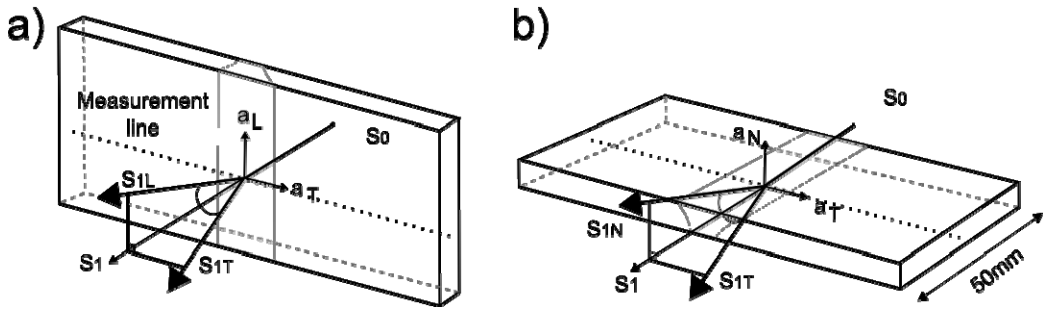

Figure 4.1. Using two detectors in the ID15A EDXRD set-up positioned such that the scattering vectors are orthogonal to each other, allows the determination of the strain in all three plate directions in only two scans by rotating the sample by 90° around the transverse axis.

Using ID15A, the unit cell parameter in the normal direction, a_N, can only be measured if the sample is short enough in the longitudinal direction to allow for the X-ray beam to penetrate along the plate length as depicted in Figure 4.1b. As part of this dissertation an investigation into the relaxation of the RS as a result of sectioning the test welds (see section 4.3) was performed. Within this study the test weld #3B29 was sectioned to a length l=50 mm (see section 4.3.3) thus with the sample orientated as depicted in Figure 4.1b

allowing for the X-ray beam to penetrate through the remaining sample length hence the measurement of a_N. The measurements in each direction were performed at identical lateral positions from the weld-line to allow for calculation of a local value for a_0 using equation 2.15. On the other hand, in test weld #2B0, which was not reduced in size, a_N was measured on the SALSA beam-line in reflection mode (compare Figure 3.7c and Figure 3.7d). The obtained d_{N311} lattice spacing was converted into a_N values using equation 2.7.

The *comb method,* as detailed in section 2.6.6.3, was applied to test specimens removed from both test welds. The samples were produced as described in section 3.3.4.2 with the #3B29 reference comb being $3\times100\times12.2\,mm^3$ ($l\times w\times t_m$, see Figure 3.10) and the #2B0 reference comb $3\times80\times5\,mm^3$ in size. The teeth in both combs are 1 mm apart over a region of 50 and 20 mm from the weld-line respectively in order to cover the weld area with sufficient spatial resolution. Further teeth were cut into the PM. The macroscopic stresses in the regions of the cutting were assumed to have relaxed completely. With the teeth of the combs pointing upwards and with respect to the original coordinate system (compare Figure 1.1) a was measured in the plate transverse and normal direction using the EDXRD technique on ID15A. While, in the #2B0 comb a single line scan at 2.5 mm below the weld surface was performed, in the #3B29 comb a 2-D map of the variation of a_0 as a function of lateral distance from the weld-line and depth below the weld surface was generated. Subsequently, a_0 was determined by taking the average of a_T and a_N in order to overcome possible differences in the detector calibrations.

The *$sin^2\psi$ method,* as detailed in section 2.6.6.3, was used to determine the variation of a_0 in the #3B29 test weld. The test specimen was essentially identical in size to that used for the comb specimen prior to machining the teeth with the longitudinal macroscopic RS assumed to be fully relaxed resulting in a biaxial in-plane stress field. The sample manipulation was performed using the robotic arm based sample manipulation system (see section 3.4) as this method requires sample rotations around two axes at each measurement location. In the current case 8 inclinations from ψ=0 to 64 ° (c.f. at 0 ° the scattering vector lies in the plane of the sample) for both directions $\varphi_{N=0^\circ}$ around ψ_N and for $\varphi_{T=90^\circ}$ around ψ_T respectively as schematically depicted in Figure 3.11 were used. Measurements were performed using the EDXRD technique on ID15A and at identical positions as with the comb method to allow for direct comparison of the strain results. However, fewer points

were measured due to the increased measurement time required for each measurement location. Finally, the quality of the linear fit on the *a vs.* $sin^2\psi$ plot acts as a measure of the validity of the measurement since shear stresses, grain size or texture effects may result in deviations from the expected linear behaviour (Cullity 1978).

In order to simplify comparison of the results of the different methods, a_0 was converted into pseudo strain using equation 2.6 and the average a_0 in the PM has been set to zero pseudo-strain (the zero value is the average of the unstrained unit cell parameter a_0 taken from material further than 50 and 20 mm from the weld-line for test welds #3B29 and #2B0 respectively). The pseudo-strain (Cullity 1978) is equal to the elastic strain that would have been wrongly inferred to exist if a global value rather than the correct local strain free unit cell parameter would have been used for the strain calculation. The advantage of plotting the strain is that results from different instruments and experiments can be compared directly, while the absolute values for a or a_0 may vary as a result of varying instrument and detector calibrations. To complement the results hardness measurements in the N-T cross-section of each weld were performed as described in section 3.7.2.

4.2.3 Results and Discussion

4.2.3.1 The unstrained unit cell parameter

Figure 4.2 compares the pseudo-strain shift determined by the three techniques at mid-thickness (6 mm from the weld surface) in the 12.2 mm thick test weld #3B29. For evaluation of the spatial distribution of the data a macrograph of the N-T cross-section is included in the figure. The results across the weld-line from each method were broadly symmetrical, hence only the advancing side is shown, and to a maximum distance of 50 mm, as further away no significant changes were observed. The lateral variation of the unstrained unit cell parameter a_0 at 6 mm below the weld surface corresponds well to the locations of the specific FSW weld zones as defined by Dumont *et. al* (Dumont *et al.* 2006).

As discussed in section 2.6.6.3, in general the lateral variation of the unstrained unit cell parameter a_0 may be attributed to the varying amount of the main alloying elements in solution. In the case of the AA7449-W51 alloy, these are Zn, Mg and Cu. The local

variation is a result of the dissolution, growth and coarsening of GP zones, as well as meta-stable and stable η'- and η-precipitates consisting of these elements due to the weld thermal cycle during FSW (see section 2.3).

In the current case the profiles of the unstrained unit cell parameter a_0, as shown in Figure 4.2, were obtained using the plane stress assumption, the comb as well as the $\sin^2\psi$ methods and exhibit a number of common features:

- a constant value in the PM (with an approximate point-to-point strain scatter of $\pm 50 * 10^{-6}$),
- a substantial decrease in a_0, beginning at ~30 mm and reaching a minimum at ~12 mm from the weld-line in the HAZ and
- a subsequent increase closer to weld (TMAZ), which reaches a plateau at ~4 mm from the weld-line (WN).

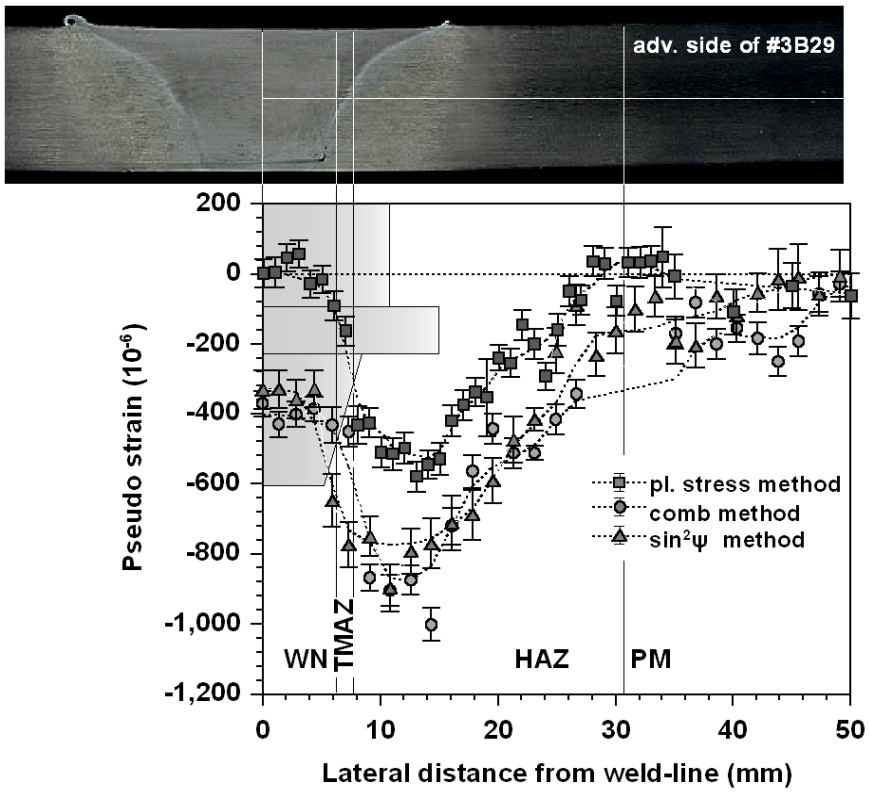

Figure 4.2: Comparison of the unstrained lattice parameter 6 mm below the weld surface set to zero strain shift in the PM in test weld #3B29 (12.2mm AA7449 W51). The data were obtained using the plane-stress assumption, the comb and the $\sin^2\psi$ method. The approximate positions of different FSW zones are marked and compared to the macrostructure of the weld. A cross-section of the FSW tool is depicted.

The primary difference between the results obtained by the various methods lies in the values of both the HAZ and WN plateau magnitude. In general, the difference between the results obtained by the plane-stress assumption method and those obtained by the comb and $\sin^2\psi$ method is ~300∗10^{-6} in the HAZ and ~350∗10^{-6} in the WN zone. The plane-stress assumption method suggests a lateral variation of a_0 of ~-500∗10^{-6} (expressed in pseudo strain) and in the WN the parameter returns to the PM value forming a plateau. On the other hand, the data obtained with the comb and $\sin^2\psi$ methods are in very close agreement with each other at 6 mm below the weld surface, as shown in Figure 4.2, as well as over the entire cross-section as shown in the 2-D maps depicted in Figure 4.3. These two methods suggest lower values for both, the HAZ minima (~-750 to ~-900∗10^{-6}) and the weld-line plateau (~-350∗10^{-6}) compared to the PM values. However, the plots of all methods tend to increase or decrease at identical locations thus displaying one and the same trend. This indicates that the differences in the results are due to systematic errors rather than random ones, which could occur since the different methods sample different amounts of material.

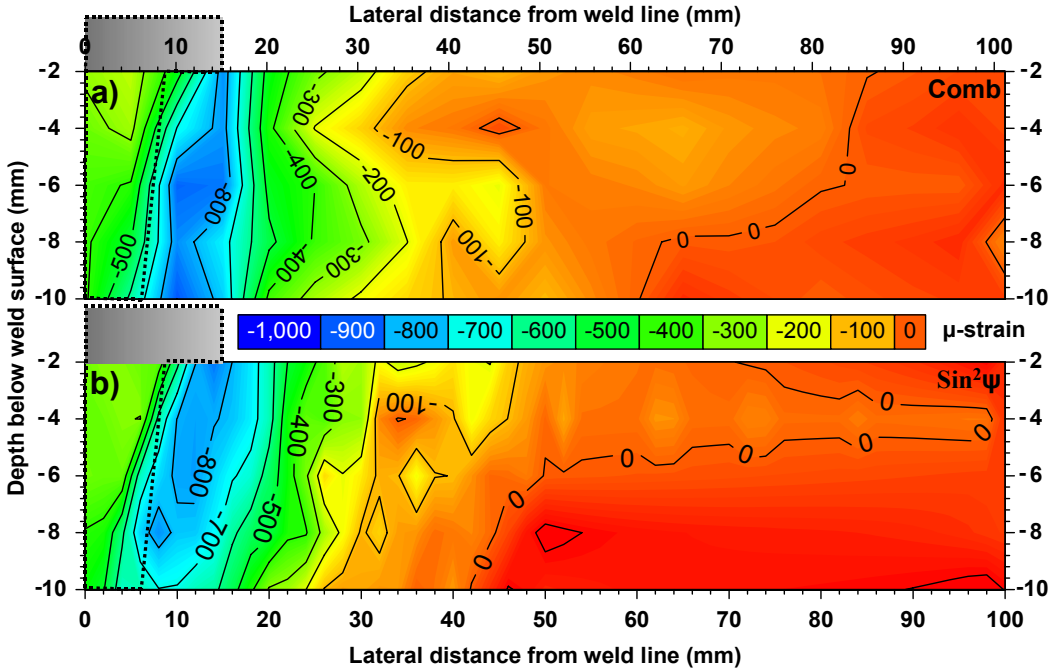

Figure 4.3: Comparison of the 2-D maps of the unstrained unit cell parameter a_0 in the 12.2 mm thick #3B29 test weld as obtained using (a) the comb and (b) the $\sin^2\psi$ method. The cross-section of the FSW tool is outlined.

The variation between the results of the plane-stress assumption method and the comb and $\sin^2\psi$ methods in the 12.2 mm thick weld may be attributed to the fact that the

assumption of a bi-axial stress condition is invalid for this particular test weld. As a result, the data obtained from the plane stress assumption methods must be considered as inaccurate. Consequently, it is useful to compare these techniques in the thinner #2B0 weld.

In the 5 mm thin #2B0 test weld the comb and plane-stress assumption methods were employed to determine the variation of a_0. The results are shown in Figure 4.4. The data obtained are qualitatively and quantitatively in very good agreement indicating, that in this thin weld a near bi-axial stress condition is likely to exist. In addition, the good match of the data proves the accuracy of the comb method. In this sample there was a significant variation of the a_0 value in the WN between the advancing and retreating side and therefore the profile is plotted over the entire weld area, but restricted to ±40 mm from the weld-line as no noteworthy changes occurred further away. Even though the weld is made from the same material (AA7449-W51), the a_0 profile is different from that observed in the 12.2 mm thick weld. The profile does not display an increase in lattice parameter in the WN plateau compared to the lower level in the HAZ. In detail it remains at the HAZ strain minimum of ~-300 to -400∗10^{-6}, while an upper limit is observed on the retreating and a lower one on the advancing weld side. This variation between the two weld sides may be due to the asymmetric character of the FSW process. Presumably, the traverse speed of 400 mm/min in combination with the high rotation speed of 800 rpm introduces more heat on the advancing weld side causing higher temperatures thus leading to more alloying elements being in solution and as such reduces the a_0 value even more.

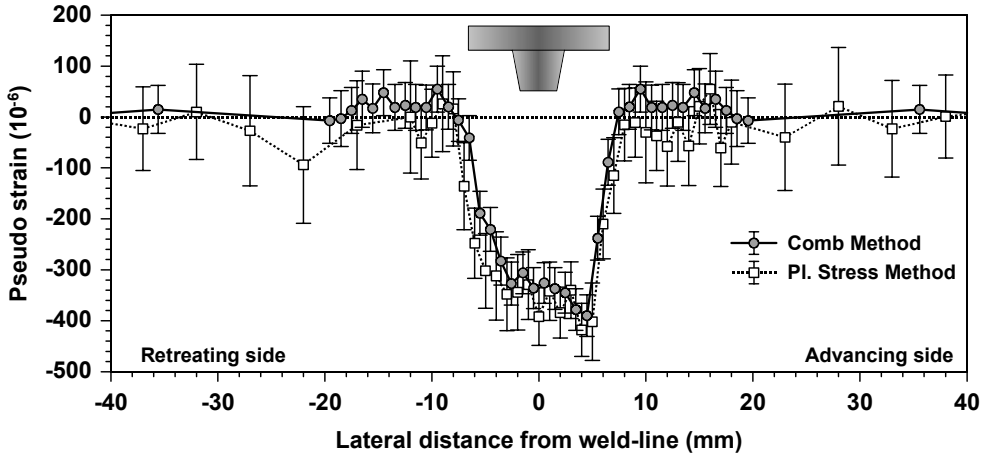

Figure 4.4: The variation of the unstrained unit cell parameter a_0 expressed in pseudo strain as obtained using the comb and the plane-stress assumption methods for the 5 mm AA7449-W51 test weld #2B0. The FSW tool cross-section is also shown.

Comparison of the strain difference between WN and PM of the 12.2 mm and 5 mm thick welds, both produced in AA7449-W51, shows the same value of ~-400∗10^{-6} even though they were joined under different FSW conditions. This similarity indicates that the temperatures under the FSW tool are similar and high enough in order to dissolve all initial strengthening particles. The subsequent formation of new precipitates and the natural aging upon cooling affect the local chemical composition in similar ways in both welds.

4.2.3.2 The hardness variation

The hardness in high strength aluminium alloys, such as the AA2xxx and AA7xxx alloys, is dominated by the strengthening effect of the precipitates forming (Polmear 1995). As a result, measurements of the hardness can be a good indication whether or not a variation of a_0 is present in weldments of high strength aluminium alloys as has been shown by Dumont *et al.* (2006) and Steuwer *et al.* (2007). However, this does not necessarily mean that a simple correlation between the hardness and the unstrained unit cell parameter exists.

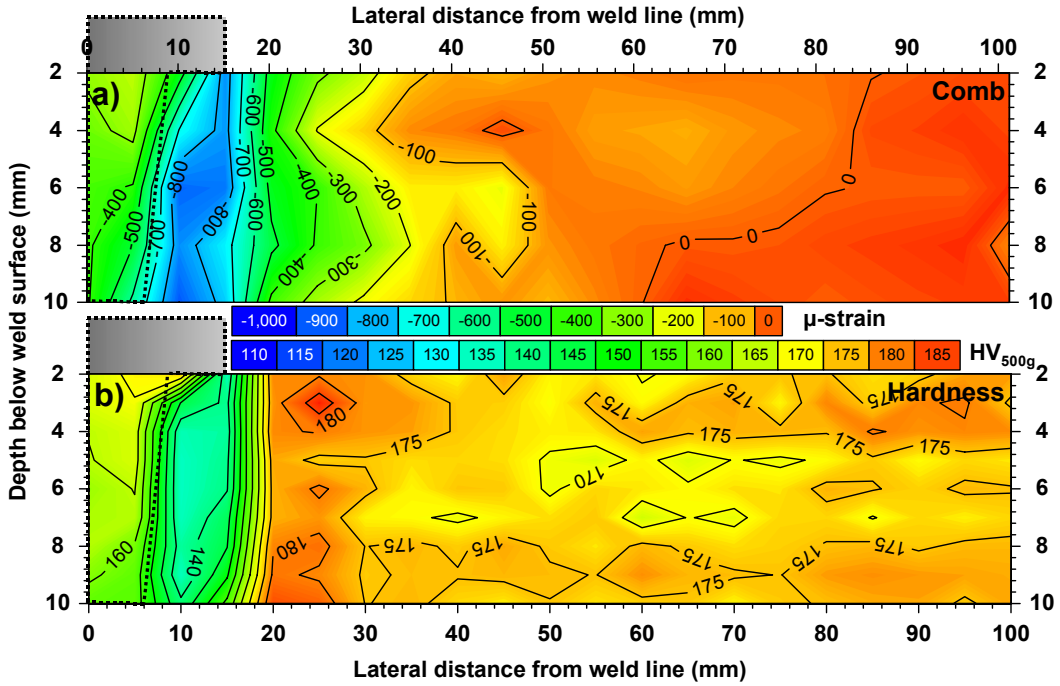

Figure 4.5: 2-D contour plots of the variation of (a) the unstrained unit cell parameter a_0 expressed in µ-strain compared to (b) the Vickers hardness (HV_{500g}) both as a function of distance from the weld-line and weld surface in sample #3B29. The outline of the FSW tool cross-section is included.

The a_0 strain map as obtained using the comb method and a hardness map as measured on the N-T plane in the 12.2 mm thick #3B29 test weld are compared in Figure 4.5. It can be seen that for the most part there is a good qualitative match between the two properties, in terms of spatial variations of each property - especially the location of the minima in the HAZ and the intermediate plateau in the WN. The influence of the wide FSW tool shoulder on the weld surface and the cone shaped pin in the material is reflected in the narrowing of the WN zone towards the root of the weld. The hardness data appear to be most supportive of the a_0 data determined using the $\sin^2\psi$ and comb methods (see section 4.2.3.1).

The primary difference between the two plots occurs on the outer edge of the HAZ at around 20-25 mm from the weld-line. In this location the strain shift begins to decrease from the PM value towards the minima in the HAZ. In contrast, the hardness initially increases from its base value of ~175 HV_{500g} by around 10 HV_{500g} before decreasing in a similar manner towards the HAZ minimum of ~140 HV_{500g}. The same behaviour was observed by Dumont *et al.* (2006) and can be seen in Figure 2.9. They concluded that this is a result of the changes of the local precipitate microstructure. It appears that this difference is due to the initial temper of the material, which is in the naturally aged condition and as such has not reached the maximum strength. The moderate temperatures experienced in this region during welding (Tang *et al.* 1999; Chao *et al.* 2003) give the material, in effect, a brief second ageing treatment thus increasing the size of the strengthening precipitates and slightly increasing the hardness. This rapidly turns into an over-ageing treatment closer to the weld-line and the hardness decreases (Dumont *et al.* 2006).

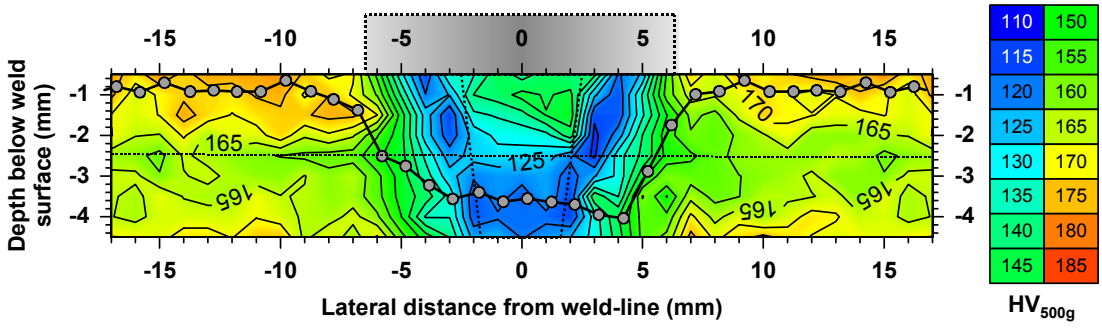

Figure 4.6: 2-D map of the hardness variation of the #2B0 test weld including the cross-section of the FSW tool. In addition the profile of the unstrained unit cell parameter a_0 as obtained at mid material thickness (line plot) is superimposed to illustrate the spatial correlation of both quantities.

On the other hand, the hardness map for the #2B0 weld as displayed in Figure 4.6 does not reveal an increase in hardness immediately outside the FSW tool shoulder. In this case,

the hardness decreases steadily towards the WN which is in accordance with the trend of the superimposed a_0 profile (line plot). Further, even the asymmetry between retreating and advancing side as observed in the a_0 profile can be seen in the hardness plot at mid plate thickness. This indicates a strong correlation between the hardness and the unstrained unit cell parameter a_0. However, the unstrained unit cell parameter a_0 is to some extent independent from the hardening effect as it is influenced only by the continuing migration of solute to the evolving precipitates. On the other hand, the local hardness rises and falls with increasing removal of solute and in addition depends on the size and distribution of the local precipitates.

From these results it can be taken that a local variation of the hardness indicates that a change in a_0 is likely. As a result, it is necessary to determine this spatial variation in order to allow for the accurate determination of the RS present in the component.

4.2.3.3 The effect of a_0 on the calculation of RS

The shift in the unstrained unit cell parameter a_0 as a function of distance from the weld-line and weld surface is substantial in both test welds and has a considerable effect on the strain and subsequent RS determination as depicted in Figure 4.7. In the figure the RS profiles for test weld #3B29, one determined with the locally varying a_0 and one with a constant global a_0 value, are shown.

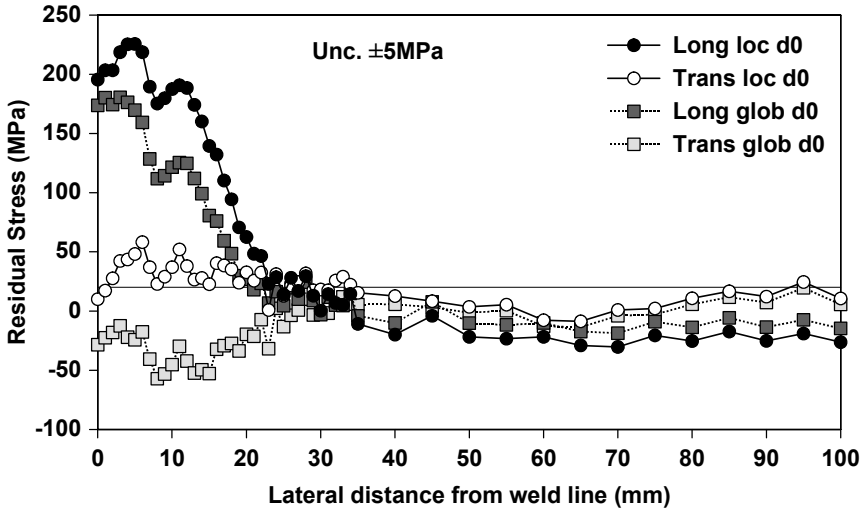

Figure 4.7: Comparison of the RS distribution in test weld #3B29 as determined with a locally varying and a constant global a_0 value at 6 mm below the weld surface. Significant differences in the RS amplitude as well as the width of the tensile zone occur.

Up to ~70 MPa (~0.12 σ_{YS}) higher longitudinal RS are derived using the varying a_0 (obtained with the comb and $\sin^2\psi$ methods) rather than a constant global a_0. Also the transverse RS show significant variations. Applying the local a_0 results in low tensile RS of ~40 MPa, but a global a_0 leads to low compressive RS of ~-40 MPa. Further, the tensile region appears to be narrower when a global a_0 is applied.

The differing RS profiles arise from the fact that with a global a_0 no profile variation is introduced. In the current case, using a locally varying a_0, superimposes an additional profile as shown in Figure 4.2, thus changing the lateral distribution of the strained unit cell parameter profile and consequently the RS profile. From this observation it can be concluded that it is of significant importance for the stress determination in this dissertation to quantify whether or not the unstrained unit cell parameter a_0 varies as a function of lateral distance from the weld-line as well as from the weld surface.

4.2.4 Conclusions

The results obtained in this comparative study allow for the following conclusions:

- All three techniques for the determination of the unstrained unit cell parameter a_0 in the investigated AA7449 friction stir welds resulted in the same trend. A decrease from the PM towards the WN with a minimum in the HAZ and an intermediate magnitude in the WN was observed. This change of a_0 may be attributed to a varying precipitate microstructure as a result of the local thermal cycle experienced during FSW leading to a varying amount of the alloying elements being in solution, which in turn alters the value of a_0.
- While the comb and $\sin^2\psi$ methods display nearly identical results with a higher variation of a_0 in a 12.2 mm thick weld, the plane stress assumption method displays less difference between the PM, the HAZ and the WN. This is believed to be due to the fact that the assumption of a biaxial stress state in a 12.2 mm thick weld is simply not valid.
- The results obtained using the plane stress assumption and the comb method in a 5 mm thin weld show nearly identical results. This indicates that the comb method is a reliable technique independently of the material thickness, while the plane stress assumption method is very sensitive to this parameter.

- The plane stress assumption method for determination of a local a_0 can be applied directly provided the diffraction technique in use allows measurement of the strain in the plate normal direction (for example neutron diffraction). The comb method requires significant effort for the sample preparation, but can be used with both synchrotron X-ray and neutron diffraction. The $\sin^2\psi$ method requires less sample preparation than the comb method, but the sample manipulation requires sophisticated hard- and software to allow for easy and fast application independent of the diffraction technique in use.
- Both, the hardness and the unstrained unit cell parameter a_0 are a function of the precipitation distribution. While the former also depends on the size and distribution of the precipitates, the latter is a function solely of the amount of alloying elements remaining in solution. However, the results obtained by comparing both quantities shows, that a correlation with respect to the local variation exists. As a result a variation in hardness can be taken as a good indicator for a varying a_0 parameter.
- The effect of applying a constant global as well as the real local a_0 parameter on the subsequent residual strain and stress magnitude for the investigated case was found to be most significant in the HAZ and the WN. In the current case, the application of a constant value for a_0 leads to ~$0.12\sigma_{YS}$ lower RS in the WN and HAZ than if the real local value for the unstrained condition was used. Eventually this may lead to significant underestimation of the effect of the RS on the life time performance of the component.
- As a result of the current study for the investigation of the effectiveness of the mechanical stress engineering techniques, in this dissertation the comb method is used for determination of a_0 in all test welds.

The results from this study indicate the importance of the right choice of method for determination of the local unstrained unit cell parameter for the subsequent strain and stress calculation. However, another source of possible underestimation of the RS present in a welded structure is related to its size. An investigative study into the effect of stress relaxation as a function of the sample size is presented in the following section.

4.3 RESIDUAL STRESS RELAXATION vs. SAMPLE SIZE

4.3.1 Introduction

As described in section 2.6.6.4 RS in sectioned test welds may not be representative of those existing in full size engineering components as the initial stresses may have relaxed due to material removal. This is also true for test welds produced in small plates because there may not be enough restraining material to allow for welding RS to develop to the same level as in full scale components (Masubuchi 1980). As a consequence, some general guidelines are required when excising samples in order to estimate the severity of the stress relaxation effect on the magnitude of welding RS.

The experimental investigation presented in this section aims to determine the RS relaxation behaviour in butt welded plates, due to progressive reduction of the test weld length l as well as width w. The aim is to determine the minimum weld dimensions that should remain in order to maintain RS comparable to those present in real size welded structures and which may, therefore, be considered as representative. The results of this study thus allow an evaluation of the representative character of the RS measured in the test welds, compared to those present in full size components produced in the same material under identical welding conditions.

4.3.2 State of the Art

It is well known that RS redistribute and tend to relax when material is removed (Masubuchi 1980; Kou 2003). In fact the hole drilling and contour methods (Peyrac *et al.* 1996; Prime *et al.* 2000) for determination of the RS rely on this phenomenon. As with these techniques restraining material is removed, the initial RS relax by deforming the material at the new free surface. Measurement of this deformation allows for back-calculation of the initial RS. On the other hand, using diffraction techniques to investigate the RS distribution in test welds is to some extent limited by the maximum sample size, as some diffraction instruments may have restricted space only. In many cases the test welds are too long or cumbersome to be investigated in their entirety, hence smaller cross-weld test-pieces need to be cut out in order to determine the RS. Consequently, the magnitude of the partially relaxed RS is a function the size of the sectioned test-piece. If not accounted for this may lead to the RS determined being significantly less in magnitude than those in

the original component. As a result the effect of RS on the component life cycle performance may be seriously underestimated.

As discussed in section 2.6.6.4, cutting butt welds to reduce the plate length, or width, leads to partial relaxation of the longitudinal RS and a redistribution of the stress field to maintain self-equilibrium (Masubuchi 1980). For a fixed point this redistribution will depend on its distance from the cutting region. The relaxation will tend to zero at large separations as described qualitatively by St. Venant's Principle for a static load on the free end of a beam (Timoshenko *et al.* 1987). Toupin (1965) provided a mathematical interpretation of this Principle for the stored elastic energy *U(s)* per unit volume in a cylindrical beam of length *l* at a distance *s* from the end:

$$U(s) \leq U(0)\exp-\left(\frac{s-l}{s_c(l)}\right) \qquad \textbf{Equation 4.1}$$

where the *U(0)* is the total stored energy and the dimensionless decay length constant $s_c(l)$ depends upon the elastic properties of the material. This equation reflects the fact that the effect of self-equilibrating RS decays exponentially over a distance. As detailed in section 2.6.6.4, St. Venant referred to the extent of notable relaxation as the '*characteristic distance*' (Timoshenko *et al.* 1987), while Toupin (1965) referred to the '*characteristic cross-section dimension'*. However these dimensions have not been quantitatively defined in the context of thin plate butt welds. For this dissertation some of the test welds were removed from larger plates (set #4 and #5) and as such it is important to quantify the extent of stress relaxation in order to validate the significance of the RS results obtained in this work.

4.3.3 Experimental details

In order to establish general guidelines for the estimation of stress relaxation, the degree of longitudinal RS relaxation is quantified systematically upon cutting butt welded plates in the longitudinal and transverse direction respectively. Four test welds (#1 - #4) produced in different geometries and with various welding techniques in different aluminium alloys as well as a structural steel were investigated. The aim was to examine the stress relaxation behaviour in specimens representing a wide variety of material and welding conditions. The welding details as well as the initial and intermediate weld

dimensions are shown in Table 4.2. While the friction stir welding samples were produced by Airbus UK in Filton Bristol, UK, on a *Crawford Swift Powerstir 360*® machine, the remaining steel welds were produced at the Welding Engineering Research Centre at the Cranfield University as part of the SEALS program (see chapter 1).

The welds were progressively sectioned to shorter and shorter lengths by cutting of the ends maintaining the measurement line at the mid-length of the test weld as shown in Figure 4.8a. The longitudinal and transverse RS distribution was determined for each intermediate length *l*. Further, one test weld (#5) was reduced in its width *w* in order to determine possible effects arising form plate narrowing. The width was reduced by removing material from both sides, keeping the weld-line centred as depicted in Figure 4.8d. In each case the cutting was performed using a common band saw with sufficient cooling and at a low feed rate in order to minimize possible arising cutting stresses that may influence the remaining RS field.

#	**Technique / Material**	**Details**	**Orig. dimensions**	**Intermediate dimensions**
#1 (#3B29)	FSW / AA7449-W51	80 kN down-force, 225 rpm, 250 mm/min, Tri-flate™, shoulder Ø 30mm, threaded pin Ø 17 mm and 11.7mm length	1000×300×12 mm^3, weld path length 800 mm	**Lengths:** 1000, 800, 400, 200, 100 and 50 mm
#2	FSW / AA2098	8 kN down-force, 1200 rpm, 500 mm/min, shoulder Ø 13 mm, tapered pin Ø 4.91 mm and 3 mm length,	880×300×3 mm^3, weld path length 880 mm	**Lengths:** 880, 800, 400, 200, 100 and 50 mm
#3	Hybrid Laser-MIG / S355	2.5 m/min, 4 kW laser power (27 V, 185 A), 11.43 m/min wire feed, 16 mm CTDW, 2 mm laser-arc distance, ar+20%CO_2+2%O_2 shielding gas, 15 l/min gas flow rate	500×400×4 mm^3, weld path length 500 mm	**Lengths:** 500, 400, 300, 200, 100, 70 and 40 mm
#4	Pulsed MIG / S355	0.42 mm/min, 30.7 V, 193 A, 8.61 wire feed, 13 mm CTDW, Ar+20%CO_2+2%O_2 shielding gas, 16 l/min gas flow rate	500×400×4 mm^3, weld path length 500 mm	**Lengths:** 500, 400, 300, 200, 100, 70 and 40 mm
#5	Pulsed MIG / S355	0.63 mm/min, 37.8 V, 220A, 11.5 wire feed, 13 mm CTDW, Ar+20%CO_2+2%O_2 shielding gas, 16 l/min gas flow rate	500×400×4 mm^3, weld path length 500 mm	**Widths:** 400, 300, 200, 140, 100 and 60 mm

Table 4.2: Welding details for the butt welds investigated and the sectional lengths and widths.

Using the EDXRD technique on the ID15A beam-line (see section 3.3.3), the longitudinal and transverse RS were determined along the measurement line at mid material thickness. After measuring the initial RS distribution, the test weld length or width was progressively shortened.

To account for possible variations of the unstrained unit cell parameter a_0 in test weld #1 (this is test weld #3B29 (see section 3.2.1), the results from the comb method (see section 4.2) were used. In the test welds #2, #3 and #4, the normal strain was measured after cutting the welds to the shortest length with the sample being orientated as illustrated in Figure 4.8c. These welds are comparatively thin (3 – 4 mm) and as shown in section 4.2 it is valid to assume a plane-stress situation, thus allowing calculation of a local value for the unstrained condition using equation 2.15.

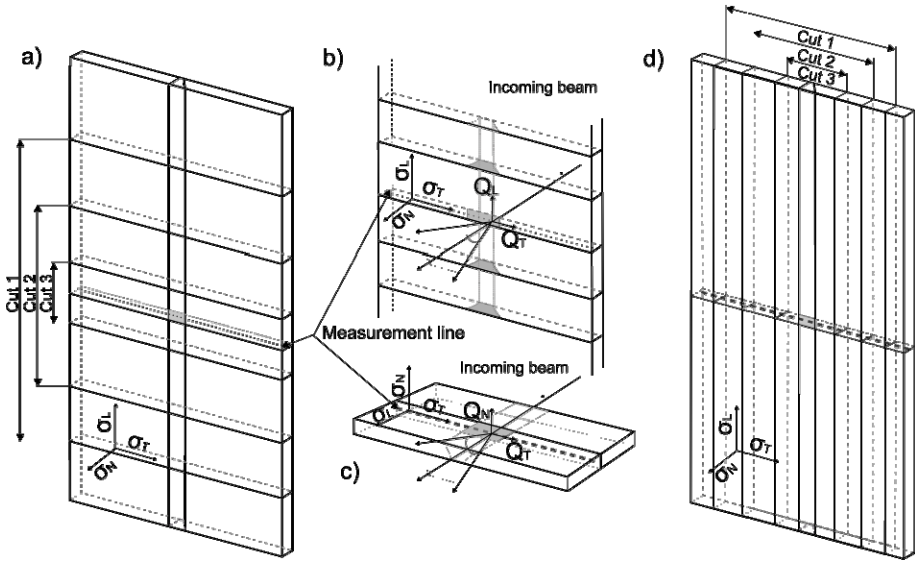

Figure 4.8: Illustration showing (a) the progressive reduction in test-piece length keeping the measurement line at mid-length. The sample orientation relative to the incident beam S_0 for the measurement of the longitudinal and transverse strain is shown in (b) while (c) illustrates the sample orientation for the measurement of the normal strain at the final weld length. All measurements were performed on ID15A using the EDXRD set-up. Graph d) illustrates the progressive reduction in test-piece width.

Test weld #5 was reduced in width rather then length, hence deriving the a_0 variation as in test welds #2 to #4 was not possible. As a consequence of this and due to time restrictions for this dissertation a constant global a_0 was assumed for the RS calculation. Consequently, the RS presented for this test weld are not representative of the actual stresses. However, in each case the effect of the material removal and the resulting stress relaxation can be observed independently whether or not the 'real' unstrained unit cell parameter a_0 is applied for the strain and hence stress calculation. On the other hand, in order to derive the correlation for stress relaxation as a function of test piece size knowledge of the real RS present in the test welds is required.

4.3.4 Results and Discussion

4.3.4.1 Stress relaxation due to longitudinal shortening

Figure 4.9 shows the longitudinal RS distribution determined using the EDXRD set-up on ID15A for all test welds as they were progressively cut to shorter lengths. The profiles are characteristic of butt welds with large tensile RS close to the weld-line balanced by low compressive RS in the unaffected PM, as described by Masubuchi (1980). For clarity only the RS in the region around the weld-line are shown, as no noteworthy changes in RS were observed further away.

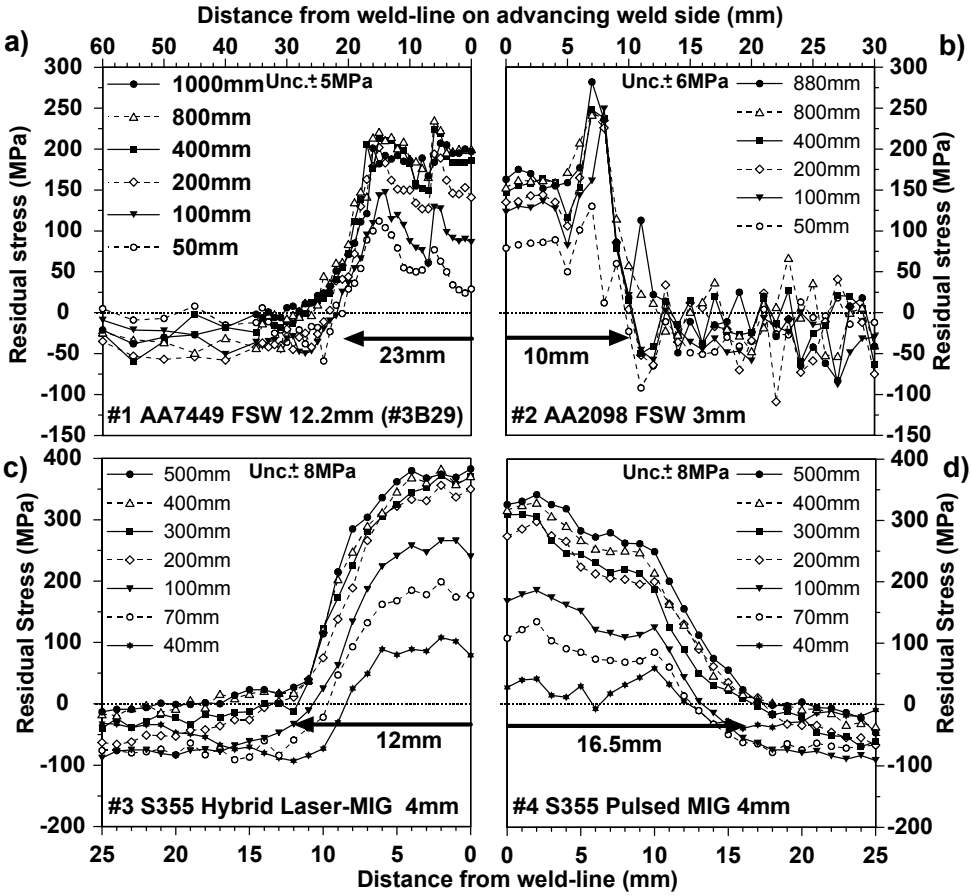

Figure 4.9: Longitudinal RS distributions of (a) weld #1, a FSW in AA7449-W51 (#3B29), (b) weld #2, a FSW in AA2098; (c) weld #3, a hybrid laser-MIG weld in the steel S355 and (d) weld #4, a pulsed MIG weld in S355 as progressively sectioned. The approximate half width of the tensile zone, $\frac{1}{2}w_t$, is shown for each sample. Though not clear from these central sections the RS do balance over the entire plate widths.

The form of the RS distribution naturally depends on the welding technique, but such details are beyond the scope of this investigation. Upon progressive sectioning the

longitudinal RS start decreasing significantly once the test weld is shortened to a certain length. On the other hand, the transverse RS do not display any effect upon cutting and are therefore not shown here. Further, the width of the tensile peak, w_t, as indicated by the horizontal arrows in Figure 4.9 decreases for shorter weld lengths although this effect is weak for the plates joined by FSW.

For simplicity in the following the degree of stress relaxation will be described solely in terms of the average longitudinal RS present in the area ±3 mm from the weld-line, while any changes in the stress distribution are neglected. The normalized weld-line RS for each sample as a function of normalized plate length are shown in Figure 4.10 (markers). As noted previously, the RS are largely unaffected by material removal until a critical fraction of the weld length has been removed. Beyond this point the RS reduction follows an exponential decrease which can be described by a simple empirical parametric equation:

$$\sigma = \sigma_0 \left[1 - \exp\left(- \frac{\left(l - l_{relax} \right)}{l_{char}} \right) \right] \qquad \textbf{Equation 4.2}$$

where σ is the longitudinal weld-line RS for the current weld length l, σ_0 is the RS in a long (strictly infinite) weld, l_{relax} is the test-piece length at which there is essentially zero macroscopic RS and l_{char} is the characteristic length. It should be noted from the form of equation 4.2 that the expression is an essentially elastic relation in that the relaxed stress is linearly related to the initial stress. In this respect it might be anticipated that for most thin plate welds the cutting does not introduce significant plastic deformation.

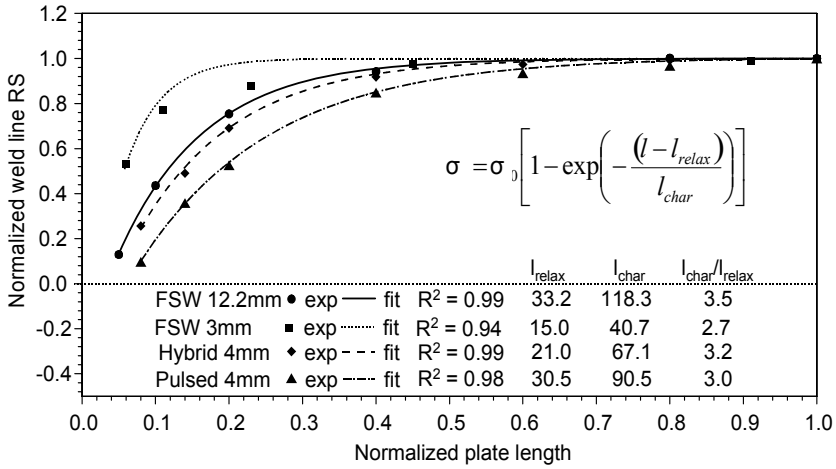

Figure 4.10: RS at the weld-line normalized by the initial (long weld) value vs. normalized plate length. Markers represent the measured data, lines represent the best non-linear fits achieved using equation 4.2 with the parameters given in the figure.

The characteristic length l_{char} may be reasonably compared to the '*characteristic distance'* of St. Venant's Principle (i.e. stresses in a given location are unaffected by changes in loading if such changes occur beyond this distance from the area being measured (Toupin 1965; Timoshenko *et al.* 1987; Ugural *et al.* 1994; Berdichevsky *et al.* 2003)). In the current case l_{char} and l_{relax} were determined by non-linear fitting to the measured weld-line RS data. For instance fitting the stress data determined in test weld #4 (4 mm thick S355 pulsed-MIG weld) gives values of 90 and 30 mm for l_{char} and l_{relax} respectively with a high quality of fit. That the RS approaches zero at l_{relax} (0.06 = 30/500 in normalized units) is evident in Figure 4.10. An overview of the fit parameters for each weld is given in Figure 4.10. It is noteworthy that in all welds l_{relax} corresponds closely to the width of the tensile peak w_t (compare Figure 4.9); perhaps indicating that at this length the tensile region is no longer constrained to a meaningful degree by the surrounding material. On the other hand, empirical evidence suggests that l_{char} is approximately three times w_t (Figure 4.10), although the reason for this is not clear at the present time. From these observations equation 4.2 may be simplified by taking $l_{relax}=w_t$ and $l_{char}=3\times w_t$:

$$\sigma = \sigma_0 \left[1 - \exp\left(\frac{1}{3}\left(1 - \frac{l}{w_t} \right) \right) \right] \qquad \textbf{Equation 4.3}$$

This simplification reduces the number of variables and has the advantage that the remaining variable, w_t, can be determined directly from the RS distribution plot in the uncut weld. This means that the level of stress relaxation can be estimated without the need to cut up a trial weld and measure the RS. Using equation 4.3 and the w_t values obtained from the unrelaxed RS distributions as shown in Figure 4.10 the stress relaxation was calculated for each weld and the results are shown in Figure 4.11 and compared to the experimental data.

The good agreement with equation 4.3 supports the hypothesis that the characteristic and relaxation lengths are both proportional to the width of the tensile region for these welds. It also means that the data can all be collapsed onto a single relaxation line using equation 4.3 when the weld length is normalized by the width of the stress peak w_t rather than the original weld length (l_o). This is shown in Figure 4.12.

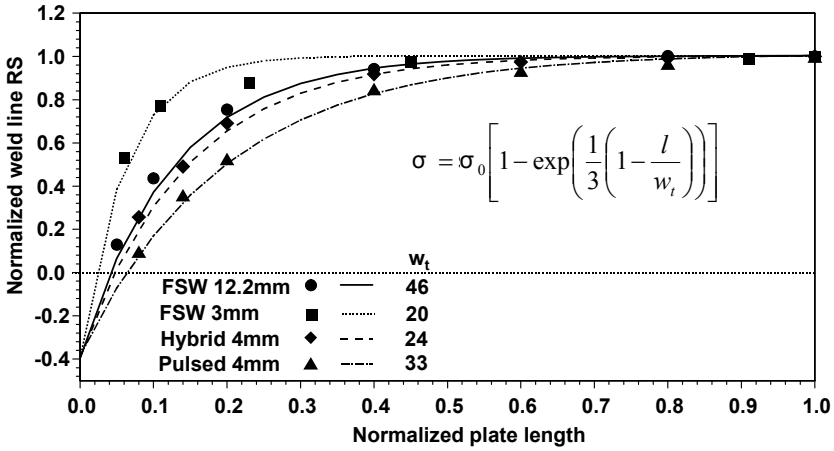

Figure 4.11: The measured RS (markers) as a function of weld length (normalized to the stress and length in the original (long) weld) compared to the empirical relation described by equation 4.3 (lines) using the measured width of the stress peak, w_t, as taken from the RS distribution plots in Figure 4.9.

The excellent agreement evident in Figure 4.12 suggests that it is possible to predict the amount of stress relaxation occurring in a test weld on cutting to a given length, as long as w_t is known or can be estimated. For FSW, for example, w_t appears to be largely determined by the diameter of the tool shoulder $ø_t$ (see Figure 2.2). In the two friction stir welds investigated w_t is approximately $1.5\times ø_t$. The literature reveals that this value does change somewhat as a function of alloy type, tool speeds and the down force applied (Peel *et al.* 2003; Steuwer *et al.* 2006b). Nevertheless a value for w_t determined from the shoulder dimensions does provide a good indicator of the likely relaxation levels and suggests a guideline figure for the minimum size of test weld if little relaxation is required.

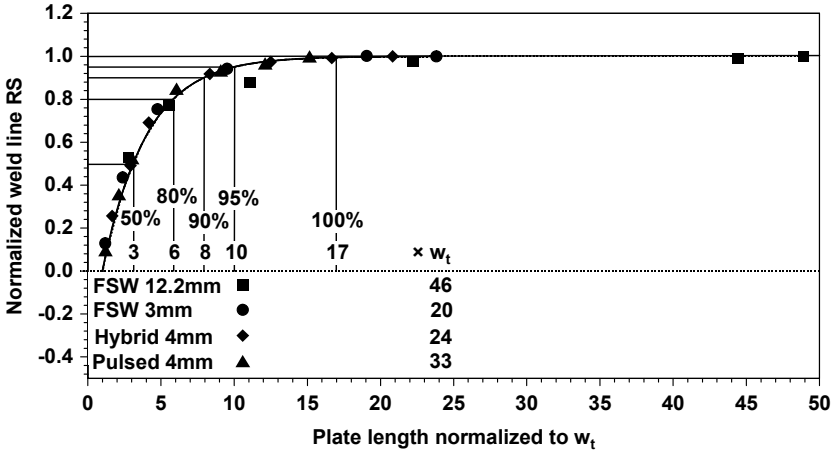

Figure 4.12: The experimental data normalized by the long (strictly infinite) weld stress, σ_0, and the w_t value for each weld compared to the empirical mother curve described by equation 4.3 describing the stress relaxation behaviour upon progressive sectioning.

From Figure 4.12 it can be seen that relaxation is less than 10 % if the retained section of the weld is eight times longer than the tensile peak is wide. Thus, equation 4.3 permits an evaluation of the minimum length of a weld retained for a cross-weld sample to have negligible stress relaxation compared to the original weld. Conversely, it is possible, if undertaken carefully, to infer the unrelaxed RS level for a long (infinite) weld on the basis of measurements made on shorter sections. However, care must be taken when choosing the value for w_t since, as noted above, this varies slightly as the retained weld-length decreases (Figure 4.9). Finally, in cases where cross-weld tests are used to extract mechanical performance metrics (Mahoney *et al.* 1998; Peel *et al.* 2003; Sutton *et al.* 2004) it may be desirable to remove the effects of RS. In such a case it would be beneficial to choose a test-piece length less than the lateral width of the tensile zone w_t so that macroscopic RS are negligible.

4.3.4.2 Stress relaxation due to transverse narrowing

The magnitude of the longitudinal tensile RS might be expected to fall as the width of the plate containing the weld decreases. This is of concern because in many trials relatively narrow test plates are used, either for convenience or economy. In other cases narrow regions must be cut out of wider welded plates or structures for the purposes of evaluation.

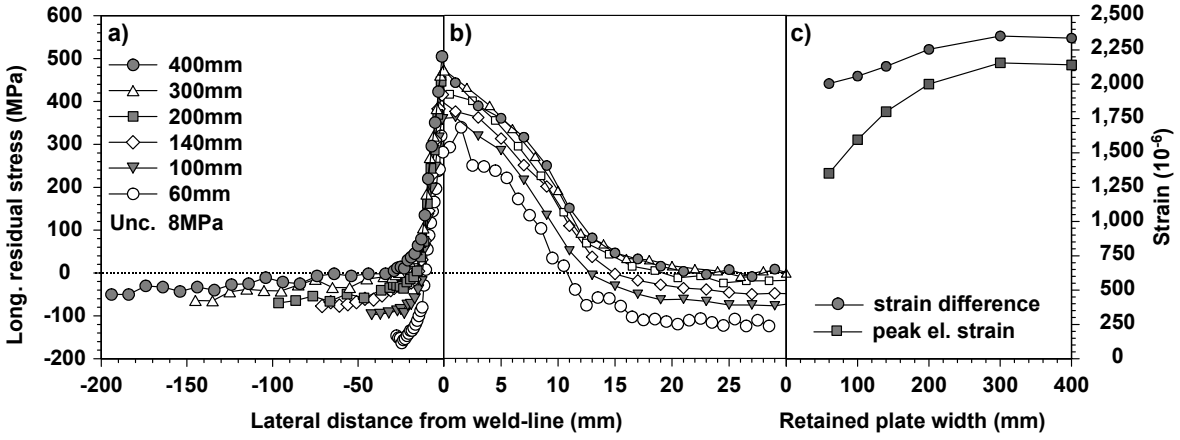

Figure 4.13: Longitudinal RS distribution across the N-T cross-section for test weld #5 as a function of retained plate width. In (a) the stress profile across one half of the plate is shown, (b) displays a close-up of the stress profile local to the weld-line, while (c) plots the variation in the peak elastic strain (squares) with retained plate width alongside the difference in elastic strain between the centre and the edges of the plate (circles).

The extent of RS relaxation with decreasing plate width has been evaluated for test weld #5 and the results are summarized in Figure 4.13. The longitudinal RS decrease due to stress redistribution occurring so as to maintain stress balance within the plate, while the transverse RS are low and largely unaffected by progressive narrowing of the plate and therefore not shown. It is evident that while the shape of the longitudinal stress profile remains essentially constant as the plate is reduced in width, the profile begins to shift downwards when the plate becomes less than 300 mm wide. In fact, the weld-line RS (averaged over ±3 mm of the peak centre) falls from around ~480 to ~300 MPa as the width is reduced step-wise from 300 to 60 mm and the elastic strain decreases from $2{,}150\times10^{-6}$ to $1{,}300\times10^{-6}$ (Figure 4.13c).

All residual stresses arise from an elastic accommodation of stress-free misfit (Withers *et al.* 2001b); in this case between the near weld region which is longitudinally too small, and the parent plate further from the weld that is relatively longer. RS can normally be relaxed either by reducing the misfit itself, or by lessening the constraint offered by the surrounding material. In the current case, the misfit can be reduced by plastic deformation of the weld or PM, while the constraint is clearly reduced by narrowing the width of the plate. Figure 4.13c shows the difference in elastic strain between the edge and the centre of the plate, which for a long weld is essentially equal to the stress-free misfit between weld and PM. For an infinitely wide plate all the misfit would be accommodated elastically in the weld region because of the large extent of the restraining PM. When the plate is 400 mm wide the difference in longitudinal elastic strain between the parent and the weld is $\sim2{,}300\times10^{-6}$ with ~90 % accommodated in the weld. As the width of the restraining PM is reduced the misfit is accommodated increasingly by compressive strain in the base metal. When the plate is 60 mm wide the misfit strain is accommodated approximately 40 % : 60% so that parent plate experiences a compressive strain of approximately -700×10^{-6} (-150 MPa) and the weld $1{,}300\times10^{-6}$ (300 MPa). As a result the misfit is approximately 2000×10^{-6} as shown in Figure 4.13c. In other words, the stress-free misfit is decreased by only $\sim300\times10^{-6}$ by the cutting procedure, indicating that the stresses have been relieved primarily elastically rather than by plastic deformation.

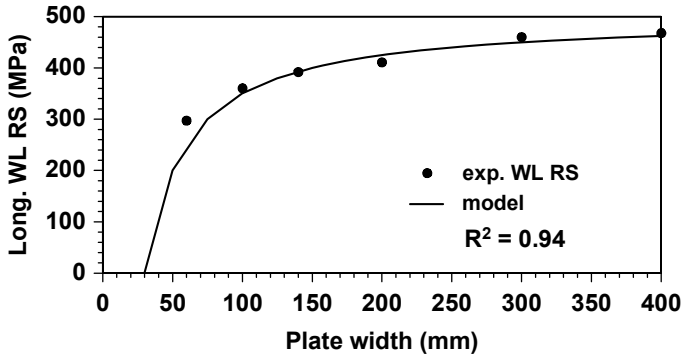

Figure 4.14: Longitudinal peak stress as measured (symbols) and as predicted (line) on the basis of the 400 mm data using equation 4.4 for weld #5 as a function of retained plate width.

Assuming a stress balance and simple downward shifting of the peak longitudinal RS σ, as the plate width w narrows, the remnant RS can be inferred by applying stress balance to the tensile (w_t) and compressive (w-w_t) regions from the initial peak RS σ_o, that would arise in an infinitely wide plate, by using a simple parametric equation:

$$\sigma = \sigma_0 * \left(1 - \frac{w_t}{w}\right) \qquad \textbf{Equation 4.4}$$

where w_t again is the width of the tensile stress peak as defined earlier from the RS profile. In the current case one can infer from equation 4.4 that the stress in an infinite plate, σ_o of ~500 MPa and 33 mm for w_t, a value very close to that of the actual width of the stress peak in Figure 4.13b, result in a stress relaxation curve that fits the experimental data well as shown in Figure 4.14. From these results it can be concluded that equation 4.4 reflects the longitudinal stress reduction behaviour for progressive reduction of the width of a welded plate surprisingly well. However, further work is required for validation of this equation.

4.3.5 Conclusions

In this part of this dissertation the extent of elastic relaxation of RS in thin welded plates that are progressively cut-down to form test-pieces of shorter and shorter length, or narrower width was studied. With regard to a reduction in retained weld length for cross-weld samples, the relaxation behaviour for welds produced in different materials and with different welding methods was found to collapse onto a single empirical relaxation curve

using just the width of the stress peak w_t as a governing parameter in a simple exponential equation. From this equation the minimum length of test-pieces needed when making stress measurements to maintain the RS at 90 % of its unrelaxed value was found to be eight times the stress peak width. For shorter test-pieces the relation could be used to back-calculate the unrelaxed stress state that would arise for a long weld. As a consequence, in order to attain a maximum (100 %) steady state welding RS the weld length should be some seventeen times as long as the tensile zone is wide neglecting start-up and stop issues. Conversely, if the length of the weld in the test-piece is approximately equal to the width of the longitudinal stress peak then the RS are likely to be almost completely relaxed in the mid-length of the test-piece. While the utility of this relationship has been investigated for a range of butt welds in thin plates, further work needs to be conducted to investigate whether this relation is also applicable to thicker welds. In this respect it should be borne in mind that thick welds can have high multi-axial stresses which may introduce plastic deformation on cutting or out-of-plane bending that may complicate the analysis.

With regard to the reduction of the width of the welded plate, the largest longitudinal tensile stresses would be expected in a plate of infinite width. It has been shown that narrowing the plate width reduces the maximum longitudinal tensile stresses in the weld-line primarily by shifting the overall profile downwards in order to establish a balancing compressive stress in the PM. The shape of the stress profile is maintained. In this case, the redistribution in order to achieve stress balance as the constraining effect of the PM is reduced is essentially achieved elastically with relatively little reduction in the stored misfit strain. Again a simple analytical equation based on stress balance for the derivation of the fall in peak tensile longitudinal RS was established allowing those stresses that would arise in a wide plate to be calculated from measurements of a narrow one. This effect should also be borne in mind when welding narrow plates to assess RS. By contrast to the longitudinal stresses the transverse RS were not affected, neither when reducing the length nor the width of the test welds.

Finally, to simplify the application of the stress relaxation relation as determined in this investigation it would be worth to extend future work to determine possible relations of the geometry (for example width) of the weld hardness profile or the macrostructure. In case similar relations can be defined it would significantly simplify the determination of the minimum weld size for stress determination purposes.

Set	#1 AA2199-T8E74 5mm	#2 AA7449-W51 5mm	#3 AA7449-W51 12.2mm	#4 AA7449-W51 20mm	#5 AA2024-T3 5mm	#6 AA2199-T8E74 5mm	#7 AA7136-T6 7mm
w_t (mm)	20	18	42	60	21	19	30
$l_{90\%} = 8 \times w_t$ (mm)	160	144	336	480	168	152	240
$l_{100\%} = 17 \times w_t$ (mm)	340	306	714	1020	357	323	510
l_{actual} (mm)	1000	515	1000	450	500	500	1000
Status	Ok	Ok	Ok	Too short	Ok	Ok	Ok

Table 4.3: Evaluation of the test weld length with respect to the RS relaxation that may occur if the test weld is not sufficiently long. Except for test welds from set #4 all test welds were long enough in order to represent RS as they may occur in real size engineering components under the given FSW conditions.

With respect to this dissertation the aim of current research was to allow for evaluation whether the dimensions of the test welds in question are sufficient in size in order for the RS determined in the plates to be representative of those present in real size engineering components. This may be irrelevant for the determination of the effect of the stress engineering techniques (see chapter 5 and 6) as the stress mitigation achieved is always compared to the as-welded condition and as such it is not required for the RS to be representative. However, this dissertation is part of the SEALS project (see section 1.1) and therefore it is of significant importance for the participating industrial partners to obtain RS results that represent those in full size engineering components. As a result it is vital to be able to evaluate the stress results determined in the test welds. In Table 4.3 the required length of the test welds in order to remain 90 and 100 % of the original RS magnitude is determined from the width w_t of the tensile zone as obtained at material mid thickness from of the RS distribution plots presented in section 5.3.4 and 6.3. As shown in Table 4.3 the test welds in all sets except for set #4, are long enough such that the RS determined can be considered to be representative of those present in real size components. As the stress relaxation behaviour was investigated in thin (3 to 12.2 mm) test welds only, no firm conclusion about set #4 can be drawn as this is 20 mm thick and as such the stress redistribution upon cutting may differ from that in thin welds.

4.4 SUMMARY

In this chapter the experimental results of two fundamental studies, namely a comparative investigation of three techniques for the determination of the unstrained unit cell parameter a_0 and one into the stress relaxation behaviour in thin welds as a function of

retained weld length and width were presented. The former investigation aimed to identify the technique(s) best suited for the determination of the elastically unstrained unit cell parameter a_0 for the subsequent calculation of the residual strain and stress in the test welds of interest for this dissertation. The second investigation was performed in order to allow for evaluation in how far the RS results obtained in the test welds investigated are representative of those acting in real size welded components.

In summary the following results were obtained:

- The investigated methods for determination of the elastically unstrained unit cell parameter a_0 can be used depending on the stress condition present in the test weld.
- While the plane stress assumption method is well suited for thin (5 mm) material with a presumably biaxial stress field only, the comb and $\sin^2\psi$ method can be applied for any weld geometry containing bi - or triaxial stress fields. However, these two techniques require intensive sample preparation (cutting thin specimen and small teeth) and in case of the $\sin^2\psi$ method complex sample manipulation techniques. On the other hand, the plane stress assumption method may require the use of an instrument that allows measurement of three orthogonal directions (for example SALSA) or by cutting down the weld length one can measure the normal strain on a beam-line like ID15A in case the beam energy is high enough to penetrate the remaining material length.
- As a consequence of the results obtained in this study and depending on the instruments available for this dissertation the determination of a_0 was performed using the plane stress assumption method in thin welds only while the comb method was applied in thin and thick welds.
- In welds in high strength aluminium alloys the variation of a_0 correlates spatially with the hardness distribution, which is technically easy to obtain and as such can be taken as an indicator for the variation of a_0.
- RS may seriously be underestimated if the variation of a_0 is not accounted for.
- In thin welded plates stress relaxation as a function of the weld size can significantly affect the magnitude of the longitudinal RS.
- With regard to a reduction in retained weld length for cross-weld samples, the relaxation behaviour of the longitudinal RS in welds produced in different

materials and with different welding methods was found to collapse onto a single relaxation curve. This behaviour can be described using just the width of the stress peak, w_t, as the governing parameter in the simple exponential equation 4.3.

- From this equation the minimum length of test-pieces needed to maintain the RS at 90 % of its unrelaxed value was found to be eight times w_t while in order to attain the maximum steady state welding RS the weld length should be some seventeen times as long as the tensile zone is wide.
- With regard to narrowing the width of the welded plate a reduction of the maximum longitudinal tensile stresses in the weld-line essentially by shifting the overall profile downwards in order to establish a balancing compressive stress in the parent material was observed, while the stress profile shape is maintained. The redistribution in order to achieve stress balance is accompanied by relatively little reduction in the stored misfit.
- A simple exponential equation (equation 4.4) for the derivation of the fall in peak tensile longitudinal stress was established allowing those RS that would arise in a wide plate to be calculated from measurements of a narrow one. However, as this equation is based on the results from one test weld only it can not be considered as valid for the general case.
- Regardless of the reduction in weld length or width the transverse RS were not observed to be affected.

With respect to the test welds investigated in this dissertation (see section 3.2.1 and 3.2.2 and chapter 5 and 6), all thin welds (≤ 12.2 mm) were found to be long enough in order to attain RS that are representative of those existing in real size components. The 20 mm thick test welds in set #4 are too short, but considering the fact that equation 4.3 is based on results obtained in significantly thinner welds, this remains arguable.

5 STRESS ENGINEERING BY GLOBAL MECHANICAL TENSIONING

In this chapter the effectiveness of in-situ global mechanical tensioning (ISGMT) for mitigation of the tensile longitudinal RS developing during FSW is investigated. The results of RS determination in four sets of test friction stir welds with different levels of ISGMT applied are presented and discussed. Along with the RS results, the plate bending and angular distortion, the weld microstructure and hardness distribution are investigated and the data presented and discussed along with their merits.

5.1 INTRODUCTION

ISGMT applied along the welding direction has been shown to significantly mitigate the longitudinal tensile RS around the weld-line as well as the plate distortion (Staron *et al.* 2004; Price *et al.* 2007; Richards *et al.* 2008a; Williams *et al.* 2008). The current state of the art is reviewed in detail in section 2.5.3.3. Even though there is a reasonable amount of research reported on ISGMT it appears that there is no general consensus on the precise correlation between the applied ISGMT, load and the resulting reduction of the RS. To date it is not clear what parameter or quantity defines the optimum ISGMT load required to mitigate the tensile weld-line RS to zero and minimize the weld bending and angular distortion. It is this question that the experimental research reported in this chapter aims to answer. In the following sections the results of the systematic experimental investigation of the effect of ISGMT on the RS distribution in high strength aluminium alloy friction stir welds are presented and put into context with the current knowledge on ISGMT.

5.2 EXPERIMENTAL DETAILS

In this dissertation four systematic sample sets consisting of three or four test welds in the high strength aluminium alloys AA2199-T8E74 and AA7449-W51, joined by FSW and subject to differing ISGMT loads, were investigated in terms of the mitigation of the RS as a function of the applied ISGMT load. The welding details, the varying ISGMT load levels applied during FSW and the corresponding test weld designations are given in Table 3.2. The angular dispersive neutron diffraction (ADND) and the energy dispersive synchrotron X-ray diffraction (EDXRD) techniques and the corresponding instruments SALSA and

ID15A used to determine the residual strain and hence the RS distribution as a function of the applied ISGMT load are detailed in section 3.3.2 and 3.3.3. The comb and plane stress assumption methods applied to obtain the local variation of the elastically unstrained unit cell parameter a_0 are detailed in section 3.3.4. The ISGMT technique was primarily applied to reduce the longitudinal tensile RS. However, it is also worth determining the effect of ISGMT on the plate distortion, as this phenomenon is closely related to the RS existing in the component. The technique used for this investigation is detailed in section 3.6. The tensile loading was applied during FSW and, as such, may influence the welding process itself. As a result, possible variations of the weld microstructure and the post weld properties such as the hardness may occur. These characteristics were investigated using the methods detailed in section 3.7.

5.3 RESULTS AND DISCUSSION

5.3.1 Microstructure

Microstructural characterisation of the effect of ISGMT applied to high strength aluminium alloys joined by FSW was performed using light microscopy (LM) as well as scanning electron microscopy (SEM), as detailed in section 3.7. Figure 5.1a shows the schematic outline of the N-T cross-section of the 20 mm thick AA7449-W51 test weld #4B0 (as-welded). Figure 5.1b and Figure 5.1c display the corresponding macrostructure of the as welded (#4B0) and with 198 MPa tensioned (#4B198) condition. The approximate positions where SEM micrographs, as depicted in Figure 5.2, were acquired are marked in the macrograph illustrations. Further, magnifications of the TMAZ on the weld retreating (d) and advancing side (e) are shown, as well as a close-up of the WN grain distribution, as observed ~8 mm below the weld surface (f) magnified 5 × and 50 × (g).

The macrographs are representative for the results in all investigated test welds and display the typical weld nugget (WN) shape correlating well with the FSW tool position and cross-section of the tool profile. On both sides of the WN the thermo-mechanically affected zone (TMAZ) can be observed and, according to the literature (James *et al.* 1999; Dumont *et al.* 2006), is somewhat indistinct and wide on the retreating (Figure 5.1d) but sharp and distinct on the weld advancing side (Figure 5.1e). The heat affected zone (HAZ) in between the TMAZ and the parent material (PM) manifests as a dark-grey region

following the thermal contours through the thickness: namely wide near the tool shoulder contracting towards the weld root. Further, in the WN one can observe to some extent the material flow pattern (Figure 5.1f) occurring during FSW. This appears as alternating bands of fine and coarse grains as depicted in Figure 5.1g). This is similar to the so-called onion ring structure reported in the literature (Rhodes *et al.* 1997; Krishnan 2002; Attallah *et al.* 2006).

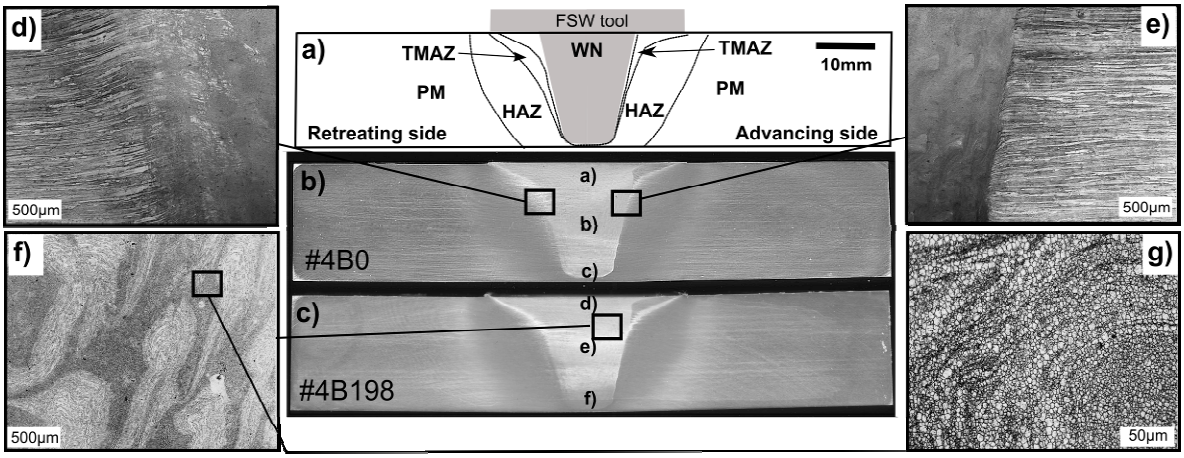

Figure 5.1: A schematic (a) of the weld cross-section as obtained from the macrographs shown in (b) for the as-welded (#4B0) and (c) 198 MPa tensioned (#4B198) test welds in 20 mm thick AA7449-W51 as produced using light microscopy. SEM micrograph positions according to Figure 5.2 are marked in b) and c). The WN is surrounded by a sharply formed TMAZ on the advancing side (e) and a more indefinite wider TMAZ on the retreating side (d), the HAZ manifests itself as the dark grey zone. Graphs f) and g) display the alternating bands of smaller and bigger grains displaying the material mixing patterns.

There is no evidence of macroscopic weld defects leading to the assumption that the FSW parameters have been adjusted properly for the production of the test welds in set #4. There was no obvious difference in the macrostructure of the test welds either in the WN, the TMAZ or HAZ as a result of the applied ISGMT leading to the assumption that ISGMT has no effect on the metallurgical changes occurring during the FSW process.

5.3.1.1 Grain size

Figure 5.2 compares the grain size distribution in the WN of the two test welds #4B0 and #4B198, as obtained using backscattered SEM. While graphs a-c display the grain size distribution of the as-welded test weld at 1, 10 and 18 mm below the weld surface respectively the illustrations in d), e) and f) illustrate the grain structure at identical positions for the tensioned test weld #4B198.

In agreement with the literature (Mahoney *et al.* 1998; Murr *et al.* 1998; Hassan *et al.* 2003; Mishra *et al.* 2005; Wei *et al.* 2007) the as-welded friction stir weld displays roughly equiaxed grains in the WN with 5-10 µm grain size near the weld surface (see Figure 5.2a) decreasing to below 1 µm near the weld root (see Figure 5.2c). Presumably, the thermal gradient through the weld thickness (Tang *et al.* 1999), either influencing the initial recrystallised grain size or simply altering the extent of post-weld grain growth, may be responsible for this variation. *Wei et al.* (2007) and Sato *et al.* (2002) reported increased grain size in the WN due to higher temperatures during welding as a result of higher FSW tool rotation speeds. This supports the assumption that the grains are bigger near the weld surface, where an essentially higher heat input and resulting higher temperatures act during welding (see section 4.1).

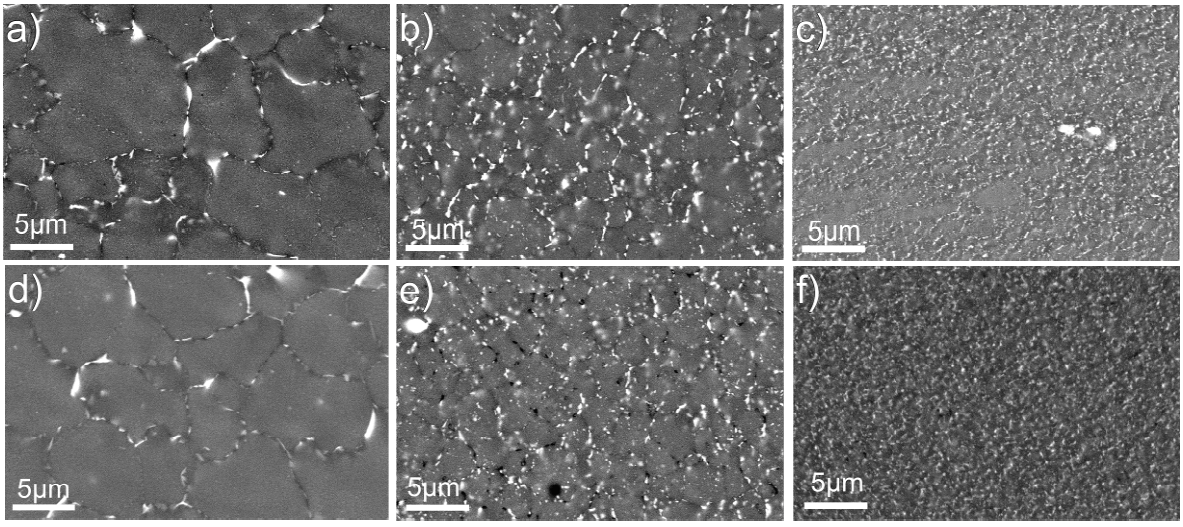

Figure 5.2: SEM (backscatter mode at 20 kV) micrographs in 20 mm thick AA7449-W51 test welds in the as-welded (test weld #4B0, a, b, c) and to 198 MPa tensioned (test weld #4B198, d, e, f) condition at the weld-line at 1 mm (a, d), 10 mm (b, e) and 18 mm (c, f) below the weld surface. The grain size decreases from 5-10 µm near the weld surface to < 1 µm at the weld root, grain boundary precipitates that were over-attacked by the etching appear as dark spots in Figure 4e.

Comparison of the grain size distribution for the as-welded condition #4B0 (Figure 5.2a-c) and tensioned weld #4B198 (Figure 5.2d-f) reveals no significant differences arising from the application of ISGMT. As a result one can again conclude that the ISGMT process has no effect on the FSW process itself in terms of microstructure evolution.

5.3.1.2 Weld Defects

Figure 5.3 displays light microscopy macrographs as taken in the N-T cross-section of the four AA7449-W51 test welds of set #3 that were subject to different ISGMT loads. As observed before (Figure 5.1) no obvious microstructural changes as a result of the increased ISGMT loads are apparent. However, compared with the test welds in set #4, the macrographs of these welds display tunnel defects on the weld advancing side near the weld root indicating that the FSW parameters require further adjustment to optimize the material consolidation (Leonard *et al.* 2003; Wei *et al.* 2007).

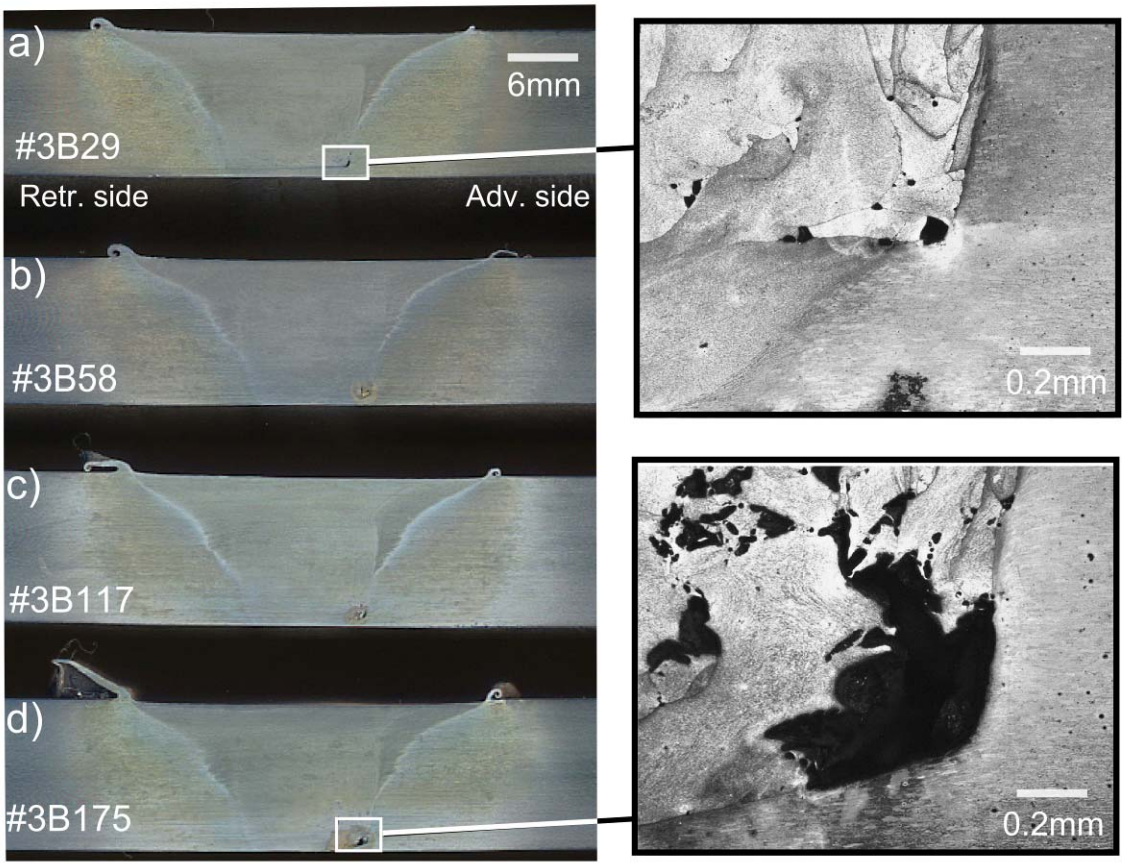

Figure 5.3: Macrographs of the test welds of set #3 produced with vary ISGMT loads of 29, 58, 117 and 175 MPa as indicated by the second number in the sample designation (see Table 3.2). No obvious effect on the macrostructure of the weld zone is apparent. The size of the tunnel defects near the weld root, as well as the amount of weld surface flash increase with increasing ISGMT loads.

It was reported that the application of increased ISGMT loads reduces the occurrence of weld defects in non optimized FSW set-ups (Price *et al.* 2007). This is not apparent in the current case. In fact, with increasing ISGMT loads the tunnel defects apparently enlarge and the amount of single defects increases, as can be observed comparing the magnified

inlays for Figure 5.3a and Figure 5.3d. However, as this occurred only on this set of test welds, no firm conclusion can be drawn and additional investigation is required.

In Figure 5.3a-d it can be observed that an increasing amount of flash on the weld surface on both sides of the weld-line with the significantly higher portion on the weld retreating side is produced with increased tensioning. Flash occurs as a result of the FSW tool down force exceeding the optimum value leading to the tool shoulder being pushed into the weld surface and squeezing softened surface material to each side of the weld, whereby the retreating side usually receives more flash (Wei *et al.* 2007). However, as the FSW conditions were identical for each test weld in set #3, it appears that increasing ISGMT results in higher down forces leading to the FSW tool shoulder being pushed into the material surface. This is supported by the fact that the observed tunnel defects in the test weld #3B175 (175 MPa ISGMT load) was found closer to the weld root as compared to that in the as-welded condition (see Figure 5.3a and d). On the other hand, it is unlikely that higher down forces were acting, as the welds were produced on a FSW machine in load control mode (see section 3.2.1) and as such a constant down force can be assumed. In fact, the load cell of the FSW machine is optimized for high down forces up to 100 kN. The welds in set #3 were produced with a programmed 80 kN down force and as such only minor absolute variations in down force may be expected. In addition, there is no reason why an increase of the ISGMT load in the plate longitudinal direction should increase the FSW tool down force in the plate normal direction.

On the other hand, it was observed that the plates were lifted off the backing plate once the ISGMT load was applied. This is due to a misalignment between the axes of loading and the plate mid thickness. The FSW tool pushes the abutting edges of the two plates back onto the backing plate during welding while the plate outer edges remain at the lift off height. This mechanism is also indicated by an increase in angular distortion as discussed in section 5.3.3. However, the lift-off causes the FSW tool shoulder to penetrate the material surface at the weld path edges more than at the weld-line itself due to the angle between the two plates. This may result in increased amounts of flash building up with higher tensioning loads. Further, the angle between the two abutting plates causes a gap at the weld root, which subsequently may result in an insufficient amount of material around the FSW tool pin at the weld root. Consequently, this may result in bigger defects (holes or tunnels) as it was observed in the current case and is shown in Figure 5.3.

5.3.2 Hardness

The hardness maps shown in Figure 5.4 were obtained using a Vickers hardness testing machine on the N-T cross-section of test welds #4B0 and #4B198. The maps are characteristic for friction stir welded age-hardening aluminium alloys and qualitatively representative for the investigated sets produced in AA7449-W51 (set #2 - #4) for this dissertation. In the plot of the as-welded test weld the cross-section of the FSW tool is included while in the #4B198 plot the different weld zones, as obtained from the macrographs depicted in Figure 5.1 are outlined. Even though the weld zone spreads over only ±25 mm from the weld-line, the hardness maps cover ±48 mm in order to allow for comparison with the unaffected PM.

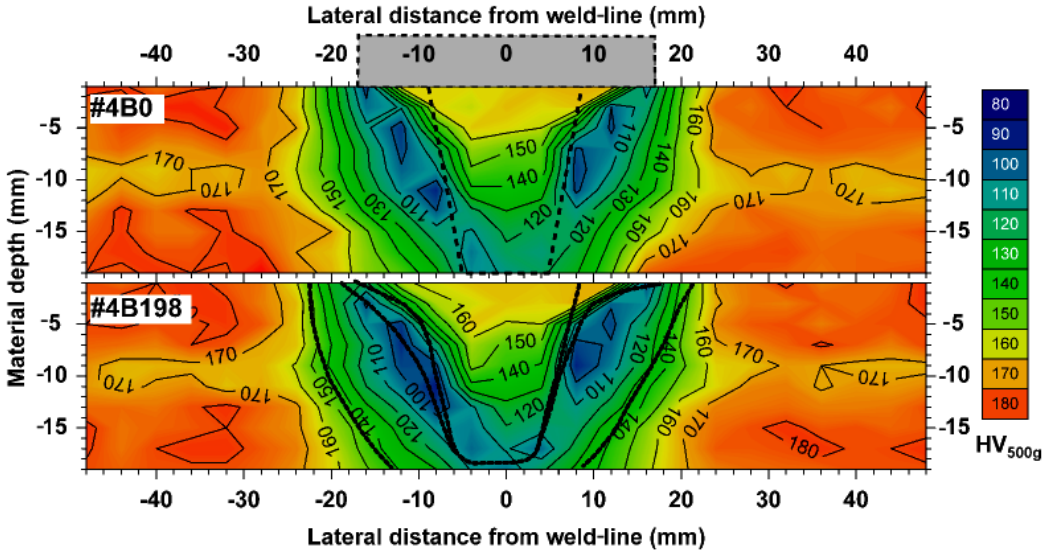

Figure 5.4: A comparison of the Vickers hardness in welds from set #4 (20 mm AA7449-W51) in the as-welded (top) and with 198 MPa tensioned (bottom) condition. The dashed lines represent the FSW tool cross-section profile and the solid lines mark the different weld zones as shown in Figure 5.1a. No significant differences in the hardness distribution due to ISGMT were observed.

The original PM hardness has a hardness of 175 -185 HV_{500g} near the material surfaces and has slightly lower values towards the plate middle. Such deviations may be attributed to the non-uniform through thickness quenching and rolling effects during production of the plates. From the graphs it can be seen that FSW clearly affects the PM hardness distribution. Near the tool shoulder the WN hardness reaches that of the PM, but is lower close to the bottom (110 -120 HV_{500g}). The HAZ displays a minimum of 90 -100 HV_{500g} following the cone shape of the tool pin to both sides of the WN. In general the weld zone contours as obtained from the macrographs match the nearly symmetrical hardness

distribution well. The precise exploration of the precipitation mechanisms on the hardness distribution in FSW exceeds the aim of this section, but a detailed discussion is given in section 2.3.4.4 and 4.2. With respect to ISGMT, no significant differences in the hardness distribution are evident in the plots. However, the strong local deviation of the hardness suggests that significant variations of the unstrained unit cell parameter a_0 may be expected as discussed in section 4.2 and as such must be determined for the residual strain and stress calculations.

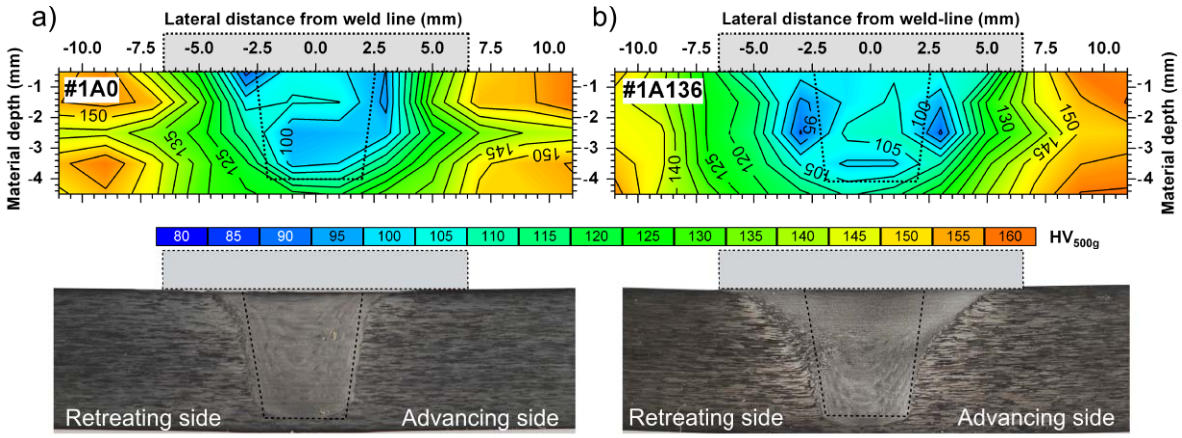

Figure 5.5: Comparison of 2-D maps of the hardness distribution and the macrostructure for the as-welded test weld #1A0 (a) and the 136 MPa tensioned test weld #1A136 (b). While the upper half of weld #1A136 is much wider, the lower half of both welds appears similar in dimension. The hardness also displays this difference in width, but through the entire plate thickness.

The hardness distribution and the corresponding macrographs obtained by light microscopy for the as-welded (#1A0) and with 136 MPa tensioned (#1A136) test welds in 5 mm thick AA2199-T8E74 material are depicted in Figure 5.5. The FSW tool shape is projected on to each graph. The varying hardness and microstructure zones of the two test welds themselves correspond well with respect to the shape and dimensions of the WN and the FSW tool. In general they display similar characteristic weld zone shapes, as observed in the AA7449-W51 test welds: a wide weld zone near the tool shoulder narrowing towards the weld root. Further, the TMAZ on the advancing is distinct, while on the retreating weld side it is wider and somewhat indefinite.

The hardness in the PM of both test welds displays a noteworthy through thickness variation (~155 HV_{500g} near the surfaces and ~140 HV_{500g} at mid thickness) which may again be attributed to the production process as mentioned for the AA7449-W51 plates. However, in comparison with the test welds in set #4 (see Figure 5.4) the hardness

distribution differs. In general in the AA2199-T8E74 test welds the low hardness of ~100 HV_{500g} observed in the HAZ remains constant across the width of the WN and increases only slightly towards the weld root. There is also no significant increase in hardness as was observed in the AA7449 welds. The different hardness distribution may be attributed to different precipitation behaviour of the alloy being used. However, this is beyond the scope of this section and shall not be discussed here.

Direct comparison of the two welds produced without and with 136 MPa tensile loading, reveals a significant disparity of the width of the weld zone in both the hardness and the macrostructure. In the as-welded (#1A0) condition the hardness and microstructural changes over the WN width correspond closely to the local FSW tool pin diameter. On the other hand, in the #1A136 test weld in the upper half of the weld area over which hardness and microstructure change is similar, but ~5 mm wider than the local tool pin diameter. In the lower half the width of WN microstructure and the pin diameter correspond well, but the low hardness zone in the WN is still wide. This anomalous behaviour could be due to an increase in the ISGMT load causing different levels of lift-off of the backing plate resulting in temperature and precipitation hence hardness differences. However, as this observation was not made in sets #2, #3 and #4 the widening is not believed to be caused by ISGMT. Instead, the increasing width may be due to a sudden increase in tool down force and hence temperature leading to a widening of the hot region thus affecting the precipitation sequences hence hardness profile (see section 2.2). In fact, even though the welding machine runs in load control mode with the load cell being optimized for high loads up to 100 kN a constant deviation of the controlled load over the entire loading capacity (0-100 kN) may result in significant relative changes in down force for smaller loads. The test welds in set #1 (AA2199-T8E74) were produced with a low down force of 1.5 kN. Therefore a small absolute shift in down force results in a significant relative variation in the down force during FSW of these plates. In addition, material thickness variations of ~±0.1 mm were observed (Poad 2007) which could cause a temporary change of the FSW tool down force before the machine control has adjusted this parameter. As a consequence, variations in heat input during welding may have occurred meaning that in addition to the varying ISGMT loads the test welds in set #1 may have been produced under welding conditions that varied with time and position even within one and the same weld.

As discussed in section 4.2, the variation in hardness in friction stir welds produced in age-hardening aluminium alloys appears to correlate locally with the variation of the unstrained unit cell parameter a_0. As a result, the observations made on the hardness, indicate that a careful determination of the unit cell parameter a_0 in each test weld is required. This is especially the case for test welds in set #1, as there are different hardness distributions apparent in welds that were produced under presumably identical conditions.

5.3.3 Distortion

ISGMT is applied to mitigate longitudinal tensile RS and the related weld distortion to improve weld quality and to avoid otherwise required work and cost intensive post weld straightening procedures (Williams *et al.* 2008).

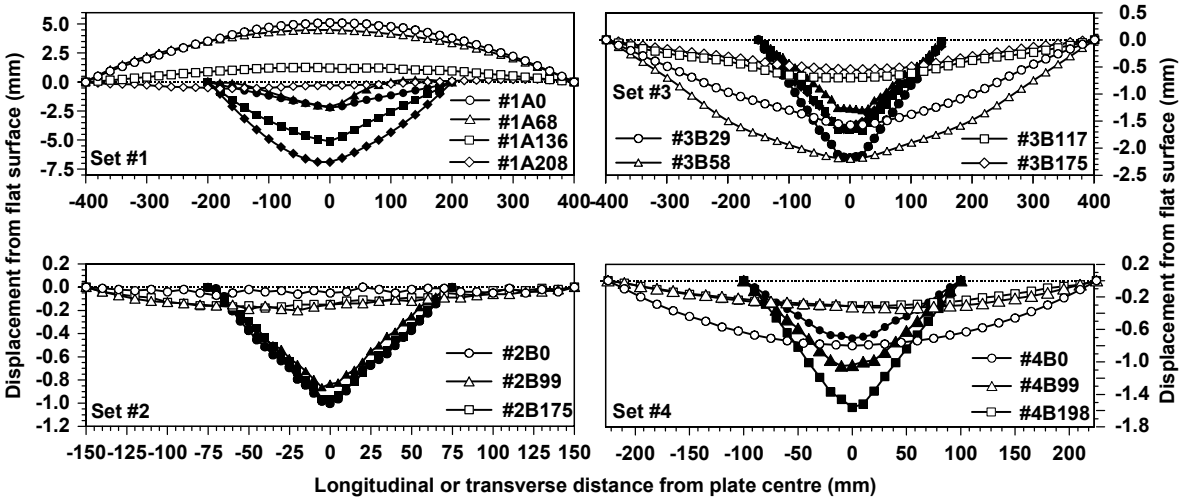

Figure 5.6: The bending (open markers) along the welding direction and angular (filled markers) distortion along the transverse direction for sets #1 - #4 as a function of distance from the plate centre and the applied ISGMT load (the load in MPa is indicated by the second number in the sample designation, see Table 3.2). Note the different scales for the out-off-plane distortion.

Figure 5.6 shows the bending and angular distortion, as determined using a coordinate measuring machine (CMM) equipped with a touch probe (see section 3.6) and measured on the weld surface of each test weld from set #1 - #4. While the sense of the bending direction (concave or convex with respect to the weld surface) may vary for the as-welded test weld for different materials and welding conditions, the application of ISGMT diminishes the magnitude of bending in set #1, #3 and #4 and in case the loading was sufficient may reduce the longitudinal distortion to negligible amounts. On the other hand,

the angular distortion appears to increase for higher ISGMT loads. For set #2 the ISGMT effect on the bending and angular distortion is negligible indicating that the weld may have been too small for the RS to take significant effect on the plate distortion.

The fact that the bending distortion reduces with increased ISGMT is in accordance with previous observations (Masubuchi 1980; Price *et al.* 2007), but an increase in angular distortion with increased ISGMT has not been described before. At this point it is not clear why this occurs especially since ISGMT has little to no effect on the transverse RS (see section 5.3.4). However, while producing the welds for set #3 it was observed that with increased ISGMT loads the plates were lifted off the backing plate, which is believed to be due to a misalignment of the tensioning and the plate mid thickness axis. As a result during welding the plates were pushed down by the FSW tool while the outer plate edges remained at the initial height above the backing plate leading to a 'V'-shaped set-up during welding. This may lead to increased angular distortion for higher loads as the magnitude of lift-off may increase. However, this is only speculation and requires further investigation.

With regard to the varying sense of the bending distortion (concave or convex) this can be affected by through-thickness variations of the RS. The longitudinal tensile RS are assumed to be bigger near the weld surface and decrease towards the weld root, hence concave bending may be expected as observed in sets #2 to #4. Alternatively, a longitudinal misfit can lead to buckling distortion that is stable in both convex and concave configurations as it may be the case for set #1 (Masubuchi 1980).

5.3.4 Residual Stress

In section 5.3.2 a ~5 mm difference in width of the low hardness region in the weld-line was observed for the as welded and with 136 MPa tensioned test welds in set #1. This indicated that for each weld in set #1 the variation of the unstrained unit cell parameter a_0 had to be determined. Assuming a bi-axial stress field in the 5 mm thin plates allowed calculation of a_0 using equation 2.15 as the three strain directions were measured on the SALSA beam-line. The distribution of the unstrained unit cell parameter a_0 for all test welds in set #1 is displayed in Figure 5.7. The plots are very similar for all test welds in set #1 and typical for FSW as discussed in detail in section 4.2.3.1. In opposite to the hardness distribution the plots do not display a difference in the lateral width of the a_0 distribution. However, in section 4.2.3.2 it was demonstrated that the hardness and a_0 parameter

correlate with respect to spatial changes and as such in the current case a lateral variation was expected. It is not clear whether the hardness or strain results are erroneous. One explanation for the differences could be that the welding conditions along the weld-line change significantly and as the hardness and microstructure samples were removed from the approximate position of the strain measurements only, slight deviations of the actual strain measurement position could result in the observed disparity. Irrespective of this discrepancy the RS were calculated using the in Figure 5.7 presented data for the unstrained unit cell parameter a_0.

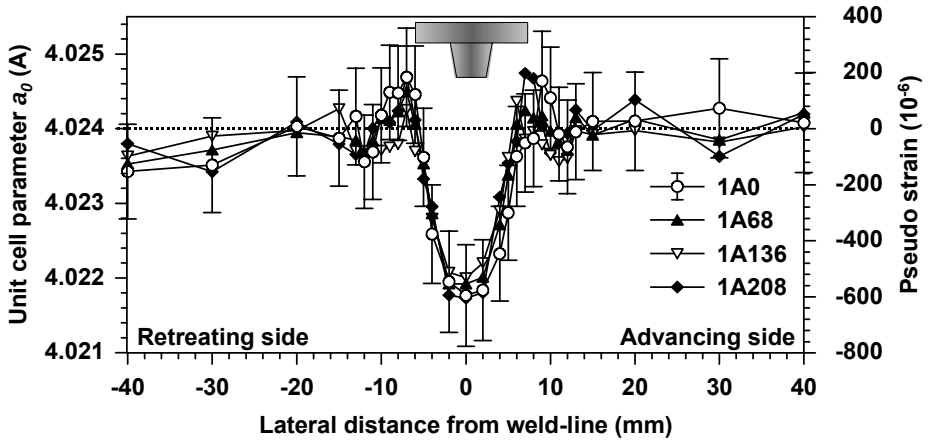

Figure 5.7: The variation of the unstrained unit cell parameter a_0 expressed in Å as well as pseudo strain determined assuming a bi-axial stress condition in 5mm thick AA2199 test welds from set #1. The data were obtained on the SALSA beam-line. Error bars are included only for test weld #1A0 for clarity.

The influence of the ISGMT load level on the mid thickness longitudinal and transverse RS distribution in set #1 (5 mm AA2199-T8E74) as determined by angular dispersive neutron diffraction (ADND) on the SALSA beam-line (see section 3.3.2) is shown in Figure 5.8a and Figure 5.8b respectively. The lateral range plotted is restricted to ±40 mm in order to improve visualization of the RS data around the weld-line and because no significant variation of the RS was observed beyond this distance. However, with respect to the boundary conditions applied for the calculation of the RS (see section 3.3.5) it should be noted that the longitudinal RS balance over the entire width of the test weld while the transverse RS are zero at the plate edges. The RS results are consistent with those found in the literature insofar that the longitudinal stress profile in the as-welded plate exhibits a characteristic 'M' shape (Donne *et al.* 2001; Peel *et al.* 2003; Staron *et al.* 2004; Price *et al.* 2007; Richards *et al.* 2008a). The origin of this 'M' shaped profile was

discussed by Richards *et al.* (2008a) and is reviewed in section 2.4.4. As expected, the highest tensile RS are observed in the as-welded condition in the longitudinal direction. A stress plateau of ~170 MPa exists in the WN being ~12 mm in width which corresponds closely to the diameter of the FSW tool shoulder (∅ = 13 mm). The peak tensile RS of ~210 MPa magnitude occur in the HAZ at ±7 mm from the weld-line. No significant difference is observed between the advancing and retreating sides.

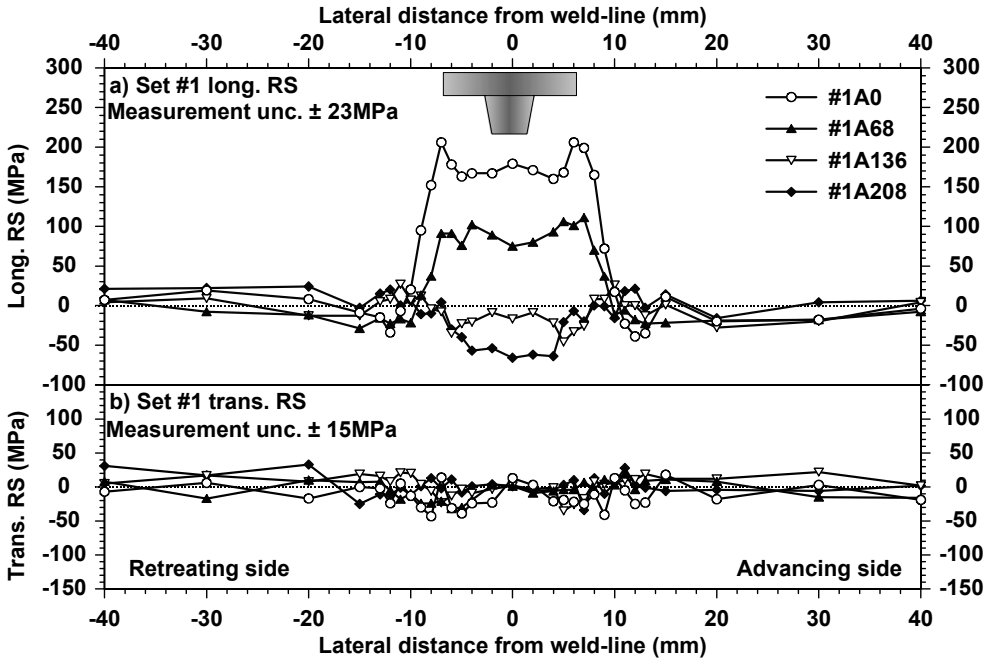

Figure 5.8: The effect of ISGMT on a) the longitudinal and b) the transverse RS in 5 mm thick AA2199-T8E74 (set #1), the cross-section of the FSW tool is shown above the long. RS profile. The ISGMT load in MPa is indicated by the second number in the sample designation (see Table 3.2).

Applying an ISGMT load of 0.17 σ_{ys} = 68 MPa (test weld #1A68) results in a reduction of the longitudinal RS of ~70 MPa at the weld-line with an associated disappearance of the distinct tensile RS peaks in the HAZ though widening the stress plateau to ~±8 mm. ISGMT with even higher loads leads to a progressive reduction in the RS and the weld becomes effectively stress-free when the applied load reaches ~0.34 σ_{ys} = 136 MPa (test weld #1A136), a value close to that of the initial weld-line RS. Excessive tensioning to 0.52 σ_{ys} = 208 MPa (test weld #1A208) results in the development of a compressive RS plateau of ~ - 50 MPa over ~±4 mm as was reported by Staron *et al.* (2004). In common with previous data (Donne *et al.* 2001; Peel *et al.* 2003; Staron *et al.* 2004; Price *et al.* 2007), the transverse stresses (Figure 5.8b) are substantially lower than those in the

longitudinal direction. They vary between ± 40 MPa and are not noticeably influenced by ISGMT (Staron *et al.* 2004). With respect to the observed widening of the weld zone in the microstructure and hardness distribution (compare Figure 5.5) for weld #1A136, this effect was not observed neither in the distribution of the unstrained lattice parameter a_0 (see Figure 5.7) nor the stress plots as can be seen in Figure 5.8.

Figure 5.9 shows the longitudinal RS distribution as determined using energy dispersive synchrotron X-ray diffraction (EDXRD) on ID15A across the weld-line at mid-thickness for sets #2 (5 mm AA7449-W51) and #3 (12.2 mm AA7449-W51) as a function of the applied ISGMT loads. Again the lateral range plotted is restricted to ±40 and ±60 mm respectively for improved visualisation and because the RS do not vary significantly beyond this distance.

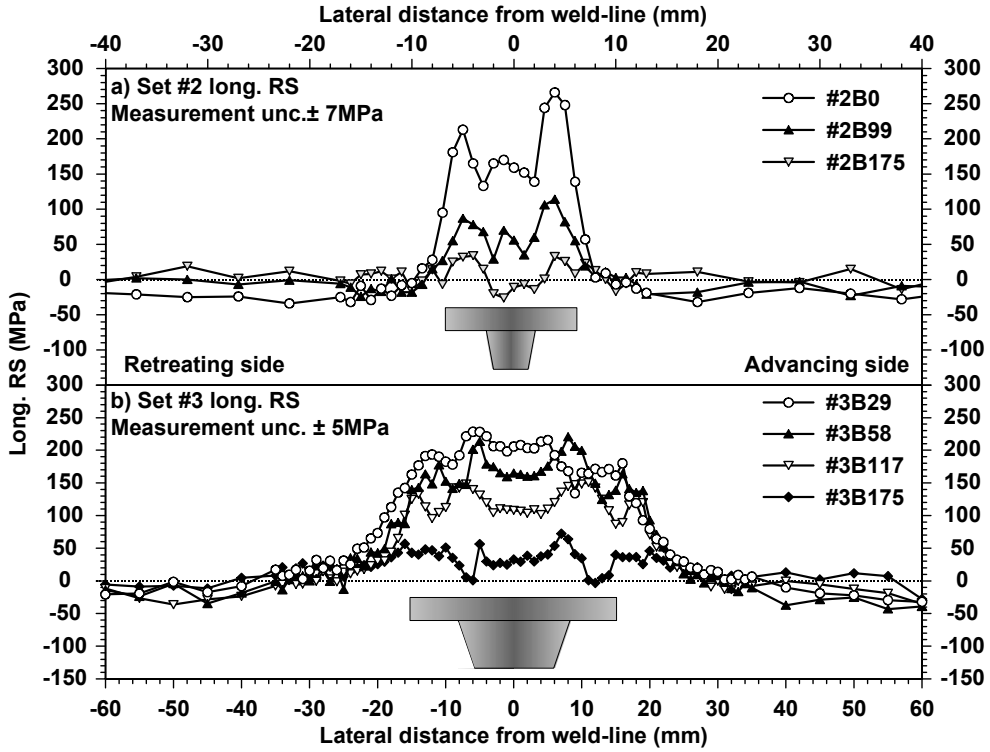

Figure 5.9: The effect of ISGMT on the mid thickness longitudinal RS in a) 5 mm (set II) and b) 12.2 mm (set III) AA7449-W51 friction stir welds. For each set the cross-section of the FSW tool is shown below the RS profile. The ISGMT load in MPa is indicated by the second number in the sample designation (see Table 3.2).

The boundary conditions of stress balancing in the longitudinal direction over the plate width and zero transverse RS at the plate edges are fulfilled. The stress plots for set #2 and #3 show similar results upon increased tensioning as for the test welds in set #1: a

progressive reduction in RS and the essentially stress-free state being reached when the applied load corresponds to the initial weld-line stress. For the welds in set #2 this is the case for $\sim 0.3\sigma_{ys} = 175$ MPa which corresponds to the initial weld-line RS of ~170 MPa. Application of the same ISGMT load to the 12.2 mm thick AA7449-W51 welds (set #3) results in a weld-line RS of ~30 MPa remaining, which is close to the difference between the initial (as-welded) weld-line stress of ~200 MPa and the applied load of 175 MPa, thus indicating that an ISGMT load comparable to the initial weld-line RS leads to a stress free weld. Similar to the observations made in set #1 the stress peaks in the HAZ in the as-welded condition (see test weld #2B0) disappear even at low tensioning levels, indicating that the local yield strength σ_{YS} is reached earlier in the stress peaks than in the WN. This is supported by the low hardness in the region of the stress peaks, as can be observed in Figure 5.4 and Figure 5.5.

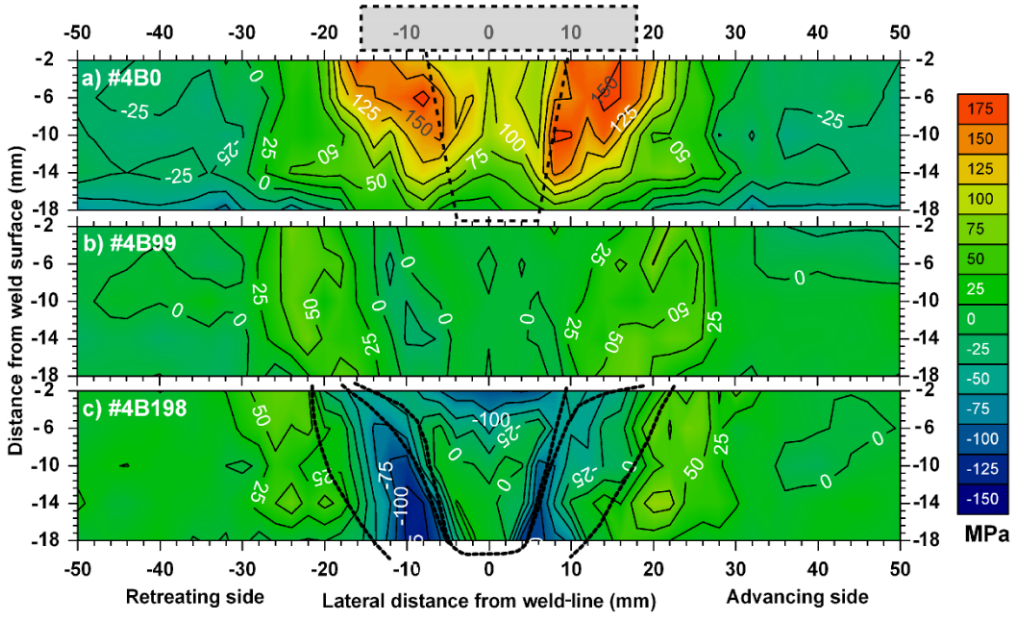

Figure 5.10: The longitudinal RS distribution in 20 mm thick AA7449-W51 FSW from set #4 in (a) the as-welded condition, (b) an applied ISGMT load of 99 MPa and (c) of 198 MPa. The measurement uncertainty is ±7 MPa. Additionally the cross-section of the FSW tool as well as the macrograph outline are projected onto the 2-D plots.

Figure 5.10 displays the 2-D longitudinal RS distribution in the N-T cross-section of the 20 mm thick AA7449-W51 test welds of set #4 for varying ISGMT loads. Measurements in the longitudinal and transverse plate directions were performed on ID15A using the EDXRD set-up, while the normal strain was determined on the SALSA beam-line with the ADND set-up. The cross-section profile of the FSW tool and the outline of the

weld area as obtained from the macrographs in Figure 5.1 are projected onto the 2-D stress maps.

In common with the thinner welds in the as-welded sample an 'M' shaped stress profile with lateral distance is observed at all depths. At 2 mm below the weld surface a stress plateau of ~100 MPa reaching over ±5 mm from the weld-line is apparent with ~4 mm wide tensile peaks of ~175 MPa within the HAZ at ~± 15 mm. At this depth the overall lateral extent of the tensile zone is ~60 mm wide.

With increasing depth the weld-line RS plateau magnitude and the width of the tensile zone reduce and the RS peaks in the HAZ become less distinct and shift towards the weld-line. These effects may be attributed to the shape and magnitude of the thermal profile which is a result of the FSW parameters employed as well as the cone shaped tool pin. The shape of the stress distribution in the weld zone is in accordance with both, the macrostructure plotted in Figure 5.1b and the hardness distribution in Figure 5.4. Further, the tensile peak is slightly higher on the advancing side, which may be attributed to the asymmetric nature of the FSW process (Sutton *et al.* 2002; Peel *et al.* 2003) and suggests that higher temperatures may have occurred on this side during welding leading to more compressive yielding in front of and less tensile yielding behind the FSW tool which generates more volumetric misfit, hence higher RS. The through-thickness variation in RS at the weld-line is ~70 MPa with the higher RS near the weld surface. It is this difference that may be responsible for the concave bending of the as-welded sample as shown in Figure 5.6d.

In accordance with the results obtained for sets #1 to #3, the application of an ISGMT load of 0.17 σ_{ys} = 99 MPa leads to a reduction of the RS peaks in the HAZ and the weld-line RS level at -2 mm reduces by ~100 MPa to approximately zero. Again this is equivalent to the ISGMT load applied. However, at greater depths the effect of the ISGMT decreases such that at 18 mm below the weld surface the weld-line RS decrease by only ~30 MPa, which is ~70 MPa less than applied by ISGMT. As a result the through-thickness RS variation vanishes leading to low levels of stress across the weld and through the weld thickness resulting in decreased sample bending as depicted in Figure 5.6d. This reduction of the ISGMT effect with increasing depth from the weld surface may be due to a temperature gradient through thickness during FSW with lower temperatures near the weld root lead to less material softening. In turn, the degree of softening affects the extent of reduced compressive and induced tensile yielding for a given ISGMT load. Softer material

yields earlier and more under the tensioning load than cooler and stronger material. This may explain why ISGMT is more effective near the weld surface of thick welds and in thin welds in general (see set#1 to #3) where the high temperatures presumably occur through the entire plate thickness.

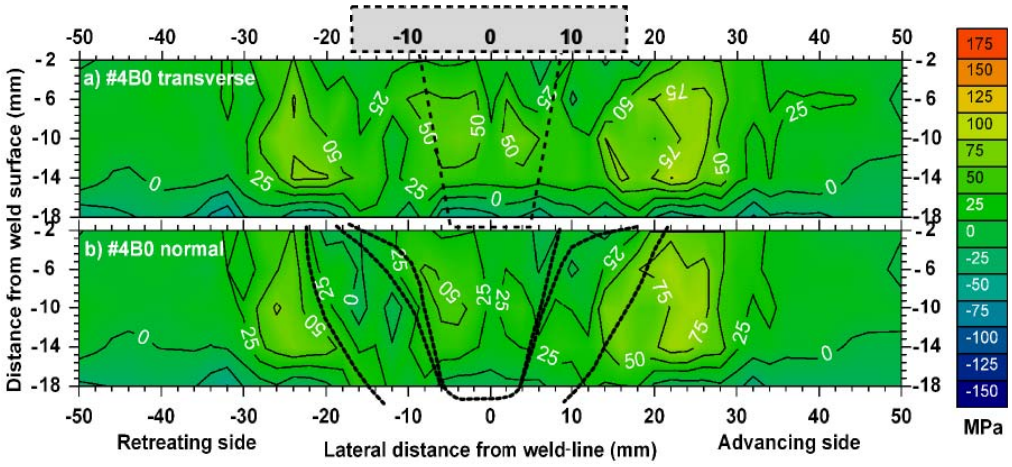

Figure 5.11: The transverse (a) and normal (b) RS distribution in 20mm thick AA7449-W51 friction stir welds in the as-welded condition. The measurement uncertainty is ±7MPa.

With respect to test weld #4B198 with an ISGMT load of 0.34 σ_{ys} = 198 MPa the same tendency of RS mitigation was observed. In comparison to the as-welded condition at -2 mm depth the weld-line RS reduce by ~200 MPa, which equates to the applied tensioning load. However, with increasing depth the level of reduction of tensile RS decreases once more resulting in a similar mitigation of RS near the weld root as was obtained with only half of the ISGMT load. The trapezoidal weld profile seen in the as-welded test weld is also evident for the #4B198 test weld (Figure 5.10c), but the sign of the RS has reversed with the largest compressive peaks lying towards the base of the weld at a distance slightly greater than the local size of the FSW tool pin (~ ± 8.5 mm). Here, the retreating side shows highest compressive stress of ~130 MPa at -18 mm. These compressive peaks correspond to the location of lowest hardness (see Figure 5.4) and may reflect early plastic misfit under the ISGMT load leading to compressive RS maxima upon releasing the ISGMT load. This may also be the reason why the tensile RS peaks below the tool shoulder edge disappear even at lower ISGMT loads.

Figure 5.11 shows the through thickness RS profiles for the transverse and normal directions for the as-welded condition of the 20 mm thick AA7449-W51 friction stir weld (#4B0). Similar to the results for thinner plates (for example set #1, see Figure 5.8b) and as

reported in the literature (Donne *et al.* 2001; Peel *et al.* 2003; Staron *et al.* 2004; Price *et al.* 2007) the RS in these directions are significantly lower than those acting parallel to the weld-line. However, RS peaks of up to ~80 MPa are evident at ± 20 mm from the weld-line which is somewhat further apart than the longitudinal stress peaks. Again the advancing weld side displays slightly higher stress values. In between the peaks the transverse and normal stresses vary between ± 50 MPa depending on the depth below the weld surface. In both cases to a depth of 14 mm the RS are in low level tension, while the near weld root material is in compression. This through thickness variation in transverse RS may be responsible for the concave angular distortion of the test welds as depicted in Figure 5.6d. However, the application of ISGMT during FSW of 20 mm thick AA7449-W51 material has only a marginal effect on the transverse and normal stress profiles which are therefore not displayed here.

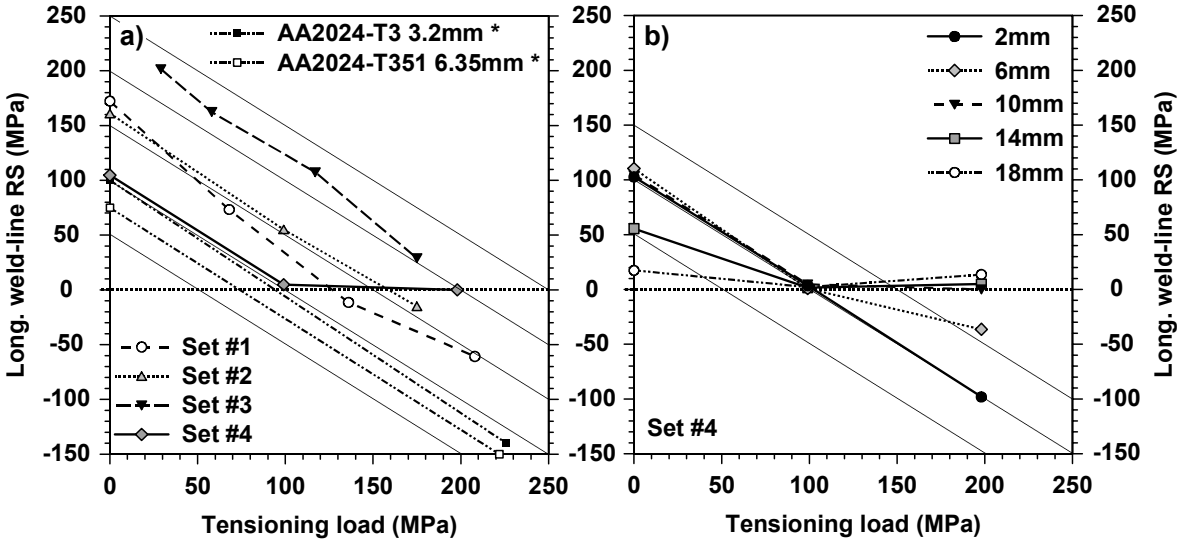

Figure 5.12: In (a) the averaged RS at mid-thickness averaged over ±2 mm from the weld-line as a function of applied ISGMT load for sets #1-#4 and data (*) from literature Staron *et al.* (2004) are shown. In (b) the effect of ISGMT for the longitudinal weld-line RS at different material depths below the weld surface in the 20 mm thick AA7449 plate is depicted. The dashed guide-lines represent a 1:1 relationship between stress reductions and applied tensioning level.

The evidence from sets #1 to #4 appears to suggest a 1:1 correlation between weld-line RS reduction and ISGMT load. An applied 1 MPa tensioning load results in a 1 MPa reduction of the tensile weld-line RS. This effect is summarized in Figure 5.12a, where the weld-line RS at mid-thickness for the four sets investigated are plotted as a function of the applied ISGMT load. The with depth varying effect of in-situ tensioning as found in set #4 is shown in Figure 5.12b. As the tensile RS peaks observed in the as-welded condition

disappear even at low loads, the applied level of ISGMT is correlated to the weld-line RS averaged over ±2 mm from the weld-line. It can be seen in Figure 5.12a that the test welds produced in AA7449-W51 (set #2 to #4) also show a simple inverse 1:1 linear relationship: the weld-line RS reduce by 1 MPa for every 1 MPa of tensioning load applied.

In broad terms, the same behaviour can be observed for the AA2199-T8E74 test welds in set #1, although the rate of stress mitigation is marginally higher. Indeed, the essentially 1:1 linear stress reduction is found in all sets investigated in this study, thus indicating that the RS are reduced by an amount approximately equal to that applied by ISGMT. This means that the optimum ISGMT load may simply be estimated to be equal to the weld-line RS in the as-welded condition. Further, the experimental data published by Staron *et al.* (2004) for AA2024-T3 friction stir welds support this rule of thumb of a 1:1 linear stress reduction as depicted in Figure 5.12a. Even though they reported results only on the as-welded condition and one tensioned weld for 3.2 and 6.3 mm thick plates respectively, the actual reduction of the weld-line RS of ~235 MPa corresponds well to the 0.70 σ_{ys}= 241 MPa ISGMT load applied.

In some cases the optimum ISGMT level may be equal to a fixed percentage of 30 to 40 % of the PM yield strength σ_{YS} as proposed in the literature (Price *et al.* 2007; Richards *et al.* 2008a). However, assuming a fixed and material dependent fraction of σ_{YS} for the optimum tensioning load does not account for differences in RS due to variations of the welding parameters. Consequently, this fixed value could result in significant deviations from the actual tensioning magnitude required to produce stress free welds. For the currently investigated sets produced in AA7449-W51 a fixed fraction of the yield strength for example 0.30 σ_{YS} =175 MPa would result in an overestimation of the optimum ISGMT load for the welds in set #4 thus introducing significant compressive stresses (see Figure 5.10). On the other hand, 0.30 σ_{YS} ISGMT load applied to welds from set #3 would result in ~30 MPa tensile weld-line stresses remaining in the weld (see Figure 5.9b). So in conclusion, the principle that the optimum tensioning load should be a fixed fraction of the yield strength σ_{YS} appears over-simplistic and would not necessarily lead to low RS in all cases.

With regard to the mitigation of RS as a function of tensioning load the 1:1 rule should be treated with caution. As depicted in Figure 5.12b, a significant reduction of the linear stress mitigation effect with increasing depth can be observed. This may be due to the lower

welding temperatures at greater depths leading to less material softening. In turn this requires higher tensioning levels to reach the local yield point, but the tendency to counteract the bending distortion may also be a factor. A way to overcome this problem may be the combination of ISGMT superimposed with a longitudinal bending to introduce a load gradient through thickness. This should result in increased tensioning at the weld surface or root depending on the bending direction That approach was first suggested by Prof. P. Prangnell, University of Manchester, UK, within the SEALS project (see section 1.1) but significant difficulties regarding the FSW tool positioning would need to be overcome to achieve this practically.

The linearity of stress mitigation with increased tensioning loads is also evident in the FEM work reported by Richards *et al.* (2008a) and shown in Figure 2.27. While a 1:1 correlation was broadly followed, it was found that in some cases the gradient became slightly shallower when the power, or heat input into the weld was reduced. This observation is in accordance with the reduced stress mitigation with greater distance from weld surface (see Figure 5.12b) where the temperatures presumably are lower (for example as in set #4). In the following section the results of the FEM work performed by D. Richards at the University of Manchester, UK, for set #3 as part of the SEALS project and as carried out within this dissertation for sample set #2 are presented.

5.3.5 FEM Predictions

As indicated in section 3.5 the FEM work performed within this dissertation is confined to creating and optimising a FE model for the test welds in set #2 based on the original FE model (see section 3.5) developed by D. Richards for the test welds in set #3. The experimental stress data obtained in this dissertation were used to evaluate the quality of each model and to adjust the input parameters as such that the FE results match the experimental results for the starting condition. The FEM predictions are presented in this section and compared and put into context with the experimental data reported in the previous sections.

The longitudinal RS distribution for various ISGMT loads, as obtained from the FE model for the test welds in the 5 mm thin AA7449-W51 plate (set #2) are shown in Figure 5.13a and directly compared with the experimental results (see Figure 5.9a). The range of data plotted in the figure is an exploded view over ±30 mm, as further away from the weld-

line no changes of the stress profiles occur. While the experimental results exhibit an asymmetry of the RS distribution, the model does not differentiate between the advancing and retreating sides of the weld and therefore predicts a symmetrical stress profile. In this case, the input welding parameter (power input and tool shoulder to pin ratio of heat generation) in the FE mode were not adjusted l as well due to a lag of time and consequently the experimental stress results were not predicted well. Consequently, these FEM predictions must be considered as preliminary. Nevertheless, the predicted width of the tensile zone and the RS peaks are relatively close in magnitude and lateral position to those experimentally determined, but the averaged weld-line RS (±2 mm) are overestimated by ~50 MPa for the as-welded condition. A similar behaviour can be observed for profiles with in-situ tensioning of 99 and 175 MPa applied. This deviation may be attributed to the fact that the heat generation assigned to the FSW tool pin is overestimated and the heat input ratio between tool shoulder and pin is wrong (Richards 2008). Apart from that, the FEM and experimental results are in good qualitative agreement.

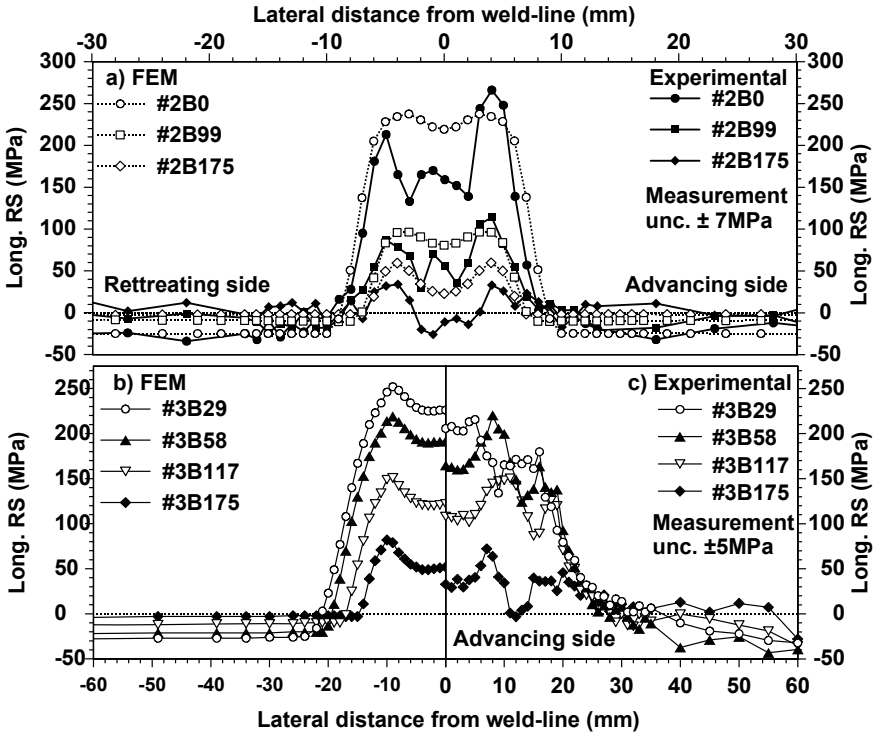

Figure 5.13: Comparison of the FEM and experimental results for the test welds from (a) set #2 and (b) and (c) set #3 for varying ISGMT loads in MPa (indicated by the second number in the sample designation). Note, the FEM results for test welds from set #2 were produced using a FE model that was created by the author but was based on the FE model developed for set #3 test welds by D. Richards at the University of Manchester, UK.

The FEM results for set #3 were produced by D. Richards and must therefore be considered as work not arising from this dissertation. However, the results are depicted and compared with the experimental data in Figure 5.13b and Figure 5.13c. For clarity and as the experimental results for set #3 are broadly symmetrical, only one side of the stress profile for each set of curves is shown to a distance of 60 mm from the weld-line as further away no significant changes occur. The FEM predictions for this set of test welds are broadly in line with the experimental observations, albeit there is also a tendency of slightly higher predicted stresses than was measured. This may again be attributed to the fact that the heat input of the FSW tool for the thermal model was overestimated. Further, while the model predicts stress peaks in the HAZ that shift downwards with increased ISGMT loads, the experimental data neither show this feature of distinct RS peaks in the as-welded condition nor is a systematic trend of stress mitigation apparent in this region. On the other hand, the predicted stress behaviour around the weld-line is in agreement with the experimental stress data displaying a linear reduction of RS for increased in-situ tensioning loads.

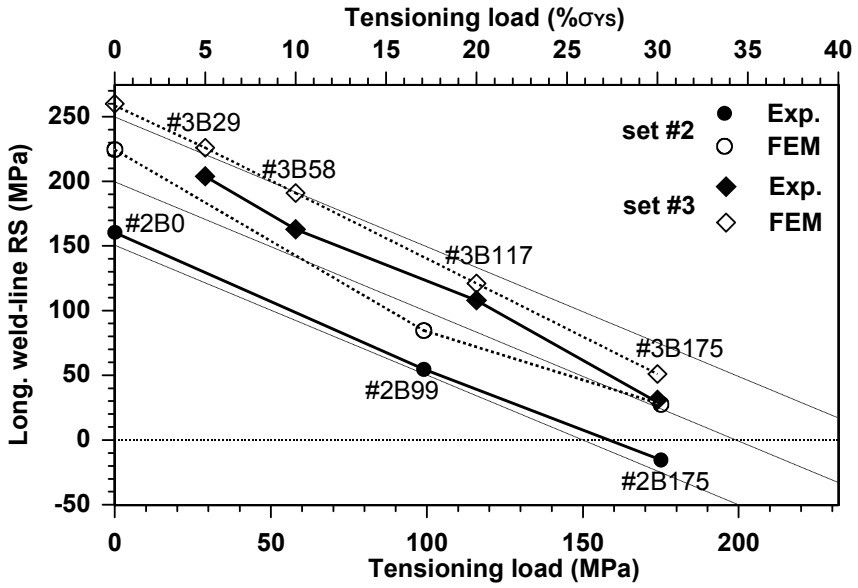

Figure 5.14: Comparison of the weld-line RS as a function of the applied tensioning load for the experimental and FE-modelled data. The dashed line represent the 1:1 stress mitigation effect.

One feature that is predicted by the model, but is only partly observed in the experimental data is a slight narrowing of the stress field around the weld zone (area of tensile stress) with increased tensioning. The origin for this is not known at present, but

could be attributed to the fact that the FE model predicts a constant stress gradient from the RS peak in HAZ towards the PM. In fact, the stress peaks are always at the same position with respect to the weld-line as can be seen in Figure 5.13a and Figure 5.13b and consequently a constant stress gradient results in narrowing of the tensile zone for decreasing magnitudes of RS.

Figure 5.14 depicts the average RS at ±2 mm from the weld-line as a function of the applied ISGMT load for the FEM as well as experimental results for sets #2 and #3. The predicted reduction in RS as a function of the applied ISGMT load is essentially linear for set #3 and to some extent linear for set #2 (even though based on three data points only). This is in agreement with the stress data obtained in the real test welds (see Figure 5.12a). However, as a result of the overestimation of the initial weld-line RS the ISGMT load required to produce an essentially stress-free weld is also higher. In detail for set #3 the experimental data suggested zero RS at ~200 MPa (=0.34 σ_{YS}) tensioning load while the FEM simulation predicts zero RS for a load of ~220 MPa (=0.38 σ_{YS}). The divergence of 20 MPa corresponds roughly to the difference in weld-line stress for the as-welded condition (as measured and predicted) and once more indicates the linear correlation of tensioning load and stress mitigation though supporting the 1:1 rule of thumb. The same tendency is observed for set #2, albeit the difference between FEM with ~200 MPa (=0.34 σ_{YS}) and experimental results with 160 MPa (=0.27 σ_{YS}) is greater. The higher ISGMT level necessary to achieve zero stress on the weld-line is due to the higher starting stress values predicted by the models.

5.4 CONCLUSIONS

Global mechanical tensioning applied during welding is an effective method for reducing RS in high strength aluminium alloy components joined by FSW. The superimposed ISGMT load changes the yield path during welding as stated by Price *et al.* (2007) and modelled by Richards *et al.* (2008a): With increased ISGMT loads the developing RS and the superimposed tensioning stress reach the temporary local yield strength σ_{YS} sooner and as a consequence more material deforms plastically. This reduces the accumulated elastic misfit and the final RS once the weld has cooled (Richards *et al.* 2008a) and the load is removed. The aim of this dissertation was to investigate the

correlation between the degree of applied ISGMT and the remnant RS. By examining four sets of friction stir welds at different thicknesses, welding conditions and ISGMT levels it has been demonstrated that:

- The application of ISGMT reduces the longitudinal tensile RS in a weld although the use of excessive load results in a reversal of the stress field with compressive stresses forming in the weld zone.
- In thin plate welds (sets #1 and #2), for which a nearly constant through thickness temperature profile may be assumed, there is a linear relationship between the applied ISGMT load and the mitigation of the resulting RS. As a rule of thumb 1 MPa of applied ISGMT renders the longitudinal weld-line stress 1 MPa less tensile. This means that the initial weld-line RS can be taken as the load that must be applied to produce essentially stress-free welds.
- For thicker plate material (set #4), the mitigation in RS due to ISGMT reduces with increasing depth from the weld surface. Near the weld surface ISGMT has been shown to have the same RS mitigation effect as in thin plates, namely the 1:1 MPa reduction. The effect reduces with increasing depth which is believed to be due to the decreasing temperatures and hence higher temporary local yield strength σ_{YS} allowing for less plastic deformation as the superimposed RS and tensioning load do not exceed σ_{YS} as much.
- Tensile RS peaks forming outside the WN in the as-welded condition disappear even at low levels of ISGMT and can reverse to form compressive peaks if the tensioning load is excessive.
- Only longitudinal RS are altered significantly by ISGMT along the welding direction: no significant effect is seen on the low stresses in the transverse and normal directions.
- The bending distortion is reduced with increased ISGMT loads which is possibly due to the lower magnitude of longitudinal RS and a reduction of the through thickness variation of the stress. However, the butterfly distortion as a result of transverse RS and their through thickness variation increases even though no direct effect of ISGMT on the stress profile in that direction was observed. Instead, a misalignment of the tensile loading and the plate mid thickness axis occurring with the set-up used for this dissertation (see Figure

2.22) is believed to lead to a lift-off of the plates from the backing plate. As a result the FSW tool pushes down the plates locally at the weld-line while welding them together in this configuration though possibly leading to increased angular distortion.

- As expected, the ISGMT affects neither the weld microstructure nor the mechanical properties such as the weld hardness except for cases where the plates are lifted off the backing plate resulting in a variation of the thermal field and as such the precipitation microstructure, which ultimately may result in variations of the hardness. A reported improvement of the weld quality by increased ISGMT resulting in a reduction of the amount and size of weld defects (Price *et al.* 2007) was not observed in the current investigation.
- FEM predictions performed by D. Richards as well as done in this dissertation displayed a good agreement with the experimental data obtained in this work.

In-situ global mechanical tensioning applied along the welding direction was found to a very effective method for mitigation of tensile longitudinal RS. An essentially stress free weld can be obtained when the tensile loading stress is equal to the weld-line stress that would occur in the as-welded condition. The application of the tensile stress to the test welds investigated in this dissertation required comparatively heavy machinery already. Consequently for bigger and more complex welding geometries this stress engineering technique is applicable only with sufficiently strong and cumbersome equipment and as such reasonable in-field applications of this technique are unlikely. On the other hand, for pre-manufacturing big panels, for example wing skin panels for aircrafts, this technique appears to be very useful.

Nevertheless, an alternative stress engineering technique to the ISGMT is the roller tensioning of welds. The main advantage of this mechanical stress engineering technique is that it can be applied to any weld geometry as long as sufficient component support to withstand the rolling forces can be supplied. The effectiveness of this technique for stress mitigation is explored in the following chapter.

6 STRESS ENGINEERING BY ROLLER TENSIONING

6.1 INTRODUCTION

Roller tensioning as a means of stress engineering the longitudinal residual stresses (RS) developing along the weld-line during friction stir welding (FSW) of high strength aluminium alloys, has been proposed only recently (Williams *et al.* 2008; Wen *et al.* 2009) and predominantly studied through finite element modelling (FEM) as discussed in section 2.5.3.4. This dissertation reports the first experimental investigations into the efficacy of the technique, with respect to the mitigation of the longitudinal RS and the associated weld distortion.

Several variations of the roller tensioning technique have been proposed (Wen *et al.* 2009). However, in this dissertation in-situ roller tensioning (ISRT) and the post weld roller tensioning (PWRT) techniques were of primary interest (see section 2.5.3.4). ISRT was applied by two cylindrical flat faced rollers placed each side of the weld-line trailing the FSW tool, such that the rolling affects the hot and softened material. The aim of this technique is to increase the tensile yielding of the weld-line material upon cooling by elongating the material alongside the weld-line. On the other hand, the PWRT technique as investigated in this dissertation is based on rolling a single cylindrical flat faced roller similar in width to the FSW seam directly along the cold weld. The rationale behind this method is to plastically elongate the weld-line material itself in order to reduce the elastic misfit with the parent material (PM). Further, the effect of roller tensioning with a cylindrical corrugated roller is examined. This roller is similar in shape to a gear wheel but with much smaller teeth on the rolling surface (see Figure 3.3d). The aim of these corrugations was to increase the local normal stress induced by the rolling to increase the amount of plastic elongation in the weld longitudinal direction and the mitigation of the longitudinal tensile RS (Poad *et al.* 2006). Within this dissertation, one test weld produced with a corrugated roller was investigated. A general description of the application of each roller tensioning technique and the respective parameters applied to the test welds investigated in this dissertation is given in section 3.2.2. In order to gain some understanding of the efficacy of the roller tensioning technique three sets of test butt welds in high strength aluminium alloys joined by FSW are investigated. While two sets were produced from flat sheet, the third set is a near application test series produced in so-called

integrated stiffener panels (ISP) with the stiffeners protruding at the welding and rolling surface as depicted in Figure 3.2. These ISP test welds are representative of industrially produced uniform and seamless wing skins for aircraft: a new approach to reduce the amount of work and productions costs as compared with the commonly used riveting technique. Further, welding of ISP plates allows for weight reduction and higher structural integrity as there are fewer joints within the final wing skin component.

In this chapter the experimentally obtained RS, the weld distortion and hardness results as a function of the applied roller tensioning technique and roller down force are presented and discussed.

6.2 EXPERIMENTAL DETAILS

For the investigation of the roller tensioning technique applied either during (ISRT) or post (PWRT) welding three sets of test welds (sets #5 - #7) were produced. The material details, weld production and rolling parameters are described in section 3.2.2. Within each set one test weld was produced in the as-welded condition (#5C0, #6A0 and #7D0) without any rolling applied to allow for comparison of the stress engineered with the as-welded condition. While the test welds in set #5, were subject to varying ISRT down forces, the weld seam in welds in set #6 and #7 were roller tensioned with different down forces after welding had finished and the weld cooled down (PWRT). In set #7 an additional test weld (#7D50) was produced and post weld stress engineered with a corrugated roller. The geometry and dimensions of each roller applied are shown in Figure 3.3. The greater diameter of the rollers for set #7 were necessary as these welds were produced in the ISP plates where the stiffeners protrude at the rolling surface and as such prohibited the use of smaller diameter rollers.

For the calculation of the RS in all test welds ($\leq$7.5 mm in thickness) a plane stress situation was assumed with the out-off-plane stress component σ_N equal zero. Therefore, it was sufficient to use the ID15A beam-line with the EDXRD technique and sample set-up as described in section 3.3.3 to measure the unit cell parameter a in the two in-plane directions. While in set #5 and #6 (5 mm thick) a single line scan at the mid material thickness was performed, in the 7.5 mm thick test welds from set #7 three line scans were performed at 2, 4 and 6 mm below the weld surface. The materials used for the test weld production are age-hardening aluminium alloys, hence for the correct determination of the

RS the local variation of the unstrained unit cell parameter a_0 must be determined. This was done using the comb method as described in section 3.3.4.2. As presented in section 4.2, this method appears to be reliable for thin and thick materials joined by FSW. Possible weld to weld variations of a_0 were ruled out by investigating the hardness variation in the N-T cross-section of each test weld, as described in section 3.7.2. For evaluation of the weld bending and angular distortion a coordinate measuring machine (CMM) equipped with the laser scanner LC50 (see section 3.6) has been used.

6.3 RESULTS AND DISCUSSION

6.3.1 In-situ roller tensioning

6.3.1.1 Distortion

The bending and angular distortion of the test welds in set #5 for the as-welded and the two with ISRT down forces of 50 and 75 kN stress engineered welds are shown in Figure 6.1. The rolling paths are marked as light grey areas either side of the weld-line. In the as-welded condition (#5C0) significant convex bending distortion of up to ~4 mm ranging over the plate length of 500 mm and the entire width of the test weld, being slightly more significant on the weld advancing side, is apparent. In addition, concave angular distortion similar in magnitude is superimposed onto the bending distortion leading to buckling as defined by Bhide *et al.* (2006).

In comparison, the test welds with ISRT down forces of 50 kN (#5C50) and 75 kN (#5C75) display slightly less convex bending and concave angular distortion. However, while the amount of bending distortion reduces at the weld-line for increased ISRT down forces, it increases on the weld advancing side for both loading levels, and in case of the 75 kN down force, this is also true on the weld retreating side. The ends of each test weld at ±250 mm display less angular distortion while the change is much less at the middle of the length of the welding path. In addition, in test weld #5C75 a kind of twisted distortion along the weld-line is apparent.

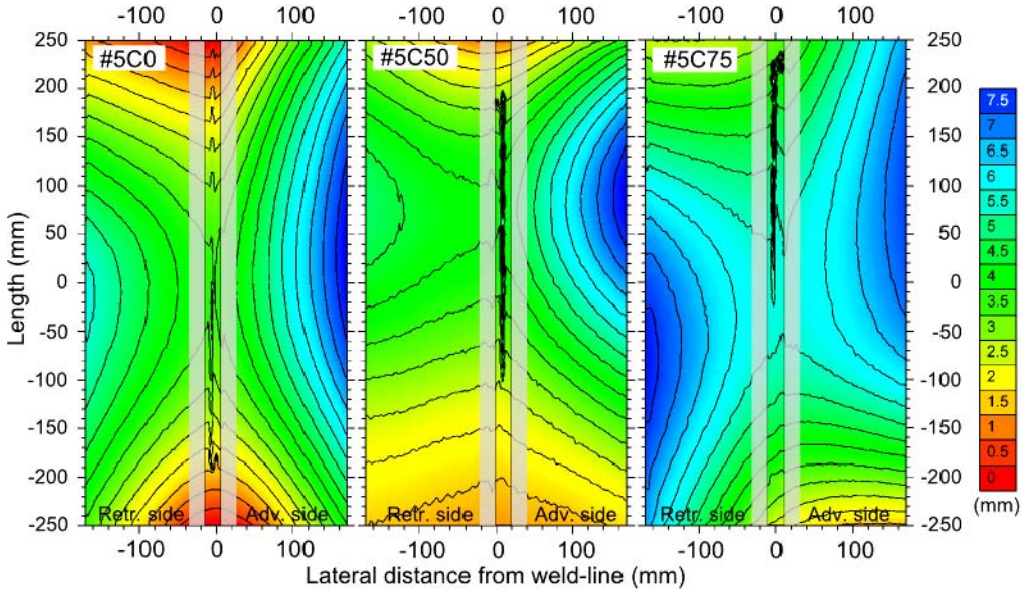

Figure 6.1: Bending and angular distortion in the as-welded condition (#5C0), with 50 kN (#5C50) and 75 kN (#5C75) ISRT down forces applied FSW in AA2024-T3. The light grey stripes represent the rolling path of the double roller.

In comparison with the results obtained in the test welds produced with in-situ global mechanical tensioning (see section 5.3.3) in the current results no clear mitigation effect of the sample distortion due to ISRT can be observed. There is a tendency towards a reduced magnitude of out-off plane distortion, but the limited amount of test welds does not allow to conclude for any systematic trends. As reported in the following paragraph, ISRT does not have a significant mitigation effect on the RS either.

6.3.1.2 Residual Stress

The RS distributions across the weld-line as a function of the varying ISRT down forces applied to the test welds in set #5, as determined using the ID15A EDXRD set-up, are shown in Figure 6.2. The profile of the cross-section of the FSW tool, as well as the 'foot print' of the ISRT rollers to both sides of the weld-line are shown in the figure. It is evident that, at least for the range of roller down forces tested in this investigation, there was no significant effect on the RS distribution. As a result, no further work has been carried out in order to determine the variation of the unstrained unit cell parameter a_0. Consequently the RS distributions presented here are not representative of the actual stress present in the test welds. However, regardless of whether or not the variation of a_0 is applied for the calculation of the residual strain and hence stress, the magnitude and distribution of the calculated longitudinal RS for the as-welded condition are in agreement

with those observed previously in this dissertation (see Figure 5.8) and elsewhere for friction stir welded AA2024-T3 plates (Staron *et al.* 2004; Price *et al.* 2007). An M-shaped longitudinal RS distribution across the weld-line with tensile stress peaks located just outside the edge of the tool shoulder in the HAZ can be observed. Similarly, the tendency for the RS on the advancing side to be slightly larger than on the retreating side is also well documented (Mishra *et al.* 2005; Threadgill *et al.* 2009). The uncertainty in the stress determination can be estimated from the difference between the RS distribution curves for the different test welds to around ±15 MPa, which is in agreement with the ±12 MPa determined from the statistical errors in fitting the diffraction peak data.

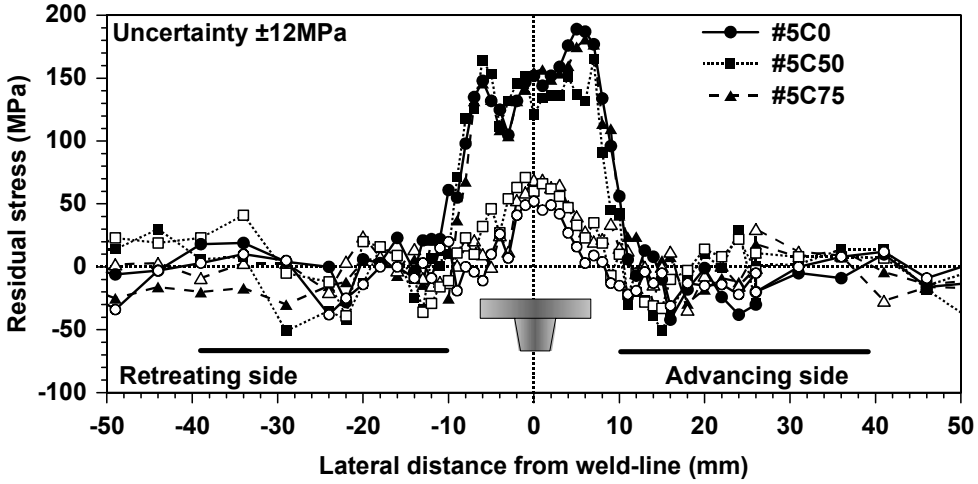

Figure 6.2: Measured RS in the longitudinal (solid markers) and transverse (open markers) direction for the as-welded and the ISRT (50 kN and 75 kN down force) test welds produced in AA2024-T3. The horizontal bars represent the relative position of the double roller and a cross-section of the FSW tool is shown.

From the experimental results it can thus be concluded that ISRT, under the range of conditions investigated in this dissertation, appears to have no effect, either beneficial or detrimental. In contrast, the FEM predictions reported by Wen *et al.* (2009) and depicted in Figure 2.29 display significant compressive RS in the locations where the rollers acted and a 20 % reduction in the longitudinal tensile weld-line and peak RS. These predictions were obtained on the basis of the same size rollers, but at trailing distances of 15 mm and 25 mm respectively. In reality this was impractical with the current FSW tool and double roller design (40 mm trailing distance). From the predictions (see Figure 2.29) it can be concluded that at shorter trailing distances RS may be reduced and in the roller contact area compressive RS can be introduced. This may be attributed to the softer material closer to

the FSW tool as the temperatures are higher allowing for more plastic deformation for a given compressive stress in the plate normal direction. However, examination of the thermal profile and the RS profile as predicted for the as-welded condition in AA2024-T3 by Richards *et al.* (2008a) suggests that the area on either side of the weld-line at the weld tool position would be less than 200 ºC and residually stressed to around -50 MPa in the longitudinal direction. The instantaneous compressive longitudinal stress applied by rollers next to the weld-line would tend to inhibit tensile plastic flow in the weld-line, while significant softening would not be expected at such low temperatures. Therefore, the mitigation effect on the longitudinal weld-line and peak RS should be highest when the rollers are placed right next to the FSW tool. However, due to the geometry of the FSW tool and the design of the double roller this is impractical; hence the rollers have to follow the FSW tool at a certain distance. Unfortunately, with increasing distance the material below the roller is cooler and therefore the rolling effect decreases as the possible plastic deformation for a constant roller down force reduces. In the current experimental investigation the rollers were placed at 40 mm behind the FSW tool (see Figure 3.4a). This greater distance in combination with an insufficient ISRT down force may be the reason for the ineffective ISRT applied in this experimental study, as the material directly beneath the roller was insufficiently soft to allow for plastic deformation.

In order to improve the efficacy of the ISRT technique it would therefore be necessary to use either higher roller down forces, or to get the rollers closer to the hot zone by using much smaller diameter rollers. In turn, this would also increase the normal rolling stress as the contact area reduces. One way to get the roller closer to the weld-line is to apply post-weld roller tensioning (PWRT). The results for the PWRT tensioning studies as performed in this dissertation are presented in the following section.

6.3.2 Post Weld Roller Tensioning

In this section the hardness, the plate distortion and the RS distribution as a function of PWRT down force obtained from the test welds in set #6 produced in 5 mm thick AA2199-T8E74 are presented and discussed.

6.3.2.1 Hardness

The hardness distributions, determined using an automated *Buehler* Vickers hardness testing machine (see section 3.7.2) in the N-T cross-sections of the test welds from set #6 as a function of the applied PWRT down force are shown in Figure 6.3.

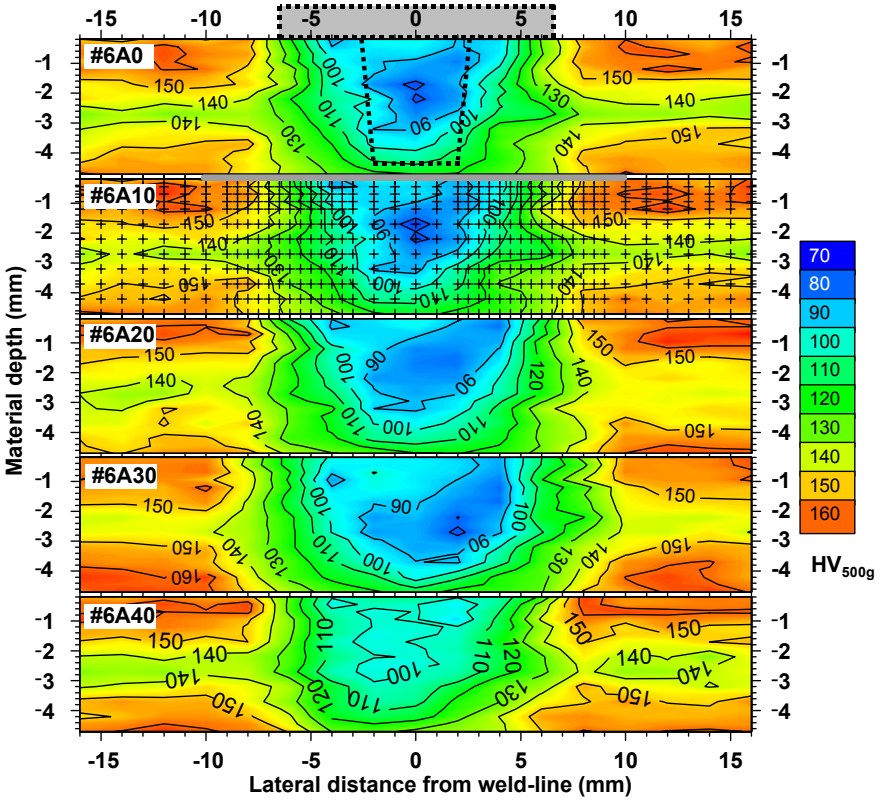

Figure 6.3: 2-D hardness maps on the N-T cross-section plane at mid length of the welding path as a function of PWRT down force in kN (indicated by the second number in the sample designation) for the AA2199-T8E74 welds. In the map corresponding to the as-welded condition (#6A0) the outline of the FSW tool pin and shoulder is shown, while the footprint of the single roller is indicated below. In the 2-D map of test weld #6A10 the measurement positions are marked.

It should be noted that the PM displays a considerable level of through thickness hardness variation, as observed before in this dissertation in the same material (see Figure 5.5), namely: higher hardness near the surfaces (~160 HV_{500g}) relative to the mid-thickness hardness of 130 - 140 HV_{500g}. Such an observation is not unusual for age-hardening aluminium alloy plates and can also be observed in other materials, such as AA7449 (compare Figure 4.6 and 5.4). The variation is likely to be due to the through-thickness gradients of the quenching rate after solutionizing and plastic deformation during the T8E74 aging treatment (for example rolling).

In common with the measurements reported earlier in this dissertation (see section 4.2.3.2 and 5.3.2), the PM hardness falls dramatically in the region that was passed over by the FSW tool with the softened zone being slightly broader at the weld surface than at the weld root, which is due to the shape of the FSW tool and the resulting introduced thermal profile during FSW. The hardness reaches its lowest value (~90 HV_{500g}) on the weld-line ~ 2 mm below the weld surface. There is some evidence that the hardness falls less, but with a broader minimum as the PWRT down force is increased reaching a value of around 100 HV_{500g} for 40 kN down force. Precipitation-hardening aluminium alloys respond to work hardening depending on the their temper, but compared to age-hardening this effect is little (Polmear 1995). However, in the current case the slight increase in hardness may be attributed to this mechanism. Apart from this slight effect, PWRT applied to the cold weld appears to have little influence on the hardness distribution. The hardness at the root of the weld is around 120 HV_{500g} regardless whether PWRT is applied.

6.3.2.2 Distortion

The plate bending and angular distortion for test welds from set #6, as a function of the varying down forces applied by PWRT, are presented in Figure 6.4. The as-welded test weld #6A0 exhibits significant convex bending and concave angular distortion (~3 mm and ~2.5 mm respectively) over the entire test weld length and width. This is qualitatively in agreement with the distortion results obtained in the as-welded test weld in set #1 (see Figure 5.6) produced in the same material with identical FSW parameters. The application of increased PWRT down force results in decreasing levels of distortion, which again is similar to the effect of ISGMT (see Figure 5.6). In particular, in the current investigation, the test weld with 20 kN PWRT down force applied (#6A20) displays the least angular and bending distortion, while higher PWRT down forces reverse the sense of the bending distortion to a concave profile. On the other hand, the angular distortion retains the original concave orientation with respect to the FSW surface, but with less magnitude. However, all the distortion amplitudes are less than those observed for the as-welded test weld #6A0 and therefore PWRT can be considered as an effective method for reducing post weld distortion.

Nevertheless, the precise load required to produce a virtually distortion free test weld may depend on the material in use, the weld and plate dimensions and of course the roller

dimensions. From the results for the current work no firm conclusions with respect to these characteristics are possible and further work is required.

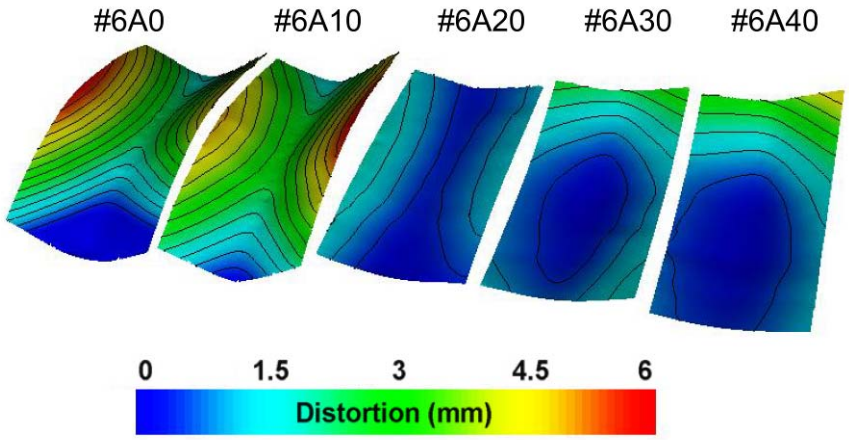

Figure 6.4: Out-of-plane distortion (in mm) of the AA2199-T8E74 friction stir welded plates with increasing PWRT down force in kN (indicated by the second number in the sample designation). The out-of-plane axis is exaggerated by a factor of 20. Each contour line represents an interval of 0.5 mm.

6.3.2.3 Residual Stress

The variation of the unstrained unit cell parameter a_0 was measured in a comb reference sample produced from the as-welded test weld #6A0 on ID15A using the EDXRD set-up (see section 3.3.3). The distribution of the varying local a_0 is shown in Figure 6.5. The data agree well with those obtained in the same material and joined under identical FSW conditions, but with global mechanical tensioning applied during welding (compare Figure 5.7). In detail, there is a slight increase in a_0 at ~±7 mm from the weld-line, which may indicate, that remaining solute precipitated resulting in growth of existing precipitates. This is supported by a slight decrease in hardness at these lateral positions. Closer to the weld-line higher temperatures occur during welding and the a_0 value decreases significantly by ~ 500 micro strain to a constant level across the weld-line. This can be attributed to the fact that in this region the precipitates dissolved, which is supported by Figure 2.37, indicating a decrease in lattice parameter as the alloying elements, for the AA2199 alloy mainly Li and Cu, go into solution. However, in contrast to the data obtained in test weld #3B29 (see Figure 4.2), there is no increase in unit cell parameter at the weld-line. This may be due to the high traverse speed of 400 mm/min, which results in a very short peak temperature exposure sufficient to dissolve existing precipitates, but afterwards

insufficient time at elevated temperature for precipitation to take place. The absence of strengthening precipitates in this region is also indicated by the low hardness at the weld-line.

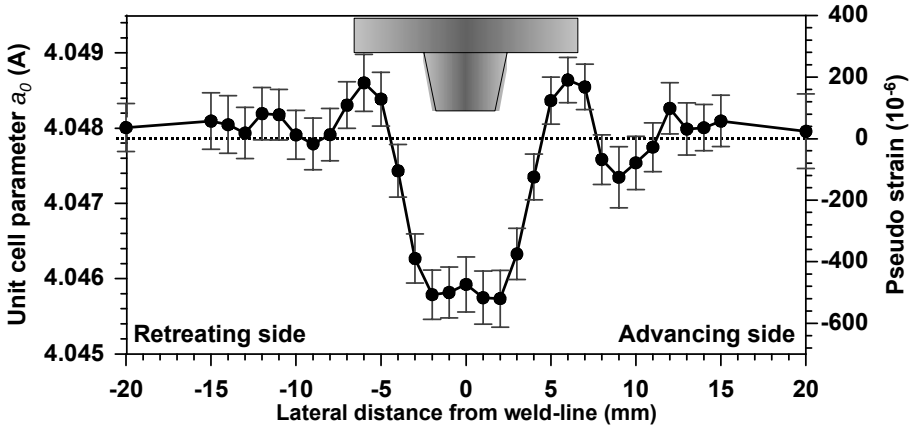

Figure 6.5: The variation of the unstrained unit cell parameter expressed in Ångstrom as well as pseudo strain as determined using the comb method in the AA2199 reference sample extracted from test weld #6C0 produced without any rolling applied.

With the data presented in section 4.2 it has also been shown that the variation of a_0 and the hardness correlate with respect to the spatial distribution across the weld-line as well as through thickness. As such, the hardness is an indicator for variations of a_0 possibly existing in the different test welds. With respect to the hardness variation depicted in Figure 6.3 for the test welds from set #6 no noteworthy changes of the spatial distribution of a_0 for the different PWRT down forces are expected. In fact, it would be surprising if the cold work applied after welding leads to changes in the mainly temperature history dependent unstrained unit cell parameter a_0. As a result the a_0 distribution obtained from the as-welded condition and as shown in Figure 6.5 was used to calculate the residual strain and stress in all test welds in set #6.

The longitudinal RS for the test welds in set #6 that were subject to differing levels of PWRT are shown in Figure 6.6. In accordance with the literature (Peel *et al.* 2003; Staron *et al.* 2004; Price *et al.* 2007; Richards *et al.* 2008a) the longitudinal RS profile for the as-welded condition (#6A0) displays a characteristic M-shape, with weld-line RS of ~170 MPa and peaks of ~220 MPa at ±6 mm from the weld-line, a distance which corresponds closely to the tool shoulder diameter of 13 mm, before falling to 0 MPa, forming a ~20 mm wide zone of tensile RS. In fact, the RS profile for the as-welded condition is very similar in magnitude and shape to that determined in test weld #1A0 (see Figure 5.8), which was

produced under the same FSW conditions, but at a different date indicating the repeatability and reliability of the FSW process. The origin of this M-shaped profile is explained in detail by Richards *et al.* (2008a) and was discussed in section 2.4.4.

In contrast to in-situ roller tensioning (see section 6.3.1), PWRT appears to have a significant effect on the longitudinal RS distribution. With increasing rolling down force the tensile peaks near the edge of the FSW tool shoulder essentially disappear and the weld-line tensile RS decrease. A PWRT down force of 10 kN significantly reduces the weld-line tensile RS to approximately 60 MPa. The comparatively low yield strength σ_{YS} in the weld area, as indicated by the low hardness in the as-welded condition (see Figure 6.3), allows for plastic deformation even at low rolling down forces. For a roller down force of 20 kN the longitudinal RS at the weld-line has reversed in sign, reaching a compressive plateau of around - 70 MPa over ± 5 mm from the

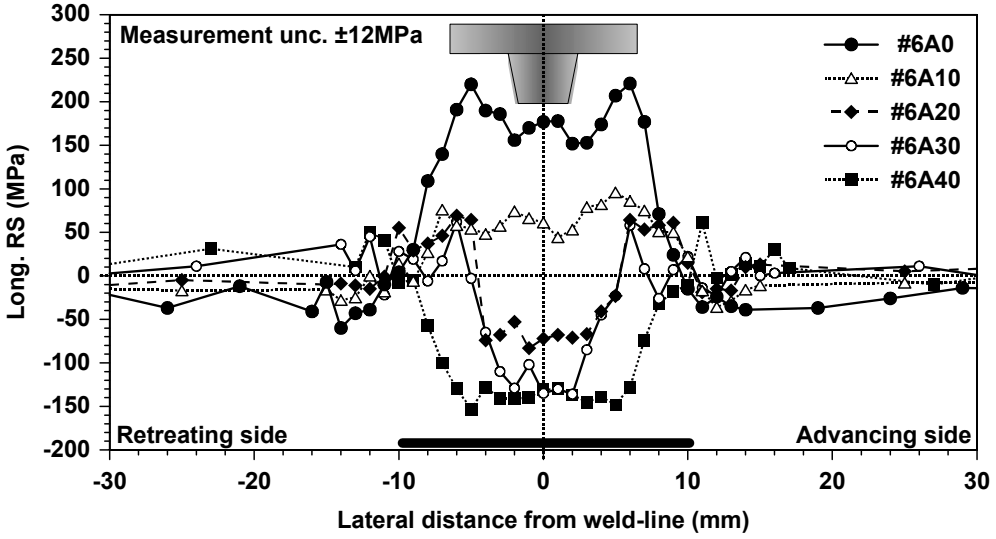

Figure 6.6: Longitudinal RS profiles as a function of PWRT down force in kN (indicated by the second number in the sample designation) for AA2199-T8E74 friction stir welds at mid-thickness. The bar below the stress profiles represents the footprint of the single roll and above the plots a cross-section of the FSW tool is shown.

weld-line bordered by two tensile regions (~70 MPa) approximately 4 mm wide, before falling essentially to zero beyond the footprint of the roller. For 30 kN PWRT down force the compressive stress region around the weld-line has increased to around -120 MPa having a similar width (±5 mm) and is bordered by very narrow tensile peaks (~70 MPa) of ~1 to 2 mm width located at -6 mm and +7 mm from the weld-line. The compressive weld-line RS do not increase further with an even higher down force of 40 kN. This may be

attributed to the fact that the local compressive yield strength is reached, which is supported by the low hardness found in the weld nugget, as shown in Figure 6.3. However, the compressive zone is significantly wider than for 30 kN PWRT and the tensile RS peaks are now located further from the weld-line (±11 mm), i.e. beyond the edge of the roller. This indicates a possible weld zone and hence plate widening, but also the fact that the higher rolling down force may influence the region towards the PM that increases in strength and hardness. The transverse RS are not affected by PWRT and are therefore not displayed.

Interestingly, Wen *et al.* (2009) predicted a similar behaviour for the mitigation of the longitudinal tensile RS in AA2024-T3 plates joined by FSW and subject to different PWRT down forces (see Figure 2.26b). Their model not only predicted a compressive stress limit as was found in this investigation for the 30 kN PWRT test weld but also the widening of the compressive zone with increased roller down forces as was the case for the 40 kN PWRT test weld. However, a slight difference may be found in that the model predicted compressive stress peaks at positions similar to the original tensile peaks for the as-welded condition. Unfortunately, the FEM predictions were carried out for a different alloy and rather than reporting the applied PWRT down force Wen *et al.* (2009) used the thickness reduction upon rolling as a parameter. Hence direct comparison with the experimental results from this investigation is impractical. It is even more complicated, as in reality the PWRT is applied to the rough surface of the weld seam and as such the determination of the thickness reduction by rolling is impractical.

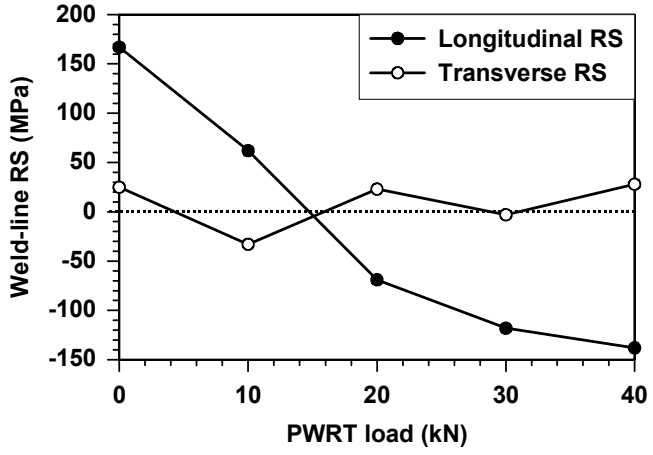

Figure 6.7: Longitudinal and transverse RS as averaged over ±2 mm from the weld-line at material mid-thickness as a function of applied PWRT down forces for AA2199-T8E74 friction stir welds.

Nevertheless, in accordance with observations made on in-situ global mechanical tensioned samples (compare section 5.3.4) the relatively low level transverse RS at ±2 mm from the weld-line appear to be essentially insensitive to the roller tensioning level varying between ±50 MPa as shown in Figure 6.7. Presumably this is because in thin plates the transverse plastic strain is fairly uniform through the depth and varies little along the sheet such that it is simply accommodated by a slight widening of the welded joint in a stress free manner. Figure 6.7 further displays the effect of increased roller down force on the longitudinal RS as averaged over a distance of ±2 mm from the weld-line. In the current case, even though only a few test-welds were available for the investigation a nearly linear decrease in longitudinal RS can be seen for down forces up to 20 kN, with the stress reversing in sign at around 15 kN. For higher PWRT down forces the rate of stress mitigation decreases, which may be attributed to the fact that with increased down force the roller-plate contact area increases and so the rate of the effective compressive stress in the plate normal direction decreases for higher down forces. In addition at some point the local material compressive yield strength σ_{YS} (which in the current case from the maximum compressive RS in Figure 6.6 can be assumed to be ~-150 MPa) may be reached beyond which no further elastic but plastic strain is introduced and as such the compressive RS can no longer increase.

6.3.3 Post Weld Roller Tensioning of Near Application Welds

The investigation of the effect of PWRT in the near application test welds in set #7, namely friction stir welds in integrated stiffener panels (ISP, see Figure 3.2 for schematic of cross-section) made from 7.5 mm thick AA7136-T6 aluminium alloy, is ongoing work and consequently in this section only preliminary results are presented. In addition to the original flat faced roller applied with different PWRT down forces a corrugated roller, as depicted in Figure 3.3d, was used. The rationale of this rolling technique was to increase the local normal stress applied by a single gear tooth and consequently affect a smaller region. As a result, the normal compression and hence longitudinal elongation effect to mitigate the longitudinal tensile RS is expected to increase. The stress results from this experiment are presented here and compared with those obtained in the as-welded test weld. In accordance to the experimental work performed on set #6 the effect of PWRT on the hardness distribution in the ISP joined by FSW is also presented here.

6.3.3.1 Hardness

The variation of the hardness as a function of distance from the weld-line and the weld surface for test welds #7D0 and #7D40 determined as described in section 3.7.2 is shown in Figure 6.8. In both welds the PM displays a hardness of ~200 HV_{500g}, which supports the general assumption that the yield strength σ_{YS} = 628 MPa (Poad 2006) may be assumed to be approximately three times the hardness of the material (Kamp *et al.* 2007). In the AA7136-T6 alloy no noteworthy through thickness variation can be observed. The ISP panels were extruded to near net shape and have been heat treated, quenched and artificially aged before the final cross-section shape, as depicted in figure 3.2, was machined (Poad 2006).

In accordance with previous hardness data (see figure 4.7 and 5.4) in plates made from the AA7xxx series (set #2 – to #4) and joined by FSW, the weld zone in the welds of set #7 is marked by low hardness in the HAZ located just outside the tool pin, while the WN region displays an increased hardness as depicted in Figure 6.8. In the as-welded condition the hardness drops to ~145 HV_{500g} in the HAZ, but increases towards the WN reaching a plateau of ~165 HV_{500g} below the FSW tool shoulder and ~155 HV_{500g} at the weld root. In fact, these hardness profiles are very similar to those found in set #3 and #4 (AA7449-W51 alloy) displaying the typical trapezoidal cross-section shape for FSW in high strength aluminium alloys (compare figure 4.7 and 5.4 or Steuwer *et al.* (2007).

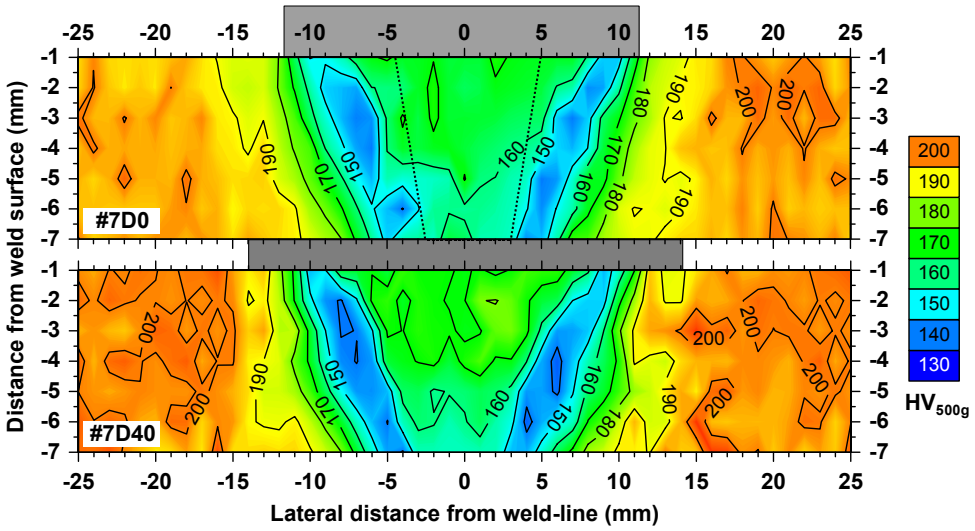

Figure 6.8: 2-D hardness maps as obtained in friction stir welded ISP plates for the as-welded (#7D0) and the 40 kN PWRT (#7D40) condition. A cross-section of the FSW tool is shown in the #7D0 plot while the foot print of the cylindrical PWRT roller is schematically depicted in between the two plots.

With respect to the 40 kN PWRT down force applied to test weld #7D40 similar observations to those in set #6 (see Figure 6.3) as a result of the roller tensioning can be made: a slight increase in hardness and of the width of the WN zone for increased roller loads. However, in the current case the low hardness in the HAZ is depressed to even lower values, which was not observed in the welds in set #6. It is not clear what this could be due to, especially as all test welds in set #7 were produced under identical FSW conditions and the PWRT was applied to the cold weld.

From the local variation in hardness it can be concluded that a significant variation of a_0 as a function of lateral distance from the weld-line, as well as through the material thickness, is likely. On the other hand, no significant differences in the distribution of a_0 between the as-welded and roller tensioned conditions should appear within the test welds of set #7. This is especially the case as the rolling is applied to the cold weld and as such should not affect the unstrained unit cell parameter. However, in order to derive the RS present in the welded components one has to determine the local a_0 carefully.

6.3.3.2 Residual Stress

As mentioned before the investigation of the PWRT effect on the longitudinal RS distribution in the ISP test welds is ongoing work. As a result, to date only the elastically strained unit cell parameter a in the longitudinal and transverse direction in the test welds #7D0, #7D25, #7D40 and #7D50 as a function of lateral distance from the weld-line as well as from the weld surface has been determined. The variation of the unstrained unit cell parameter a_0 is unknown to date. Consequently, the RS as presented in this section can not be taken to be representative of those actually present in the ISP test welds. However, it should be possible to observe the effect of the increased PWRT down forces as long as the raw diffraction data are treated in the same manner.

Figure 6.9 compares the longitudinal RS distribution as a function of lateral distance from the weld-line and through material thickness for a) the as-welded and b) and c) the flat roll roller tensioned conditions in the AA7136-T6 ISP panels with 25 and 40 kN down force respectively. The stress plots cover a region of ±29 mm from the weld-line as in the region from ±30 to ±44 mm the integrated panel stiffeners prohibited the strain measurements due to beam attenuation (material thickness of ~40 mm). However, beyond the stiffeners further measurements were performed in the region from ±45 to ±80 mm from

the weld-line. For the RS calculations the longitudinal and transverse stress boundary conditions: longitudinal stress balancing and zero transverse stress at the outer edges respectively were applied over the region of ±80 mm. As a result the longitudinal stresses shown in Figure 6.9 may appear to be in imbalance over the displayed area in the figure.

Regardless of errors arising from inappropriate use of a global a_0, the stress distribution in the as-welded condition is similar to that found in the test welds in set #3 (see section 5.3.4). No distinct stress peaks, as sometimes reported for the HAZ of friction stir welds (Donne *et al.* 2001; Sutton *et al.* 2002; Mishra *et al.* 2005) are apparent in this case.

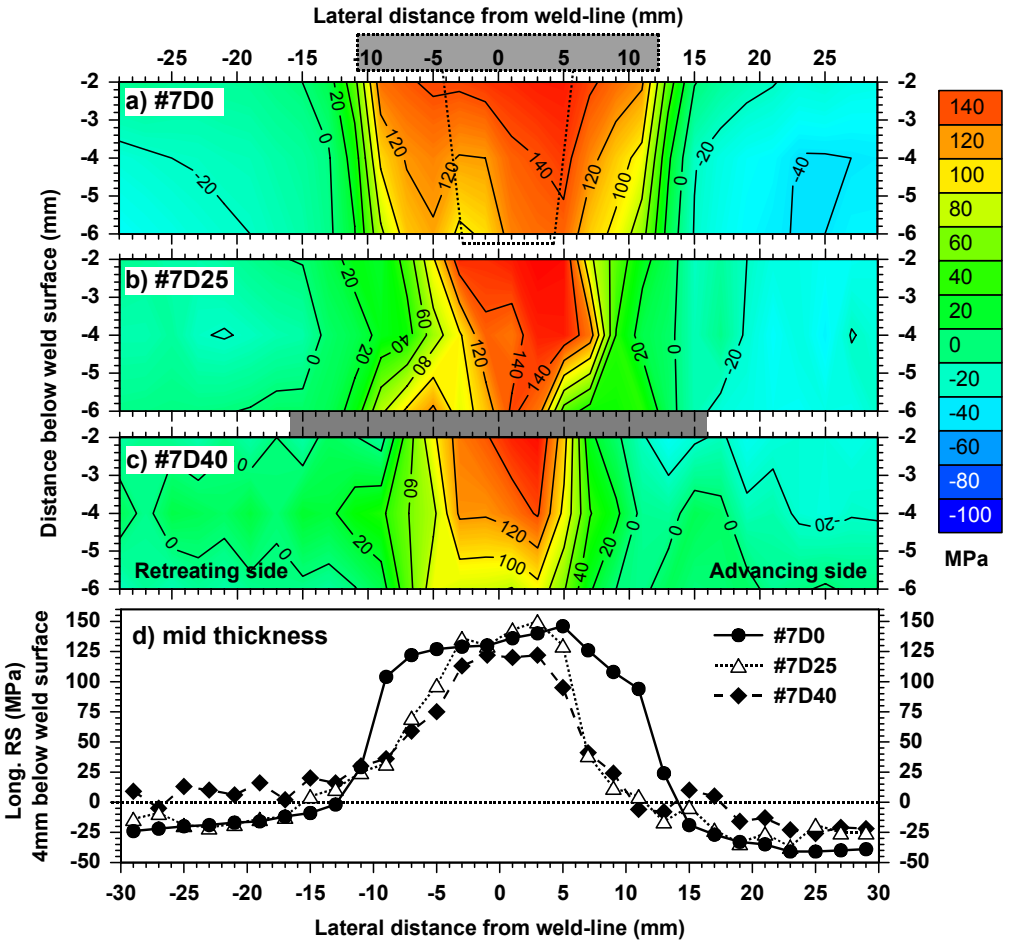

Figure 6.9: 2-D maps (a-c) of the longitudinal RS distribution in ISP test welds in AA7136-T6 joined by FSW and subject to varying PWRT down forces in kN (indicated by the second number in the sample designation). Further, line plots of the stress distribution 4 mm below the weld surface were extracted for direct comparison (d). Note these are preliminary results as the local variation of the unstrained unit cell parameter a_0 was not applied for the stress calculation. The cross-section profile of the FSW tool and the foot print of the cylindrical flat roller are included. The measurement uncertainty is ±17 MPa.

However, the difference in the stress profile may be due to the in this case not applied variation of the unstrained unit cell parameter. In the current case, the RS range from the compressive PM (-20 to -40 MPa) turning tensile at ~±14 mm and rising steadily towards the weld-line before reaching a tensile stress plateau of ~130 to ~140 MPa ranging over ±10 mm from the weld-line near the weld surface. The width of this tensile plateau reduces towards the weld root forming the typical trapezoidal weld zone shape (Sutton *et al.* 2002; Mishra *et al.* 2005; Threadgill *et al.* 2009). A slight tendency of higher stresses on the weld advancing side can be observed in the as-welded condition, which is also a common feature (see Figure 5.9a and Figure 6.2).

The effect of PWRT with increasing down force on the longitudinal RS distribution is clearly visible in the figure. The width and at some point even the depth of the tensile zone reduces with increasing down forces. The narrowing of the tensile zone may be due to the low hardness in the HAZ as can be seen in Figure 6.8 and therefore low yield strength σ_{YS} resulting in more plastic elongation in the longitudinal direction and as such a decrease in RS. The same behaviour can be observed in the results obtained from set #6 (Figure 6.6), but the narrowing was not predicted by Wen *et al.* (2009). Somewhat surprising is the fact that the region of tensile RS appears to decreases in depth for high loads indicating that PWRT is more effective near the weld root even though it was applied to the weld surface. It is not clear why this is the case, but here also the low hardness (compare Figure 6.8) hence low local yield strength σ_{YS} may allow for more plastic elongation hence a decrease in longitudinal RS. However, this remains arguable. On the other hand, the peak tensile RS of ~150 MPa on the weld advancing side just below the tool shoulder is not significantly affected by PWRT which may be due to the fact that the applied rolling down forces are insufficient to cause plastic deformation in this region of the WN. Presumably the higher hardness (compare Figure 6.8) and yield strength as a result of post weld natural aging before PWRT is responsible for the less effective PWRT in this area. This is in agreement with the predictions made by Wen *et al.* (2009) who reported a decrease of the tensile weld-line RS while tensile stress peaks remained at the outer edge of the WN zone (compare Figure 2.26b).

As depicted in Figure 6.9d, at the weld-line at mid material thickness the trend of the predictions by Wen *et al.* (2009) and the experimental results obtained in set #6 agree with the current data even though the reduction in longitudinal tensile RS is less. At the weld-line the RS reduce from ~140 MPa for the as-welded condition by ~20 MPa in test weld

#7D40, while in set #6 a reduction of ~110 MPa was observed for the same PWRT down force. Wen *et al*. (2009) reported an even greater reduction of ~440 MPa for a 10 kN PWRT down force. Such differences may be attributed to the fact that the welds in set #6 and the FEM predictions were both based on less strong materials (set #6: AA2199-T8E74 σ_{YS} = 400 MPa, predictions: AA2024-T3, σ_{YS} = 345 MPa) and in both cases smaller rollers (ø = 100 mm and 20 mm wide compared to the current ø = 160 and 28 mm width) were used resulting in a much higher normal stress. Nevertheless, in general the stress data from set #6, set #7 and the predictions made by Wen *et al.* (2009) agree. All data suggest the trend that PWRT with increased rolling down forces or smaller diameter rollers significantly mitigates the longitudinal tensile RS and in similarity to in-situ global mechanical tensioning (see section 5.3.4) may introduce compressive stresses to the WN region.

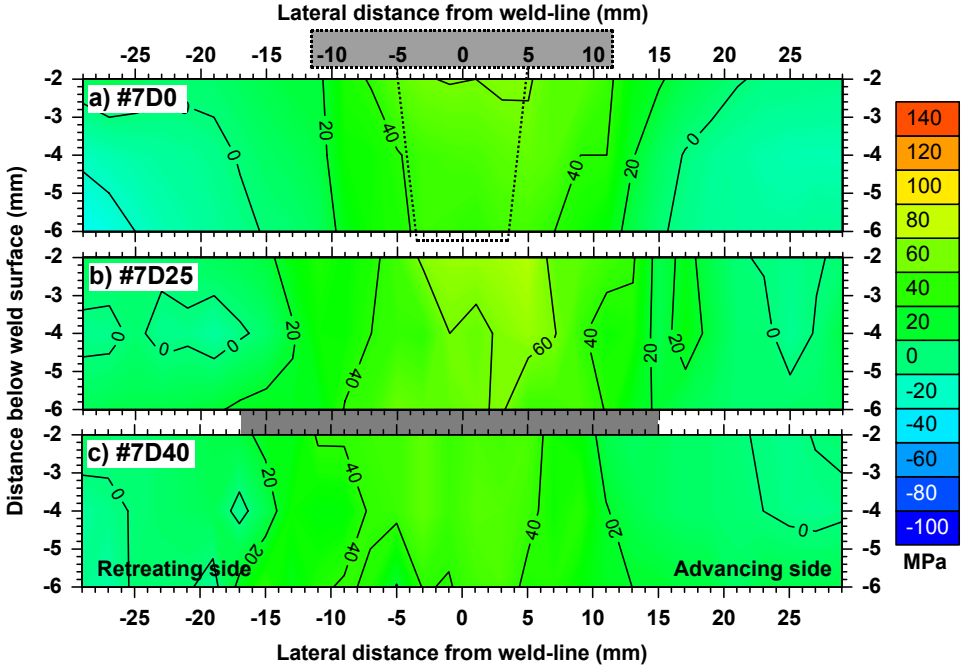

Figure 6.10: The distribution of transverse RS in ISP test welds in AA7136-T6 joined by FSW and subject to varying PWRT down forces in kN (indicated by the second number in the sample code). Note these are preliminary results as the local variation of the unstrained unit cell parameter a_0 was not applied for the stress calculation. The cross-section profile of the FSW tool and the foot print of the cylindrical flat faced PWRT roller are included. The measurement uncertainty is ±15 MPa.

As seen before the RS in the transverse direction is largely unaffected as displayed in Figure 6.10. As is common for FSW in this direction significantly lower magnitude stresses occur (Staron *et al.* 2004) and in the current investigation reach up to ~60 MPa only, which is less than 10 % of the original PM yield strength σ_{YS} of 628 MPa (Poad 2006).

As a result of the relatively low effect of PWRT in the ISP welds in set #7 with respect to the magnitude of the high weld-line tensile RS the cylindrical flat faced roller was replaced by a corrugated roller with a gear-wheel shaped profile as shown in Figure 3.3d. The rationale behind this idea is to decrease the contact area and thereby increase the local stress in the plate normal direction. In addition the rolling down force was raised to 50 kN. The preliminary longitudinal and transverse RS results (the variation of the unstrained unit cell parameter a_0 was not determined) in the N-T plane are shown in Figure 6.11.

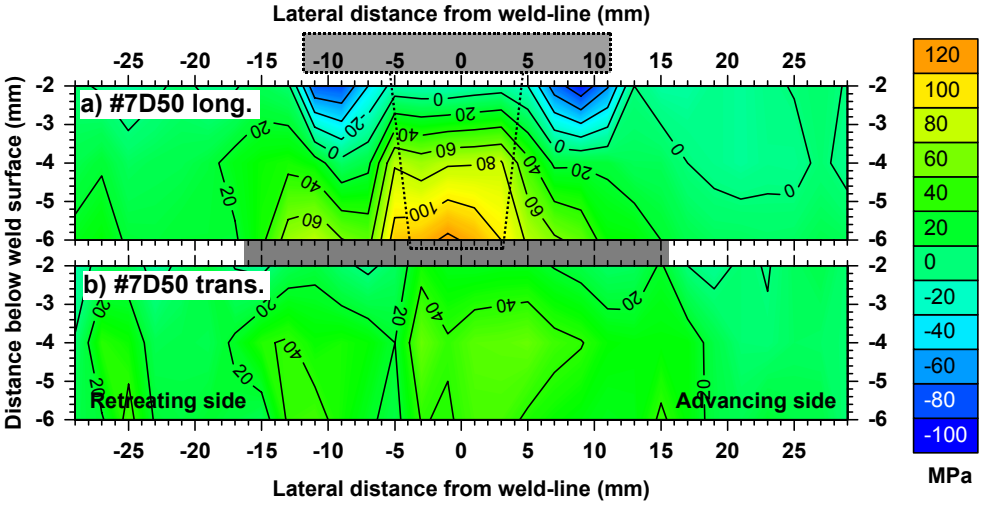

Figure 6.11: The longitudinal (a) and the transverse(b) RS across the weld-line in test weld #7D50 rolled with a corrugated roller and 50 kN PWRT down force. The cross-section profile of the FSW tool (a) and the foot print of the width of the corrugated PWRT roll (in between the two plots) are displayed. The measurement uncertainty is ±17 MPa.

In comparison to the as-welded condition (see Figure 6.9a) the test weld #7D50 treated with the corrugated roller displays significant differences in the stress profile: namely a stress free region in the WN right below the welding and rolling surface with adjoining compressive stress peaks of up to ~-80 MPa on each side of the weld. With increasing depth these peaks turn tensile. On the other hand, near the weld root the lateral RS distribution is very similar to that observed in the test weld #7D40 with a stress plateau of ~100 MPa ranging over ±4 mm from the weld-line before falling to the low PM stress level to each side. The corrugated roller has a much stronger RS mitigation effect in the longitudinal direction than the flat roller, but apparently over a shorter distance through depth. The reduced contact area (solely due to reduction of the contact length along the rolling direction, the roller width is identical to that of flat face roller) in combination with the increased PWRT down force introduces sufficient compressive stress in the plate normal

direction and elongates the material along the rolling direction and as such reduces the RS near the rolling surface. Hereby, the areas with a lower yield strength σ_{YS} as indicated by low hardness values (see Figure 6.8) are more prone to the plastic elongation effect and high compressive stresses may form. In accordance with the previous results the corrugated roller does not affect the RS in the transverse plate direction.

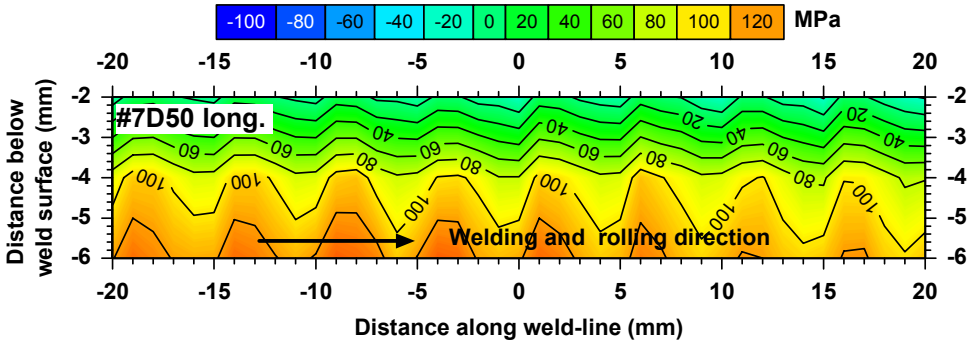

Figure 6.12: The longitudinal RS profile as a result of the applied corrugated roller with 50 kN PWRT down force along the welding direction in the N-L cross-section plane as determined at 0 mm from the weld-line. Rolling and FSW direction coincide.

The through thickness distribution of the RS acting along the welding direction determined at the weld-line is plotted in Figure 6.12. In this graph the effect of the numerous small contact locations of each tooth of the corrugated roller along the rolling path can be observed, which is marked by the periodically repeating wave-like formed low stress areas near the weld surface. Naturally, two stress minima are separated corresponding to the distance of two neighbouring teeth on the roller. In the current case this amounts to 5 mm. Unsurprising, the rolling effect reduces with increased material depth. Presumably, the plastic deformation at one depth level leads to a reduction in the normal stress as well as compression and hence longitudinal plastic elongation at an even deeper level. As a result the stress free surface level turns tensile towards the weld root reaching a level of ~120 MPa, which is similar in magnitude to what was observed in the RS plot displayed in Figure 6.11a.

6.4 CONCLUSIONS

In conclusion from the preliminary results of this first systematic experimental investigation into the effect of ISRT and PWRT on the RS distribution and weld distortion in high strength aluminium alloys joined by FSW the following observations were made:

- ISRT as applied in the current case has little, to no, mitigation effect on neither the plate distortion nor the RS distribution.
- Higher rolling down forces, or smaller diameter rollers trailing the FSW tool at shorter distances are believed to increase the RS and distortion mitigation effect, even though this may be restricted geometrically.
- The results obtained for the PWRT applied to the cold weld show this technique to be a powerful tool for the reduction of longitudinal tensile RS and is believed to work by a combination of normal compression as a result of the rolling down force and subsequently plastic elongation along the rolling direction.
- If applied carefully, essentially stress free welds can be produced along with low magnitudes of distortion. Excessive rolling down forces may even introduce compressive stresses to the weld-line area in combination with a change of the sense of the plate distortion.
- The transverse RS are not significantly affected by PWRT.
- The amount of the reduction of longitudinal RS is a function of the applied PWRT down force as well as the roller size and shape of the rolling surface. Increased rolling down forces applied with smaller diameter rollers increase the mitigation effects.
- Alternatively, the application of corrugated rollers results in significantly smaller contact areas and as such can be used to increase the local normal stress and subsequently introduce more plastic elongation in the plate longitudinal direction. However, a smaller contact area appears to result in a reduction of the depth of the rolling effect.
- The efficacy of PWRT as applied to the cold weld depends mainly on the local distribution of the yield strength, which is indicated by the hardness variation across the weld and through thickness. Low hardness and hence yield strength allow for increased plastic elongation by rolling and as such the RS mitigation effect is higher than in harder regions.

The results of this preliminary investigation are promising in terms of effectiveness for the reduction of weld RS and plate distortion. Especially the PWRT technique appears to be very effective and due to its simple application may seriously be considered for industrial applications. Nevertheless, as the conducted research and the presented results are only of

preliminary character, significantly more detailed research is required in order to understand the mechanisms acting. Ideally, future research should result in a simple rule of thumb for these stress engineering techniques in order to allow for simple and fast application of these techniques during design and industrial production of welded components.

7 SUMMARY AND FUTURE WORK

7.1 SUMMARY

The application of stress engineering methods intends to influence the welding process itself or the final weld such that the welding residual stresses (RS) in combination with the in-service loads allow for the best possible component life cycle performance. In most cases this requires a reduction of tensile RS, as these stresses generally develop during welding processes. These tensile stresses in combination with external tensile in-service loads may cause premature failure of the component as the material yield strength is exceeded leading to deformation or fracture of the component.

Stress engineering techniques reduce tensile stresses by minimizing the elastic misfit between the tensile weld-line and the parent material (PM) which usually balances the tensile stresses by compression. This misfit arises during welding by plastic compressive yielding in front of the welding tool due to expansion of the hot material and the constraining cold PM. Upon cooling behind the welding tool the material shrinks which is again constrained by the PM and as a result tensile plastic yielding occurs. Finally, in the cold weld the weld-line material remains too ‘short’ compared to the PM and as such it is in tension.

Closely related to the RS distribution in welds is the component distortion. Through thickness gradients of tensile or compressive stresses acting along or across the weld-line may relax by deforming the component resulting in bending / buckling or angular distortion. A reduction of the magnitude of RS or stress gradients by stress engineering should therefore result in reduced component distortion.

In this dissertation the stress mitigation effects of three mechanical stress engineering techniques for mitigation of welding residual stress (RS) in high strength aluminium alloy plates joined by friction stir welding (FSW) were investigated experimentally using neutron and synchrotron X-ray diffraction. In detail the in-situ global mechanical tensioning (ISGMT), the in-situ roller tensioning (ISRT) and the post weld roller tensioning (PWRT) techniques, applied to friction stir welds in various aluminium alloys and different geometries as well as joined under different FSW conditions thus representing a wide variety of material and welding conditions, were investigated.

ISGMT is the elastic stretching of the cold plates along the weld-line prior to and during welding. The load is released when the weld has cooled down. This tensile loading reduces the compressive plastic yielding in front of the approaching FSW tool and increases the tensile plastic yielding behind the tool and as such reduces the resulting elastic misfit between the weld-line and the PM. If applied properly, ISGMT can be used to produce essentially stress free welds or even introduce compressive RS to the weld-line. To date a value of 20 to 40 % of the material room temperature yield strength σ_{YS} was reported as the optimum tensioning load for producing a stress-free weld in high strength aluminium alloys using FSW. However, this wide range results in significant uncertainty about the post welding condition of the component.

Roller tensioning was only recently proposed for mitigation of welding RS in high strength aluminium friction stir welds. Very little was known about the precise mechanisms acting during the application of roller tensioning and the precise parameter values necessary for stress-free weld production are unknown. However, it is believed that ISRT by rolling the softened material next to the weld-line using a double roller trailing the welding tool closely compresses the material below the roller in the plate normal while elongating it in the rolling direction. Ideally, this process leads to elongation of the weld-line material which results in increased plastic tensile yielding upon cooling and as such reduces the final elastic misfit. On the other hand, PWRT applied directly to the cold weld-line material using a single roller plastically reduces the plate thickness slightly, but enough to plastically elongate the weld-line material, thus reducing the elastic misfit between weld-line and PM. As the roller tensioning techniques in combination with FSW are relatively new no systematic experimental work had previously been reported in the literature. To date it is not clear what roller down force is required to produce stress free welds.

The aim of this dissertation was to identify the precise correlation of the applied ISGMT load and the achieved reduction in RS and component distortion. Further it was of interest to identify possible effects of this technique on the post weld mechanical and microstructural properties of the test welds investigated. A similar approach was used to study the roller tensioning techniques, even though the primary aim was to show the effectiveness of these techniques and to give a first approach for an optimized application of these techniques.

The RS as a function of the applied stress mitigation technique, in case of the ISGMT as a function of the tensioning load and for ISRT and PWRT as a function of the roller down force, were investigated at mid material thickness and mid weld path length. In case of thick material, the RS distribution was determined at several material depths. The RS were obtained using angular dispersive neutron diffraction (ADND) and energy dispersive synchrotron X-ray diffraction (EDXRD). The experimental RS results were compared with finite element modelling predictions. In addition the component distortion, the weld microstructure and the hardness distribution were investigated as functions of the applied stress mitigation techniques.

The investigations performed in this dissertation revealed that the ISGMT and the PWRT are very powerful techniques for mitigation of RS and distortion in the welding direction, while the ISRT technique, at least for the welds tested in this work, did not result in noteworthy stress mitigation. The following conclusions were made:

- ISGMT was found to mitigate the longitudinal tensile RS following a simple rule of thumb: namely that 1 MPa of in-situ tensile loading results in a reduction of the weld-line stress by 1 MPa. While this rule of thumb can directly be applied to thin welds (up to 5 mm) with a low through thickness variation of the longitudinal RS, in thick welds (in this dissertation a 20 mm thick weld was tested) a decreasing tensioning effect with increasing material depth was observed. This is believed to be due to the lower welding temperatures towards the weld root resulting in less material softening and, as such, reduced plastic yielding effect by ISGMT. However, in the thick welds right below the tool shoulder the tensioning effect was 1:1. In each case tested, the ISGMT along the welding direction did not affect the RS in the transverse or normal plate direction. Along with the reduction in RS decreased component bending distortion was observed and in some cases the optimum ISGMT load for RS minimisation coincided with that required to diminish the bending distortion. On the other hand, in each case tested the angular distortion increased with increasing ISGMT loads. This is believed to be due to a misalignment effect of the ISGMT load and the mid thickness plane of the plates leading to a plate lift off of the backing plate during FSW. With respect to the post weld microstructural and mechanical properties (to the extent tested in this dissertation) little to no variation due to the ISGMT was found.

- ISRT, to the extent studied in this dissertation, was found to be more or less ineffective with respect to mitigation of RS and distortion. This may be due to the rolling down force being too small or the roller diameter and consequently the contact area being too big, resulting in too little plastic normal compression and consequently longitudinal elongation next to and as such an elongation of the weld-line material. An additional reason could be that the trailing distance between the double roller and FSW tool was too big and as such the advantage of plastically elongating the softened material close to the weld zone could not be made use of.
- PWRT was found to be very effective for reduction of the welding RS and distortion. When the roller down force exceeded a certain value even compressive stresses were produced. It was also shown that a reduction of the contact area, which can be achieved by using a corrugated or a smaller diameter roller, results in increased elongation. However, this resulted in less penetration depth of the elongation effect. From the welds tested no firm conclusion about an optimized rolling down force can be made, but in similarity to the ISGMT, this parameter may depend on the RS present in the as-welded condition. Further parameters affecting the RS reduction may be the roller diameter and width defining the roller contact area as well as the surface geometry.

Each of the stress engineering techniques tested was applied to plates with straight FSW paths only. While the ISGMT can be applied only to such weld geometries, the roller tensioning is applicable to various non-linear weld paths as the rollers can be guided along a complex weld path contour. However, in any case heavy and expensive machinery to produce either the high ISGMT loads or to supply the roller down forces and to insure appropriate support of the components during rolling is required and as such these techniques are primarily applicable for weld fabrication in factories. For in-field application these techniques are less useful. With respect to the SEALS program from which this dissertation originated, the experimental results obtained in this work and the finite element modelling work performed by D. Richards at the University of Manchester, UK, were used to finalize the working package for the investigation of mechanical stress engineering techniques successfully. Further, while the ISGMT is considered for application during the production of wing ribs and fuselage skin panels by the AIRBUS company, the PWRT will

be investigated in more detail in a future project. However, the Bombardier company is using this technique for test fabrication of large scale single segment wing skin components from integrated stiffener panels for production of their business aircraft. Especially for this application further testing will be performed.

While the above summarized experimental studies are of applied research character, in this dissertation two additional experimental studies were performed with a scientifically orientated background. On the one hand, the importance of the local variation of the elastically unstrained unit cell parameter a_0 for the determination of RS in weldments of high strength aluminium alloys using diffraction methods was investigated. Several methods for the determination of this parameter exist. However, to date no systematic comparative study was performed and as a result it is not clear to what extend these methods are applicable to differently welded structures. This dissertation aims to clarify this issue to some extent. The second fundamental study performed in this dissertation was to determine the effect of relaxation of welding residual stresses as a function of component size. It is well known that RS relax and redistribute upon material removal. However, the extent of stress relaxation in butt welded structures has not been quantified in a systematic manner before. This problem was also subject to this dissertation. The investigations performed on these two issues lead to the following conclusions:

- Three different methods, namely the plane stress assumption, the comb and the $\sin^2\psi$ methods for measurement of the local unstrained unit cell parameter a_0 were compared. The aim was to identify the method best suited for the determination of RS in the test welds for the investigations of stress engineering techniques. In this study, each of the methods was applied to identical samples and the results compared with each other. It was found that the plane stress assumption method is very sensitive to the material thickness while the comb and the $\sin^2\psi$ methods can be applied to any weld geometry. However, these techniques require careful sample preparation and extensive sample manipulation during the strain measurements. The plane stress assumption technique is simple to apply and applicable to welds below or equal to 5 mm thickness. With respect to the effect of the varying a_0 parameter it was shown that in case of joining high strength aluminium alloys failure to apply this locally varying parameter for the stress determination using diffraction

techniques may result in significant deviations from the real RS present in the components. Consequently, the lifetime performance of the component may seriously be over –or underestimated.

- Stress relaxation as a function of component size was investigated to determine the degree to which the RS in the test welds investigated in the above summarized work are representative of those present in real size engineering components. Therefore a series of welds produced in different materials using different welding techniques were progressively sectioned to smaller size. For each step the RS distribution was determined. It was found that the RS start decreasing once the weld is cut shorter than a certain length which, by using an empirical approach, was found to depend on the width of the tensile region around the weld-line. In order to contain RS comparable in magnitude (100 % to 90 %) to those in real size components, test welds should have a minimum length of 17 × to 8 × the width of this tensile region respectively. For reduction of the plate width a similar effect was found, but the limited number of test welds investigated in this dissertation does not allow for firm conclusions. With respect to the welds investigated for the stress engineering techniques it was found, that except for one set of test welds (set #4) all welds were sufficiently long to represent RS magnitudes present in real size components.

7.2 FUTURE WORK

With respect to ISGMT, the experimental investigations performed in this dissertation in combination with the FEM work by D. Richards from the University of Manchester were successful in terms of understanding the mechanisms acting and the parameter optimization. However, while the RS can effectively be reduced, the effect on the post weld mechanical properties such as fatigue or crack corrosion should be studied in order to verify the advantages achieved by ISGMT. While the technique was applied to friction stir welds in age-hardening aluminium alloys in this dissertation, future work should be extended to the application of ISGMT to other materials and welding techniques. This could generalize the 1:1 relationship. Further, the technique can be applied to other weld geometries, such as lap- or T-joints with linear weld paths. Further, for industrial application of ISGMT improvement of the technique for applying high loads may be desired in order to optimize

and simplify the process. To date FEM predictions were performed only for thinner welds. Consequently the stress behaviour in thick welds due to ISGMT should be subject to future modelling activities.

The roller tensioning techniques are recent approaches for stress and distortion mitigation and as such this dissertation aimed to give a first insight into the effectiveness of each technique. For improved understanding of the mechanisms acting during rolling systematic sets of test welds should be investigated with a view of the RS and distortion mitigation as well as the post weld mechanical and microstructural property response. Ideally, the test welds should be produced with varying parameters such as the down force, the roller diameter and width as well as the roller surface. The effect of machining off the weld seam before PWRT is applied could be investigated as this increases the reliability and repeatability of the process as the rolling conditions are better controlled. Further, in order to generalize the results the investigations should be extended to different materials and welding techniques and experimental results should form the basis for FEM model validation. Further, detailed studies of the post weld rolling effect on texture formation in the weld-line may be of interest. This is especially the case for materials with an initial preferred orientation which can be of use for the component design. Besides the reduction of welding RS the local rolling introduces a preferred orientation to the grain structure in the weld-line that is similar to that of the PM.

With respect to the investigation of the stress relaxation as a function of the component size it is worth continuing the work in thicker welds as well as different weld geometries (for example lap- or T-joints). Ideally, in order to generalize the rule of thumb determined in this dissertation, thick welds should contain a tensile zone less wide then the material thickness. This would allow to quantify, whether the correlation between the width of the tensile zone and the achieved stress relaxation depends solely on the width or if it depends on the greatest dimension of the tensile zone, which would be the plate thickness in that case. However, experimental results from such investigations could be incorporated for FEM predictions.

An additional project that requires further attention is the robotic arm sample manipulation system. In this dissertation the advantages of using serial robotic arms for complex sample manipulation were discussed and shown by application to one sample manipulation process. However, to date the system has been developed to prototype level

only and improvement to a level for simple use and fast implementation on any strain measurement beam-line is desired.

8 REFERENCES

Ahmed, M. M. Z. and Wynne, B. P. (2008). "*An Investigation of Hardness, Microstructure and Crystallographic Texture in Thick Sectioned Friction Stir Welded AA6082-T6.*" 7th International Symposium on Friction Stir Welding., Awaji Island, Japan, 11p.

Ali, A., An, X., Rodopoulos, C. A., Brown, M. W., O'Hara, P., Levers, A. and Gardiner, S. (2007). "*The effect of controlled shot peening on the fatigue behaviour of 2024-T3 aluminium friction stir welds.*" International Journal of Fatigue, **29**(8), 1531-1545.

Allehaux, D., Petit, G. and Campagnac, M. H. (2003). "*Microstructure and Properties of a FSW 7349-T6 Aluminium Alloy.*" 4th International Symposium on Friction Stir Welding, Park City, Utah, USA, 8p.

Allen, A. J., Hutchings, M. T. and Windsor, C. G. (1985). "*Neutron diffraction methods for the study of residual stress fields.*" Advances in Physics, **34(4)**, 445-473.

Altenkirch, J. (2005). "*Entwicklung einer robotergestuetzten Messplattform zur Eigenspannungsmessung in metallischen Werkstoffen (Development of a Robotic Arm based Sample Manipulation System for Residual Stress Determination in Metals).*" Diploma thesis, BTU Cottbus, Cottbus, 100p.

Aoki, S., Nishimura, T. and T, H. (2003). "*Reduction Method for Residual Stress of Welded Joint using Random Vibration.*" 17th International Conference on Structural Mechanics in Reactor Technology (SMiRT 17), Prague, Czech Republic, 4p.

ASM_2. (2001). "*ASM Handbook - Volume 2 Properties and Selection: Nonferrous Alloys and Special-Purpose Materials."* AMERICAN SOCIETY FOR METALS, Materials Park, OH, USA.

ASM_4. (2001). "*ASM Handbook - Volume 4 Heat Treating."* AMERICAN SOCIETY FOR METALS, Materials Park, OH, USA.

ASM_9. (2001). "*ASM Handbook - Volume 9 Metallography and Microstructures."* AMERICAN SOCIETY FOR METALS, Materials Park, OH, USA.

Attallah, M. M., Davis, C. L. and Strangwood, M. (2006). "*The influence of intermetallic particles on the formation of the 'onion rings' structure in aluminium-based alloys friction stir welds.*" 6th International Symposium on Friction Stir Welding, Saint-Sauveur, Montreal, Canada, 11p.

Attallah, M. M., Davis, C. L. and Strangwood, M. (2007). "*Influence of base metal microstructure on microstructural development in aluminium based alloy friction stir welds.*" Science and Technology of Welding and Joining, **12**(4), 361-369.

Barret, C. and Massalski, T. B. (1980). "*Structure of Metals."* A. Wheaton & Co. Ltd., Exeter.

Benavides, S., Li, Y., Murr, L. E., Brown, D. and McClure, J. C. (1999). "*Low-temperature Friction Stir Welding of AA2024 aluminium.*" Scripta Materialia, **41**(8), 809-815.

Berdichevsky, V. and Foster, D. J. (2003). "*On Saint-Venant's principle in the dynamics of elastic beams.*" International Journal of Solids and Structures, **40**(13-14), 3293-3310.

Bhide, S. R., Michaleris, P., Posada, M. and DeLoach, J. (2006). "*Comparison of buckling distortion propensity for SAW, GMAW, and FSW.*" Welding Journal, **85**(9), 189-195.

Birch, S. (2005). "*Airbus Advances A350, A380.*" Aerospace Engineering: Technology update, **2005**(11).

Bussu, G. and Irving, P. E. (2003). "*The role of residual stress and heat affected zone properties on fatigue crack propagation in friction stir welded 2024-T351 aluminium joints.*" International Journal of Fatigue, **25**(1), 77-88.

Cavaliere, P., Nobile, R., Panella, F. W. and Squillace, A. (2006). "*Mechanical and microstructural behaviour of 2024-7075 aluminium alloy sheets joined by friction stir welding.*" International Journal of Machine Tools and Manufacture, **46**(6), 588-594.

Chao, Y. J., Qi, X. and Tang, W. (2003). "*Heat Transfer in Friction Stir Welding--- Experimental and Numerical Studies.*" Journal of Manufacturing Science and Engineering, **125**(1), 138-145.

Christner, B., McCoury, J. and Higgins, S. (2003). "*Development and Testing of Friction Stir Welding (FSW) as a joining method for Primary Aircraft Structure.*" 4th International Symposium on Friction Stir Welding, Park City, Utah, USA, 9p.

Clausen, B., Leffers, T. and Lorentzen, T. (2003). "*On the proper selection of reflections for the measurement of bulk residual stresses by diffraction methods.*" Acta Materialia, **51**(20), 6181-6188.

Clausen, B., Lorentzen, T. and Leffers, T. (1998). "*Self-consistent modelling of the plastic deformation of fcc poly-crystals and its implications for diffraction measurements of internal stresses.*" Acta Materialia, **46**(9), 3087-3098.

Colegrove, P. (2000). "*3 Dimensional Flow and Thermal Modelling of the Friction Stir Welding Process.*" 2nd International Symposium on Friction Stir Welding, Gothenburg, Sweden, 10p.

Colegrove, P. and Shercliff, H. R. (2005). "*3-Dimensional CFD modelling of flow round a threaded friction stir welding tool profile.*" Journal of Materials Processing Technology, **169**(2), 320-327.

Colegrove, P., Shercliff, H. R. and Threadgill, P. L. (2003). "*Modelling and development of the Trivex friction stir welding tool.*" 4th International Symposium on Friction Stir Welding, Park City, Utah, USA, 16p.

Csontos, A. A., Gable, B. M., Gaber, A. and Starke, J. E. A. (2000). "*The Effect of Quench Rate on the Microstructure and Properties of AF/C-458 and AF/C-489 Al-Li-Cu-X Alloys.*" Mat. Sci. Forum, **331-337**, 1333-1340.

Cullity, B. D. (1978). "*Elements of x-ray diffraction."* Addison-Wesley publishing company.

Dawes, C. J., Karger, S. A., Dickerson, T. L. and Przydatek, J. (2000). "*Strength and Fracture Toughness of Friction Stir Welds in Aluminium Alloys.*" 2nd International Symposium on Friction Stir Welding, Gothenburg, Sweden, 9p.

Daymond, M. R., Bourke, M. A. M., Dreele, R. B. V., Clausen, B. and Lorentzen, T. (1997). "*Use of Rietveld refinement for elastic macrostrain determination and for evaluation of plastic strain history from diffraction spectra.*" Journal of Applied Physics, **82**(4), 1554-1562.

Donne, C. D., Lima, E., Wegener, J., Pyzalla, A. and Buslaps, T. (2001). "*Investigations on residual stresses in friction stir welds.*" 3rd International Symposium on Friction Stir Welding, Kobe, Japan, 10p.

Dumont, M., Steuwer, A., Deschamps, A., Peel, M. and Withers, P. J. (2006). "*Microstructure mapping in friction stir welds of 7449 aluminium alloy using SAXS.*" Acta Materialia, **54**(18), 4793-4801.

Evans, A., Kim, S. B., Shackleton, J., Bruno, G., Preuss, M. and Withers, P. J. (2005). "*Relaxation of residual stress in shot peened Udimet 720Li under high temperature isothermal fatigue.*" International Journal of Fatigue, **27**(10-12), 1530-1534.

Fernandez, G. J. and Murr, L. E. (2004). "*Characterization of tool wear and weld optimization in the friction-stir welding of cast aluminum 359+20% SiC metal-matrix composite.*" Materials Characterization, **52**(1), 65-75.

Gabzdyl, J., Johnson, A., Williams, S. W. and Price, D. (2001). "*Laser Weld Distortion Control by Cryogenic Cooling.*" 20th Icaleo 2001, 1236-1245.

Genevois, C., Deschamps, A., Denquin, A. and Doisneau, B. (2005). "*Quantitative investigation of precipitation and mechanical behaviour for AA2024 friction stir welds.*" Acta Materialia, **53**(8), 2447-2458.

Genevois, C., Deschamps, A. and Vacher, P. (2006). "*Comparative study on local and global mechanical properties of 2024 T351, 2024 T6 and 5251 O friction stir welds.*" Materials Science and Engineering: A, **415**(1-2), 162-170.

Godard, D., Archambault, P., Aeby-Gautier, E. and Lapasset, G. (2002). "*Precipitation sequences during quenching of the AA 7010 alloy.*" Acta Materialia, **50**(9), 2319-2329.

Greitmann, M. J. and Deimel, P. (2005). "*Reibrührschweißen - eine innovative Verfahrenstechnologie zum Fügen von Halbzeugen aus Aluminium (Friction Stir Welding - Innovative Technology for Joining Aluminium Components).*" Otto Graf Journal (Annual Journal on Research and Testing Materials), **16**, 185-192.

Guan, Q., Zhang, C. X. and Guo, L. (1994). "*Dynamic Control of Welding Distortion by Moving Spot Heat Sink.*" Welding in the World, **33**(4), 308-313.

Hammersley, G., Hackel, L. A. and Harris, F. (2000). "*Surface pre-stressing to improve fatigue strength of components by laser shot peening.*" Optics and Lasers in Engineering, **34**(4-6), 327-337.

Hassan, K. A. A., Norman, A. F., Price, D. A. and Prangnell, P. B. (2003). "*Stability of nugget zone grain structures in high strength Al-alloy friction stir welds during solution treatment.*" Acta Materialia, **51**(7), 1923-1936.

Hatamleh, O., Lyons, J. and Forman, R. (2007). "*Laser and shot peening effects on fatigue crack growth in friction stir welded 7075-T7351 aluminum alloy joints.*" International Journal of Fatigue, **29**(1), 421-431.

Hauk, V. (1997). "*Structural and residual stress analysis by nondestructive methods."* Elsevier, Amsterdam; Oxford.

Heinz, A., Haszler, A., Keidel, C., Moldenhauer, S., Benedictus, R. and Miller, W. S. (2000). "*Recent development in aluminium alloys for aerospace applications.*" Materials Science and Engineering A, **280**(1), 102-107.

Holden, T. M., Root, J. H., Holt, R. A. and Hayashi, M. (1995). "*Neutron-diffraction measurements of stress.*" Physica B: Condensed Matter, **213-214**, 793-796.

Huang, B.-P. and Zheng, Z.-Q. (1998). "*Effects of Li Content on Precipitation in Al-Cu-(Li)-Mg-Ag-Zr Alloys.*" Scripta Materialia, **38**(3), 357-362.

Hughes, D. J. (2008). Personal Communication, SALSA details.

Hughes, D. J., James, M. N., Hattingh, D. G. and Webster, P. J. (2003). "*The Use of Combs for Evaluation of Strain-free References for Residual Strain Measurements by Neutron and Synchrotron X-ray Diffraction.*" Journal of Neutron Research, **11 (4)**, 289-293.

Hutchings, M., Withers, P. J., Holden, T. M. and Lorentzen, T. (2005). "*Introduction to the Characterisation of Residual Stress by Neutron Diffraction."* CRC Press Taylor & Francis, London, New York.

Hutchings, M. T. and Krawitz, A. D. (1992). "*Measurement of Residual and Applied Stress Using Neutron Diffraction."* Kluwer Acadamic Publishers, Dordrecht, Netherlands.

ILL. "*LAMP, The Large Array Manipulation Program*." http://www.ill.fr/data_treat/lamp/lamp.html, Grenoble.

ISO/TTA3. (2001). "*Polycristaline Materials - Determination of residual stress by neutron diffraction*." Technology Trends Assessment.

ISO/VAMAS/TWA20. (2001). "*ISO TTA 3:2001(E).*" International Organization for Standardization, International Organization for Standardization.

James, J. A. and Edwards, L. (2007a). "*Application of robot kinematics methods to the simulation and control of neutron beam line positioning systems.*" Nuclear Instruments & Methods In Physics Research Section A-Accelerators Spectrometers Detectors And Associated Equipment, **571**(3), 709-718.

James, J. A., Santisteban, J. R., Edwards, L. and Daymond, M. R. (2004). "*A virtual laboratory for neutron and synchrotron strain scanning.*" Physica B: Condensed Matter, **350**(1-3, Supplement 1), 743-746.

James, M. and Mahoney, M. W. (1999). "*Residual stress measurements in friction stir welded aluminium alloys.*" 1st International Symposium on Friction Stir Welding, Thousand Oakes, USA, 9p.

James, M. N., Hughes, D. J., Chen, Z., Lombard, H., Hattingh, D. G., Asquith, D., Yates, J. R. and Webster, P. J. (2007b). "*Residual stresses and fatigue performance.*" Engineering Failure Analysis, **14**(2), 384-395.

Jata, K. V., Sankaran, K. K. and Ruschau, J. J. (2000). "*Friction-Stir Welding Effects on Microstructure and Fatigue of Aluminium Alloy 7050-T7451.*" Metallurgical and Material Transactions, **31A**(9), 2181-2192.

Jones, M. J., Heurtier, P., Desrayaud, C., Montheillet, F., Allehaux, D. and Driver, J. H. (2005). "*Correlation between microstructure and microhardness in a friction stir welded 2024 aluminium alloy.*" Scripta Materialia, **52**(8), 693-697.

Kamp, N., Sullivan, A. and Robson, J. D. (2007). "*Modelling of friction stir welding of 7xxx aluminium alloys.*" Materials Science and Engineering: A, **466**(1-2), 246-255.

Kamp, N., Sullivan, A., Tomasi, R. and Robson, J. D. (2006). "*Modelling of heterogeneous precipitate distribution evolution during friction stir welding process.*" Acta Materialia, **54**(8), 2003-2014.

Khelifati, G., Guillaumin, V., Naze, L. and Laurrain, N. (2006). "*Microstructural and Mechanical Characterization of the new Aeronautical 2199 Al-Cu-Li Alloy.*" Aluminium 2006, Essen, Germany, 4p.

Kou, S. (2003). "*Welding Metallurgy."* John Wiley & Sons, Hoboken, New Jersey.

Krishnan, K. N. (2002). "*On the formation of onion rings in friction stir welds.*" Materials Science and Engineering, **A327**, 246-251.

Larson, A. C. and Von Dreele, R. B. (1994). "*General Structure Analysis System (GSAS).*" LAUR 86-748, Los Alamos National Laboratory.

Leonard, A. J. (2000). "*Microstructure and aging behaviour of FSW in Al alloys 2014A-T651 and 7075-T651.*" 2nd International Symposium on Friction Stir Welding, Gothenburg, Sweden, 14p.

Leonard, A. J. and Lockyer, S. A. (2003). "*Flaws in friction stir welds.*" 4th International Symposium on Friction Stir Welding, Park City, Utah, USA, 10p.

Lequeu, P., Lassince, P., Warner, T. and Raynaud, G. M. (2001). "*Engineering for the future: Weight saving and Cost Reduction Initiatives.*" International Journal of Aircraft Engineering and Aerospace Technology, **73**(2), 147-159.

Liu, W., Tian, X. and Zhang, X. (1996). "*Preventing Hot Cracking by Synchronous Rolling during Welding.*" Welding Research Supplement, 297-304.

Lombard, H., Hattingh, D. G., Steuwer, A. and James, M. N. (2008). "*Optimising FSW process parameters to minimise defects and maximise fatigue life in 5083-H321 aluminium alloy.*" Engineering Fracture Mechanics, **75**(3-4), 341-354.

Lombard, H., Hattingh, D. G., Steuwer, A. and James, M. N. (2009). "*Effect of Process Parameters on the Residual Stresses in AA5083-H321 Friction Stir Welds.*" Materials Science and Engineering: A, **501**(1-2), 119-124.

Macherauch, E. (1992). "*Praktikum in Werkstoffkunde."* Vieweg & Teubner.

Magnusson, L. and Kallman, L. (2000). "*Mechanical properties of friction stir welds in thin thin sheet aluminium 2024, 6013 and 7475.*" 2nd International Symposium on Friction Stir Welding, Gothenburg, Sweden, 10p.

Mahoney, M. W., Rhodes, C. G., Flintoff, J. G., Spurling, R. A. and Bingel, W. H. (1998). "*Properties of FSW 7075-T651 Al.*" Metallurgical and Material Transactions, **29A**, 1955-1964.

Maloney, S. K., Hono, K., Polmear, I. J. and Ringer, S. P. (1999). "*The chemistry of precipitates in an aged Al-2.1Zn-1.7Mg at.% alloy.*" Scripta Materialia, **41**(10), 1031-1038.

Maniruzzaman, C., Nowill, C., Sisson, R. D. and MacKenzie, D. S. (2007). "*Aging Behavior of AA7136.*" ASM Materials Conference, Detroit, MI, USA, 19p.

Marie, F. (2001). "*Development of Friction Stir Welding of 7000 series extrusions for central wing box applications.*" 3rd International Symposium on Friction Stir Welding, Kobe, Japan, 8p.

Masubuchi, K. (1980). "*Analysis of Welded Structures."* Pergamon Press, Oxford.

Masubuchi, K. (2003). *Residual Stresses and Distortion in Welds - Encyclopedia of Materials: Science and Technology*, Elsevier Science Ltd, Oxford, 8121-8126.

Michaleris, P., Dantzig, J. and Tortorelli, D. (1999). "*Minimization of welding residual stress and distortion in large structures.*" Welding Research Supplement, **11**, 361-366.

Michaleris, P. and Sun, X. (1997). "*Finite element analysis of thermal tensioning techniques mitigating weld buckling distortion.*" Welding Journal, **76**(11), 451-457.

Michaleris, P., Zhang, L., Bhide, S. R. and Marugabandhu, P. (2006). "*Evaluation of 2D, 3D and applied plastic strain methods for predicting buckling welding distortion and residual stress.*" Science and Technology of Welding and Joining, **11**(6), 707-716.

Midling, O. T., Kvale, J. S. and Dahl, O. (1999). "*Industrialisation of the friction stir welding technology in panels production for the maritime sector.*" 1st International Symposium on Friction Stir Welding, Thousand Oaks, California, USA, 7p.

Mishra, R. S. and Ma, Z. Y. (2005). "*Friction stir welding and processing.*" Materials Science and Engineering: R: Reports, **50**(1-2), 1-78.

Murr, L. E., Li, Y., Trillo, E. A., Flores, R. D. and McClure, J. C. (1998). "*Microstructures in Friction Stir Welded Metals.*" Journal of Materials Processing and Manufacturing Science, **7**, 145-161.

Murr, L. E., Liu, G. and McClure, J. C. (1997). "*Dynamic recrystallisation in friction-stir-welding of aluminium alloy 1100.*" Journal of Materials Science Letters, **16**, 1801-1803.

Noyan, I. C. and Cohen, J. B. (1987). "*Residual Stress: Measurement by Diffraction and Interpretation."* Springer-Verlag.

Peel, M. J. (2005). "*The friction-stir welding of dissimilar aluminium alloys.*" The University of Manchester, Manchester, 275p.

Peel, M. J., Steuwer, A., Preuss, M. and Withers, P. J. (2003). "*Microstructure, mechanical properties and residual stresses as a function of welding speed in aluminium AA5083 friction stir welds.*" Acta Materialia, **51**(16), 4791-4801.

Peel, M. J., Steuwer, A. and Withers, P. J. (2006a). "*Dissimilar friction stir welds in AA5083-AA6082. Part II: Process parameter-microstructure effects.*" Metallurgical and Material Transactions, **37**(7), 2195-2206.

Peel, M. J., Steuwer, A., Withers, P. J., Dickerson, T., Shi, Q. and Shercliff, H. R. (2006b). "*Dissimilar friction stir welds in AA5083-AA6082. Part I: Process parameter effects on thermal history and weld properties.*" Metallurgical and Material Transactions A, **37**(7), 2183-2193.

Perrett, J. G., Martin, J., Threadgill, P. L. and Ahmed, M. M. Z. (2007). "*Recent developments in friction stir welding of thick section aluminium alloys.*" 6th World Congress, Aluminium Two Thousand, Florence, Italy, 8p.

Peyrac, C., Convert, F., Flavenot, J. F. and Lu, J. (1996). "*The step by step hole drilling method for residual stresses measurements:experimental and theoretical study.*" Forth European Conference on Residual Stress, 173-182.

Pilipenko, A. (2001). "*Computer Simulation of Residual Stress and Distortion of Thick Plates in Multielectrode Submerged Arc Welding: Their Mitigation Techniques.*" Norwegian University of Science and Technology, Trondheim, 222.

Pirling, T., Bruno, G. and Withers, P. J. (2006). "*SALSA - A new instrument for strain Imaging in engineering Materials & Components.*" Materials Science and Engineering A, **437 A**, 139-144.

Poad, M. (2006). Personal Communication, Material and Welding details.

Poad, M. (2007). Personal Communication, Varying AA2199-T8E74 Material Thickness.

Poad, M., Williams, S. W. and Wen, S. W. (2006). Personal Communication, Corrugated Roller Details.

Polmear, I. J. (1995). "*Light Alloys: Metallurgy of the Light Metals."* Arnold.

Prado, R. A., Murr, L. E., Shindo, D. J. and Soto, K. F. (2001). "*Tool wear in the friction-stir welding of aluminum alloy 6061+20% Al2O3: a preliminary study.*" Scripta Materialia, **45**(1), 75-80.

Price, D. A., Williams, S. W., Wescott, A., Harrison, C. J. C., Rezai, A., Steuwer, A., Peel, M., Staron, P. and Kocak, M. (2007). "*Distortion control in welding by mechanical tensioning.*" Science and Technology of Welding & Joining, **12**(7), 620-633.

Prime, M. B., Gnaupel-Herold, T., Baumann, J. A., Lederich, R. J., Bowden, D. M. and Sebring, R. J. (2006). "*Residual stress measurements in a thick, dissimilar aluminium alloy friction stir weld.*" Acta Materialia, **54**(15), 4013-4021.

Prime, M. B. and Gonzales, R. (2000). "*The contour method: simple 2-D mapping of residual stress.*" The 6th International Conference on Residual Stress, Oxford, UK, 617-624.

Rankin, J. E., Hill, M. R. and Hackel, L. A. (2003). "*The effects of process variations on residual stress in laser peened 7049 T73 aluminum alloy.*" Materials Science and Engineering A, **349**(1-2), 279-291.

Reimers, W., Pyzalla, A., Broda, M., Brusch, G., Dantz, D., Schmackers, T., Liss, K. D. and Tschentscher, T. (1999). "*The use of high-energy synchrotron diffraction for residual stress analyses.*" Journal Of Materials Science Letters, **18**(7), 581-583.

Reynolds, A. P., Tang, W., Gnaupel-Herold, T. and Prask, H. (2003). "*Structure, properties, and residual stress of 304L stainless steel friction stir welds.*" Scripta Materialia, **48**(9), 1289-1294.

Rhodes, C. G., Mahoney, M. W., Bingel, W. H., Spurling, R. A. and Bampton, C. C. (1997). "*Effects of FSW on the microstructure of 7075 aluminium.*" Scripta Met, **36**, 69-75.

Richards, D. G. (2008). Personal Communication, FEM details.

Richards, D. G., Prangnell, P. B., Williams, S. W. and Withers, P. J. (2008a). "*Global Mechanical Tensioning for the Management of Residual Stresses in Welds.*" Materials Science and Engineering A, **489**(1-2), 351-362.

Richards, D. G., Prangnell, P. B., Withers, P. J., Williams, S. W., Nagy, T. and Morgan, S. A. (2008b). "*Simulation of the Effectiveness of Dynamic Cooling for Controlling Residual Stresses in Friction Stir Welds.*" 7th International Symposium on Friction Stir Welding, Awaji Island, Japan, 11p.

Robson, J. D. (2004a). "*Microstructural evolution in aluminium alloy 7050 during processing.*" Materials Science and Engineering A, **382**(1-2), 112-121.

Robson, J. D. (2004b). "*Modelling the overlap of nucleation, growth and coarsening during precipitation.*" Acta Materialia, **52**(15), 4669-4676.

Robson, J. D. and Prangnell, P. B. (2001). "*Dispersoid precipitation and process modelling in zirconium containing commercial aluminium alloys.*" Acta Materialia, **49**(4), 599-613.

Robson, J. D., Sullivan, A., Shercliff, H. R. and McShane, G. (2004). "*Microstructural Evolution during Friction Stir Welding of AA7449.*" 5th International Symposium on Friction Stir Welding, Metz, France.

Santisteban, J. R., Steuwer, A., Edwards, L., Withers, P. J. and Fitzpatrick, M. E. (2002). "*Mapping of unstressed lattice parameters using pulsed neutron transmission diffraction.*" Journal of Applied Crystallography, **35**(4), 497-504.

Sato, S. Y., Urata, M. and Kokawa, H. (2002). "*Parameters controlling microstructure and hardness during friction-stir welding of precipitation-hardenable aluminum alloy.*" MatTrans A, **33**(3), 625-635.

Sato, Y. S., Park, S. H. C. and Kokawa, H. (2001). "*Microstructural Factors Governing Hardness in Friction-Stir Welds of Solid-Solution-Hardened Al Alloys.*" Metallurgical and Material Transactions, **32A**(12), 3033-3042.

Schmuck, C., Auger, P., Danoix, F. and Blavette, D. (1995). "*Quantitative analysis of GP zones formed at room temperature in a 7150 Al-based alloy.*" Applied Surface Science, **87-88**, 228-233.

Sha, G. and Cerezo, A. (2004). "*Early-stage precipitation in Al-Zn-Mg-Cu alloy (7050).*" Acta Materialia, **52**(15), 4503-4516.

Shercliff, H. and Ashbey, M. (1990). "*A process model for age-hardening of aluminium alloys - I: The Model.*" Acta Metall. Metalurgica, **38**(10), 1789-1802.

Srivatsan, T. S., Anand, S., Sriram, S. and Vasudevan, V. K. (2000). "*The high-cycle fatigue and fracture behavior of aluminum alloy 7055.*" Materials Science and Engineering A, **281**(1-2), 292-304.

Staron, P., Kocak, M., Williams, S. W. and Wescott, A. (2004). "*Residual stress in friction stir-welded Al sheets.*" Physica B: Condensed Matter, **350**(1-3, Supplement 1), 491-493.

STAUBLI. (2001). "*Arm RX90B Family Characteristics.*" Faverges, ed.

Steuwer, A., Dumont, M., Peel, M., Preuss, M. and Withers, P. J. (2007). "*The variation of the unstrained lattice parameter in an AA7010 friction stir weld.*" Acta Materialia, **55**(12), 4111-4120.

Steuwer, A., Peel, M. and Buslaps, T. (2006a). "*Aspects of Residual Stress Determination Using Energy-Dispersive Synchrotron X-Ray Diffraction.*" Materials Science Forum, **524-525**, 267-272.

Steuwer, A., Peel, M. J. and Withers, P. J. (2006b). "*Dissimilar friction stir welds in AA5083-AA6082. The effect of process parameters on residual stress.*" Materials Science and Engineering A, **441**(1-2), 187-196.

Steuwer, A., Santisteban, J. R., Turski, M., Withers, P. J. and Buslaps, T. (2004). "*High-resolution strain mapping in bulk samples using full-profile analysis of energy-dispersive synchrotron X-ray diffraction data.*" Journal of Applied Crystallography, **37**(6), 883-889.

Su, J. Q., Nelson, T. W., Mishra, R. and Mahoney, M. (2003). "*Microstructural investigation of friction stir welded 7050-T651 aluminium.*" Acta Materialia, **51**(3), 713-729.

Su, J. Q., Nelson, T. W. and Sterling, C. J. (2005). "*Microstructure evolution during FSW/FSP of high strength aluminium alloys.*" Materials Science and Engineering: A, **405**(1-2), 277-286.

Sullivan, A. and Robson, J. D. (2008). "*Microstructural properties of friction stir welded and post-weld heat-treated 7449 aluminium alloy thick plate.*" Materials Science and Engineering: A, **478**(1-2), 351-360.

Sutton, M. A., Reynolds, A. P., Wang, D. Q. and Hubbard, C. R. (2002). "*A Study of Residual Stresses and Microstructure in 2024-T3 Aluminium Friction Stir Butt welds.*" Journal of Engineering Materials and Technology, **124**(2), 215-221.

Sutton, M. A., Yang, B., Reynolds, A. P. and Yan, J. (2004). "*Banded microstructure in 2024-T351 and 2524-T351 aluminum friction stir welds: Part II. Mechanical characterization.*" Materials Science and Engineering A, **364**(1-2), 66-74.

Tang, W., Guo, X., McClure, J. C. and Murr, L. E. (1999). "*Heat input and temperature distribution in friction stir welding.*" Journal of Materials Processing & Manufacturing Science, **37**(2), 163-172.

Thomas, W. M., Nicholas, E. D., Needham, J. C., Murch, M. G., Temple-Smith, P. and Dawes, C. J., (1991), *"Friction stir butt welding."* International Patent No. PCT/GB92/02203.

Thomas, W. M., Norris, I. M., Staines, D. G. and Watts, E. R. (2005). "*Friction Stir Welding – Process Developments and Variant Techniques.*" THE SME SUMMIT 2005, Oconomowoc, Wisconsin, USA, 23p.

Threadgill, P. L., Leonard, A. J., Shercliff, H. R. and Withers, P. J. (2009). "*Friction Stir Welding of Aluminium Alloys.*" International Materials Reviews, **54**(2), 49-93.

Timoshenko, S. P. and Goodier, J. N. (1987). "*Theory of Elastics."* McGraw-Hill Book Company, Singapore.

Toupin, R. A. (1965). "*Saint-Venant's principle.*" Archives for Rational Mechanics and Analysis, **18**, 83-96.

Ugural, A. C. and Fenster, S. K. (1994). "*Advanced Strength and Applied Elasticity."* P T R Prentice Hall Inc., Englewood Cliffs.

van der Aa, E. M. (2007). "*Local Cooling during Welding: Prediction and Control of Residual Stresses and Buckling Distortion.*" Delft University of Technology, Delft, 231p.

van der Aa, E. M., Hermans, M. J. M., Richardson, I. M., van der Pers, N. M. and Delhez, R. (2006). "*Experimental study of the influence of a trailing heat sink on the welding residual stress distribution*." *Residual Stresses VII*, 479-484.

Walker, C. A., Waddell, A. J. and Johnston, D. J. (1995). "*Vibratory stress relief—an investigation of the underlying processes.*" Proc. Inst. Mech. Eng, **209**, 51-58.

Wang, X. L., Feng, Z., David, S. A., Spooner, S. and Hubbard, C. R. (2000). "*Neutron diffraction study of residual stresses in friction stir welds.*" The 6th International Conference on Residual Stress, Oxford, UK, 1408-1414.

Webster, P. J., Hughes, D. J., Withers, P. J. and Fitch, A. N. (2001a). "*Synchrotron Strain Scanning on BM16 at the ESRF.*" Journal of Neutron Research, **9**, 93-98.

Webster, P. J. and Kang, W. P. (2002). "*Optimisation of Data Collection and Processing for Efficient Strain Scanning.*" The Journal of Neutron Research, **10**(2), 93-110.

Webster, P. J., Oosterkamp, L. D., Browne, P. A., Hughes, D. J., Kang, W. P., Withers, P. J. and Vaughan, G. B. M. (2001b). "*Synchrotron X-ray Residual Strain Scanning of a Friction Stir Weld.*" Journal of Strain Analysis for Engineering Design, **36**(1), 61-70.

Webster, P. J., Wang, X. D. and Mills, G. (1996). "*Strain scanning using neutrons and synchrotron radiation.*" Forth European Conference on Residual Stress, Cluny, France, 127-134.

Wei, S., Hao, C. and Chen, J. (2007). "*Study of friction stir welding of 01420 aluminum-lithium alloy.*" Materials Science and Engineering: A, **452-453**, 170-177.

Wen, S. W., Williams, S. W., Morgan, S. A., Wescott, A. and Poad, M. (2009). "*Rolling of Friction Stir Welds for Residual Stress and Distortion Control.*" Science and Technology of Welding & Joining, Accepted for Publication.

Williams, J. C. and Starke, J. E. A. (2003). "*Progress in structural materials for aerospace systems.*" Acta Materialia, **51**(19), 5775-5799.

Williams, S. W., Morgan, S. A., Wescott, A., Poad, M. and Wen, S. W. (2008). "*Stress Engineering – Control of Residual Stresses and Distortion in Welding.*" 2nd International Workshop on Thermal Forming and Welding Distortion, Bremen, Germany, 9p.

Williams, S. W., Price, D. A., Wescott, W., Steuwer, A., Peel, M., Altenkirch, J., Withers, P. J. and Poad, M. (2006). "*Distortion Control in Welding by Mechanical Tensioning.*" 6th International Symposium on Friction Stir Welding, Saint-Sauveur, Montreal, Canada, 6p.

Withers, P. J. (2007). "*Residual stress and its role in failure.*" Reports on Progress in Physics, **70**, 2211-2264.

Withers, P. J. and Bhadeshia, H. K. D. H. (2001a). "*Residual stress. I. Measurement techniques.*" Materials Science and Technology, **17**(4), 355-365.

Withers, P. J. and Bhadeshia, H. K. D. H. (2001b). "*Residual stress. II. Nature and origins.*" Materials Science and Technology, **17**(4), 366-375.

Withers, P. J., Buschow, K. H. J., Robert, W. C., Merton, C. F., Bernard, I., Edward, J. K., Subhash, M. and Patrick, V. (2001c). "*Residual Stress: Definition*." *Encyclopedia of Materials: Science and Technology*, Elsevier, Oxford, 8110.

Withers, P. J., Preuss, M., Steuwer, A. and Pang, J. W. L. (2007). "*Methods for obtaining the strain-free lattice parameter when using diffraction to determine residual stress.*" Journal of Applied Crystallography, **40**(5), 891-904.

Withers, P. J., Preuss, M., Webster, P. J., Hughes, D. J. and Korunsky, A. M. (2002). "*Residual Strain Measurement by Synchrotron Diffraction.*" Materials Science Forum, **404-407**, 1-12.

Withers, P. J. and Webster, P. J. (2001d). "*Neutron and Synchrotron X-ray strain scanning.*" Strain, **37**(1), 19-33.

Withers, P. J., Webster, P. J. and Avis, N. J. (2001e). "*An Engineering Body Scanner for 3D Stress and Damage Measurement and Co-visulalisation.*" E. P. S. R. Council, ed., EPSRC.

Xu, W., Fan, C., Fang, H. and Tian, X. (2004). "*New Development in Welding Thin-shell Aluminum Alloy Structures with High Strength.*" China Welding, **13**(1), 27-30.

Yang, Y. P., Dong, P., Tian, X. and Zhang, Z. (1998). "*Prevention of Hot Cracking of High Strength Aluminum Alloy by Mechanical Rolling.*" 5th Int. Conf. on Trends in Welding Research, Pine Mountain, GA, USA, 700-705.

Zhang, P. and Lindemann, J. (2005). "*Influence of shot peening on high cycle fatigue properties of the high-strength wrought magnesium alloy AZ80.*" Scripta Materialia, **52**(6), 485-490.

Zhu, X. K. and Chao, Y. J. (2002). "*Effects of temperature-dependent material properties on welding simulation.*" Computers & Structures, **80**(11), 967-976.

9 APPENDIX

In the following copies of the journal papers are included where the work documented in this dissertation has been published. In detail this includes:

- Altenkirch J., Steuwer A., Withers P. J., Buslaps T. and Berger U. (2007): *Robotic sample manipulation for stress and texture determination on neutron and synchrotron X-ray diffractometers*: Nuclear Instruments and Methods in Physics Research Section A: Accelerators, Spectrometers, Detectors and Associated Equipment, **584 (2-3)**, 248-255.
- Altenkirch J., Steuwer A., Peel M. and Withers P. J. (2009): *The extent of relaxation of weld residual stresses on cutting out cross-weld test piece:* Powder Diffraction, **24 (S1)**, 31-36.
- Altenkirch J., Steuwer A., Peel M., Richards D. G. and Withers P. J. (2008): *The effect of tensioning and sectioning on residual stresses in aluminium AA7749 friction stir welds*: Materials Science and Engineering: A, **488 (1-2)**, 16-24.
- Altenkirch J., Steuwer A., Peel M. J., Withers P. J., Williams S. W. and Poad M. (2008): *Mechanical Tensioning of High-Strength Aluminum Alloy Friction Stir Welds*: Materials Transactions: A, **39 (13)**, 3246-3259.
- Altenkirch J., Steuwer A., Withers P. J., Williams S., Poad M. and Wen S. (2009): *Residual stress engineering in friction stir welds by roller tensioning*: Science and Technology of Welding & Joining, **14 (2)**, 185-192.

Available online at www.sciencedirect.com
ScienceDirect
Nuclear Instruments and Methods in Physics Research A 584 (2008) 428–435
NUCLEAR INSTRUMENTS & METHODS IN PHYSICS RESEARCH Section A
www.elsevier.com/locate/nima

Robotic sample manipulation for stress and texture determination on neutron and synchrotron X-ray diffractometers

J. Altenkirch[a,b,e,*], A. Steuwer[c], P.J. Withers[a], T. Buslaps[d], U. Berger[e]

[a]*Manchester Materials Science Centre, University of Manchester, Grosvenor Street, Manchester M17HS, UK*
[b]*Institute Laue-Langevin, 6 rue J Horowitz, 38042 Grenoble, France*
[c]*FaME38 at the ILL-ESRF, 6 rue J Horowitz, 38042 Grenoble, France*
[d]*European Synchrotron Radiation Facility, 6 rue J Horowitz, 38042 Grenoble, France*
[e]*BTU Cottbus, Fakultät 3, Siemens-Halske-Ring 14, 03046 Cottbus, Germany*

Received 16 August 2007; received in revised form 3 October 2007; accepted 3 October 2007
Available online 13 October 2007

Abstract

In this paper we report on a new robotic arm system for fast, accurate and flexible sample manipulation for stress and texture analysis in geometrically complex engineering components on neutron and synchrotron X-ray diffractometers. A Staeubli serial six-axis robotic arm offering full six degrees of freedom for sample movement, with a spatial positioning accuracy of the order of tens of microns has been commissioned. Reverse engineering and 3D visualization techniques are employed to control the sample manipulation procedure. Two basic applications of the system, one for stress measurements using synchrotron X-ray diffraction using the $\sin^2\psi$ inclination method, and one for pole figure determination for texture analysis using neutron diffraction, are presented. The former required measurements at eight angles for each measurement location; the latter a full quadrant of solid angle with the centre of the sample maintained stationary. With new robotic arms being produced with higher payloads (the current one is limited to 9 kg), but similar positional uncertainties, robotic sample manipulation offers very flexible measurement strategies for complex geometries, without the need for repeated manual intervention for sample reorientation.

PACS: 61.05.Fm; 61.05.Cp; 06.60.Sx; 45.40.Ln

Keywords: Neutron diffraction; Synchrotron X-ray diffraction; Sample manipulation; Robotics; Automation

1. Introduction

Strain and texture measurements in engineering components by neutron and X-ray diffraction require flexible, precise and fast sample manipulation with respect to the gauge volume location (position and orientation). Strain tensor determination at a point of interest within a component is based on the measurement of lattice spacing in typically three or more orientations from a gauge volume centred on that point [1]. Similarly, stress determination techniques such as the $\sin^2\psi$ technique also require the inclination of the sample to many different angles [2,3] with respect to the scattering vector while maintaining the position of the sampling volume. Also, quantitative texture analysis is based on the ability to rotate the sample around the point of interest to many orientations with respect to the scattering vector to obtain detailed and accurate pole figures [4].

Current sample positioning methods rely mostly on combinations of linear translation devices with Eulerian-type cradles for rotation. Conventional linear translation tables are capable of precisely moving samples of a wide range of weights along mostly Cartesian coordinates (XYZ). On ENGIN-X at ISIS, UK, an XYZ-translation table with an integrated ω rotation capable of holding samples of up 1.5 t is installed allowing translation of ± 250 mm in x and y and 700 mm in z as well as ω sample rotation of 370°. The nominal accuracy is 10 μm/100 mm

*Corresponding author. Institute Laue-Langevin, 6 rue J Horowitz, 38042 Grenoble, France. Tel.: +33 4 76 20 7947.
E-mail address: altenkirch@ill.fr (J. Altenkirch).

0168-9002/$ - see front matter © 2007 Elsevier B.V. All rights reserved.
doi:10.1016/j.nima.2007.10.012

for a 500 kg sample [5]. Using two theodolites and triangulation the position of a sample within the beam line coordinate system may be determined. A similar sample manipulation approach is applied on the SMARTS beam line at Lujan Centre, USA [6]. On the other hand on SALSA at the ILL, France, a novel six-piston hexapod, a so-called Gough or Stewart-platform, capable of manipulating large components (rated to 940 kg) has been installed offering precise (to better than 50 μm) six-axis movement for the first time but only over a restricted range of tilt angles ($\pm 30^\circ$ with ± 300 mm translation in the horizontal directions and ± 175 mm in z-direction) [7].

To perform strain measurements in several orientations intermediate changes of the sample mounting are usually required on such instruments. In some cases, additional rotational axis (e.g. Euler-cradles) may be added on top of the manipulation devices hence increasing the degree of freedom to orientate samples and lessening the times of intermediate sample mounting changes. Eulerian cradles allowing 360° sample rotations are typically designed for small and light samples of simple geometries (model specimen). On the other hand cradles for bigger samples offer only limited rotational freedom. However, additional axes increase the complexity of controlling the sample movements due to the serialization of the axes of movements. Also these set-ups are often specialized arrangements devised for a particular experimental purpose and therefore require significant time for precise alignment.

Nevertheless, there is a strong drive towards measuring stress/texture in real engineering components with complex geometries, such as turbine blades, crank shafts, gears, etc., which pose considerable challenges to conventional sample manipulation methods.

The idea of capturing the geometrical 3D outline of the component digitally using a coordinate measurement machine (CMM) for subsequent precise placement and manipulation on a neutron strain diffractometer was initially proposed by Withers in 2001 [8,9], and was first incorporated within a sample scanning software environment by James et al. [10] for use on the ENGIN-X instrument and now being rolled out to many strain instruments worldwide. James et al. [10] use the 3D model of the sample to calculate the location of each planned measurement point relative to three fiducial points on the sample surface prior to the experiment. When the sample is mounted on the beam line the positions of the three fiducial points are determined within XYZ-translation table coordinate system and subsequently the software calculates all table coordinates to move the measurement points into the gauge volume location automatically. The virtual laboratory software is also used to simulate the entire sample movement to detect and avoid eventual collisions between the sample and surrounding beam line hardware [10].

The desire for less restricted movement as well as automated sample manipulation has led to the development of a novel sample manipulation approach based on robotic arms at the FaME38 facility at the ILL-ESRF in Grenoble, France. What makes robotic arms, commonly used in the assembly industries, attractive for complex sample manipulation is the fact that the six degrees of freedom are fully available ($\pm 360^\circ$ rotations around, and linear translations along, three sample axes). Furthermore, both rotation and translation are accessible at each step with a high absolute and reproducible accuracy of the order of tens of microns. This is of particular interest for neutron instruments where the required positioning accuracy in strain and texture measurements rarely exceeds hundreds of microns. Furthermore, robotic arms offer ease of use as all axes are controlled by the system control unit. In principle, only the final location coordinates of the working point of the tool, or in this application the sample measurement point within the tool coordinate system ($X_T Y_T Z_T$) and the gauge volume location within the robotic arm global coordinate system ($X_0 Y_0 Z_0$) need to be programmed. All algebraic coordinate manipulations are taken care of by the control unit. Additionally, the robotic arm controller allows seamless switching from the global (laboratory) coordinate system to the local tool or, in this case, sample coordinate system, see Fig. 1(a). In order to make best use of the advantages offered by robotic arms we have used reverse-engineering techniques in order to create 3D models of the sample within which the measurement locations may be specified, and which further enhance the visualization of the measured data. Off-line preparation and simulation ensure safe operation of the system on the beam line and the optimal use of the allocated beam time.

The aim of this paper is to describe a robotic arm based sample manipulation prototype system and to illustrate the capability and advantages of such a system by presenting initial strain and texture measurements.

2. The principle of robotic sample manipulation

2.1. The prototype system

Our prototype system is based on a serial six-axis robotic arm that enables manipulation of samples of moderate weight with the full six degrees of freedom. The current implementation uses a STAUBLI RX90L high precision robotic arm (see Fig. 1(a)) equipped with a CS7M control unit. The RX90L offers six full degrees of freedom to move within a 2000 mm in diameter nearly spherical work envelope (see Fig. 1(b)). The robotic arm can manipulate samples of up to 9 kg weight with a specified positioning accuracy of ± 25 μm at 10% of the nominal speed and 6 kg payload [11]. The RX90L is equipped with a $125 \times 75 \times 12$ mm VAMAS base-plate [12] attached to the robot tool mounting flange to enable fast and repeatable precision mounting of VAMAS sample holders. The CS7M control unit, operated and programmed via TCP/IP (Ethernet) network cable by an external PC, not only controls the robotic arm axes, but also allows

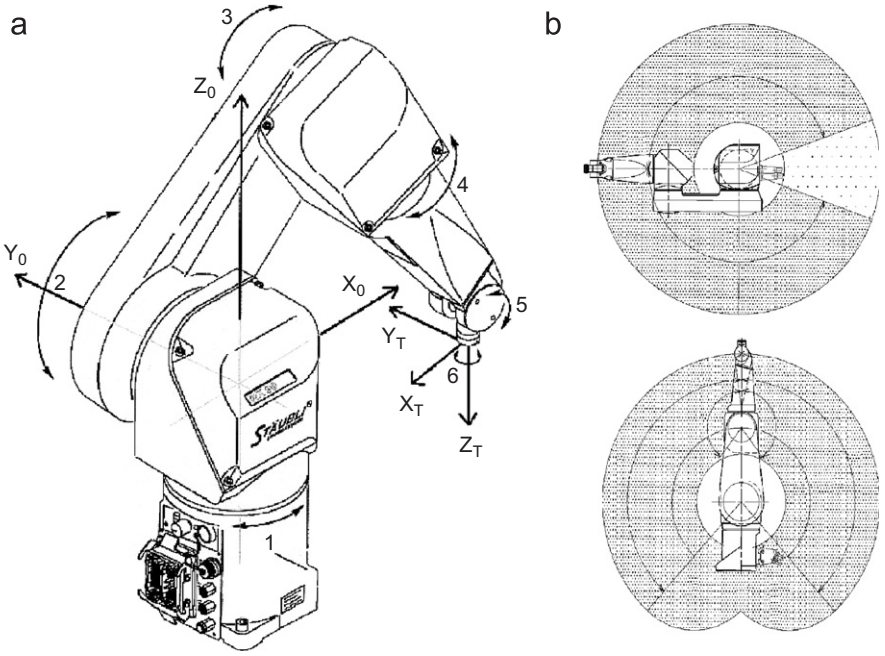

Fig. 1. (a) Illustration of a Staeubli RX90L, its axes of rotation (1–6), global (laboratory) ($X_0Y_0Z_0$) and tool (sample) ($X_TY_TZ_T$) coordinate systems and (b) working envelope of the RX90L robotic arm, within the working envelope the robot tool mounting flange and hence the sample can be oriented in any programmed orientation.

communication to other systems such as the beam-line control system, via 16 digital input/output signal channels. In this manner it is possible to set up uncomplicated communication between the beam-line and robotic arm control systems.

In this paper we extend the application of the robotic arm to take advantage of 3D information about the sample. The reverse engineering of the digital form of the component has been undertaken using a MITUTOYO Euro-C-A776 CMM equipped with a METRIS LC50 laser scanner, or alternatively a RENISHAW touch probe. Finally, METRIS Scan 4.02 software has been used to create the 3D model of the sample (see Fig. 2). This equipment facilitates scanning the geometry of the sample of interest within the sample coordinate system ($X_SY_SZ_S$) to obtain a point cloud representing the sample surface. Additional manipulation of the point cloud data is undertaken using software routines developed in-house based on the platform independent open-source software VTK and ParaView,[1] and Python routines.[2]

2.2. The sample manipulation procedure

By creating a digital representation of the sample within $X_SY_SZ_S$ using the reverse engineering technique, it is a relatively straightforward task to connect any measurement point within the sample to the laboratory frame. In doing so, any measurement location on the sample surface or within the sample may be programmed as the so-called current robot tool tip point location within $X_TY_TZ_T$ and hence can automatically be moved into the work point location or in this case the gauge volume location defined in $X_0Y_0Z_0$ by the incoming and diffracted beam apertures. Furthermore, digitization allows the virtual visualization of the specimen, which enables the preparation and simulation of the complete sample manipulation procedure (all measurement locations) offline and prior to the experiment, hence saving a substantial amount of beam time whilst ensuring safe operation of the robotic arm and the attached sample as each pre-programmed measurement location is moved sequentially into the gauge volume. Digital interfacing of the control unit and hence the control PC with the beam-line control system allows the beam-line control script to ensure each measurement location receives sufficient illumination with the beam before movement of the specimen to the next measurement location.

The typical working procedure to prepare and perform e.g. a strain scanning experiment is as follows:

(i) Mounting the sample in a standard VAMAS sample holder before attaching it to a VAMAS base plate on the CMM identical to the one mounted onto the robotic arm.
(ii) Scanning the sample surface in $X_SY_SZ_S$ using the CMM (see Fig. 3).
(iii) Development of the sample CAD model to reduce point-cloud data volume (see Fig. 2).
(iv) Specification of the measurement grid within the CAD model and definition of the measurement location coordinates (position and orientation) within $X_SY_SZ_S$ (software under development).

[1] http://www.kitware.com.
[2] http://www.python.org.

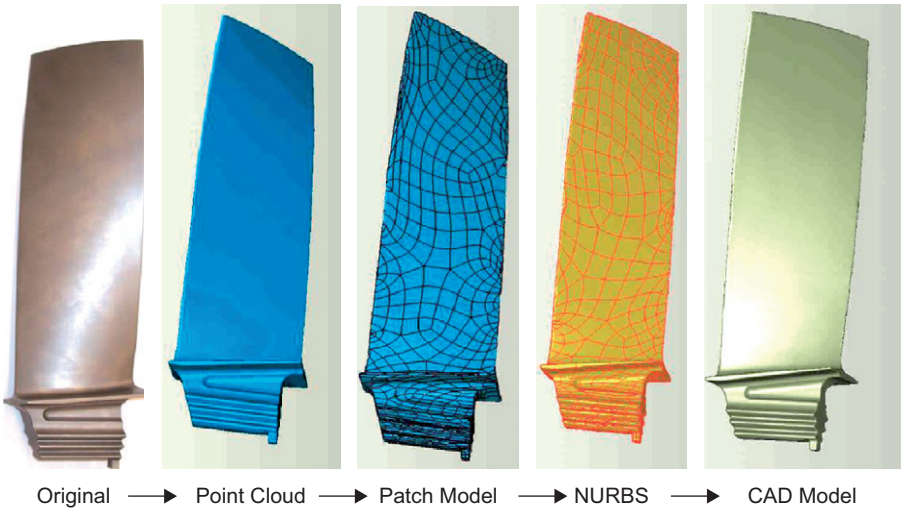

Fig. 2. The reverse engineering process used to obtain a faithful digital reproduction of the component: in the illustration a compressor turbine blade of the SNECMA Olympus 593 Mark 610 Turbojet engine (Concorde engine) is shown. It involves scanning the object to obtain a point cloud and subsequent triangulation to create a NURBS (Non Uniform Rational B-Splines, for generating and representing curves and surfaces) and subsequently a CAD model. A photo of the blade is also shown (left). Once digitized measurement locations can then be defined within the model.

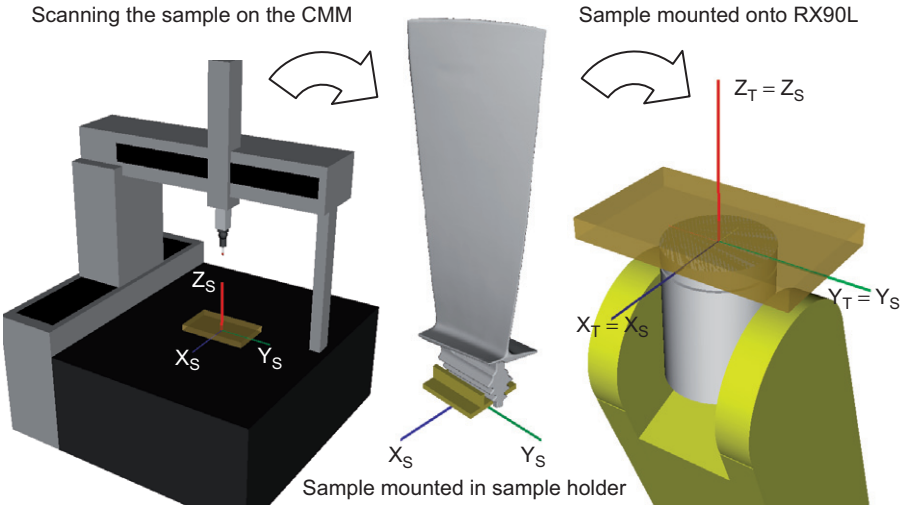

Fig. 3. Illustration of the digitization procedure on the CMM and the transformation of the sample coordinate system $X_S Y_S Z_S$ to the robot tool coordinate system $X_T Y_T Z_T$ by moving the sample in the VAMAS sample holder from the CMM to the robotic arm.

(v) Automatic creation of the sample manipulation script for the robotic arm for the experiment.
(vi) Mounting the VAMAS sample holder with the sample onto the VAMAS base plate attached to the robot tool mounting flange, such that the two coordinate systems $X_S Y_S Z_S$ and $X_T Y_T Z_T$ coincide (see Fig. 3).
(vii) During strain measurement each sample measurement location is successively defined as the current robot tool tip point in $X_T Y_T Z_T$ (this may be done, because the two coordinate systems $X_S Y_S Z_S$ and $X_T Y_T Z_T$ coincide).
(viii) At each location, once the acquisition period for the current point is complete, a digital signal from the beam-line control to the robotic arm control unit to initiate robotic arm to move the next defined robotic tool tip point (or sample measurement location) into the work point location, which in this case is the location of the gauge volume represented in $X_0 Y_0 Z_0$ (see Fig. 1).
(ix) Once the movement is complete the control unit returns a signal to the beam-line control to commence strain measurement corresponding to that sample measurement location.

Procedures (viii) and (ix) are repeated automatically until all defined sample measurement locations have been measured.

This system exploits the significant advantage of robotic arms, namely that any programmed measurement location

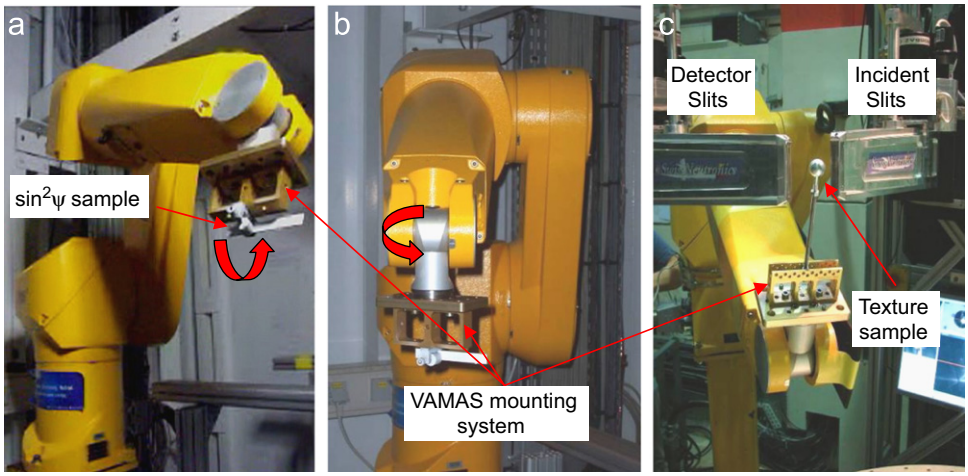

Fig. 4. RX90L installed on ID15A (ESRF) for manipulating a slice of an AA7449 friction stir welding sample for $\sin^2\psi$ d_0 measurements in 2640 different locations (in (a) rotation around sample Y-axis and in (b) rotation around sample Z-axis); RX90L installed on SALSA (ILL) for texture measurement in the centre of an AA7449 sphere with 100 different orientations covering one octant of the sphere (c).

can be moved directly into the gauge volume and correctly oriented for measurement. This means, for example, that the complete strain tensor can be determined for large arrays of measurement points without having to remount and realign the sample to reorient, as would be necessary on simpler XYZ translation systems.

In future development it is planned to simulate each robotic arm movement throughout the experiment before the actual experiment with appropriate industrial software routines (Delmia,[3] ProEngineer[4]) or other approaches described elsewhere [10,13,14] to avoid possible collisions with obstacles such as collision sensitive slits, detectors, etc. Indeed the control unit can be programmed such that the robotic arm avoids any number of fixed objects in the working range.

2.3. Alignment and accuracy

The precise determination of the gauge volume location of the diffractometer within the robotic arm $X_0Y_0Z_0$ system can be undertaken using established methods [1]. For example, a small metal pin having a known location within $X_TY_TZ_T$ can be scanned through the gauge volume with the incoming and diffracting beams correctly oriented to collect a relevant diffraction peak ($h\,k\,l$). The centre of the diffracted signal defines the position of the gauge volume in $X_0Y_0Z_0$.

The positioning accuracy of the RX90L was investigated according to ISO 9283:1998 by installing it in front of the CMM equipped with a touch probe. A 5 kg steel sphere was attached to the robotic arm tool mounting flange, such that the centre of the sphere was at (0,0,100) in $X_TY_TZ_T$. Subsequently an arbitrary location within the workspace of the CMM was repeatedly approached ($50\times$) by the robotic arm at 10% of nominal speed and each time the sphere centre position was determined by the CMM. Essentially the same measurement locations on the sphere surface were assessed by the CMM to determine the centre of the sphere. Therefore the determination of the sphere centre was not sensitive to errors in the roundness of the sphere. This procedure was repeated for six significantly differing locations of the sphere to provide a good statistical basis upon which it can be said that the RX90L robotic arm in use has a repeatable positioning accuracy of $\pm 21\,\mu m$ for the specified set-up. The precise details of the ISO 9283:1998 testing procedure can be found elsewhere [15].

3. Feasibility studies

Two feasibility studies are presented which highlight the most important aspects of robotic arm based sample manipulation, namely, performing repeated measurements at a sequence of positions in the sample each involving a range of different orientations for stress/strain measurements based on the $\sin^2\psi$ method, and at a fixed position but with a wide range of sample orientations for pole-figure determination as part of quantitative texture determination. In both cases the sample was installed once on the robotic arm and all subsequent translations and rotations were undertaken automatically by the robotic arm script.

3.1. The $\sin^2\psi$-technique

The robotic arm sample manipulation system was installed on beam line ID15A at the ESRF, France, to investigate its suitability for undertaking an array of stress measurements using the $\sin^2\psi$ method [2,16,17]. The method is commonly used for residual stress determination because it allows the measurement of the stresses in two orthogonal directions as well as the unstrained lattice spacing, d_0 in cases where the stress-state is essentially biaxial. In this particular case it was used to measure the

[3] http://www.3ds.com/corporate/about-us/brands/delmia/.
[4] http://www.proengineer.com/.

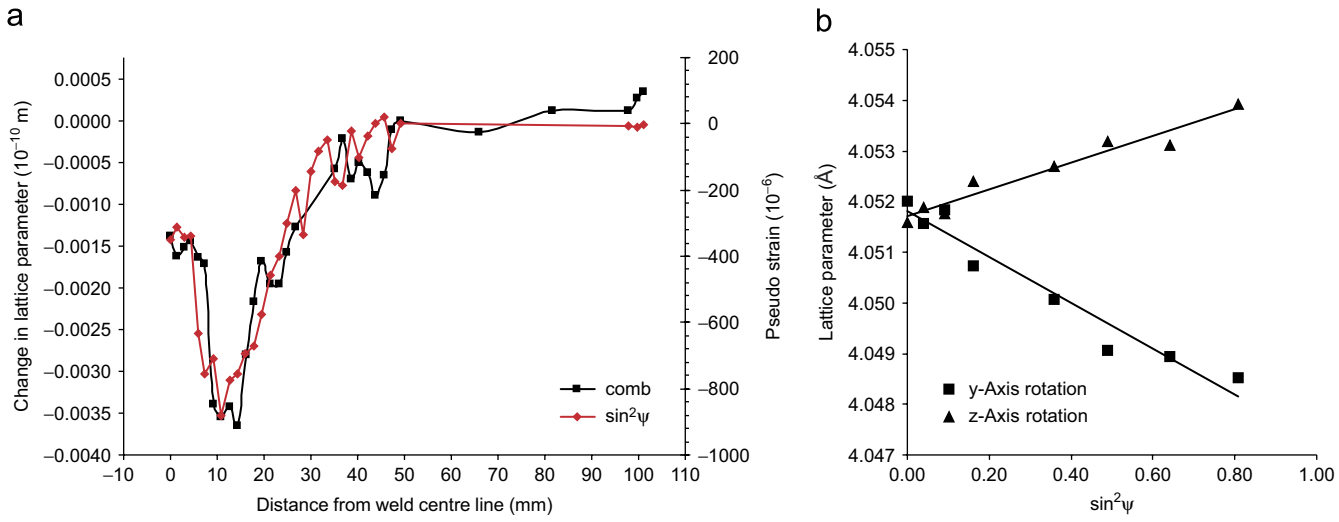

Fig. 5. (a) The variation of the unstrained lattice parameter measured in the material mid thickness as a function of distance from the weld line in an AA7449 friction stir weld as determined by the $\sin^2\psi$ technique using a robotic arm for sample manipulation and as determined from a stress-relaxed comb reference sample. The lattice parameter is given in relative variation because the same experimental set-up but at different dates was used hence absolute measured values are not comparable. (b) Lattice parameter as a function of tilt angle around two perpendicular sample axes measured at 2.84 mm distance from the weld centre line.

variation of d_0 across a slice of an AA7449 aluminium friction stir weld, where rotations of a flat sample around two perpendicular axes were required (see Figs. 4(a) and (b)). A detailed discussion of the importance of the unstrained lattice spacing for stress measurements in aluminium friction stir welds is beyond the scope of this paper and can be found elsewhere [16,17].

The experiment was carried out in accordance with the work procedure. Since the sample and the required measurement grid were of simple geometrical shape no CAD model was developed (steps (iii) and (iv) unnecessary). Instead, the measurement coordinates were calculated directly from the point cloud data obtained from the geometry scanning process. With this set-up 2640 measurements on 165 locations (5 lines, 33 points) rotating the sample in 8 steps of eight degrees per step around two orthogonal axes, respectively (see Figs. 4(a) and (b)) over 33 h was carried out successfully.

The recorded d_0 variation occurs because solute elements move into and out of solution due to the thermal excursion near to the weld. These solute changes affect the strain-free lattice parameter. The observed variation is in very good agreement with d_0 data achieved independently using the comb method [17] as shown in Fig. 5(a). Fig. 5(b) shows an example of the lattice spacing measured as a function of tilt angle around the two perpendicular sample axes Y and Z in one position in the weld nugget of the friction stir weld.

3.2. Quantitative texture analysis (pole figure determination)

In order to examine the applicability of the system for texture measurements, the robotic arm based sample manipulation system was installed on the SALSA neutron beam line at the ILL, France, as shown in Fig. 4(c). The aim was to determine part of a pole figure of a 25 mm diameter sphere made from cold-rolled AA7449 aluminium alloy by measuring the diffraction peak intensity of the Al-311 reflection for 100 different orientations of the centre of the sphere to the scattering vector. A sphere was chosen to avoid the complexity of attenuation of the beam through the sample as the path length is constant when the sphere is rotated around its centre.

Again, the experiment was carried out in accordance with the work procedure. The position of the aluminium sphere centre within the $X_T Y_T Z_T$ system was determined with the CMM and subsequently the required sphere orientations were programmed. The work procedure steps (iii) and (iv) were not necessary. The sphere was rotated around two axes in steps of 10° covering approximately one octant of the sphere. The basic set-up is shown in Fig. 4(c). The significant advantage of the big range of rotational movement by the robotic arm allowed that the complete measurement was done with only one sample set-up. In addition, the high flux of the SALSA beam line allows short counting times, hence enabling relatively quick measurement of the texture of a component. However, this demonstration experiment was intended only to illustrate the abilities of the robotic sample manipulation system (high rotational freedom) rather than to determine the component texture precisely. In practice, this simple measurement of texture could have been performed with a standard goniometer, but it amply illustrates the potential of robotic sample manipulation. More complex measurement procedures could easily be implemented; for example, it could be used to map the variation of texture across a sample. Fig. 6 compares the section of the pole figure obtained with the robotic arm sample manipulation

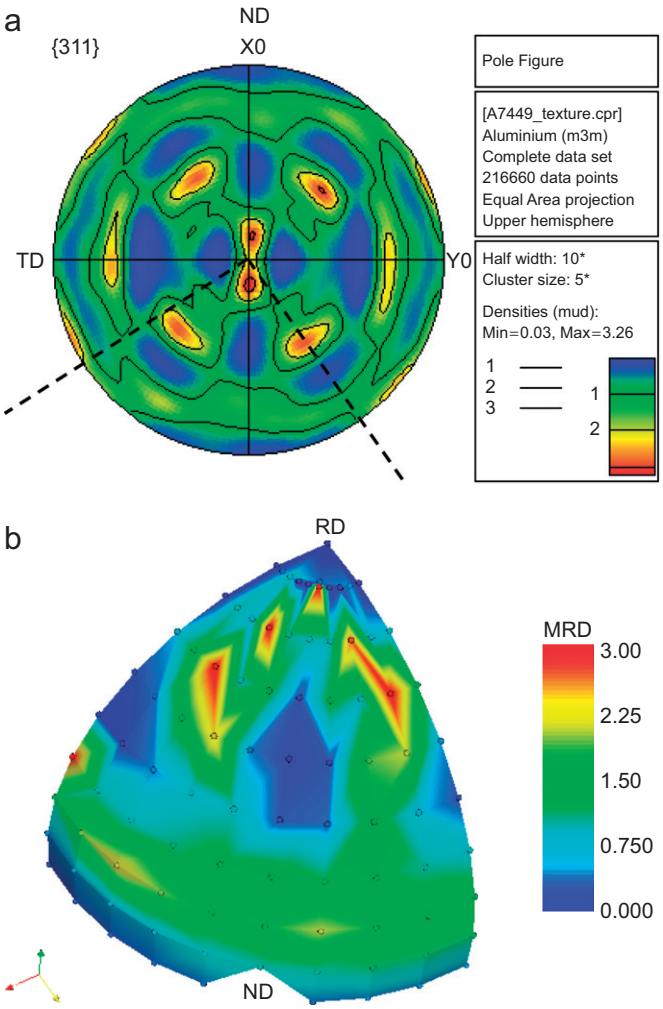

Fig. 6. Pole figure measurements by (a) EBSD and (b) neutron diffraction using the robotic arm sample manipulation system to scan a quadrant of the pole figure on a coarse $10^\circ \times 10^\circ$ step grid. The dashed bars in the EBSD pole figure indicate the range of angles assessed by the robotic arm system.

system and the pole figure obtained using EBSD, showing good agreement qualitatively as well as quantitatively, despite the relatively coarse measurement grid employed.

4. Conclusions

In this paper we have presented a novel approach for complex sample manipulation based on a Staeubli serial six-axis robotic arm. At synchrotron X-ray or neutron facilities it can be used for diffraction based measurements of strain or texture where high degrees of sample movement freedom are required. The positioning accuracy of the robotic arm system was found to be of the order of 20 μm and is therefore quite sufficient for the applications described. Similarly, the payload of the robotic arm (several kg) is adequate for a wide range of samples and applications in materials engineering research using diffraction. For the future, it is worth mentioning that newer generations of (Staeubli) robotic arms and controllers allow higher payloads at similar positional accuracy while at the same time providing more flexible means of programming the robotic arm.

Two successful applications of the robotic arm sample manipulation system have been demonstrated, one for determination of the unstrained lattice parameter d_0 in a friction stir weld using the $\sin^2\psi$ method, and one for quantitative texture measurements in cold-rolled aluminium. These applications illustrate that robotic sample manipulation offers considerable advantages over conventional sample manipulation hardware and enable one to take full advantage of strain scanning software capable of manipulating and orienting complex 3D objects for automated measurement schedules [10].

Acknowledgements

Drs. T. Pirling and D. Hughes of the ILL are gratefully acknowledged for assistance with the robot set-up during the trial measurement on SALSA at the ILL. We would like to thank A. Mauro, ESRF, for preparing the electronics to interface the robot control unit with the SPEC control system on ID15A at the ESRF. Additionally, we would like to thank Prof. P.J. Webster and P. Busby (University of Salford, UK) for developing the VAMAS mounting system. J.A. would like to thank the BTU Cottbus (Cottbus, Germany) for allowing him to undertake the research work to his diploma thesis at the ILL, which formed part of this publication.

References

[1] M. Hutchings, P.J. Withers, T.M. Holden, T. Lorentzen, Introduction to the Characterisation of Residual Stress by Neutron Diffraction, CRC Press, Taylor & Francis, London, New York, 2005.
[2] I.C. Noyan, J.B. Cohen, Residual Stress: Measurement by Diffraction and Interpretation, Springer, Berlin, 1987.
[3] M. Peel, A. Steuwer, M. Preuss, P.J. Withers, Acta Mater. 51 (2003) 4791.
[4] H.-R. Wenk, J. Appl. Crystallogr. 24 (1991) 920.
[5] J.R. Santisteban, M.R. Daymond, J.A. James, L. Edwards, J. Appl. Crystallogr. 39 (2006) 812.
[6] M.A.M. Bourke, D.C. Dunand, E. Ustundag, J. Appl. Phys. A 75 (2002) 1.
[7] T. Pirling, G. Bruno, P.J. Withers, Mater. Sci. Eng. A 437A (2006) 139.
[8] P.J. Withers, P.J. Webster, N.J. Avis, An engineering body scanner for 3D stress and damage measurement and co-visulalisation, in: E.P.S.R. Council (ed.), EPSRC, 2001.
[9] K.T.W. Tan, G. Johnson, J. Kelleher, N.J. Avis, P.J. Withers, J. Neutron Res. 11 (2003) 247.
[10] J.A. James, J.R. Santisteban, L. Edwards, M.R. Daymond, Phys. B Condens. Matter 350 (2004) E743.
[11] In: Faverges (ed.), STAUBLI, Arm RX90B family characteristics, 2001, D.183.207.34.A - 06/01 web: 〈http://www.staubli.com/WEB/Robot/PageHTML.nsf/ECR_BYNAME/RXplastics90/$File/RX90B.pdf〉.
[12] ISO/VAMAS/TWA20, ISO TTA 3:2001(E), International Organization for Standardization, 2001.
[13] P. Petruska, P. Tuleja, Control and programming of robots and automated workcells by intelligent simulation system roans,

in: Ismcr '98, Proceedings of the Eighth International Symposium on Measurement and Control in Robotics, 1998, pp. 173–178.
[14] J.A. James, L. Edwards, Nucl. Instr. and Meth. A 571 (2007) 709.
[15] J. Altenkirch, Entwicklung einer robotergestuetzten Messplattform zur Eigenspannungsmessung in metallischen Werkstoffen (Development of a robotic arm based sample manipulation system for residual stress determination in metals), vol. Diploma, Fakultaet 3: Maschinenbau, Elektrotechnik und Wirtschaftsingenieurwesen, BTU Cottbus, Cottbus, 2005, p. 113.
[16] A. Steuwer, M. Dumont, M. Peel, M. Preuss, P.J. Withers, Acta Mater. 55 (2007) 4111.
[17] P.J. Withers, M. Preuss, A. Steuwer, J. Pang, J. Appl. Crystallogr. 40 (2007) 891.

ELSEVIER

Materials Science and Engineering A 488 (2008) 16–24

MATERIALS SCIENCE & ENGINEERING A

www.elsevier.com/locate/msea

The effect of tensioning and sectioning on residual stresses in aluminium AA7749 friction stir welds

J. Altenkirch [a,b,*], A. Steuwer [c], M. Peel [c], D.G. Richards [a], P.J. Withers [a]

[a] *Manchester Materials Science Centre, University of Manchester, Grosvenor Street, Manchester M1 7HS, UK*
[b] *Institute Laue-Langevin, 6 rue J Horowitz, 38042 Grenoble, France*
[c] *FaME38 at the ILL-ESRF, 6 rue J Horowitz, 38042 Grenoble, France*

Received 22 May 2007; received in revised form 18 October 2007; accepted 21 October 2007

Abstract

Using synchrotron X-ray diffraction the residual stress distribution has been measured in a series of AA7449-W51 aluminium friction stir welds that had been tensioned to different loads during welding. By modifying the stress accumulation path, the application of a tensioning stress has reduced the tensile magnitude of the final residual weld stresses. In the present case the residual stresses were minimised when the applied load is ~35% of the room temperature yield stress of the parent material. Subsequent sectioning of the weld into shorter test lengths, as might be necessary for weld testing, resulted in a progressive and significant relaxation of the residual stress field. The effect of tensioning on the weld component distortion also has been investigated.

Keywords: Friction stir welding; AA7449; Residual stress; Mechanical tensioning; Stress relaxation

1. Introduction

The presence of residual stresses in welded components are known to have a significant influence on the lifetime [1]. Recent work [2–7] has substantially improved our understanding of the residual stress distribution in components joined by friction stir welding (FSW), however, this remains an area of uncertainty. The effect of many easily controlled parameters, such as welding speed, tool type, downward force, clamping method, alloy type/temper or the weld geometry, have not been characterised in a systematic way. Nevertheless, some features can be said to be well established and in agreement with theory [8]. In common with most, if not all, welding methods, the region around the weld is associated with tensile residual stresses which tend to be largest in the welding direction. In a number of instances residual stresses approaching the local room temperature yield point have been found in friction stir welds [7,9]. In practice there is a limit to the extent that residual stress can be reduced simply by optimising the FSW conditions [7]. Furthermore, other requirements, such as avoiding the introduction of flaws and maintaining production rates, may constrain the parameter range that can be employed.

Tensile loading of welds during the welding process has been suggested as a means of significantly reducing the residual stresses [10,11]. This loading can be performed during or after welding and can be categorised as *global*, where the entire component is mechanically loaded, or *local*, where the additional loads are applied to a small region around the location of the tool. The latter includes various localised heating or cooling methods which indirectly alter the stress state [12].

Weld tensioning works by reducing the level of local misfit that accumulates between the soft metal in the weld vicinity during welding [21]. Staron et al. used strain measurements by neutron diffraction to determine the stress state in welds produced in 3.2 mm and 6.3 mm thick AA2024 sheet with and without mechanical tensioning applied during welding [10]. They found that while low levels of tensioning reduced the tensile peak stresses, tensioning to 70% of the room temperature yield stress of the parent material caused the residual stress profile to change from tension to compression (peak stress of −200 MPa as against +150 MPa without tensioning). The same tendency has been observed using synchrotron X-ray diffraction measurements on 3.2 mm thick AA2024 over a wider range

* Corresponding author at: Manchester Materials Science Centre, University of Manchester, Grosvenor Street, Manchester M1 7HS, UK.
E-mail address: altenkirch@ill.fr (J. Altenkirch).

0921-5093/$ – see front matter © 2007 Elsevier B.V. All rights reserved.
doi:10.1016/j.msea.2007.10.055

of tensioning levels [13]. In this case the longitudinal residual stresses were predicted to be close to zero at an applied stress of ∼25% of the room temperature yield stress of the parent material. The change in the sign of the stresses was accompanied by a switch in the plate distortion from concave to convex (relative to the surface onto which the tool was forced).

Several authors have found residual stresses in simple friction stir welds that are substantially lower than the yield point of the material (∼100 MPa) [3,5,6]. However, in these cases the samples were cut from larger plates and the extent of relaxation was not quantified. This raises an important question, especially when evaluating the residual stresses or cross-weld properties in cut-down samples or test-pieces. The extent to which residual stresses relax on cutting down the plates and thus the extent to which they are representative of those which might be found in a welded engineering component is difficult to estimate.

The aims of this paper are twofold. Firstly, to present a systematic study, both experimentally and using FE modelling, of the effect of global mechanical tensioning during welding on the residual stress distribution and component distortion in friction stir welded AA7449-W51 aluminium plates. Secondly, to examine the effect of cutting up welded components on the residual stress field. In this context, we succeeded in finding a simple phenomenological formula for the prediction of stress relaxation. These results have important implications in cases where test-pieces are cut out from longer welds for evaluation, for example to determine cross-weld tensile strength or when investigating the fatigue behaviour, which is significantly influenced by residual stress fields.

2. Experimental

2.1. Weld trials

The welds were produced from 12.2 mm thick plates of AA7449 having a nominal composition of 7.5–8.7 Zn, 1.8–2.7 Mg, 1.8–2.4 Cu, 0.25 Ti/Zr and 0.20 Mn (wt%) with the remainder aluminium and minor impurities. The plates were supplied in the W51 temper, i.e. solution heat-treated and stress relieved by stretching the material to 0.5–3%. No elevated temperature ageing treatment was applied. In this condition, the material has a 0.2% yield strength, σ_{ys}, of 583 MPa. Although beyond the scope of this paper optical microscopy indicates a microstructure consistent with the prior literature, i.e. a partially recrystallised microstructure with pancake-shaped grains up to 1 mm in length in the longitudinal direction and possessing a substantial substructure with sub-grains of the order of 1–10 μm [14].

Two 1000 mm × 150 mm plates were clamped and mounted in a butt-weld configuration (see Fig. 1). Global tensioning was applied using hydraulic rams attached to each end of the plates using serrated, hardened grips that extended to 125 mm width. Slipping was further restricted by five 17.5 mm diameter pins in each grip that passed through pre-made holes in the plates. Welds were produced in a single pass with a weld track 800 mm long.

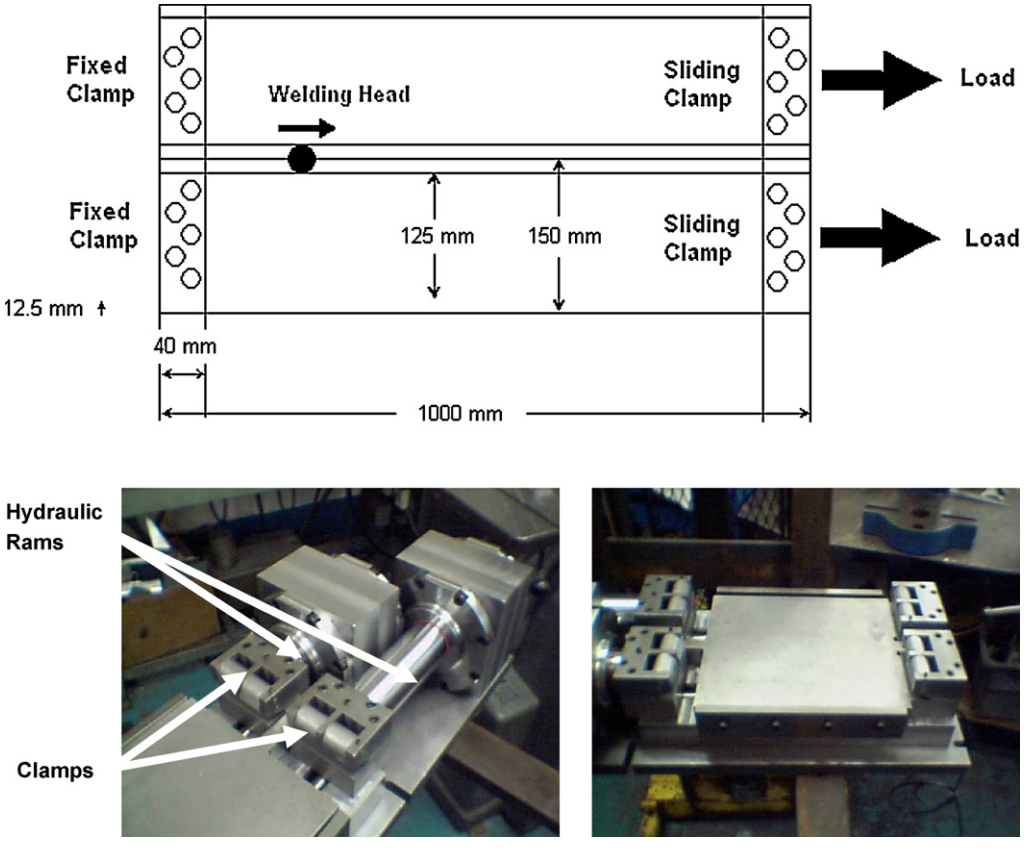

Fig. 1. Mechanical tensioning method and equipment used to generate the sample welds.

A Tri-flute™ tool was used with a shoulder diameter of 30 mm and a cone-shaped pin (Ø 17 mm, height 11.7 mm, cone angle 10°). The tool rotation speed was 225 rpm and the feed rate 250 mm/min. The FSW machine operated under load-control with a constant downwards force of 80 kN. The only parameter varied during the welding trials was the load applied by the tensioning system with each weld being preloaded to 5, 10, 20 and 30% of the room temperature yield stress of the parent material.

2.2. Temperature measurements

The temperature histories at selected locations were determined by thermocouple measurements on two welds, produced under identical circumstances but without the applied tensioning. K-type thermocouples were positioned by drilling holes from the upper surface of the weld to the required depth and then pushing the thermocouple into place along with a small quantity of thermal paste. In the first weld the thermocouples were placed so as to measure the temperature as a function of lateral distance from the weld line at the mid-thickness of the plate. The thermocouples were placed 20, 30 and 40 mm from the weld line. Thus, the temperature measurements began just outside the tool diameter where the thermocouples would not be disturbed by the passage of the tool. In the second weld, the thermocouples were placed 20 mm from the weld line but at 3, 6, 9 and 12 mm from the weld surface to determine the variation with depth. The thermocouples had a typical spacing of 2 mm in the direction of the weld line.

2.3. Residual stress measurements

The residual stress distributions have been measured non-destructively by energy dispersive diffraction using synchrotron X-rays (EDSXRD) on ID15A at the ESRF, France. This beam line offers a white-beam (all wavelengths) along with an energy sensitive Ge-detector, enabling the capture of a large range of the diffraction profile (0–300 keV) [31,32]. This method has the advantage that the strained lattice parameter can be determined by fitting the complete recorded diffraction profile comprising several diffraction peaks. This makes it less susceptible to texture and anisotropy effects [15]. In addition the range of wavelengths means more grains within the gauge volume will contribute to the diffracted signal and so grain size problems can be reduced to some extent (energy dispersive diffraction is inherently sensitive to the grain size with larger grains leading to higher experimental scatter in the measured strains). Nevertheless, the heterogeneous grain size in FS welds means the scatter would be expected to vary with location in the weld. Although the scatter was observed to be greater in the parent material this was not found to be a significant problem in the current case.

In order to penetrate the plate thickness, high X-ray energies (60–150 keV) and a low scattering angle ($2\theta = 5°$) were employed. The low scattering angle tends to elongate the gauge volume along the direction of the beam and so a small incoming beam size (100 μm × 100 μm) was used to restrict the maximum gauge volume length (~2.3 mm) so as to lie wholly within the plate thickness. On ID15A it is comparatively simple to use two detectors in order to measure the lattice spacing in two directions of strain simultaneously [16]; in this case the strain is measured in a direction 2.5°(θ) from the longitudinal and transverse directions in the weld (see Fig. 2). The difference in strain between the measured directions and the in-plane directions is negligible.

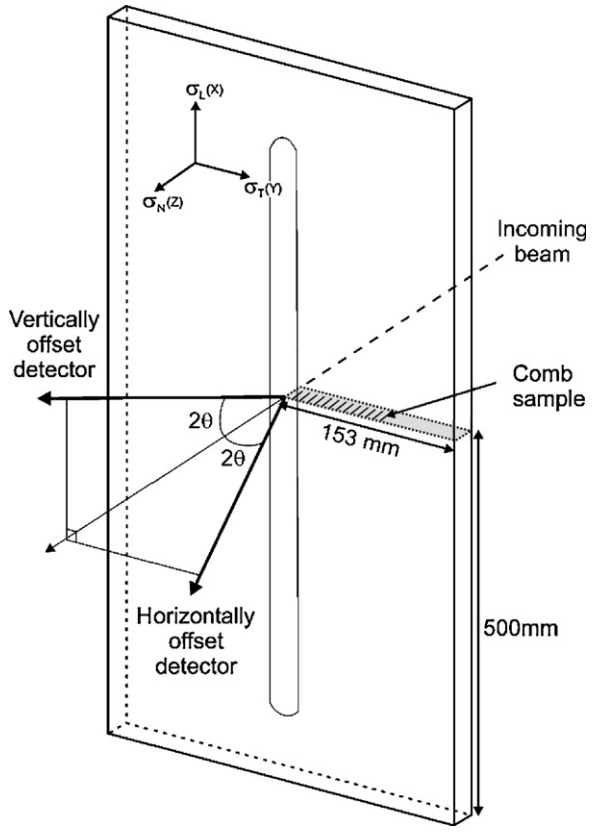

Fig. 2. Schematic of the residual strain measurement setup using two energy dispersive detectors ($2\theta \sim 5°$), offset in the vertical and horizontal directions to measure the longitudinal and transverse strains simultaneously. Note that the diffraction angles have been substantially exaggerated for clarity. The beam size is 100 μm × 100 μm and with the 5° diffraction angle restricts the maximum gauge volume length to ~2.3 mm.

The diffraction profiles were fitted using the GSAS profile refinement software with the reflection intensity being determined using the LeBail method [17]. After refinement, the unit cell parameter a can be directly extracted from the model. The strain was calculated using the conventional relationship $\varepsilon = (a - a_0)/a_0$, where a_0 is the unstrained lattice parameter The stress state was calculated from the two measured strain components under the assumption that there is no out-of-plane component to the stress tensor ($\sigma_N = 0$) over the gauge volume (i.e. a biaxial stress state):

$$\sigma_L = \frac{E}{1-\nu^2}(\varepsilon_L + \nu\varepsilon_T) \quad (1)$$

where ε_L and ε_T are the strain values in the weld longitudinal and transverse directions, E is the Young's Modulus and υ Poisson's ratio. σ_T is obtained by exchanging the two strain parameter in Eq. (1). Since fitting was performed on several peaks simultaneously, the bulk values for elastic modulus and Poisson's ratio can

be used in place of the conventional diffraction elastic constants [18].

In the case of age-hardened aluminium there is likely to be a variation in $a_0(y,z)$ ($=a_{ref} + \Delta a_0(y,z)$) across the weld ($Y$) and through weld depth (Z) due to the dissolution or coarsening of precipitates which will lead to changes in local solute concentration and hence the unstressed lattice spacing [19]. The variation in $a_0(y,z)$ was determined using a stress-free 'comb' [20]. The weld was cut in the normal-transverse plane to produce a 3 mm thick slice for which the dominant longitudinal stresses would have essentially relaxed (see Fig. 2). The remaining stresses were further reduced by using a diamond wire to cut 1.5 mm wide 'teeth' into the slice to produce a comb. The free ends of the teeth correspond to the weld surface. The lattice parameter was subsequently measured in each tooth as a function of distance from the weld line (Y) and weld surface (Z). However, the necessity of machining the comb from the weld meant that this part of the experiment was performed sometime after the initial experiment. Because this was carried out under slightly different experimental conditions, there was a small global offset between the absolute lattice parameters measured on the two occasions. As a result it was not possible to apply the absolute measured stress-free lattice parameters $a_0(y,z)$ to determine the strain and stress directly. Instead at each point (y,z), the spatial variation in the unstressed lattice parameter measured in the comb was used as a local perturbation ($\Delta a_0(y,z)$) to a global unstressed reference value a_{ref} used for each detector. These two global a_{ref} values were chosen to ensure stress equilibrium conditions, i.e. the longitudinal stresses balanced across the normal-transverse plane (presuming that the longitudinal stresses do not vary significantly through thickness) and the transverse stress was zero at the edge of the plate. A least-squares approach was used to modify the two global average a_{ref} values in order to fulfil the stress balancing and boundary conditions. Since modifying the parameter (and hence strain) in one direction alters the stress in the other direction, they were solved iteratively until the solution converged. The shift in the global unstrained lattice spacing due to this procedure was 0.0028 Å (691 $\mu\varepsilon$) for the longitudinal direction and 0.00021 Å (51 $\mu\varepsilon$) for the transverse. This corresponds to a global shift in the longitudinal stress of around 30 MPa.

3. Modelling

Direct measurements of the residual stresses in welds is both time consuming and expensive. As a result, it is desirable to be able to predict the location and magnitude of the peak stresses and how these stresses redistribute during subsequent processing. Here a model described in detail elsewhere [21] comprising sequentially linked heat transfer and mechanical stress models has been implemented. The effect of the tool is modelled as a surface heat source for the shoulder and a cylindrical volume source for the pin (neglecting threads and other features). The heat flux is fixed for the simulation with 40% of the total flux being distributed by the shoulder and 60% by the pin. The flux under the shoulder varied as a linear function of radius while that in the pin was uniformly distributed. This allocation of the shoulder and pin powers were based on calibration studies and the use of a computational fluid dynamics model created by Colegrove [22] and Colegrove and Shercliff [23], that incorporates the material flow. Since the tool was not explicitly included in the model, the material in the tool region has the thermo-mechanical properties of aluminium rather than steel. The distribution of heat at each time step was determined by the user subroutine DFLUX which calculates the flux at each integration point under the tool. This in combination with the requirement to capture the large thermal gradients in the heat transfer model necessitates the use of DC3D8 brick elements in a fine (1 mm × 1 mm × 1 mm) mesh around the weld line, which changes to DC3D6 wedge elements in a much coarser mesh further out in order to reduce the computational requirements. These heat transfer elements are substituted by their direct equivalents in the mechanical stress model to facilitate the transfer of the generated thermal profile.

The steel anvil and aluminium support structure were modelled by surfaces with specific heat transfer coefficients. The steel anvil was 1000 mm × 50 mm and placed directly under the weld line. Further from the weld line the welds were supported from underneath by aluminium blocks and pressed down by aluminium clamps. The heat loss to the support-structure and retaining clamps was simulated using artificial surface convection coefficients.

To simulate the clamping conditions, surfaces were fixed by limiting their degrees of freedom in the desired directions, thus allowing movement when additional forces were applied homogeneously to the ends of the plates in order to simulate the global mechanical tensioning. The tensioning grips themselves were not modelled.

In order to model the effect of subsequently cutting out test-pieces from the weld additional interfaces were inserted corresponding to the locations where each cut would be made. These were then fully fixed to each other to form a rigid plate. After welding, each interface was released in the order of cutting and the remaining plate was allowed to relax. The additional boundaries restricted the normal coarsening of the mesh, resulting in a substantially finer mesh and a correspondingly longer calculation time requirement. Even on a fast PC the model required 18 days to run compared to the ∼5 h for the normal thermo-mechanical model.

4. Results

4.1. Thermal trajectories

The measured temperatures are consistent with previous measurements in friction stir welds (e.g. [25]). The highest temperature measured 20 mm from the weld line was ∼270 °C, decreasing sharply to ∼150 °C at 40 mm (see Fig. 3a). No systematic difference was found on either side of the weld line, indicating that the asymmetry of the process due to the rotating tool has little impact on the thermal profile, at least for distances greater than 20 mm from the weld line (5 mm beyond the tool shoulder). The thermocouples placed at different depths below the weld surface (see Fig. 3b) indicated that beyond the tool shoulder, the thermal profile varies little through depth in

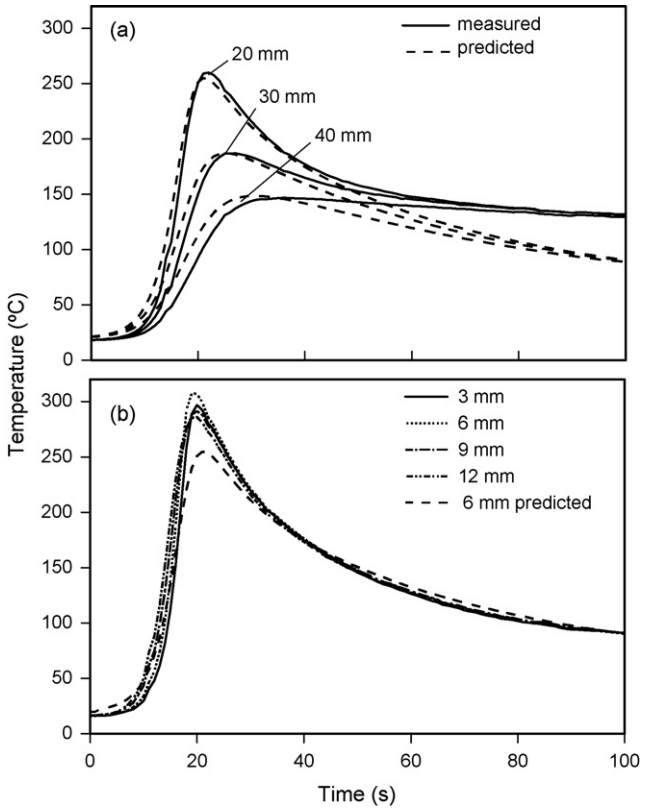

Fig. 3. Thermal trajectories as a function of time for (a) different lateral distances from the weld line in the material mid-thickness (solid lines denote measured and dotted lines predicted profiles). The model was optimised for the peak temperature distribution, but predicted somewhat greater cooling rates. Plot (b) shows the thermal profiles for different depths below the tool at a distance of 20 mm from the weld line (measured at 3, 6, 9 and 12 mm and predicted at 6 mm). Note that in (b) the thermocouples were offset 2 mm along the weld line and so there is a small time lag between the measurements.

line with the high thermal conductivity of aluminium. However, compared to the temperature measurement in the transverse direction a higher peak temperature of ∼300 °C and an increased cooling rate was observed in the through thickness temperature variation measurement. At present no clear explanation for this discrepancy has been found, although it could be due to uneven contact between the welded plates and the backing plate which can be difficult to maintain.

The thermal model was optimised for peak temperature calculation based on the temperatures measured as a function of distance from the weld line, but revealed a somewhat greater cooling rate than measured indicating that further refinement of the heat losses would be useful (although not critical given the good match for much of the welding cycle). From the measured and predicted temperature profiles a peak temperature underneath the pin of 460–500 °C may be expected which is in agreement with the literature [25].

4.2. Unstressed lattice parameter

The variation of the unstrained lattice parameter, a_0, is plotted in Fig. 4 as a function of lateral distance from the weld line. In line with previous results for the age-hardening alloys AA6082

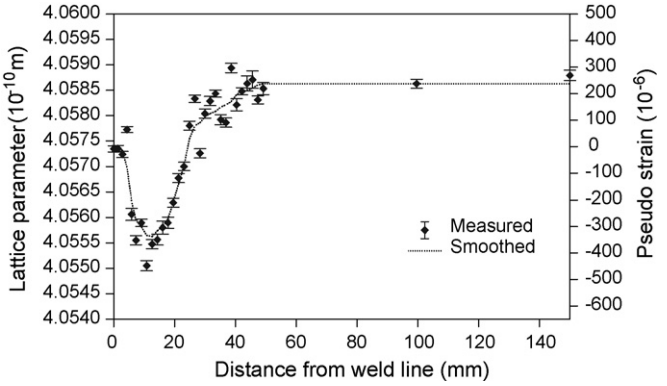

Fig. 4. The unstrained lattice parameter a_0 and the multiple peak fitting uncertainty at the mid-thickness of the weld as determined from the comb specimen. Appropriate values for the strain calculation were determined by interpolating a smoothed profile (dashed line). To account for the different detector calibrations the global a_{ref} used for the stress calculation was shifted by ∼−0.013 Å to fulfil the boundary condition of stress balancing in the longitudinal and by ∼−0.016 Å in the transverse direction to achieve zero stress at the sample edges.

and AA7010 [19] the stress-free lattice parameter decreases in the heat-affected zone, presumably due to the removal of solutes from the matrix as the precipitate structure characteristic of the parent plate over-ages. Closer to the weld line, a_0 begins to increase again as a result of the dissolution of the precipitates during welding and the subsequent natural ageing which produces a precipitate structure closer to that of the parent material. At the weld line a_0 is intermediate between that in the parent material and that in the HAZ. This is probably because some fraction of the solute is taken up in the stable and meta-stable η-phases as well as GP zones that generally form during the cooling cycle [26], which is considerably slower than the quench employed after the standard solution treatment of these alloys. Little variation of the unstressed lattice parameter with depth was found.

The variation of the unstressed lattice parameter across the weld is considerable, being equivalent to a strain of 750×10^{-6}, which is the same order of magnitude as found by Steuwer et al [19]. This is greater than the global shifts required to ensure equilibrium conditions (c.f. Section 2.3) but in fact has a disproportionate effect since it applies to both of the measured strains and hence propagates through the stress calculations. The difference in determined residual stress can be aquired by using both a fixed global and a locally varying a_{ref} for the stress calculation respectively and was found to be greatest in the HAZ, i.e. 15 mm from the weld line. In the 5% tensioned weld, for example, using the local a_0 increased the longitudinal stress from 100 MPa to 180 MPa. This is particularly significant since this region is usually associated with the poorest mechanical properties [26,27].

4.3. Effect of global mechanical tensioning

The global mechanical tensioning of welds aims to reduce or minimise both the level of residual stresses and the amount of distortion in the plates. Fig. 5 shows the plate distortion in the transverse plate direction as a function of the applied tension-

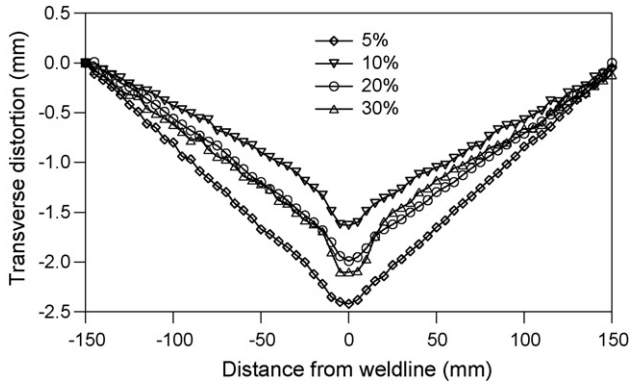

Fig. 5. Transverse plate distortion as a function of distance from the weld line for different applied global mechanical tensioning loads during welding.

ing. The distortion in the longitudinal direction was negligible. The global tensioning was found to have no simple influence on weld butterfly distortion. Fig. 6 shows the measured and predicted evolution of the longitudinal residual stress as a function of the tensioning level. Since the experimental results are broadly symmetrical around the weld line and the FE model makes no distinction between the advancing and retreating sides of the weld, only one side of each set of curves is shown and only to a distance of 100 mm from the weld line. As might be expected, the highest tensile stresses are observed for the lowest level of tensioning (5% σ_{ys}) reaching ~200 MPa in the weld zone and ~230 MPa in the peaks. With increased tensioning level, the stresses decrease reaching only ~30 MPa at the weld line for 30% σ_{ys} tensioning. The FE predictions [21] are broadly in-line with the observations, albeit with a tendency to be slightly higher than the measured values. The effect of the tensioning is well predicted by the model as can be seen in Fig. 7, which plots the residual stress on the weld line as a function of the applied tensioning level. The stress reduction as a function of the applied tensioning is essentially linear for both, the experimental and modelled data, predicting zero stress at approximately 35% and 38% tension, respectively. The higher tensioning level necessary to achieve zero stress on the weld line is due to the higher starting stress values predicted by the model. One feature that

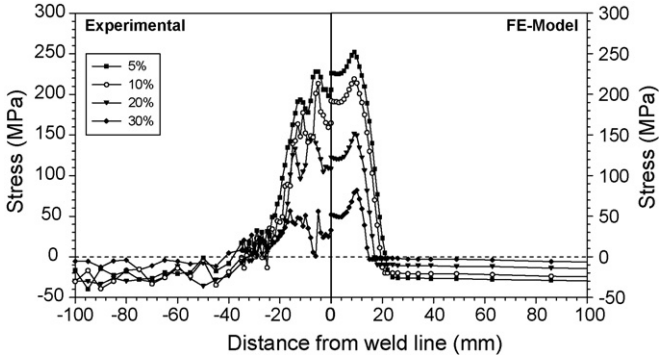

Fig. 6. Longitudinal residual stress profiles at plate mid length on the advancing side of the weld as a function of applied tensioning level (% of room temperature yield stress) as experimentally determined by EDSXRD (left) and predicted by the FE model [21] (right). Note that for reasons of clarity only the region near the weld is shown. The estimated error is ~±5 MPa.

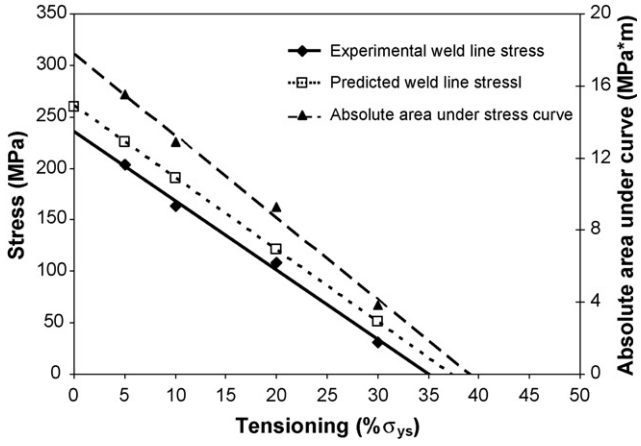

Fig. 7. The average longitudinal stress near the weld line (±2 mm) as a function of applied tensioning level (% σ_{ys}). From the experimental data ~35% and from the predicted values ~38% of the room temperature yield strength may be inferred as the optimum tensioning level, the integral of the absolute area under the stress curve also points to a linear decrease as tensioning is increased indicating an optimum tensioning level of ~39%.

is observed in practice but is not predicted by the model is a slight broadening of the stress field around the weld zone with increasing levels of tensioning. The reason for this broadening is not known at present.

In common with previous data for friction stir welds [2,3,10] the transverse stresses, which are not shown for reasons of brevity, are substantially lower than those in the longitudinal direction. The peak residual stress reaches 40–50 MPa and is not noticeably influenced by the applied global mechanical tensioning.

4.4. Effect of sectioning a test-piece on the residual stress distribution

Very rarely welds are evaluated in their complete form; instead, they are often cut-down to form shorter test-pieces for evaluation. The variation in the residual stress profile as the weld is systematically reduced in length is shown in Fig. 8. The

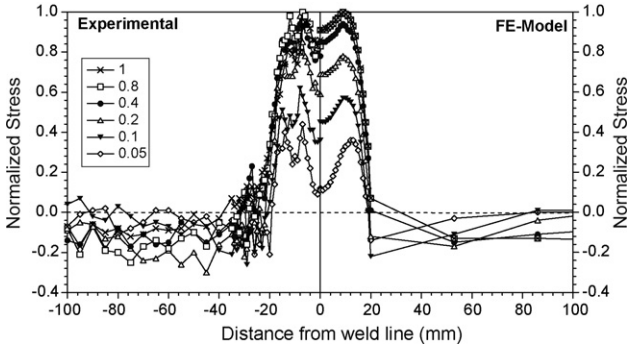

Fig. 8. The measured (left) and predicted (right) relaxation of the longitudinal residual stress profile as a function of the fractional length of the original 1 m long weld retained. The model calculations were for a non-tensioned weld while the actual measurements were performed on a weld tensioned to 5% of the room temperature yield stress resulting in lower measured than predicted residual stresses. Hence for comparison the data were normalized. The estimated measurement error is ~±5 MPa or ~±0.016 when normalized.

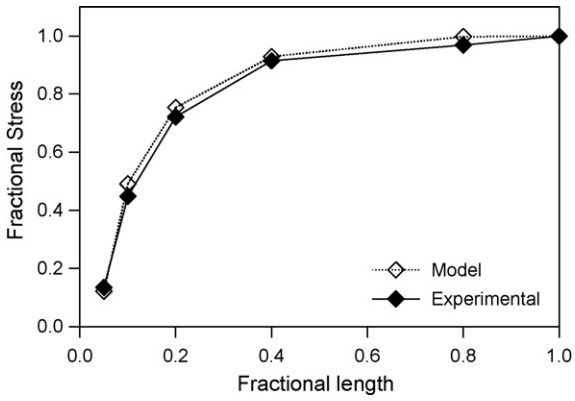

Fig. 9. The fraction of longitudinal stress remaining at the weld line as a function of the fractional length of the weld remaining. The model was run on a non-tensioned weld while the validation was performed on a weld tensioned to 5% of the room temperature yield stress.

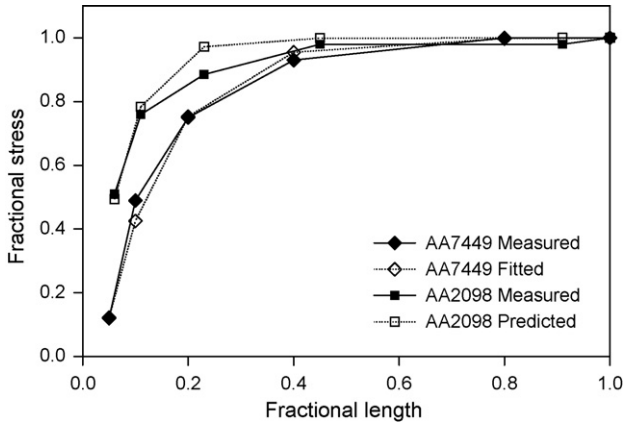

Fig. 10. The fraction of longitudinal residual stress remaining at the weld line as a function of the fractional length of the weld remaining in AA7449 and AA2098 friction stir welds with different geometries and tensile regions of different width, but applying the formulism Eq. (2).

model originally was run on a non-tensioned weld, but no non-tensioned weld was actually available to measure. As a result, the comparison was made with a 5% tensioned weld by normalizing all residual stresses as shown in Fig. 8. Fig. 9 plots the remaining longitudinal stress on the weld line as a fraction of the initial stress as a function of the fractional test-piece length. It can be seen that the stress profile across the centre of the test-piece is largely unaffected until the sample is less than 40% (400 mm) of its original length but subsequently decreases rapidly. For example, when the original weld is sectioned down to 100 mm weld length the peak stress is only 40% of that originally present. Since, in many cases, welds are tested using specimens much shorter than 400 mm notable errors could be introduced. This should be considered when designing a weld test strategy.

The behaviour observed above is not unexpected. Indeed, St. Venant's principle indicates that stresses in a given location are unaffected by changes in loading (e.g. by cutting a plate) if such changes occur sufficiently far away from the area being measured [28,29]. St. Venant's referred to this distance as the "characteristic distance". We have continued to use this term in trying to describe the relaxation behaviour by an empirical equation, but it should be noted that no rigorous definition of this distance exists in the literature.

It is desirable to describe the remaining stress σ_{relax} in the weld as a function of the remaining length l_r and the initial stress σ_0. The observed behaviour can be described by the exponential equation:

$$\sigma_{relax} = \sigma_0 \left[1 - \exp\left(-\frac{l_r - l_{relax}}{l_{char}}\right)\right] \quad (2)$$

where l_{relax} is the length at which the weld reaches zero macroscopic stress and l_{char} is the characteristic length, which essentially describes how sensitive the stress is to the removal of material. These two parameters were determined by non-linear fitting to the measured data shown in Fig. 9. The refinement provided values of 120 mm for the characteristic distance and 35 mm for the relaxed length. The latter is readily validated by visual examination of the data. Interestingly, the fully relaxed length along the weld line is similar to the width of the tensile region perpendicular to it; in line with the expectation that at this length the tensile region is no longer constrained to a meaningful degree by the surrounding material. The characteristic distance is approximately three times the width of the tensile region although there is no obvious physical reason why this should be the case and must be taken as an empirical observation at this time.

In order to test the validity of Eq. (2) for welds of different dimensions and material, further measurements were made on a 3 mm thick Al–Li AA2098 friction stir weld. This was produced with a tapered tool (13 mm shoulder diameter, 4.91 mm pin diameter and 3 mm length, 10° decreasing taper) and welding parameters of 1200 rpm clockwise rotation speed, 500 mm/min traverse speed and 8 kN down force. The width of the tensile zone in this weld was determined to be 20 mm and so l_{relax} was set to 20 mm and l_{char} to 60 mm, under the assumption that the previously observed length ratios also applied to this weld. The result is shown in Fig. 10, which compares the experimentally determined values, the fitted AA7449 values and the prediction for the AA2098. As a result of the smaller size of the tensile region in the Al–Li welds they can be cut into narrower test-pieces than the AA7449 welds before significant residual stress relaxation occurs. In general, the experimental and predicted values are in good agreement although there is some minor discrepancy at a fractional length of ~0.25 in the AA2098 weld. It should be noted that no form of data fitting was performed for the Al–Li weld. At present, only two sets of welds with differing weld geometry and material have been evaluated, but further testing will be performed to confirm the utility of Eq. (2).

5. Discussion and conclusions

The results of the current study indicate that a tensioning stress ~35% of the room temperature yield stress is needed to reduce the longitudinal residual stress at the weld line to a value around zero. This is a little higher than that found by Price et al. for friction stir welded AA2024 [13]. The stresses in the transverse direction were typically much smaller than the

longitudinal stresses and found to be largely insensitive to the tensioning level.

The mechanism by which global mechanical tensioning reduces the magnitude of the residual stresses has been discussed by Richards et al. [21]. In essence, the mechanical tensioning affects both the compressive yielding ahead of the tool and the tensile yielding behind the tool as the tool passes.

(a) Ahead and under the tool, the tensile stress reduces the amount of compressive yielding that occurs as the hot metal expands. By reducing the plastic misfit, this leads to a reduction in the magnitude of the tensile residual stress that is produced on cooling.
(b) Behind the tool, tensioning encourages increased tensile plastic straining as the hot metal cools. The tensile misfit thus generated can either decrease the magnitude of the tensile stress (for tensioning levels <35%) or introduce compressive residual stresses (for tensioning levels >35%) [21].

The response of AA7449 to high temperatures is complicated due to the behaviour of the strengthening precipitates, which will dissolve as function of both time and temperature. Given that the weld experiences a complex thermal history – resulting in an equally complex yield history – it remains difficult to determine a simple correlation between welding parameters and the necessary level of preloading.

Determining the influence of residual stresses and weld microstructure on factors such as fatigue life usually requires the excision of test-pieces from the original weld. However, in all but the largest of such samples, the removal of material will result in the relaxation of the stresses as demonstrated in Figs. 8 and 9, where relaxation was significant (>10%) below 40% of the original sample length. As a result, the relevance of stress data obtained from cut samples will clearly be compromised and misleading when data are transferred to actual components. Similar problems arise when using diffraction to determine the residual stresses in large welds because the limited space available on most beam lines or X-ray diffractometers means that samples often need to be cut-down in order to be measured [2,9]. The use of alternative methods such as the crack compliance technique require that the sample is machined into a specific shape [30]. However, the current results clearly indicate that such cutting must be done with care to ensure the stress state is not unduly altered.

It has been shown that predictions of the stress relaxation upon sample exision can be done with good accuracy by modifying the FE code used to estimate the residual stresses in such welds. However, such an approach is time consuming and will not be appropriate in many cases. As an alternative, it has been found that the current data can be described using an empirical equation with two parameters that appear to be proportional to the width of the longitudinal tensile zone. Since the width of the tensile zone is often close to the width of the tool, this equation may be used (with caution) to estimate the stress relaxation when a sample is removed from the weld even without full stress data. However, while these parameters have been confirmed in two sets of welds produced in thick (12 mm) and thin (3 mm) aluminium friction stir butt welds using larger (30 mm) and smaller (13 mm) tools, it remains to be seen how applicable this form of relaxation equation will be in the more general sense.

Acknowledgements

The authors would like to acknowledge access to the ESRF through the proposal ME-1165, M. Poad (Airbus UK, Plc) for supplying the welded samples and Prof. P.B. Prangnell (Manchester University, UK) and Prof. S.W. Williams (Cranfield University, UK) for useful and stimulating discussions. J. Altenkirch would like to acknowledge the support of the ILL & EPSRC (Portfolio Partnership in Light Alloys) for his PhD. Triflute™ is a registered trademark of TWI The Welding Institute Plc, UK.

References

[1] M.N. James, D.J. Hughes, Z. Chen, H. Lombard, D.G. Hattingh, D. Asquith, J.R. Yates, P.J. Webster, Eng. Fail. Anal. 14 (2007) 384.
[2] M. Peel, A. Steuwer, M. Preuss, P.J. Withers, Acta Mater. 51 (2003) 4791–4801.
[3] C. Dalle Donne, E. Lima, J. Wegener, A. Pyzalla, T. Buslaps, Proceeding of the 3rd International Symposium on FSW, TWI, Cambridge, Kobe, Japan, 2001.
[4] L.D. Oosterkamp, P.J. Webster, P.A. Browne, G.B.M. Vaughan, P.J. Withers, Mater. Sci. Forum 347–49 (2000) 683–687.
[5] P.J. Webster, L.D. Oosterkamp, P.A. Browne, D.J. Hughes, W.P. Kang, P.J. Withers, G.B.M. Vaughan, J. Strain Anal. Eng. Des. 36 (2001) 61–70.
[6] M.A. Sutton, A.P. Reynolds, D.-Q. Wang, C.R. Hubbard, J. Eng. Mater. Technol. 124 (2002) 215–221.
[7] A. Steuwer, M. Peel, P.J. Withers, Mater. Sci. Eng. A 441 (2006) 187–196.
[8] K. Masubuchi, Analysis of welded structures, in: Residual Stresses, Distortion and their Consequences, Pergamon Press, Oxford, 1980, 642 pp.
[9] X.L. Wang, Z. Feng, S.A. David, S. Spooner, C.R. Hubbard, Proceeding of the 6th international conference on residual stresses [ICRS-6], vol. 2, IOM Communications, Oxford, UK, 2000, pp. 1408–1414.
[10] P. Staron, M. Kocak, S. Williams, A. Wescott, Phys. B: Condens. Mat. 350 (2004) E491.
[11] S.W. Williams, D.A. Price, W. Wescott, A. Steuwer, M. Peel, J. Altenkirch, J. Withers, M. Poad, Proceeding of the 6th International Symposium on FSW, Saint-Sauveur, Montreal, Canada, 2006.
[12] P. Michaleris, J. Dantzig, D. Tortorelli, Weld. J. 78 (1999) 361–366.
[13] D. Price, C.J. Harrison, S.W. Williams, A. Wescott, A. Johnson, J. Gabzdyl, M. Smith, M. Rahim, BAe Systems Report No JS 15232 (2004).
[14] K.V. Jata, K.K. Sankaran, J.J. Ruschau, Metall. Mater. Trans. 31A (2000) 2181–2192.
[15] M.T. Hutchings, A.D. Krawitz, Measurement of Residual and Applied Stress Using Neutron Diffraction, Kluwer Acadamic Publishers, Dordrecht, Netherlands, 1992.
[16] A. Steuwer, M. Peel, T. Buslaps, Mater. Sci. Forum 524–525 (2006) 267–272.
[17] A.C. Larson, R.B. Von Dreele, General Structure Analysis System (GSAS), Los Alamos National Laboratory, 1994.
[18] M.R. Daymond, M.A.M. Bourke, R.B.V. Dreele, B. Clausen, T. Lorentzen, J. Appl. Phys. 82 (1997) 1554–1562.
[19] A. Steuwer, M. Dumont, M. Peel, M. Preuss, P.J. Withers, Acta Mater. 55 (2007) 4111–4120.
[20] P.J. Withers, M. Preuss, A. Steuwer, J. Pang, J. Appl. Crystallogr. 40 (2007) 891–904.
[21] D.G. Richards, P.B. Prangnell, S.W. Williams, P.J. Withers, Global Mechanical Tensioning for the Management of Residual Stresses in Welds. Mat. Sci. Eng. (2007), submitted.

[22] P. Colegrove, Proceeding of the 2nd International Symposium on FSW, Gothenburg, Sweden, 2000.
[23] P. Colegrove, H.R. Shercliff, J. Mater. Process. Technol. 169 (2005) 320.
[25] W. Tang, X. Guo, J.C. McClure, L.E. Murr, J. Mater. Process. Manuf. Sci. 7 (1999) 163–172.
[26] M. Dumont, A. Steuwer, A. Deschamps, M. Peel, P.J. Withers, Acta Mater. 54 (2006) 4793–4801.
[27] D. Allehaux, G. Petit, M.H. Campagnac, Proceeding of the 4th International Symposium on Friction Stir Welding, Park City, UT, USA, 2003.
[28] S.P. Timoshenko, J.N. Goodier, Theory of Elastics, McGraw-Hill Book Company, Singapore, 1987.
[29] A.C. Ugural, S.K. Fenster, Advanced Strength and Applied Elasticity, P T R Prentice Hall Inc., Englewood Cliffs, 1994.
[30] C. Dalle Donne, G. Biallas, T. Ghidini, G. Raimbeaux, Proceeding of the 2nd International Symposium on FSW, TWI, Cambridge, Gothenburg, Sweden, 2000.
[31] A.M. Korsunsky, S.P. Collins, R.A. Owen, M.R. Daymond, S. Achtioui, K.E. James, J. Synchrotron Rad. 9 (2002) 77–81.
[32] A. Steuwer, J.R. Santisteban, M. Turski, P.J. Withers, T. Buslaps, J. Appl. Cryst. 37 (2004) 883–889.

Mechanical Tensioning of High-Strength Aluminum Alloy Friction Stir Welds

J. ALTENKIRCH, A. STEUWER, M.J. PEEL, P.J. WITHERS, S.W. WILLIAMS, and M. POAD

The extent to which *in-situ* global mechanical tensioning (GMT) can be used to modify the residual stress state in friction stir (FS) welds is investigated in this article. Residual stress distributions have been determined by synchrotron X-ray and neutron diffraction for four sets of FS welds in high-strength AA7449-W51 and lithium containing AA2199-T8 aerospace aluminum alloys subjected to a systematic range of GMT levels. For the cases studied, the results indicate that the level of residual stresses present in the as-welded state is a function of the alloy. The rate of residual stress reduction brought about by GMT, however, is basically alloy independent; indeed, it is essentially linear with respect to the GMT load, so that the tensioning required to reduce the weld stresses to zero can be calculated directly from the stresses present in the untensioned case. For thin plates, proximity to the yield stress in the hot-softened zone means that a guideline rule is that 1 MPa of tensioning during welding reduces the tensile stress by approximately 1 MPa. The GMT was found to be less effective at greater depths in thick plates. Furthermore, a reduction in bending distortion and an increase in angular distortion was observed with increased GMT, while no effects on the weld microstructure and hardness were observed.

DOI: 10.1007/s11661-008-9668-1

I. INTRODUCTION

THE presence of residual stresses in welded components is known to have a significant influence on the fatigue behavior and, therefore, on the lifetime of the welded component.[1,2] As a result, much of the prior research on the residual stress distribution resulting from friction stir welding (FSW)[3–8] has been performed with a view to determining the welding parameters that minimize the residual stresses and, therefore, extend the lifetime performance of the component. The characteristic features of the residual stress distribution in FSW tend[3] to be similar to those for fusion welding.[9,10] This is largely because the mechanical effects of the FSW tool on the residual stress level appear to be slight, compared to the thermal effects of the tool.[11] In common with most welding methods, the region around the FS weld is associated with tensile residual stresses that are largest in the welding direction and that are balanced by compressive stresses further away from the weld line. The magnitude of residual stresses in FS welds varies from alloy to alloy and also depends on the welding parameters applied, but it is common for the peak residual stresses to approach the local room-temperature yield point of the alloy.[8,12] Depending on the thickness geometry of the welded component, the welding residual stresses may be partially accommodated by distortion both longitudinal (L) (bending or buckling distortion) and transverse (T) (angular or butterfly distortion) to the weld (Figure 1), as well as by rotational distortion and shrinkage.[10] Bhide *et al.*[13] encountered buckling distortion for HSLA-65 steel FS welds in 6.25-mm plates, compared to angular and bending distortions for submerged arc and gas metal arc welding, due to a broader, lower-level tensile residual stress weld zone and significant compressive stresses in the parent plate lateral to the weld. Welding distortion can be a significant problem and may require expensive postweld correction procedures.

In practice, there is a limit to the extent that residual stresses can be reduced simply by optimizing the welding conditions.[8] Furthermore, other requirements, such as the avoidance of the introduction of flaws and the drive to maintain economic production rates, may constrain the welding parameter range that can be employed in practice.

As an alternative, the mechanical tensile loading of welds has been suggested as a means of reducing the residual stress distribution and has been subject to several investigations.[14–18] This loading can be performed during or after welding and can be categorized as global, in which the entire component is mechanically tensioned, or local, in which the loads are restricted to a small region around the location of the welding tool.

J. ALTENKIRCH is with the School of Materials, University of Manchester, and the Institute Laue-Langevin. P.J. WITHERS is with the School of Materials, University of Manchester, Manchester M1 7HS, United Kingdom. Contact e-mail: philip.withers@manchester.ac.uk A. STEUWER is with ESS Scandinavia, 22350 Lund, Sweden, and the Institute Laue-Langevin, 38042 Grenoble, France. M.J. PEEL is with the European Synchrotron Radiation Facility, 38042 Grenoble, France. S.W. WILLIAMS is with the Welding Engineering Research Centre, Cranfield University, Bedfordshire MK43 0AL, United Kingdom. M. POAD is with Airbus UK, New Filton House, Filton, Bristol BS99 7AR, United Kingdom.

Manuscript submitted May 16, 2008.
Article published online October 21, 2008

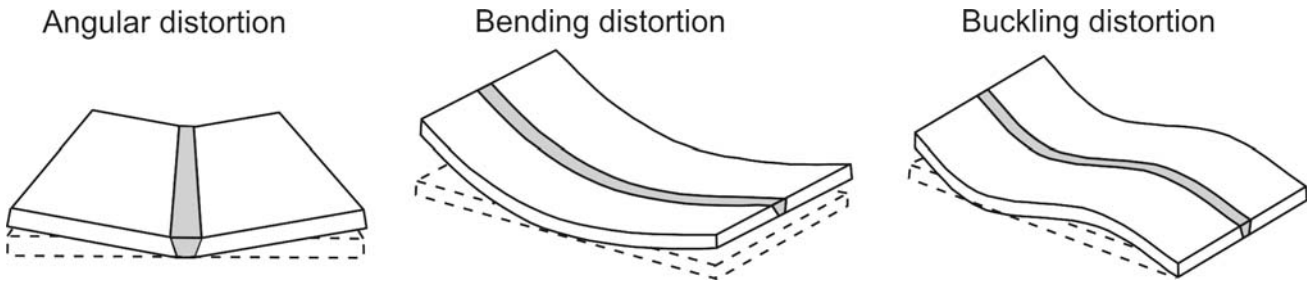

Fig. 1—The three modes of distortion typically observed in welds.[10,13]

The former can be applied either by direct uniaxial tensioning along the welding direction or by a combination of bending the part around an axis perpendicular to the welding direction and uniaxial tensioning to achieve a through-thickness tensioning gradient. Recent work[18] has shown that *in-situ* global mechanical tensioning (GMT) is much more effective than postweld tensioning. Alternatively, local mechanical tensioning can be applied directly, using rollers,[19,20] or indirectly, by thermal tensioning through localized heating and cooling techniques.[16,21,22]

A detailed description of the precise mechanisms acting during welding with GMT is given by Richards *et al.*[18] In essence, the *in-situ* GMT load applied along the welding direction works by reducing the level of local longitudinal misfit that accumulates between the soft metal in the weld vicinity and the cooler parent material (PM) further from the weld. This is because the level of compressive yielding upon heating in front of the tool is reduced, while tensile yielding just after the tool has passed by is increased. This local plastic straining is affected by relatively low levels of global tension, because the high temperatures close to the weld mean that the material is at or near the yield locus. The increased plastic straining at high temperature leads to the reduction in tensile residual stress upon releasing the GMT load after the weld cooled down.[18]

Staron *et al.* used neutron diffraction to determine the stress state in 3.2- and 6.3-mm-thick AA2024 FS welds, with and without GMT applied during welding.[14] They found that excessive GMT loads of 0.70 σ_{ys} (70 pct of the yield strength of the thermally unaffected material) cause the residual stress profile to reverse from tensile to compressive stress in the weld zone. The same tendency has been observed for synchrotron X-ray diffraction (SXRD) measurements on 3.2-mm-thick AA2024 that was FS welded over a wider range of tensioning levels.[15] In this case, the longitudinal residual stresses were extrapolated to fall to zero at a tensioning stress of ~0.25 σ_{ys}. The change in the sign of the stresses was accompanied by an inversion of the plate distortion from convex to concave (relative to the surface onto which the tool was forced). Richards *et al.* developed a finite-element model of the FSW process with applied GMT, to describe the evolution of stress throughout the welding process.[18] This has confirmed the observed inversion from tensile to compressive residual stresses as a function of the increasing tensioning load.

The aim of this article is to investigate experimentally the relationship between the final residual stress and distortion levels and the level of GMT applied *in situ* during welding. Sets of welds based on two alloys at a variety of thicknesses were produced and the residual stress levels were determined, with the aim of identifying general trends as well as alloy-specific observations.

II. EXPERIMENTAL SETUP

A. *Weld Production*

The materials studied are the emerging high-strength, low-density aluminum-lithium alloy AA2199 and the high-strength aluminum alloy AA7449. The former has a nominal composition of 2.63 pct Cu, 1.56 pct Li, 0.62 pct Zn, 0.31 pct Mn, 0.2 pct Si, and 0.17 pct Mg (wt pct), with the remainder aluminum and minor impurities. The Zn is added, to improve the corrosion resistance compared to the previous generation of aluminum-lithium alloys, such as AA2091. The 5-mm-thick AA2199 plates were supplied in the T8E74 temper, *i.e.*, solution heat treated, cold worked, and artificially aged, resulting in a yield strength (σ_{ys}) of ~400 MPa. This alloy is intended to be used for fuselage and lower wing skins applications. The AA7449 material has a nominal composition of 7.5 to 8.7 Zn, 1.8 to 2.7 Mg, 1.8 to 2.4 Cu, 0.25 Ti/Zr, and 0.20 Mn (wt pct), with the balance aluminum and some minor impurities. Plates made of AA7449 that were 5, 12.2, and 20 mm in thickness were supplied in the W51 temper, *i.e.*, solution heat treated and stress relieved by stretching the material between 0.5 to 3.0 pct. No elevated-temperature aging treatment was applied. In this condition, the material has a yield strength of ~583 MPa.[17]

During welding, different levels of GMT (expressed as a fraction of the room-temperature parent-metal yield strength σ_{ys}) was applied parallel to the welding direction (here referred to as the longitudinal direction (see Figure 2(a))), while keeping all other welding parameters constant. The tensile load was applied by hydraulic rams with serrated and hardened jaws attached, as illustrated in Figure 2(b). Slipping was further restricted by pins or bolts in each grip passing through premachined holes in the plates. After the plates were tensioned to the appropriate level, they were clamped to the backing plate, to ensure a fixed position during welding. After welding and cooling, the clamping and

loading were removed. The welding parameter, tool details, and GMT loads for the sets of welds subject to this investigation are given in Table I.

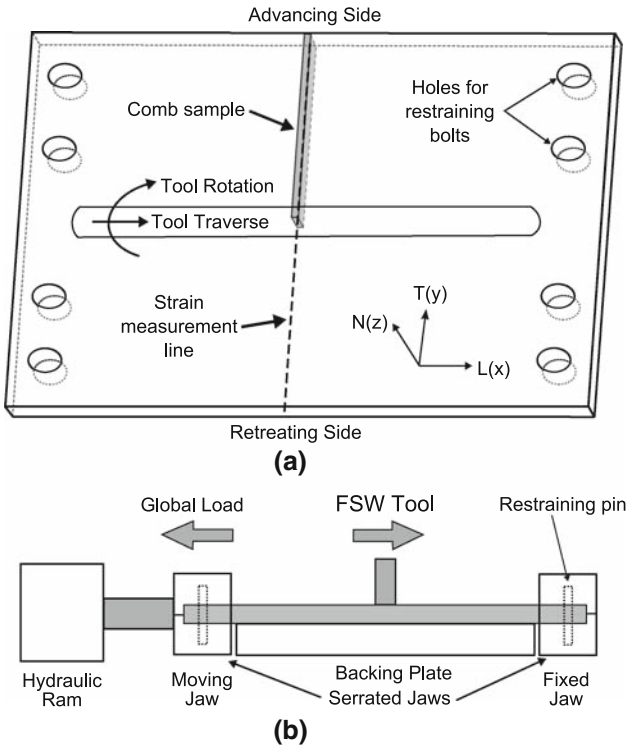

Fig. 2—(*a*) Schematic showing the coordinate system (longitudinal (*x*) and transverse (*y*), (+*y* refers to advancing side), and normal (*z*)), strain-measurement line, holes for the tensioning device, and location at which a d_0 reference comb sample was subsequently extracted from the weld. (*b*) Illustration of *in-situ* tensioning device; serrated and hardened jaws placed at each end of the plates apply the tensile load during welding; additional bolts passing through the grips and the plates were used to further prevent slipping (Ref. 16).

B. *Residual Stress Determination*

Synchrotron X-ray and neutron diffraction techniques were used to determine the residual stress profile across the welds. These nondestructive methods use the shift in the *hkl* diffraction peak position to determine the lattice spacing d_{hkl}. The strain can be calculated using the well-known relation[23]

$$\varepsilon_{hkl} = \frac{(d_{hkl} - d_{0hkl})}{d_{0hkl}} \quad [1]$$

where d_{0hkl} is the unstrained lattice spacing of the *hkl* crystallographic plane. The diffraction techniques used on the different sets of welds are summarized in Table II and are explained in detail in Sections 1 through 4.

1. *Synchrotron X-ray diffraction*

High-energy white-beam SXRD measurements were performed on ID15A at the European Synchrotron Radiation Facility (ESRF), Grenoble, France. A detailed description of this setup may be found in Reference 17. In brief, the setup consists of two energy discriminating detectors, each with a set of collimating slits placed such that the scattering vectors are orthogonal to each other with a scattering angle of $2\theta = 5$ deg. Measurements were made in transmission, to determine the longitudinal and transverse strain components simultaneously. Whole pattern refinement was performed using the General Structure Analysis System,[24] and the lattice parameter was extracted directly from the structural model.

2. *Neutron diffraction*

Neutron diffraction measurements were performed on the SALSA beam line, a dedicated angular-dispersive diffractometer at the Institut Laue-Langevin (ILL, Grenoble, France).[25] A monochromatic neutron beam

Table I. Material Details and Plate Dimensions (Length × Breadth × Thickness), FSW Parameter, Tool Geometry, and Applied GMT Loads Expressed as Percentage of σ_{ys} and in MPa

Material		FSW Conditions					Applied GMT	
Designation	σ_{ys} /UTS* (MPa)	Plate Size (mm)	rpm	mm/min	Down Force (kN)	Tool	Pct σ_{ys} of Parent	Equivalent in MPa
AA2199-T8 Set I	400/452	1000 × 400 × 5	800	400	1.5	shoulder o.d. 13 mm, threaded pin o.d. 5- and 4.5-mm long	0 17 34 52	0 68 136 208
AA7449-W51 Set II	583/636	515 × 150 × 5	800	400	1.5	shoulder o.d. 13 mm, threaded pin o.d. 5- and 4.5-mm long	0 17 30	0 99 175
AA7449-W51 Set III[14]	583/636	1000 × 400 × 12.2	225	250	80	shoulder o.d. 30 mm, threaded pin o.d. 17- and 11.7-mm long	5 10 20 30	29 58 117 175
AA7449-W51 Set IV	583/636	450 × 200 × 20	150	140	80	shoulder o.d. 34 mm, threaded pin o.d. 17- and 19.5-mm long	0 17 34	0 99 198

*Ultimate tensile strength.

Table II. Summary of the Diffraction Measurements, the Method Used for Stress Calculation, and the Technique Used to Determine the Unstrained Lattice Parameter[28]

Designation	Direction			Stress Calculation	d_0 Method
	L	T	N		
Set I	SALSA	SALSA	SALSA	biaxial	Eq. [2]
Set II	ID15	ID15	—	biaxial	comb
Set III	ID15	ID15	—	biaxial	comb
Set IV	ID15	ID15	SALSA	triaxial	comb

($\lambda \approx 1.694$ Å) was used, resulting in a diffraction angle of $2\theta \approx 88.5$ deg from the Al_{311} planes. The gage volume was defined by slits and set to $1.25 \times 1.25 \times 0.9$ mm^3 for the longitudinal and $1 \times 1 \times 10$ mm^3 for the transverse and normal (N) direction measurements. The larger volume was used to reduce the counting time; it was assumed that, at the measurement position, welding was at steady state and, therefore, no longitudinal residual stress gradients are present. The slits were moved as close to the sample surface (~25 mm) as possible, in order to minimize the effects of beam divergence on the gage volume size and position. The counting time was 15 minutes per point for the longitudinal and 5 minutes per point for the two other directions. The use of a He^3 position-sensitive area detector 80×80 mm^2 in size meant a finite arc of the Al_{311} Debye diffraction ring was collected, which required correction during azimuthal integration prior to fitting with a Gaussian profile. Both were performed with the ILL Large Array Manipulation Program software.[26]

3. *Unstrained lattice parameter*

In age-hardenable aluminum alloys, the dissolution or formation of strengthening precipitates during the local thermal excursion during welding may cause a localized change in the solute concentrations. This is likely to change the unstrained (stress-free) lattice spacing d_0, compared to the unaffected PM.[27] If not accounted for, this local variation may have a significant effect on the calculated strains and may lead to inaccuracies in the residual stresses.[28] In this study, two different methods were used to determine the local variation in d_0; their application to the different welds is summarized in Table II.

In the first method, a comb-shaped reference sample was cut from the welded plate with its teeth aligned in the normal direction (Figure 2(a)) and with the teeth small enough that the retained residual stresses are effectively zero.[28] Each tooth represents a different region laterally of the parent, heat-affected zone (HAZ), or weld material. Using a precision saw, a thin cross-sectional slice was extracted from the original untensioned weld from a region representative of that measured during the diffraction experiments (Figure 2(a)). The reference slice ($100 \times$ plate thickness $\times$ 3 mm^3) was ground and polished, to reduce possible cutting stresses. Subsequently, ~0.95-mm-wide teeth were cut using a diamond wire (o.d. = 0.65 mm) saw with a cutting speed of ~1 mm/min, starting from the weld surface. The teeth were most densely spaced within the weld region (teeth spacing ~ 1.6 mm), in order to capture the anticipated change in the unstrained lattice parameter arising from the steep thermal gradients in this region. By averaging the lattice spacings measured in the two stress-relaxed directions, a representative value of the local unstrained lattice parameter d_0 was obtained for all points across the weld line.

In the second approach, a plane-stress condition was assumed from which it was possible to calculate d_0 based on the redundant information obtained by measuring the lattice parameter in three orthogonal directions (d_N, d_L, and d_T):[28,29]

$$d_0 = \frac{(1-\nu)}{(1+\nu)} d_N + \frac{\nu}{(1+\nu)} (d_L + d_T) \qquad [2]$$

where the subscripts refer to the principal directions and ν is Poisson's ratio. As long as the normal stresses remain low, the error is likely to be less than that induced by applying an inappropriate global unstrained lattice parameter.[28]

4. *Calculation of strain and stress*

Measurements of the elastically strained d-spacing were made as a function of distance from the weld line and, in the case of set IV, also as a function of depth below the weld surface. Subsequently, the strain was calculated using Eq. [1] together with the appropriate local unstrained lattice parameter d_0, as determined in Section 3. In the thinner welds (sets I through III, 5- to 12.2-mm thick), the residual stress was assumed to be biaxial ($\sigma_N = 0$)[23,30] and was calculated using

$$\sigma_L = \frac{E}{(1-\nu^2)} (\varepsilon_L + \nu \varepsilon_T) \qquad [3]$$

where E is Young's modulus and υ is Poisson's ratio. This has the advantage that the stress can be calculated without requiring knowledge of the normal elastic strain ε_N. Bulk values for the elastic modulus and Poisson's ratio were used as an approximation to the conventional diffraction elastic constants. For the white-beam SXRD method, this is thought to be appropriate, because the Rietveld/Lebail refinement essentially averages over several peaks simultaneously, thus smoothing out the deviations of any specific peak from the bulk average.[31] In the case of the neutron diffraction experiment, the Al_{311} peak is known to have a diffraction elastic constant that approximates the bulk modulus.[32]

For the 20-mm-thick plates (set IV), the plane-stress assumption may not be valid; therefore, a

three-dimensional stress state has been assumed, using the conventional equations:[23,30]

$$\sigma_L = \frac{E}{(1+\upsilon)(1-2\upsilon)}\{(1-\upsilon)\varepsilon_L + \upsilon(\varepsilon_T + \varepsilon_N)\} \quad [4]$$

The residual stresses in the other two directions can be calculated by permuting the subscripts.

In order to ensure stress equilibrium conditions, *i.e.*, the longitudinal stresses are balanced across the normal-transverse plane and the transverse stress is zero at the edge of the plate, a least-squares approach was used. The d_0 variation was corrected globally such that the stress balancing and boundary conditions were fulfilled. Because modifying the parameter (and, hence, the strain) in one direction alters the stress in the other direction, the stresses were solved iteratively until the solution converged.[17]

C. *Distortion, Microstructure, and Hardness*

Distortion determination, microstructure examination, and hardness measurements were performed, to investigate the possible effects of GMT on the weld performance and postweld mechanical properties.

The bending and angular distortion (Figure 1) of each weld were determined using a Mitutoyo Euro-C-A776 coordinate measuring machine (Mitutoyo (UK) Ltd., Andover, UK) with a Renishaw touch probe (Renishaw plc, Gloucestershire, UK) attached, thus allowing the sample surface to be scanned along a line parallel (L) and transverse to the welding direction.

Test samples for microstructure and hardness investigations were extracted in the T-N plane from the midlength of the original weld; measurements were performed as a function of the distance from both the weld line and the weld surface. Optical macrographs and scanning electron microscope (SEM) microstructure observations using a PHILIPS* XL30 field emission gun-scanning electron microscope (FEG-SEM) in backscatter mode at 20 kV and a working distance of 10 mm were made on samples covering the weld region. The sample surfaces were polished to 1 μm and, finally, a colloidal silica emulsion polishing was applied. Keller's reagent[33] was used to reveal the macrostructure and Weck's reagent[34] was used for the microstructure. The microhardness was measured using a Buehler MicroMet 5101 hardness tester (BUEHLER, Lake Bluff, IL) with a test load of 500 g and an indentation time of 10 seconds. Measurements were focused on the weld area.

*PHILIPS is a trademark of Philips Electronic Instruments Corp., Mahwah, NJ.

III. RESULTS AND DISCUSSION

A. *Distortion, Microstructure, and Hardness*

Figure 3 shows the bending and angular surface distortion measured in samples from sets I and IV.

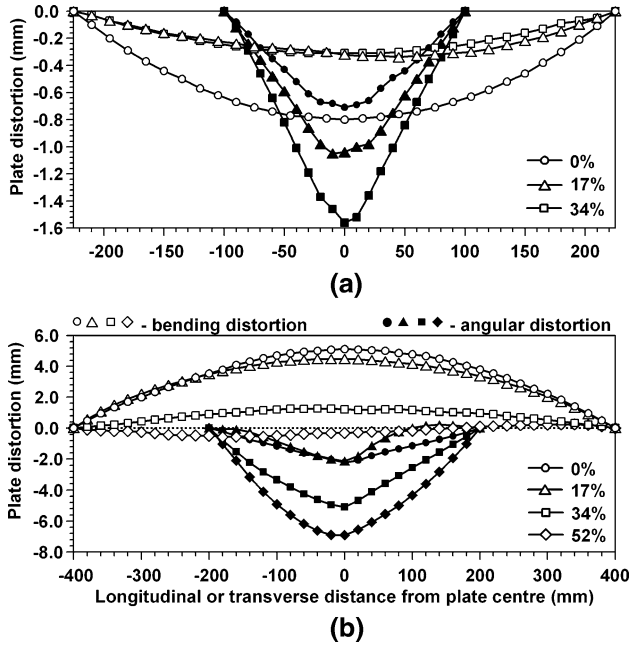

Fig. 3—Bending distortion (open markers) along the L direction and the angular distortion (filled markers) along the T direction, for (*a*) set IV (20-mm AA7449) and (*b*) set I (5-mm AA2199), as a function of distance from the plate center and the applied GMT tensioning load (in pct σ_{ys}).

In set IV (Figure 3(a)), increased GMT reduced the level of concave (negative) longitudinal bending distortion from −0.8 (untensioned) to −0.3 mm (17 and 34 pct GMT), but increased the concave transverse angular distortion from −0.7 to −1.56 mm. Similar behavior was observed for the remaining AA7449 sets. In the AA2199 welds (set I (see Figure 3(b))), GMT also reduced the bending and increased the angular distortion. However, the sense of the bending for the untensioned weld was positive rather than negative, decreasing from 5.12 to −0.3 mm.

The fact that the bending distortion reduces with increased GMT is in accordance with previous observations,[10,16] but concave sample bending and an increase in angular bending with increased GMT has not been described before. At this point, it is not clear why the angular distortion increases, because GMT has little or no effect on the transverse residual stresses (Section C). However, with regard to the sense of the bending distortion, this can be affected by through-thickness variations in residual stress. The longitudinal tensile residual welding stresses are assumed to be larger near the weld surface and decreasing toward the weld root; hence, concave bending may be expected for the AA7449 sets. Alternatively, a longitudinal misfit can lead to buckling distortion that is stable in both convex and concave configurations, as may be the case for set I.

Figures 4 and 5 illustrate the macro- and microstructure of the as-welded and 34 pct tensioned AA7449 20-mm-thick welds (set IV) and are representative for the results in all investigated sets. The approximate positions at which SEM micrographs (Figure 5) were acquired are marked in Figures 4(b) and (c). The

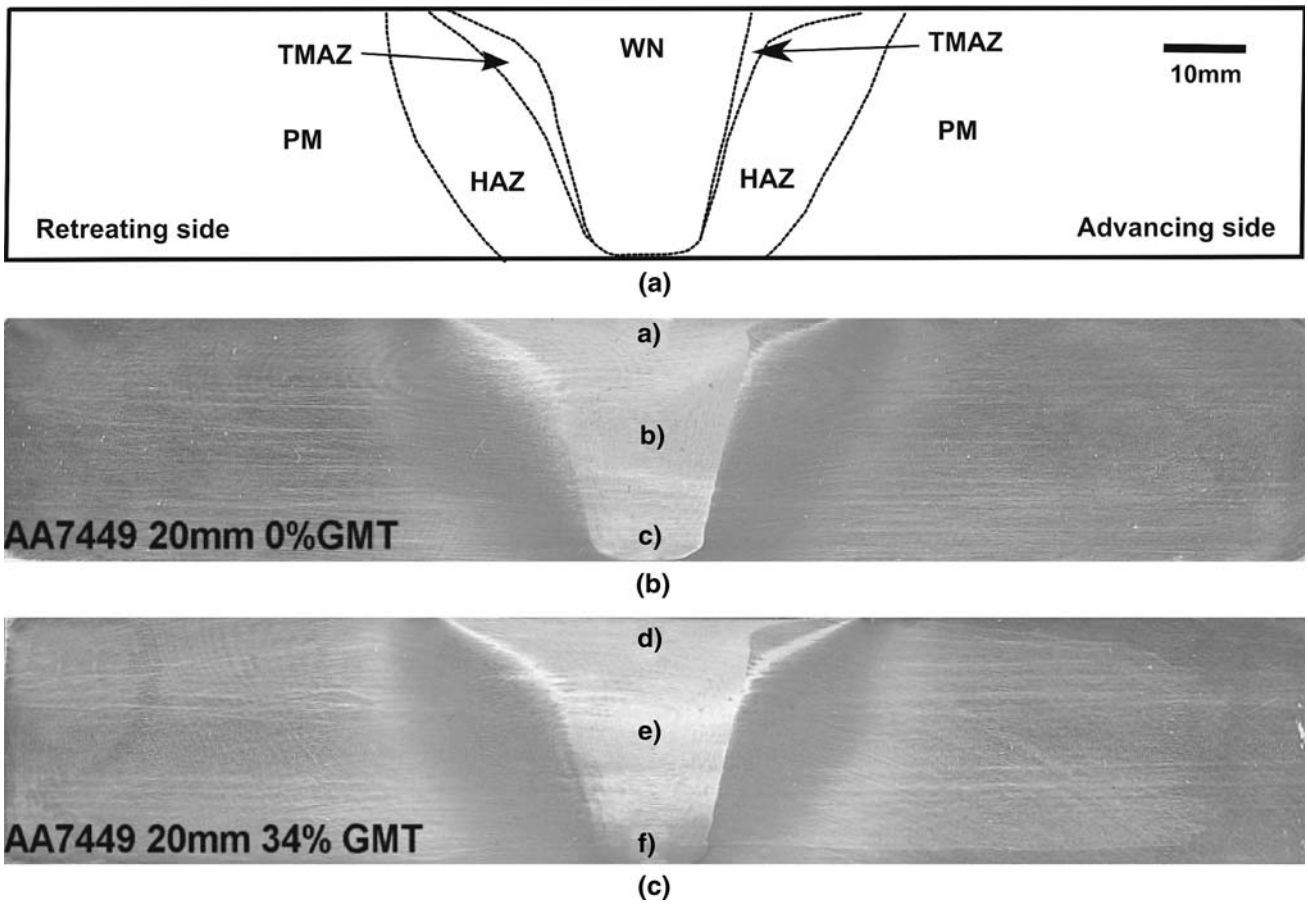

Fig. 4—Schematic of the FSW (*a*) cross section of the macrographs of the (*b*) untensioned and (*c*) 34 pct tensioned welds in 20-mm-thick AA7449 (set IV), showing the positions for the SEM micrographs marked according to Figure 5. The nugget is surrounded by a sharply formed TMAZ on the advancing side and a more diffuse wider TMAZ on the retreating side; the HAZ manifests as the dark gray zone to both sides of the WN.

macrographs display the typical weld nugget (WN) shape. There is no evidence of flaws; this leads to the assumption that the welding parameters have been adjusted properly. To both sides of the WN, a thin transition zone, the thermomechanically affected zone (TMAZ), can be observed; according to the literature, this is sharper on the advancing and somewhat indistinct and wider on the retreating weld side.[35] The HAZ in between the TMAZ and the PM manifests as a darker-gray region that follows the thermal contours through the thickness: wide near the tool shoulder and contracting toward the weld root. Perhaps unsurprisingly, there is no significant difference between the macrostructure of the welds in either the WN, TMAZ, or HAZ, as a result of the applied GMT.

As shown by Murr *et al.*, Mahoney *et al.*, and Hassan *et al.*,[36–38] and as displayed in Figure 5, roughly equiaxed grains in the WN with a 5- to 10-μm grain size near the weld surface, decreasing to below 1 μm near the root, are present. The thermal gradient through the weld thickness, either influencing the initial recrystallized grain size or simply altering the extent of postweld grain growth, may be responsible for that.

Consistent with previous work,[27,38,39] coarse second-phase particles, presumably stable η precipitates (Figures 5(a) and (d)), and smaller intragranular precipitates (Figures 5(b) and (e)) form during natural aging, after dissolution of the former precipitation structure near the welding tool and partial dissolution near the weld root due to the lower temperatures during welding. An extensive discussion of the effects on the microstructure of the competing precipitate dissolution and coarsening processes during welding and subsequent precipitation hardening during natural aging is beyond the scope of this article, but may be found in References 27, 39, and 40.

The hardness map (Figure 6) for the 20-mm-thick AA7449 samples (set IV) is characteristic for FSW in age-hardenable aluminum alloys and is representative for the investigated sample sets. Near the tool shoulder, the WN hardness nearly reaches that of the PM (170 to 180 HV_{500g}), but is rather lower near the bottom (110 to 120 HV). The HAZ displays a minimum of 90 to 100 HV_{500g}, following the cone shape of the tool pin to both sides of the WN. The precise exploration of the precipitation mechanisms on the hardness distribution in FSW exceeds the aim of this investigation, but a detailed discussion is given in References 27 and 39. However, no significant differences in the hardness distribution due to the GMT are evident in the plots, but

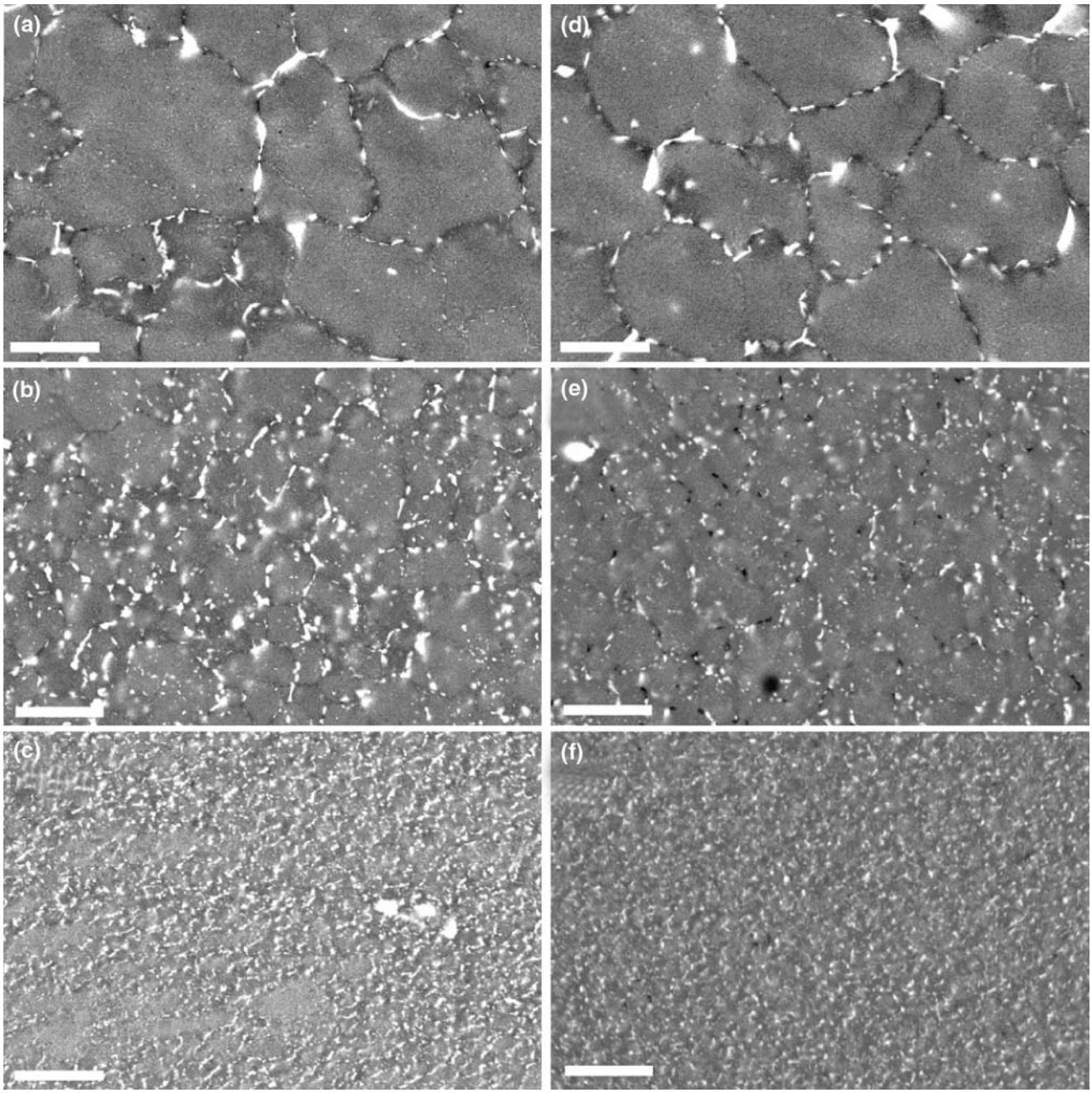

Fig. 5—SEM micrographs for the (*a*), (*b*), and (*c*) untensioned and (*d*), (*e*), and (*f*) 34 pct tensioned 20-mm-thick AA7449 welds (set IV) at the weld line at (a) and (d) 1 mm, (b) and (e) 10 mm, and (c) and (f) 18 mm from the weld surface. The white bar represents 5μm. The grain size decreases from 5 to 10 μm near the weld surface to <1 μm at the weld root. Precipitates that were overattacked by the etching appear as dark spots in (e).

the strong variation in the hardness suggests that a significant variation in the unstrained lattice parameter d_0 is to be expected,[27] as discussed in B.

B. *Unstrained Lattice Parameter*

One way of plotting the variation in the unstrained lattice parameter d_0 with lateral position is to plot the pseudostrain, which is equal to the elastic strain that would have been wrongly inferred to exist in the region if a global strain-free lattice parameter rather than the correct local value would have been used. This is plotted in Figure 7 as a function of lateral distance from the weld line, as measured at the midthickness in the as-welded plate of each sample set. The global d_0 for the pseudostrain calculation has been taken from the unaffected PM, resulting in approximately zero pseudostrain for this region. However, for clarity, the absolute scale for the d_0 variation is included on the right side of the plot. To enable comparison of the absolute values, we shifted the graphs by adding a constant value to the measured d_0 spacing variation

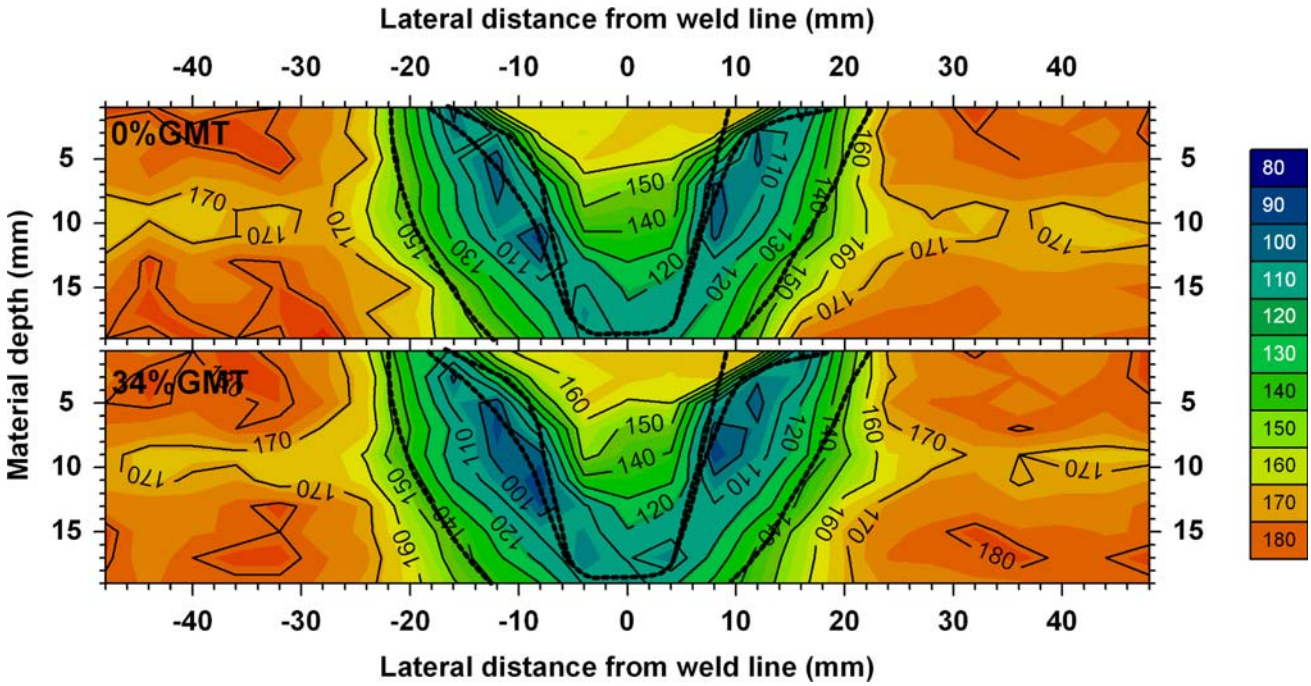

Fig. 6—Comparison of the Vickers hardness in welds from set IV (20-mm AA7449) that have undergone 0 pct (top) and 34 pct (bottom) GMT during the FSW process. The tool shoulder diameter is 34 mm; the 10-deg cone-shaped toll pin has a diameter of 17 mm at the shoulder and is 19.5 mm long. The dashed lines mark the different zones (Fig. 4). No differences in the hardness distribution due to GMT were observed.

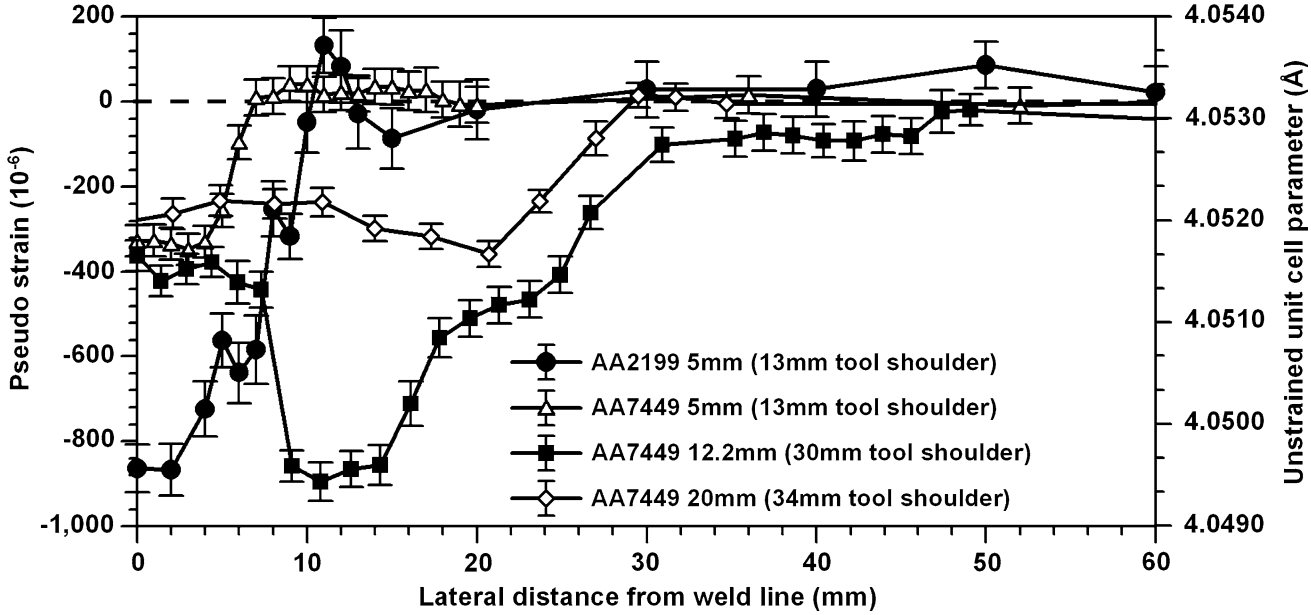

Fig. 7—Variation in the unstrained lattice parameter d_0 expressed as pseudostrain (left scale) and absolute measured values (right scale), as a function of lateral distance from the weld line measured in the midthickness, for the as-welded plate on the advancing weld side of each sample set.

such that all plots have nearly identical d_0 values in the PM. In line with previous results for age-hardening alloys, d_0 varies significantly with distance from the weld line, as a result of the locally differing thermal mechanical history and the subsequent precipitation, which leads to changes in the solute concentration and, hence, to a spatial variation in d_0.[27,28,39] In general, the behavior can be described as a decrease in d_0 from the PM toward the weld line. For the thin plates, the d_0 variation occurs over a relatively narrow region, falling significantly only beneath the tool shoulder (o.d. 13 mm). For the thicker welds (o.d. 30- and 34-mm tool shoulders), the midthickness d_0 varies over a more extended range, reaching a minimum in the HAZ for the AA7449 before recovering to an intermediate value in the WN.

In general, the variation in d_0 can be attributed to the contrasting effects of overaging or to the dissolution of the precipitates, both of which occur to different extents, depending on the thermal profile at each location.[39] However, the precise precipitation mechanisms and their effect on the unstrained lattice parameter lie beyond the aim of this investigation; a detailed discussion is given elsewhere.[27,39]

Because GMT appears to affect neither the postweld hardness distribution nor the weld microstructure, it has been assumed that the d_0 variation measured for the as-welded plate is applicable to all welds of the corresponding set.

C. *Residual Stress*

The influence of tensioning level on the longitudinal and transverse residual stresses in the 5-mm Al-Li alloy (set I) is shown in Figures 8(a) and (b), respectively. The lateral range plotted is restricted to ±60 mm from the weld line, because the stresses did not vary significantly beyond this. However, over the entire width, the longitudinal stresses balance, while the transverse stresses are zero at the plate edge. The results are consistent with previous literature, insofar as the longitudinal stress profile in the as-welded plate exhibits a characteristic "M" shape.[3,4,14,16] The origin of this M-shaped residual stress profile is explained in detail in Reference 18.

As expected, the highest tensile residual stresses are observed in the untensioned weld in the longitudinal direction. There is a stress plateau of ~170 MPa in the WN, which, being ~12 mm in width, corresponds closely to the diameter of the tool shoulder (o.d. 13 mm). The greatest stresses occur near the HAZ at ±7 mm, in the form of sharp peaks ~210 MPa in magnitude. No significant difference is observed between the advancing and retreating sides. On applying a GMT load of 0.17 σ_{ys} (=68 MPa) during welding, a reduction in the stress of ~70 MPa occurs at the weld line with an associated disappearance of the distinct tensile stress peaks in the HAZ. Increased tensioning leads to a progressive reduction in the residual stress. The weld becomes effectively stress free when the applied load reaches 0.34 σ_{ys} (=135 MPa), a value close to that of the initial weld-line stress. Additional increases in the tensioning load to 0.52 σ_{ys} (=210 MPa) result in the development of compressive stresses of around −50 MPa. In common with previous data,[3,4,14,16] the transverse stresses (Figure 8(b)) are substantially lower than those in the

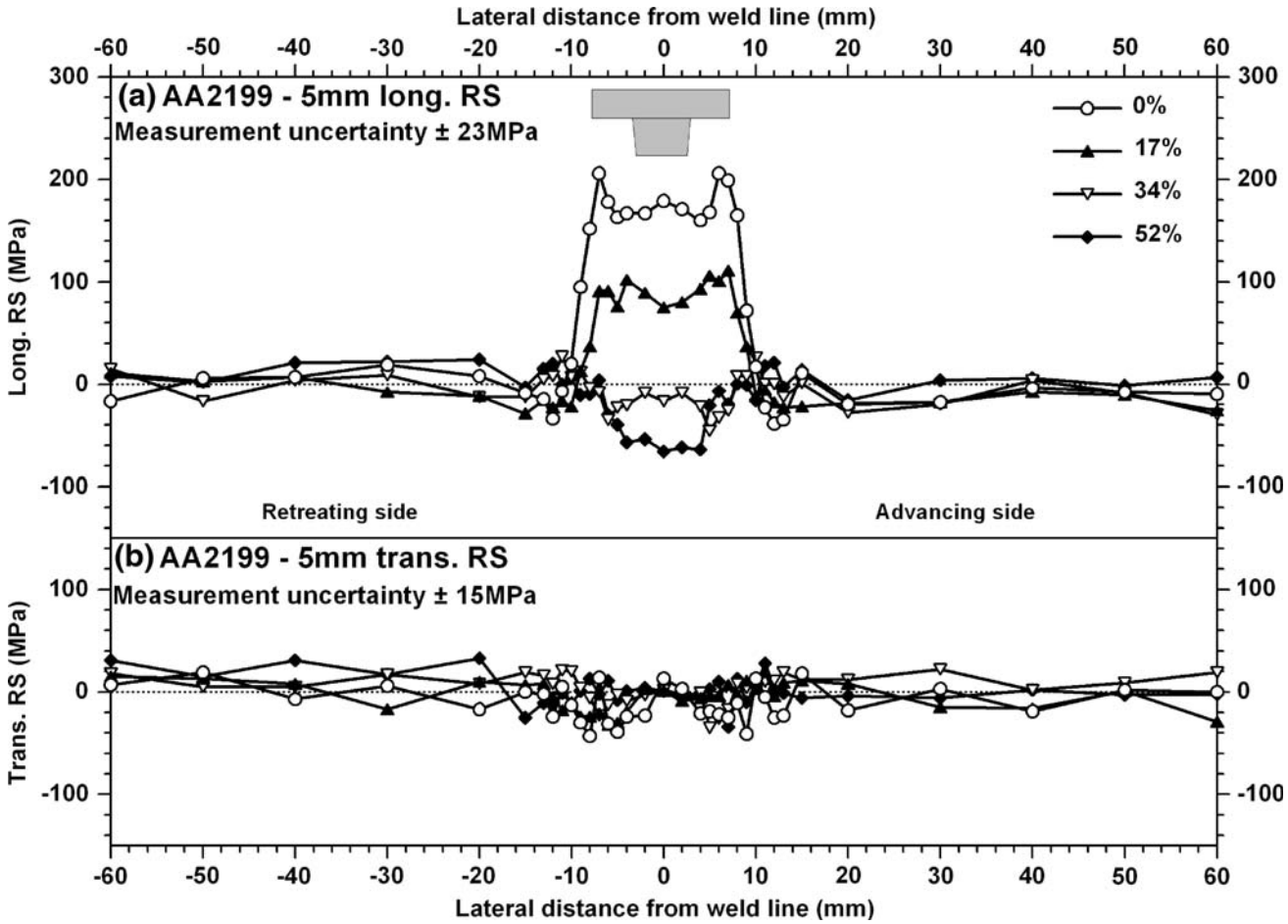

Fig. 8—Effect of GMT on (*a*) the longitudinal and (*b*) the transverse residual stresses in 5-mm-thick AA2199 (set I); the cross section of the FSW tool is shown above the long residual stress (RS) profile.

longitudinal direction; they vary between ±40 MPa and are not noticeably influenced by the GMT level applied.

Figure 9 shows the longitudinal stress measured at midthickness for sets II and III as a function of applied GMT. The plots show the same behavior upon increased tensioning, as for the AA2199 FSW: namely, a progressive reduction in stress, the essentially stress-free state being reached when the applied load corresponds to the initial weld-line stress. For the 5-mm AA7449 FS welds, this is the case for ~0.3 σ_{ys} (=175 MPa), which corresponds to the initial weld-line residual stress of ~170 MPa. After applying the same load to the 12.2-mm-thick AA7449 welds, a weld-line residual stress of ~30 MPa remains, which is equal to the difference between the initial weld-line stress of ~200 MPa and the applied load of ~175 MPa. Consequently, the evidence from sets I to III suggests a 1:1 correlation between the weld stress reduction and the tensioning level.

Figure 10 displays the through-depth variation in the longitudinal stresses for the 20-mm-thick AA7449 FS welds without and with GMT. In common with the thinner welds in the untensioned weld, an M-shaped stress profile with lateral distance is observed at all depths. At a depth of 2 mm, the stress at the weld line is ~100 MPa, with two 10-mm-wide ~175 MPa tensile peaks lying within the HAZ at ~±15 mm. At this depth, the overall lateral extent of the tensile zone is ~60-mm wide. With increasing depth, the weld-line stress and the width of the tensile zone reduce. In addition, the stress peaks in the HAZ become less distinct and shift toward the weld line. These effects may be attributed to the thermal profile and to the cone-shaped tool pin, both narrowing with distance from the weld surface. This shape is in accordance with both the macrostructures plotted in Figure 4 and the hardness distributions in Figure 6. The tensile peaks are slightly higher on the advancing side, which may be attributed to the asymmetric nature of FSW.[3,7] The through-thickness stress variation at the weld line is ~70 MPa and is probably responsible for the concave bending of the untensioned sample (Figure 3(a)).

Similar to the results from sets I to III, by applying a GMT load of 0.17 σ_{ys} (=99 MPa), the stress peaks almost disappear and the weld-line stress level at a 2-mm depth reduces by ~100 MPa to approximately zero. At greater depths, the GMT effect decreases such that, at an 18-mm depth, the weld-line stress decreases only by

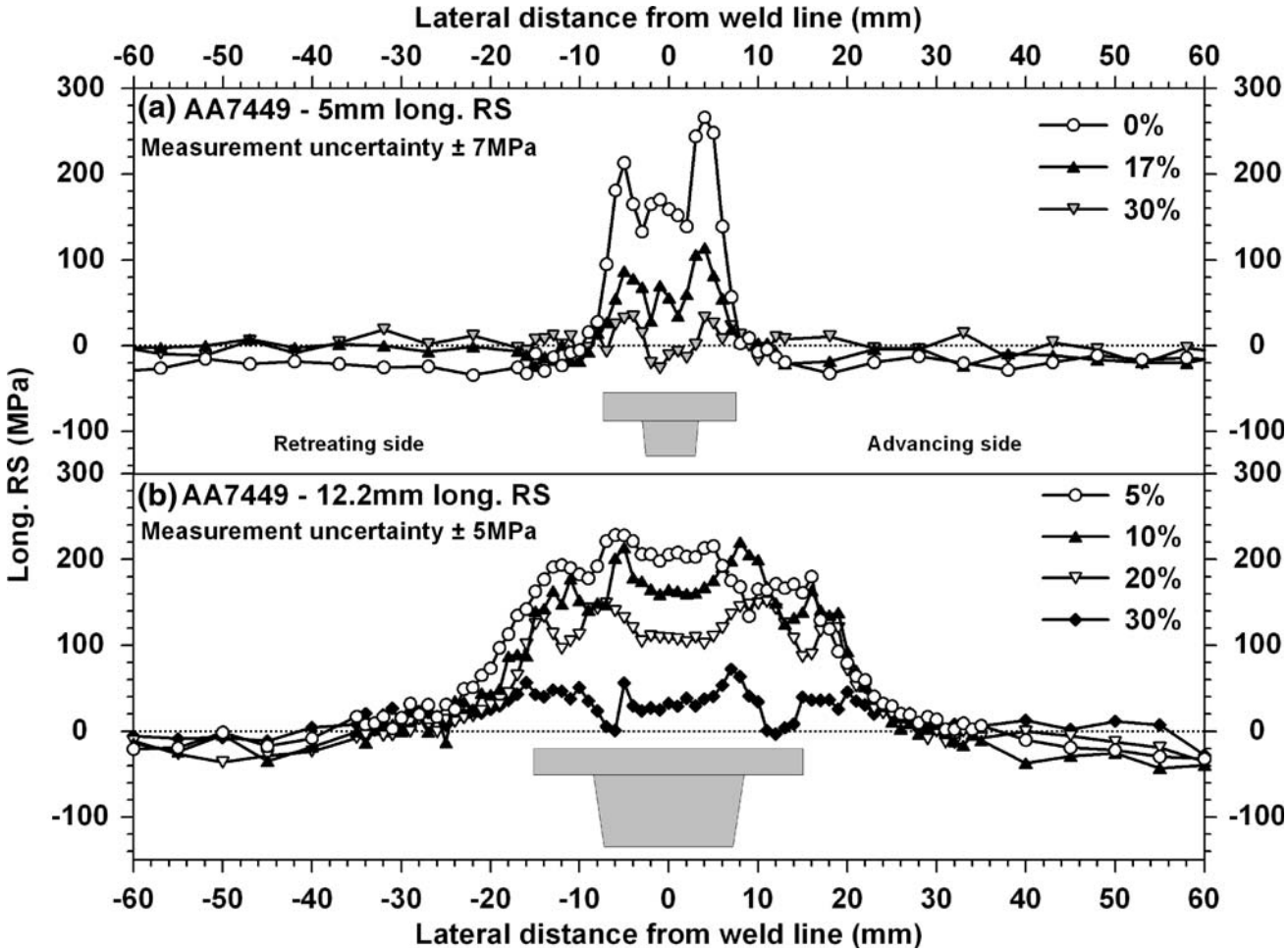

Fig. 9—Effect of GMT on the midthickness longitudinal residual stresses in (*a*) 5-mm (set II) and (*b*) 12.2-mm (set III) AA7449 FSW; for each set, the cross section of the FSW tool is shown below the RS profile.

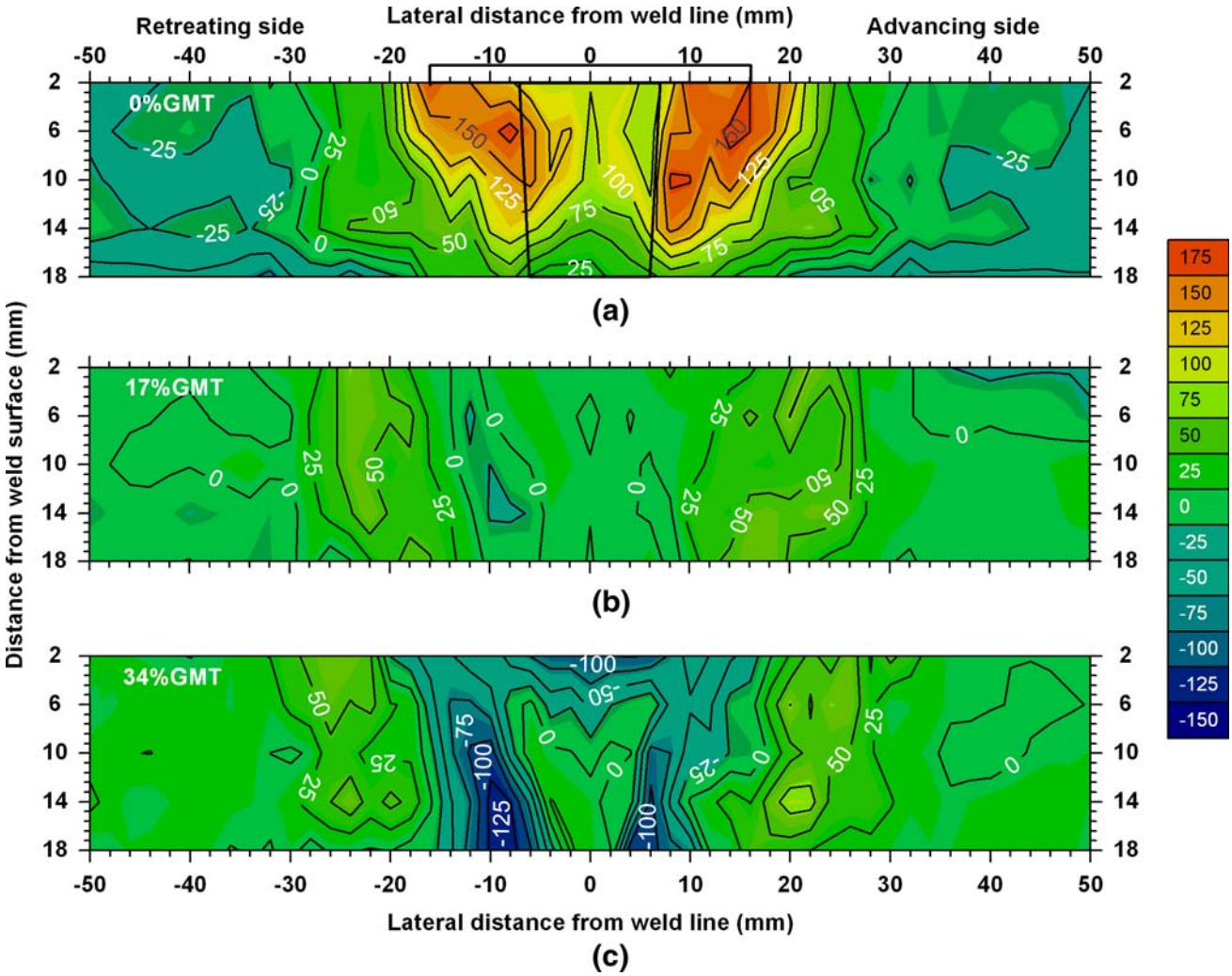

Fig. 10—Longitudinal residual stress distribution in 20-mm-thick AA7449 FSW in (*a*) the untensioned condition, (*b*) an applied GMT load of 17 pct, and (*c*) 34 pct material yield strength. The measurement uncertainty is ±7 MPa.

~60 MPa, which is 70 MPa less than the GMT level. As a result, the through-thickness stress difference vanishes, leading to low levels of stress throughout the WN and decreased sample bending (Figure 3(a)). The reduced GMT effect with increasing distance from the weld surface may be due to the temperature gradient through-thickness during welding, where lower temperatures near the weld root lead to less material softening than is the case close to the weld surface, where near-melting temperatures can be reached. The degree of softening affects the extent of induced tensile yielding for a given tensioning load; this starts earlier for the hotter and softer material close to the weld surface, but is reduced in the colder and stronger material near the weld root. This may explain why GMT is more effective near the weld surface of thick welds.

The same tendency is observed for the 0.34-σ_{ys} (198-MPa) GMT load. At a 2-mm depth, the weld-line stress reduces by ~200 MPa, compared to the untensioned weld. However, with increasing depth, the level of stress change decreases. The triangular profile seen in the untensioned weld is also evident for the 34 pct tensioned sample (Figure 10(c)), but the sign of the stress has reversed, with the largest compressive peaks lying toward the base of the weld at distances equivalent to the size of the tool pin (~±8.5 mm). Here, the retreating side shows the higher compressive stress (~130 MPa at 18 mm below the weld surface). These compressive peaks correspond to the location of the lowest hardness and may reflect an earlier plastic straining under the GMT load leading to compressive residual maxima upon releasing the GMT load. This may also be the reason for the tensile stress peaks disappearing, even at lower GMT loads.

Figure 11 shows the through-thickness stress profiles for the transverse (Figure 11(a)) and normal (Figure 11(b)) directions of the untensioned sample from set IV. Similar to the results for thinner plate (*e.g.*, 5-mm AA2199, Figure 8(b)), the stresses in the transverse and normal directions are lower than those found in the longitudinal direction. However, stress peaks of up to 90 MPa are evident at $y \approx \pm 20$ mm, which is somewhat further from the weld line than the longitudinal stress peaks. In between the peaks, the

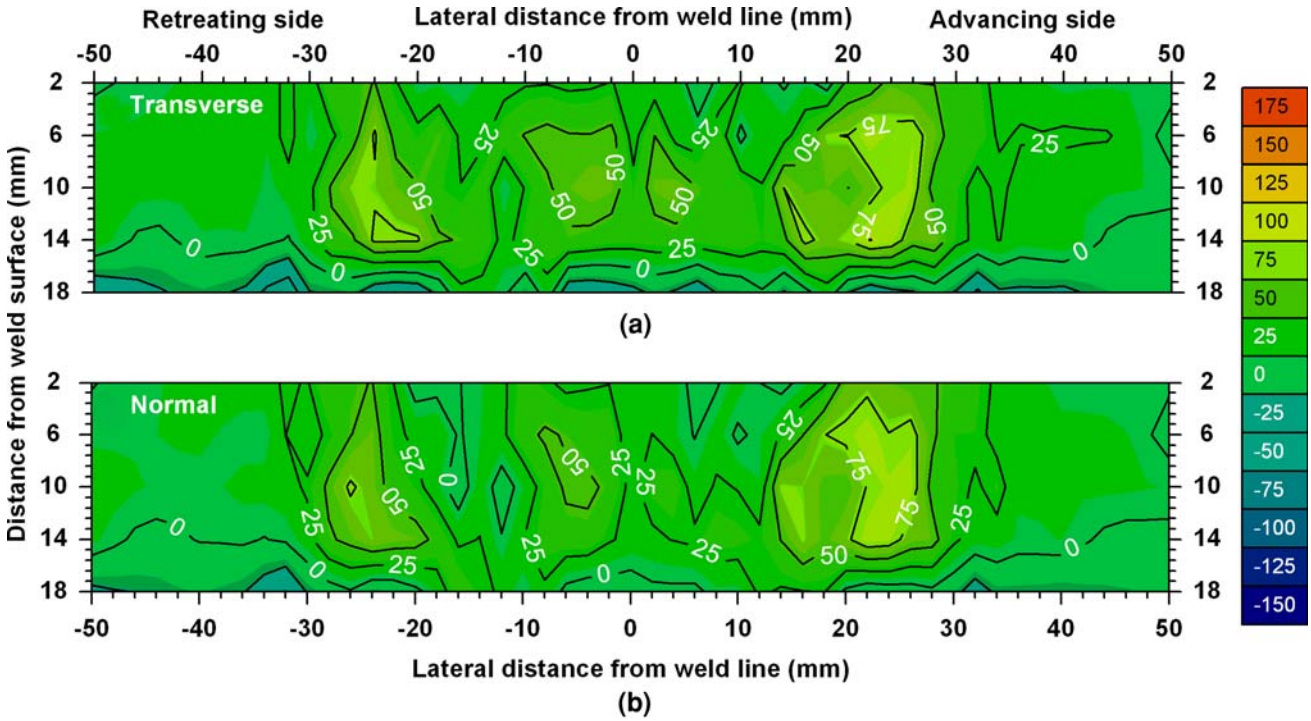

Fig. 11—(*a*) Transverse and (*b*) normal residual stress distribution in 20-mm-thick AA7449 FSW in the untensioned condition. The measurement uncertainty is ±7 MPa.

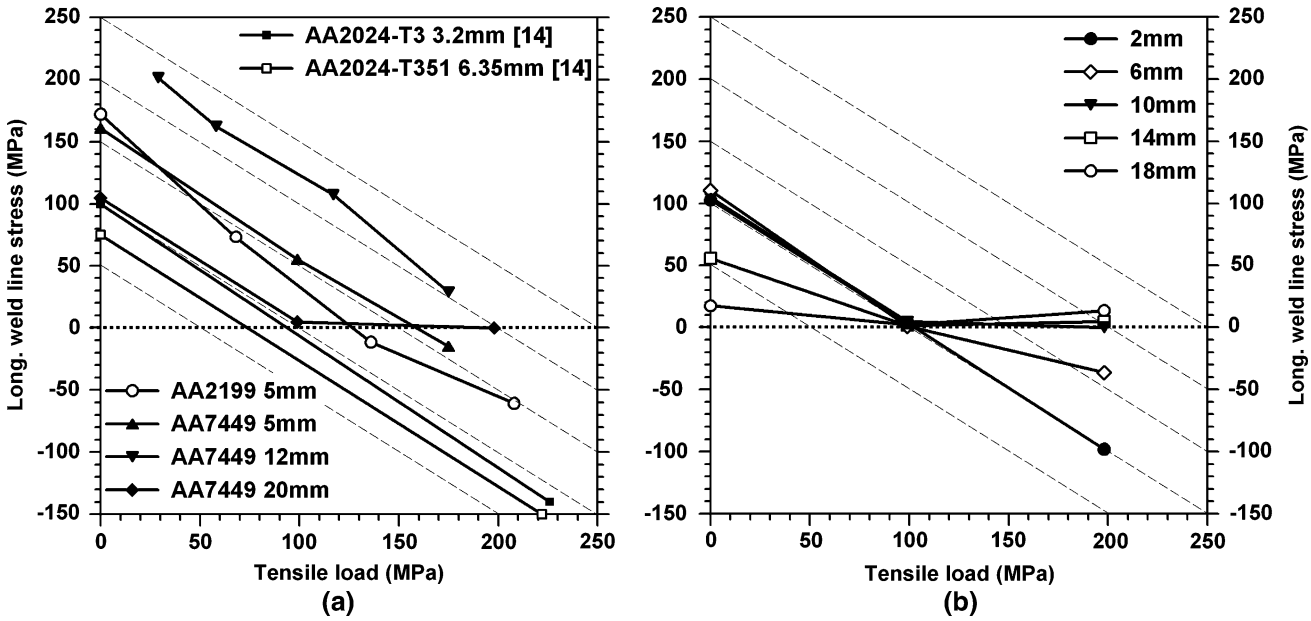

Fig. 12—(*a*) Residual stress at midthickness near the weld line as a function of applied tensioning level, for sets I through IV and data from literature.[14] (*b*) GMT effect for the longitudinal weld-line residual stresses, for different material depths below the weld surface. The dashed guidelines represent a 1:1 relationship between stress reductions and applied tensioning level.

transverse and normal stresses vary by approximately ±50 MPa, depending on the depth below the weld surface. In both cases, until a depth of 14 mm, the stresses are in low-level tension, while the near-weld-root material is in compression. However, as seen here, the application of GMT during welding has only a marginal effect on the transverse and normal stress profiles, which are, therefore, not displayed here.

The effect of GMT on the weld-line residual stress at midthickness for the four sets investigated is summarized in Figure 12(a); the through-thickness variation caused by GMT is shown in Figure 12(b) for set IV.

Because the tensile peaks observed in the as-welded case disappear even at low applied loads, the applied level of GMT is correlated to the weld-line residual stress. As discussed here, it can be seen in Figure 12(a) that the AA7449 welds show a simple inverse 1:1 linear relationship; the stress is reduced by 1 MPa for every 1 MPa of tensile load applied. In broad terms, the same behavior can be observed for the AA2199 welds, although the rate of stress decrease is marginally higher. Indeed, the essentially 1:1 linear stress reduction is found in all the experimental sets; this indicates that the residual stresses are reduced by an amount approximately equal to the tensile load applied. This means that the optimum GMT load may simply be estimated to be equal to the weld-line stress of the untensioned weld. In certain cases, this may be equal to a certain percentage of the PM yield strength, as suggested in previous work.[15–18] The rule of thumb of a 1:1 linear stress reduction is also supported by the residual stress data for AA2024 (Al-Cu) FS welds with applied GMT[14] (Figure 12(a)). A note of caution, however, should be taken from the thick plates from Figure 12(b), which shows a significant reduction in the effect of the GMT level below 1:1 with increasing depth. This may be due to the lower welding temperatures at greater depths during welding, leading to less material softening, which, in turn, requires higher tensioning levels to reach the local yield point; the tendency to counteract the bending distortion, however, may also be a factor.

The general linearity of stress reduction due to increased GMT loads is also evident in finite-element modeling.[18] While a 1:1 correlation was broadly followed, it was found that, in some cases, the gradient became slightly shallower if the power or heat input into the weld was reduced. This observation is in accordance with the decreasing stress reduction with increasing distance from the shoulder, where the temperatures are lower than near the tool shoulder, as was found in set IV.

IV. CONCLUSIONS

The GMT method is effective for reducing residual stresses in welded components. The superimposed tensioning changes the yield path during welding and, consequently, reduces the accumulated elastic misfit once the weld has cooled.[18] The aim of this article is to investigate the relationship between the degree of applied load and the remaining residual stresses. An examination of four systematic sets of FS welds at different thicknesses and tensioning levels has demonstrated the following.

1. The application of global tensioning reduces the residual stresses in a weld, although the use of excessive loads results in a reversal of the stress field, with compressive stresses forming in the normally tensile weld zone.
2. In thin-plate welds, for which a nearly constant through-thickness temperature profile during welding exists, there is a linear relationship between the applied load and the decrease in the resulting residual stress. As a rule of thumb, 1 MPa of applied tensioning renders the longitudinal weld-line stress 1 MPa less tensile.
3. For thicker plate material, the reduction in residual stress due to global tensioning decreases with the depth from the weld surface.
4. Tensile residual stress peaks forming outside the WN in the untensioned case soon disappear with increased tensioning; they can reverse into compressive peaks if the tensioning load is excessive.
5. Only longitudinal stresses are altered significantly by longitudinal tensioning; no significant effect is seen on the stresses in the transverse and normal directions.
6. Bending distortion is reduced with increased tensioning loads; the butterfly distortion, however, increases.
7. As expected, the microstructure and mechanical properties are unaffected by global tensioning.

The observed 1:1 correspondence is likely to occur only in cases in which the tensile region immediately behind the tool can be maintained at the tensile yield stress by the tensioning load. As shown by Richards *et al.*,[18] due to the high welding temperatures, the yield stress is approximately zero behind the tool, for most FSW conditions inducing local tensile yielding in proportion to the tensioning level. The GMT during welding is, therefore, particularly effective, compared to the tensioning after welding, because the applied tension stress level is applied to such a soft weld region. For thick plates, through-thickness thermal gradients may lead to yield stress variations that show that tensile plastic straining is no longer in proportion to the tensioning load. Nevertheless, the 1:1 guideline provides a good estimate of the optimal tensioning level when beginning welding trials.

The GMT method is very simple and effective to apply and requires very little modification of conventional FSW equipment. For the aluminum alloys studied here, tensioning levels of only 200 MPa or less are necessary, in order to reduce the peak tensile stresses to zero. The method is well suited to the approximately linear joints that might be encountered when assembling panels in the transport sector. For example, it is particularly well suited to the joining of prefabricated ship panels. For welding more complicated parts, or when it is not possible to apply a global mechanical tensile load during welding, local mechanical tensioning using rollers pressing down on the plate is more appropriate.[19] In contrast to GMT, it has been found that difficulties associated with placing the rollers sufficiently close to the stir-welding tool to tension the soft weld metal during welding mean that roller tensioning after welding is more effective.[20]

ACKNOWLEDGMENTS

The authors acknowledge T. Buslaps (ID15A, ESRF), T. Pirling, and D.J. Hughes (SALSA, ILL) for their support during the beam time. The authors also

acknowledge the ESRF, for the beam time provided through Proposal ME1165, and the ILL, for the beam time provided through Proposal 7-01-175. The authors thank AIRBUS UK for providing the samples. One of the authors (JA) thanks the ILL and the EPSRC Light Alloys Portfolio for financially supporting his doctoral thesis.

REFERENCES

1. M.N. James, D.J. Hughes, Z. Chen, H. Lombard, D.G. Hattingh, D. Asquith, J.R. Yates, and P.J. Webster: *Eng. Fail. Anal.*, 2007, vol. 14, pp. 384–95.
2. P.J. Withers: *Rep. Prog. Phys.*, 2007, vol. 70, pp. 2211–64.
3. M.J. Peel, A. Steuwer, M. Preuss, and P. Withers: *Acta Mater.*, 2003, vol. 51, pp. 4791–4801.
4. C.D. Donne, E. Lima, J. Wegener, A. Pyzalla, and T. Buslaps: *3rd Int. Symp. FSW*, TWI, Kobe, Japan, 2001.
5. L.D. Oosterkamp, P.J. Webster, P.A. Browne, G.B.M. Vaughan, and P.J. Withers: *Mater. Sci. Forum*, 2000, vols. 347–349, pp. 677–83.
6. P.J. Webster, L.D. Oosterkamp, P.A. Browne, D.J. Hughes, W.P. Kang, P.J. Withers, and G.B.M. Vaughan: *J. Strain Anal. Eng. Des.*, 2001, vol. 36, pp. 61–70.
7. M.A. Sutton, A.P. Reynolds, D.Q. Wang, and C.R. Hubbard: *J. Eng. Mater. Technol.*, 2002, vol. 124, pp. 215–21.
8. A. Steuwer, M.J. Peel, and P.J. Withers: *Mater. Sci. Eng., A*, 2006, vol. 441, pp. 187–96.
9. K. Masubuchi: *Welds, Encyclopedia of Materials: Science and Technology*, Elsevier Science Ltd., Oxford, United Kingdom, 2003, pp. 8121–26.
10. K. Masubuchi: *Analysis of Welded Structures*, Pergamon Press, Oxford, United Kingdom, 1980.
11. P.L. Threadgill, A.J. Leonard, H.R. Shercliff, and P.J. Withers: *International Materials Reviews*, 2008, in press.
12. X.L. Wang, Z. Feng, S.A. David, S. Spooner, and C.R. Hubbard: *6th Int. Conf. Residual Stress*, IOM Communications, Oxford, United Kingdom, 2000, vol. 2, pp. 1408–14.
13. S.R. Bhide, P. Michaleris, M. Posada, and J. DeLoach: *Weld. J.*, 2006, vol. 85, pp. 189–95.
14. P. Staron, M. Kocak, S.W. Williams, and A. Wescott: *Physica B*, 2004, vol. 350, pp. E491–E493.
15. D.A. Price, C.J. Harrison, S.W. Williams, A. Wescott, A. Johnson, J. Gabzdyl, M. Smith, and M. Rahim: BAe Systems Report No. JS 15232, BAE Systems, London, UK, 2004.
16. D.A. Price, S.W. Williams, A. Wescott, C.J.C. Harrison, A. Rezai, A. Steuwer, M. Peel, P. Staron, and M. Kocak: *Sci. Technol. Weld. Join.*, 2007, vol. 12, pp. 620–33.
17. J. Altenkirch, A. Steuwer, M. Peel, D.G. Richards, and P.J. Withers: *Mater. Sci. Eng., A*, 2008, vol. 488, pp. 16–24.
18. D.G. Richards, P.B. Prangnell, S.W. Williams, and P.J. Withers: *Mater. Sci. Eng., A*, 2008, vol. 489, pp. 351–62.
19. S.W. Wen, S.W. Williams, S.A. Morgan, A. Wescott, and M. Poad: *Sci. Technol. Weld. Joint.*, 2008, in press.
20. J. Altenkirch, A. Steuwer, P.J. Withers, S.W. Williams, M. Poad, and S.W. Wen: *Sci. Technol. Weld. Joint.*, 2008, unpublished research.
21. P. Michaleris, J. Dantzig, and D. Tortorelli: *Weld. Res. Suppl.*, 1999, vol. 11, pp. 361–66.
22. E.M. van der Aa, M.J.M. Hermans, I.M. Richardson, N.M. van der Pers, and R. Delhez: *Residual Stresses VII*, 2006, vols. 524–525, pp. 479–84.
23. V. Hauk: *Structural and Residual Stress Analysis by Nondestructive Methods*, Elsevier, Amsterdam, 1997.
24. A.C. Larson and R.B. Von Dreele: *General Structure Analysis System (GSAS)*, Los Alamos National Laboratory Report LAUR 86-748, Los Alamos National Laboratory, Los Alamos, NM, 2000, http://www.ccp14.ac.uk/ccp/ccp14/ftp-mirror/gsas/public/gsas/manual/GSASManual.pdf.
25. T. Pirling, G. Bruno, and P.J. Withers: *Mater. Sci. Eng., A*, 2006, vol. 437A, pp. 139–44.
26. Large Array Manipulation Program, http://www.ill.fr/data_treat/lamp/lamp.html.
27. A. Steuwer, M. Dumont, M. Peel, M. Preuss, and P.J. Withers: *Acta Mater.*, 2007, vol. 55, pp. 4111–20.
28. P.J. Withers, M. Preuss, A. Steuwer, and J.W.L. Pang: *J. Appl. Crystallogr.*, 2007, vol. 40, pp. 891–904.
29. I.C. Noyan and J.B. Cohen: *Residual Stress: Measurement by Diffraction and Interpretation*, Springer-Verlag, New York, NY, 1987.
30. G.A. Webster, ed., "ISO/TTA3, Polycrystalline Materials—Determination of Residual Stress by Neutron Diffraction," *Technol. Trends Assess.*, 2001, vol. 3.
31. M.R. Daymond, M.A.M. Bourke, R.B.V. Dreele, B. Clausen, and T. Lorentzen: *J. Appl. Phys.*, 1997, vol. 82, pp. 1554–62.
32. J.W.L. Pang, T.M. Holden, and T.E. Mason: *Acta Mater.*, 1998, vol. 46, p. 1503.
33. *ASM Handbook*, vol. 9, *Metallography and Microstructures*, ASM INTERNATIONAL, Materials Park, OH, 2001.
34. M.M. Attallah, C.L. Davis, and M. Strangwood: *Sci. Technol. Weld. Joining*, 2007, vol. 12, pp. 361–69.
35. M. James, M.W. Mahoney, and D. Waldron: *1st Int. Symp. FSW*, TWI, Thousand Oaks, CA, 1999.
36. L.E. Murr, Y. Li, E.A. Trillo, R.D. Flores, and J.C. McClure: *J. Mater. Process. Manuf. Sci.*, 1998, vol. 7, pp. 145–61.
37. M.W. Mahoney, C.G. Rhodes, J.G. Flintoff, R.A. Spurling, and W.H. Bingel: *Metall. Mater. Trans. A*, 1998, vol. 29A, pp. 1955–64.
38. K.A.A. Hassan, A.F. Norman, D.A. Price, and P.B. Prangnell: *Acta Mater.*, 2003, vol. 51, pp. 1923–36.
39. M. Dumont, A. Steuwer, A. Deschamps, M. Peel, and P.J. Withers: *Acta Mater.*, 2006, vol. 54, pp. 4793–4801.
40. P. Gomiero, F. Livet, Y. Brechet, and F. Louchet: *Acta Metall.*, 1992, vol. 40, pp. 847–55.

Residual stress engineering in friction stir welds by roller tensioning

J. Altenkirch[1,2], A. Steuwer[3,4], P. J. Withers*[1], S. W. Williams[5], M. Poad[6] and S. W. Wen[7]

The authors investigate the efficacy of applying rolling pressure along the weld line in thin butt welds produced using friction stir welding (FSW) as a means of controlling the welding residual stresses. Two cases are examined and in each case, comparison is made against the as welded condition. First, for FSW of AA 2024 aluminium alloy, roller tensioning was applied during welding using two rollers placed behind and either side of the FSW tool. Very little effect was seen for the down forces applied (0, 50, 75 kN). Second, for FSW AA 2199 aluminium alloy, post-weld roller tensioning was applied using a single roller placed directly on the FS weld line. In this case, significant effects were observed with increased loading, causing a marked reduction in the longitudinal tensile residual stress. Indeed, a load of just 20 kN was sufficient to reverse the sign of the weld line residual stress. Only slight differences in Vickers hardness were observed between the different applied loads. Furthermore, unlike some methods, this method is cheap, versatile and easy to apply.

Keywords: Residual stress, Stress engineering, Roller tensioning, Synchrotron X-ray diffraction, Neutron diffraction

Introduction

The presence of residual stresses in welded components is known to have a significant influence on the fatigue behaviour and therefore, on the component lifetime.[1,2] The friction stir welding (FSW) technique is relatively mature and has been described in detail elsewhere.[3,4] In essence, it relies on the generation of heat through rotational friction at the tool shoulder/material interface, followed by extrusion of a plasticised region around the probe as it moves forward constrained by the shoulder and baseplate. The process is applicable to aluminium alloys otherwise considered as 'non-weldable'.[3,4] It is highly repeatable and its parameters (rotation and translation speeds, down force, tool shape, tilt angle, etc.) can easily be controlled and optimised. Recent experimental[5–10] and finite element modelling[11] work has substantially improved our understanding of the residual stress distribution introduced into components joined by FSW. In common with most, if not all, welding methods, the region around the weld is typically associated with tensile residual stresses which tend to be largest parallel to the welding direction and are balanced by compressive stresses further from the weld line.[12] In a number of instances, tensile longitudinal residual stresses approaching the local room temperature yield stress have been found in friction stir welds.[13,14] Depending on the component and joint geometry, once the residual stresses exceed a critical value, they may lead to distortion in both the longitudinal (bending or buckling) and the transverse (angular) direction as well as rotational distortion and component shrinkage.[13] During fabrication, distortion can be a significant problem and expensive post-weld repair procedures are sometimes necessary to overcome it.

In practice, there is a limit to the extent that residual stress and distortion can be reduced by optimising the FSW parameters.[15] Furthermore, other requirements, such as avoiding the introduction of flaws and maintaining production rates, may constrain the process parameter range that can be employed.[4] An alternative option is to consider one of several stress engineering methods often referred to collectively as 'tensioning methods' that can be applied either during, or after, welding to control the residual stresses and hence the weld distortion.

While a number of stress engineering techniques based on tensioning methods have been tried and tested, the mechanisms acting are not completely understood and the associated process parameters are not yet optimised.[13]

Thermal stress engineering techniques can be applied either, globally to the entire component before and

[1]Materials Science Centre, University of Manchester, Grosvenor Street, Manchester M1 7HS, UK
[2]Institut Laue-Langevin, 6 rue J Horowitz, 38042 Grenoble, France
[3]ESS Scandinavia, Stora Algatan 4, 22350 Lund, Sweden
[4]Nelson Mandela Metropolitan University, Port Elizabeth 6031, South Africa
[5]Cranfield University, Welding Engineering Research Centre, Bedfordshire MK43 0AL, UK
[6]Airbus UK, New Filton House Filton, Bristol BS99 7AR, UK
[7]Corus Research, Development and Technology, Swinden Technology Centre, Moorgate, Rotherham S60 3AR, UK

*Corresponding author, email Philip.withers@manchester.ac.uk

Published by Maney on behalf of the Institute
Received 21 October 2008; accepted 8 November 2008
DOI 10.1179/136217108X388624

during welding, or locally to the weld tool vicinity during welding. Global preheating of the components reduces the temperature gradient between the weld material and the surrounding parent metal, hence decreasing the amount of plastic strain generated during welding, thereby lessening the final residual stresses.[16] On the other hand, local thermal tensioning by hot or cold spots positioned in front of, next to, or behind the welding tool, introduces a local tensile strain that leads to plastic elongation of the weld line material resulting in less misfit and thus residual stress between the weld line and unaffected parent material.[17,18] Even though these methods can be very effective, thermal tensioning methods can be hard to apply as there are a number of parameters that are difficult to control in practice.

On the other hand, mechanical tensioning techniques tend to have fewer and more easily controlled parameters. Global mechanical tensioning (GMT), for example, only involves determining the tensile load level that should be applied along the welding direction. It has been shown to significantly reduce longitudinal residual stresses by minimising the local plastic strain.[11,19–22] Post-weld global mechanical tensioning (PWGMT), is essentially a stress levelling technique and requires comparatively high tensioning loads in order to exceed the weld line yield strength of the cold weld metal so as to plastically elongate the weld material and thereby reducing the plastic strain that causes residual stress.[21] On the other hand, *in situ* global mechanical tensioning (ISGMT) reduces the compressive yielding ahead, and increases the tensile yielding behind, the traversing tool in the hot weld region where the local yield strength is low.[11] The reduced plastic strain leads to a pronounced reduction in the magnitude of the longitudinal tensile residual stress or can even introduce compressive residual weld stresses.[11,19–22] These mechanical tensioning methods have the significant disadvantage that they can only be applied to linear or very simple weld geometries. Furthermore, for large structures, very strong and cumbersome tensioning devices are required to apply the necessary loads.

The application of rolling pressure applied either to the material neighbouring the weld line during welding, or directly to the weld line material after the welding process is finished, is a local mechanical tensioning method that has received relatively little attention to date.[23,24] If the applied roller load is sufficient to achieve plastic compression in the normal direction, this will be compensated by plastic material elongation in the rolling direction, hence decreasing the tensile elastic strain and thereby the longitudinal residual stress.[24,25] The potential of the technique has been demonstrated by means of FE modelling by Wen *et al.* who presented extensive work on *in situ* (ISRT) and post weld roller tensioning (PWRT).[25] They predict that ISRT using two rollers placed either side of the weld following the FSW tool has little effect on the tensile weld line residual stresses but introduces significant compressive stresses in the roller contact area. On the other hand, PWRT using one roller placed along the weld line either directly trailing the FSW tool or applied to the completed (cold) weld, was predicted to reduce the tensile weld line stresses significantly, the effect increasing with increasing rolling down force or thickness reduction. However, to the authors' knowledge, to date no systematic experimental investigation into the effects of roller tensioning on the residual stress mitigation in FSW has been reported.

Consequently, the aim of this paper is to assess the effect of ISRT and PWRT on the residual stress in thin friction stir welded high strength AA 2024-T3 and AA 2199-T8 aluminium plates. In addition, the hardness profiles have been measured across the welds and the plate distortion is quantified as a function of applied roller load.

Experimental

Weld production

Friction stir welding conditions

The aluminium–copper alloy AA 2024-T3 and aluminium–lithium alloy AA 2199-T8 plates investigated in this paper have the compositions given in Table 1. The underaged (T3) and overaged (T8) tempers comprise a solution heat treatment with subsequent cold working to improve material strength by rolling the plates to the final thickness. After rolling, the T3 material is naturally aged while the T8 is artificially aged at elevated temperature. Details of the weld process parameters are given in Table 2.

Roller tensioning

ISRT and PWRT were applied to the AA 2024 and AA 2199 friction stir welds respectively using steel rollers mounted in an especially designed hydraulically controlled gantry attached to the FSW machine.[25] Two different alloys were used for this investigation as

Table 1 Chemical composition of AA 2024-T3 and AA 2199-T8, wt-%[26,27]

Material	Cu	Mg	Mn	Fe	Si	Ti	Li	Zn	Cr	Zr	Al
AA 2024	3·8–4·9	1·2–1·8	0·3–0·9	0·5	0·5	0·15	–	–	0·1	0·18	Bal.
AA 2199	2·63	0·17	0·31	0·04	0·20	0·02	1·56	0·62	–	–	Bal.

Table 2 Material, welding and FSW tool and roller tensioning down force details for weld trials

Material		FSW					
Alloy	YS/UTS, MPa	Plate size, mm	Rotation, rev min^{-1}	Traverse speed, mm min^{-1}	Down force, kN	Tool	Applied rolling strategies and details
AA 2024-T3	345/483[26]	500 × 350 × 5	800	200	1·3	Shoulder Ø13 mm, threaded pin Ø5 mm, pin length 4·35 mm, material MP156	ISRT with 0, 50 and 75 kN roller load
AA 2199-T8	400/438[27]	500 × 200 × 5	800	400	1·3		PWRT with 0, 10, 20, 30 and 40 kN roller load

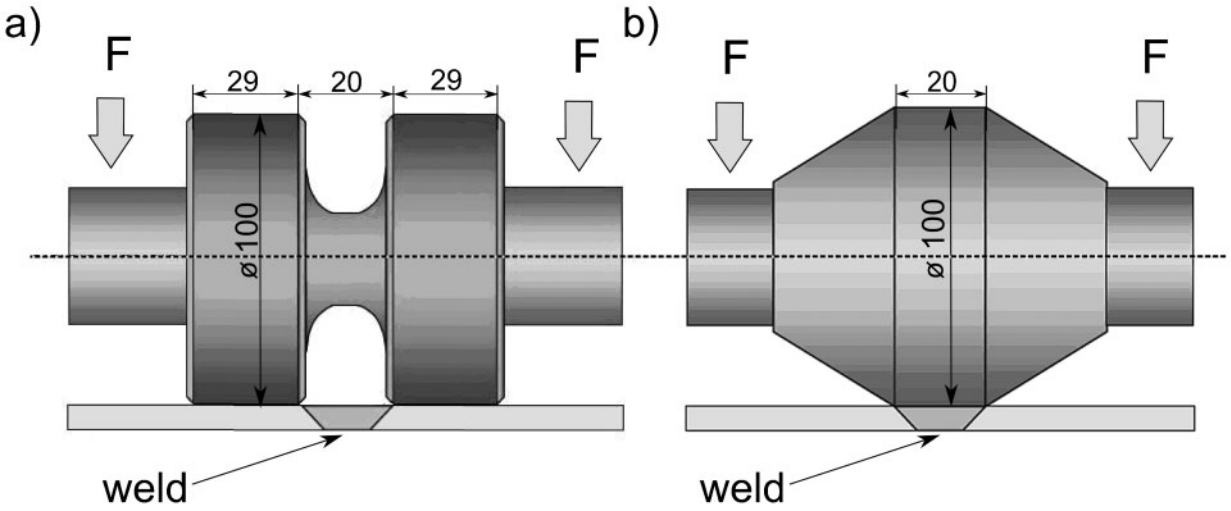

1 Schematic showing *a* double and *b* single roller tools for *in situ* roller tensioning and direct post-weld roller tensioning respectively

AA 2024 was not available for the production of the PWRT samples at the time. In each case, the stresses in the roller tensioned samples are compared against baseline samples that were not roller tensioned.

The ISRT double roll (Fig. 1*a*) is designed such that the rolling load can be applied on both sides of the weld line as close to (40 mm behind), and as soon after, the FSW tool has passed by as possible (Fig. 2*a*). In this way, the material local to the weld can be plastically deformed by the rollers while it is still hot. The rolls on the double roll have a diameter of 100 mm, an effective width of 29 mm with a gap of 20 mm between them, so as to allow the shaft of the FSW tool to be placed in between.

PWRT was applied using a single roll (Fig. 1*b*) also having a diameter of 100 mm and an effective width of 20 mm. It should be noted that PWRT was applied to the weld approximately 30 min after welding had finished. PWRT was performed directly along the weld line in the welding direction as shown in Fig. 2*b*. The roller load parameters for the investigated test welds are summarised in Table 2.

Residual stress measurement

The effect of roller tensioning on the mid-thickness residual stress distribution in the plate longitudinal (L) and transverse (T) direction has been determined non-destructively by synchrotron X-ray and neutron diffraction.

The crystallographic unit cell parameter a was measured as a function of lateral position by means of white beam energy dispersive diffraction (EDXRD) on ID15A at the European Synchrotron Radiation Facility (ESRF), France. Precise details of the measurement arrangement and the subsequent calculation of residual stress may be found elsewhere.[19] In brief, the set-up consists of two energy discriminating detectors, each having a set of collimating slits (100×100 μm), placed such that the scattering vectors are orthogonal (vertical and horizontal) to each other with a scattering angle of

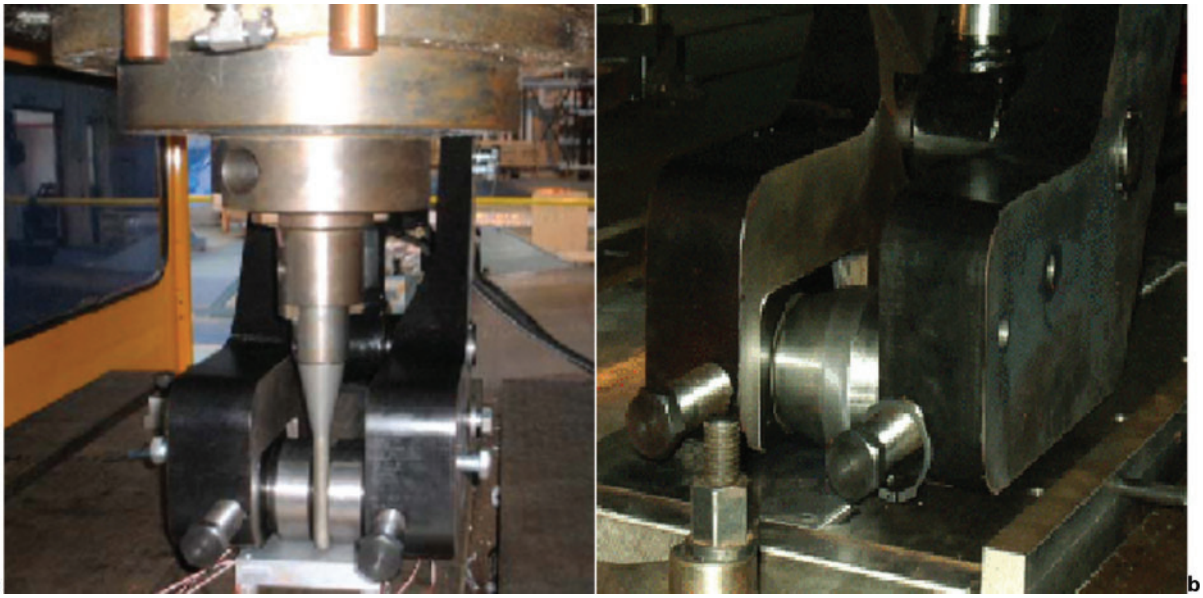

2 Illustration of roller tensioning rig with *a* double roll lying close to FSW tool for *in situ* roller tensioning and *b* single roll for post-weld direct roller tensioning

$2\theta = 5^\circ$ forming a diamond shaped gauge volume. Lattice plane spacing measurements were made in transmission such that the strain was determined in the plate longitudinal and transverse to the weld direction simultaneously. Whole pattern refinement was performed using GSAS and the unit cell parameter a was extracted directly from the structural model.[28] The strain along a particular direction was calculated using the well known relation

$$\varepsilon = (a - a_0)/a_0$$

where a_0 is the unit cell parameter in the unstrained state.

In age hardening aluminium alloys, the dissolution and/or formation of strengthening precipitates due to the local thermal excursion experienced during welding may cause a localised change in the solute concentration and hence the unstrained unit cell parameter a_0. If not accounted for, this variation may have a significant effect on the calculated strains and may lead to inaccuracies in the inferred macro residual stresses.[29] By assuming a plane stress condition (out of plane stress, $\sigma_N = 0$) for the thin (5 mm) plates, it is possible to calculate a local a_0 based on the redundant information obtained by measuring the strain in all three orthogonal directions

$$a_0 = \frac{1-v}{1+v} a_N + \frac{v}{1+v}(a_L + a_T) \quad (1)$$

where v is Poisson's ratio and the subscripts refer to the plate coordinates.

In view of the limited penetration at glancing angles for synchrotron diffraction, the a spacing in the direction normal to the plate was determined using neutron diffraction on the dedicated SALSA angular dispersive diffractometer at the Institut Laue-Langevin (ILL), France. A monochromatic beam with $\lambda \approx 1{\cdot}555$ Å was used resulting in a diffraction angle of $2\theta \approx 79{\cdot}1^\circ$ for the Al_{311} plane. The gauge volume was defined by two collimators to be $\sim 1 \times 1 \times 15$ mm^3, whereby the 15 mm dimension was oriented along the weld direction. The longer volume was used to reduce the counting time; it was assumed that the stress gradients hence variation of the unit cell parameter along the weld direction were sufficiently small. The counting time was 5 min per measurement point. The use of a He^3 80×80 mm^2 position sensitive detector meant that a finite arc of the Al_{311} Debye diffraction ring was collected. This required correction during azimuthal integration before fitting with a Gaussian profile. Both were performed with the ILL Large Area Manipulation Program (LAMP) software.[30]

In the thin plate welds, the residual stress situation was assumed to be biaxial with the out of plane stress component $\sigma_N = 0$ and thus the stresses were calculated using[31,32]

$$\sigma_L = \frac{E}{(1-v^2)}(\varepsilon_L + v\varepsilon_T) \quad (2)$$

where E is the Young's modulus and υ is the Poisson's ratio. Bulk values for the elastic modulus and Poisson's ratio were used in place of the conventional diffraction elastic constants as the strain calculation was based on the unit cell parameter rather than a specific lattice d spacing. For the white beam EDXRD method, this is thought to be appropriate as the within GSAS performed Rietveld/LeBail refinement essentially averages over several peaks simultaneously, thus smoothing out the deviations of any specific peak from the bulk average.[33]

Distortion

The angular, bending and buckling plate distortion was measured for each sample using a Mitutoyo Euro-C-A776 coordinate measuring machine with a Metris LC50 laser scanner attached. This set-up allows $\sim$19 000 surface points to be recorded per second distributed over a $\sim$50 mm laser line projected onto the sample surface.

Hardness

In order to determine whether the roller tensioning has an effect on the post-weld mechanical properties, hardness measurements were carried out on the weld cross-section (T–N plane) on specimens that were extracted at mid-length of the weld. The hardness was determined using a Buehler MicroMet 5101 hardness tester with a test load of 500 g and an indentation time of 10 s. Measurements were performed pointwise over the whole cross-section of the weld.

Results

In situ roller tensioning

The variation in residual stress across the weld line as a function of roller tensioning during welding is shown in Fig. 3. The form of the longitudinal stress distribution for the as welded case is in good agreement with those reported elsewhere[3,4] and on AA 2024 in particular,[9,21,22] being significantly tensile within a region extending slightly beyond the diameter of the shoulder of the tool with the largest stresses lying towards the edge of this region. Similarly, the tendency for the tensile stress on the advancing side to be slightly greater than on the retreating weld side is also well documented.[3,4,11,19]

From the experimental results, one can conclude that ISRT under the range of conditions in this investigation appears to have no significant effect, either beneficial or detrimental. One reason may be an insufficient load level failing to cause significant local plastic deformation in the normal and longitudinal direction. On the other hand, the geometric constraints associated with the FSW tool (Fig. 2) prevented the rollers from being placed close enough to the hot zone (in this case, the rollers were placed 40 mm behind the FSW tool) for the material directly beneath the roller to be sufficiently softened. Further, the uncertainty in the stress determination can be estimated from the difference between the curves to around 15 MPa which is in good agreement with the 12 MPa determined from the statistical errors in fitting the diffraction peak data.

It should be noted that the experimental results are in contrast to the predictions of the FE model produced by Wen *et al.* which show the introduction of significant compressive stresses ($\sim$150 MPa) under the locations of the rollers and thereby a 20% reduction in the longitudinal tensile weld line and peak stresses.[25] These differences may be due to the fact that the FEM predictions were obtained using the same size rollers, but at smaller trailing distances, namely, 15 and 25 mm respectively, compared to 40 mm in the authors' case, and a down force leading to 0·5% thickness reduction.

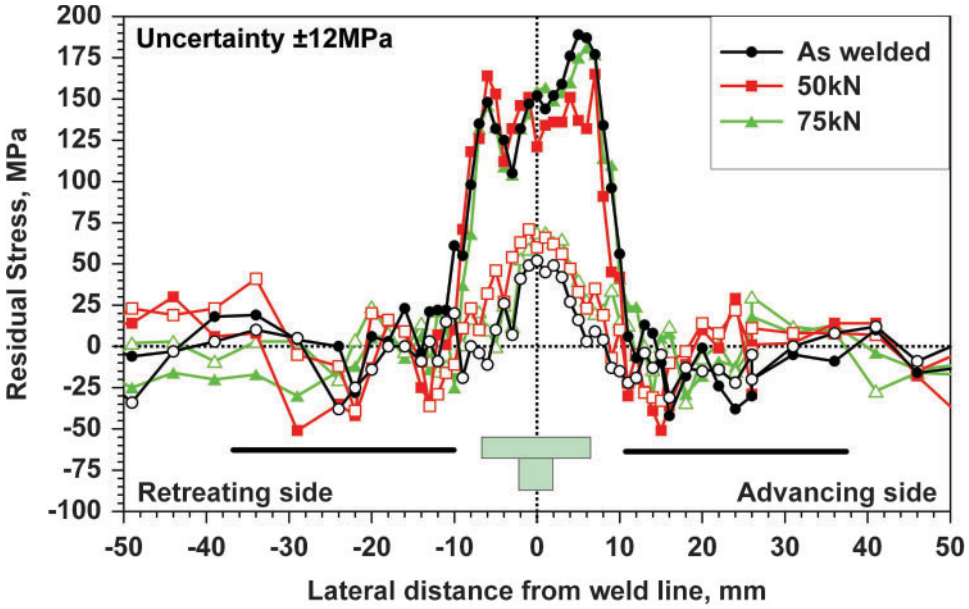

3 Residual stress in longitudinal (solid markers) and transverse (open markers) plate direction measured lateral to weld line for as welded and *in situ* roller tensioned (50 kN and 75 kN down force) AA 2024-T3 FS welds: horizontal bars represent relative position of double roll and cross-section of FSW tool is shown

Such short distances could not be achieved in practise with the authors' experimental set-up. From the FEM predictions, it could be concluded that at shorter trailing distances, the longitudinal weld line stresses are reduced more and that closer trailing rollers would have had a more pronounced effect. This can be attributed to the softer material closer to the FSW tool where the temperatures are higher, hence introducing more plastic deformation. Examination of the thermal profile and the residual stress profile predicted for the as welded AA 2024 FS weld by Richards *et al.* suggests that the area on either side of the weld line would be around 250°C at 15 mm and 150°C at 40 mm and residually stressed longitudinally to around −50 MPa.[11] Examination of the softening model in the same paper suggests that the yield stress would be around 225 and 350 MPa for these locations. Consequently, the rollers need to be closer to the weld line and less far behind. However, due to the geometry of the FSW tool and the size of the rollers this is impractical. In order to improve the efficacy of the technique, it would therefore be necessary to use either higher roller down forces or to get the rollers closer to the hot zone using much smaller diameter rollers which would increase the rolling stress as the contact area reduces. Of course, one way to get the roller closer to the weld line is to roller tension after welding is completed.

Post-weld roller tensioning

Distortion

The level of PWRT was found to have a strong effect on the level of distortion determined for the AA 2199 welds, as presented in Fig. 4. While the as welded sample exhibits significant convex angular and bending modes of distortion (~3 and ~2·5 mm respectively), the post-weld roller tensioned samples show much lower levels of distortion. In particular, the sample treated with a 20 kN PWRT down force shows the least angular and bending distortion while higher down forces reverse the bending distortion to a concave profile. However, all the distortion amplitudes are less than those observed for the as welded plate.

Hardness

The variation in hardness for all the PWRT trial samples is shown in Fig. 5. It should be noted that the parent metal displayed a low level of through thickness hardness variation, namely, higher hardness near the surfaces (~160 $HV_{500\ g}$) relative to the mid-thickness (130–140 $HV_{500\ g}$). Such an observation is not unusual for aluminium plate and is probably due to the through thickness variation in quenching rate after solutionising and plastic deformation during the T8 aging treatment.

The hardness falls dramatically in the region that was passed over by the FSW tool shoulder, the softened zone being slightly broader at the top as a result of the thermal profile during FSW.[34,35] The hardness reaches its lowest value (~80 $HV_{500\ g}$) on the weld line ~2 mm below the weld surface. This is typical for cases where there has been little post-weld age hardening.[4] There is some evidence that it falls less, but with a broader minimum as the rolling down force is increased reaching a value of around 100 $HV_{500\ g}$ at 40 kN down force. Apart from this slight effect, increasing the PWRT load

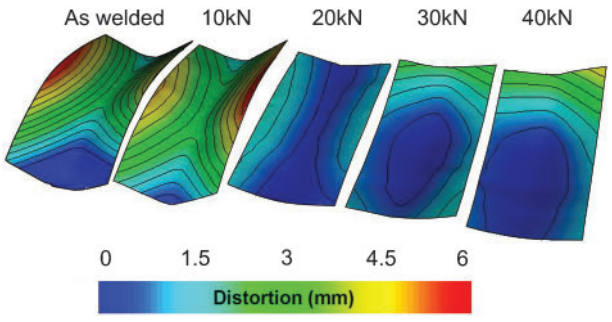

4 Out of plane distortion (in mm) of AA 2199 FSW plates with increasing PWRT down force: vertical axis is exaggerated by factor of 20; each contour represents an interval of 0·5 mm

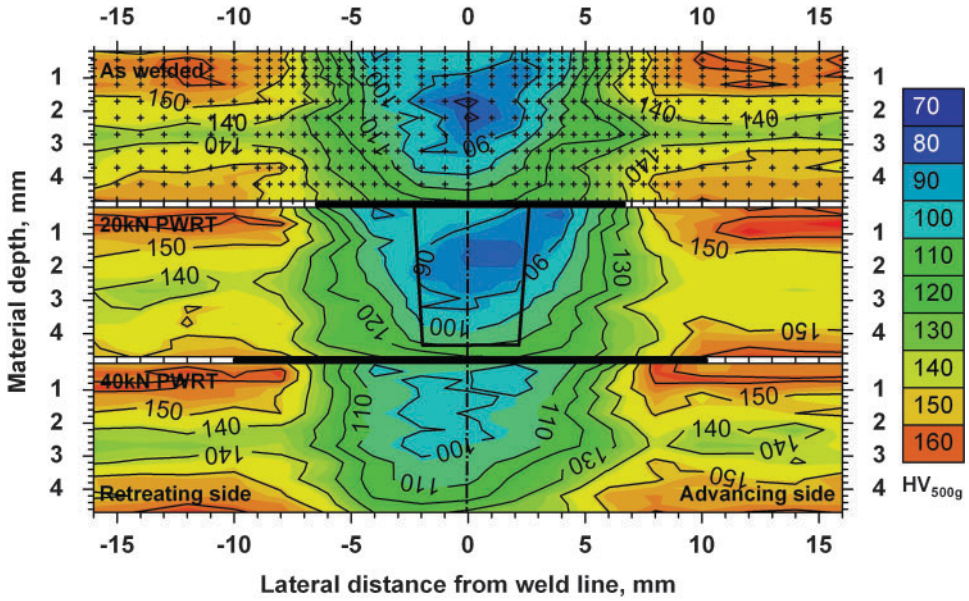

5 Hardness maps (note that the thickness direction has been stretched relative to the lateral direction for clarity) over T–N plane at mid-weld length as a function of PWRT load for AA 2199 T8 welds: in *a* as welded condition, measurement positions are marked by crosses; for map *b* corresponding to 20 kN, outline of tool pin and shoulder is traced, while footprint of single roll is marked in *c* above 40 kN map

appears to have little influence on the hardness. The hardness at the root of the weld is around 120 $HV_{500\ g}$ whether roller tensioning is applied or not.

Residual stress

Knowledge of the variation in the unstrained parameter a_0 is important in order to infer the elastic component of the lattice strain variation. In this investigation, a significant a_0 variation was found being equivalent to $\sim 800 \times 10^{-6}$ strain between the weld nugget and the HAZ just outside the tool shoulder. An extensive discussion on the precipitation effects on the variation of the unstrained lattice parameter and the hardness distribution for this aluminium–lithium alloy may be found in Steuwer *et al.* and Altenkirch *et al.*[15,36]

The residual stresses for the PWRT sample welds as a function of the roller load are shown in Fig. 6. In accordance with previous literature,[7,9,11,20,22,37] the longitudinal residual stress profile for the as welded condition displays a characteristic M shape with weld line stresses of $\sim$170 MPa and peaks of $\sim$220 MPa at $\pm$6 mm from the weld line, a distance which corresponds to the tool shoulder diameter of 13 mm, before falling to 0 MPa forming a $\sim$20 mm wide tensile zone.

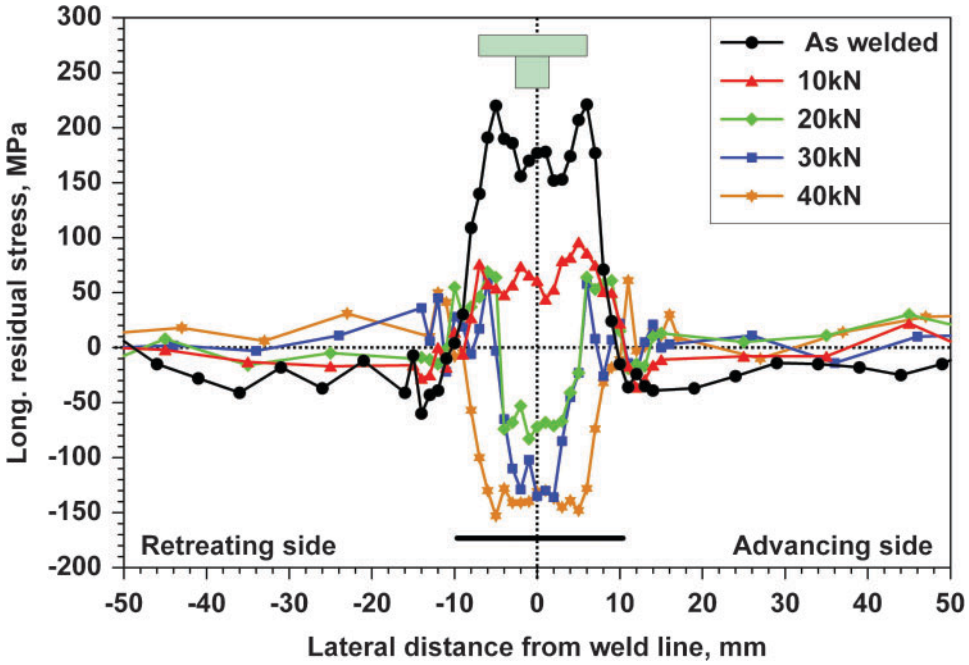

6 Longitudinal mid-thickness residual stress profiles as function of post-weld roller tensioning load for AA 2199-T8 FS welds: estimated point to point measurement scatter is $\pm$12 MPa; bar below stress profiles represents footprint of single roll and above plots cross-section of FSW tool is shown

The origin of this M shaped profile is explained in detail in Richards *et al.*,[11] but may be summarised as following: ahead of the tool, compressive stresses caused by the expanding hot material lead to plastic straining due to the low compressive yield strength, while behind the tool, tensile stresses begin to generate longitudinally as the weld material cools. However, the weld line stress development is limited due to the low tensile yield strength due to the high welding temperatures and therefore cause local plastic straining at the weld line, which then results in the formation of a dip in the developing residual stresses leading to an 'M' shaped residual stress profile.

In contrast to ISRT, PWRT appears to have a significant effect on the longitudinal residual stress distribution. With increased roller tensioning down force, the tensile peaks found near the edge of the FSW tool shoulder essentially disappear and the weld line stresses reduce as predicted by the FE model for PWRT developed by Wen *et al.*[25] This has also been observed with increased GMT loads.[19,20] A PWRT load of 10 kN significantly reduces the weld line tensile stresses to $\sim$60 MPa with the width of the tensile zone similar to the as welded case. At a roller down force of 20 kN, the stress at the weld line has reversed reaching a compressive plateau of around -70 MPa over ± 5 mm from the weld line bordered by two tensile regions ($+70$ MPa) $\sim$4 mm wide, before falling essentially to zero beyond the footprint of the roller. For 30 kN down force, the compressive stress at the weld line has increased to around -120 MPa having a similar width (± 5 mm), bordered by very narrow tensile peaks ($\sim$70 MPa) of about 1–2 mm width located -6 and $+7$ mm from the weld line giving an 'M' shaped profile width of $\sim$16 mm. The compressive weld line stresses do not increase further with an even higher down force (40 kN). This may be attributed to the fact that the local compressive yield strength is reached, which is supported by the low hardness found in the weld nugget as shown in Fig. 5. The compressive zone is significantly wider than for 30 kN, with the tensile stress peaks now located further from the weld line (± 11 mm), i.e. beyond the edge of the roller. These results are broadly in agreement with the predictions of Wen *et al.* who studied AA 2024 FS welds subjected to different PWRT loads.[25] Their model predicted not only a compressive stress limit but also the widening of the compressive zone with increased roller loads. One difference is that the model predicted compressive stress peaks at positions similar to the tensile peaks for the as welded condition, but these are not apparent in the authors' results. Unfortunately, the FE predictions were made for AA 2024 rather than AA 2199 studied here and hence, a direct quantitative comparison of the results with the predictions is not possible.

Nevertheless, in accordance with observations made on globally mechanical tensioned samples, the relatively low level transverse residual stresses appear to be essentially insensitive to the tensioning level varying between ± 50 MPa as shown in Fig. 7.[19–21] Presumably, this is because for thin plates, the transverse plastic strain is fairly uniform through the depth and varies little along the sheet such that it is simply accommodated by a slight widening of the welded joint in a stress free manner. Further, Fig. 7 shows the effect of increased roller down force on the longitudinal residual stress as averaged over the weld line. In the current case, a nearly linear decrease in longitudinal residual stress can be seen for loads up to 20 kN, with the stress reversing in sign at around 15 kN. For higher loads, the rate of stress reversal decreases, which may be attributed to the fact that with increased down force, the roller plate contact area increases, though the rate of the effective compressive stress decreases for higher loads.

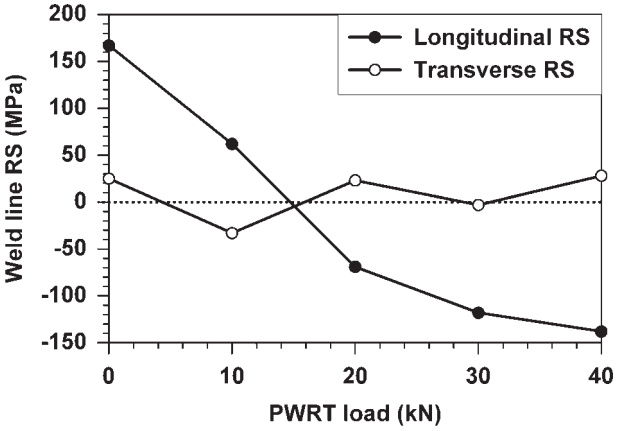

7 Weld line longitudinal and transverse residual stresses measured at material mid-thickness as a function of applied PWRT loads for AA 2199 FS welds

Discussion and conclusions

Under the conditions used in this study, ISRT with a two roller system showed essentially no effect on the residual stresses introduced by FSW of AA 2024-T3 alloy. This is probably because the applied roller loads are too low and the rollers located too far behind the welding tool in a region where the thermal softening of the material is slight during welding. Hence, the compressive loads do not plastically deform and elongate the metal under the roller, which in turn diminishes the elongation of the weld line material and thus mitigating the tensile stress. A possible means of increasing the efficacy of the method would be to apply smaller diameter rollers closer behind the FSW tool or a single roller just behind the tool along the weld line while the metal is still soft. The latter method may have an effect similar to the PWRT but because the metal close to the FSW tool is soft might require lower ISRT loads. However, significant geometrical difficulties would need to be overcome. Furthermore, the finite element modelling results of Wen *et al.* suggest that the current ISRT method is at any rate less effective at reducing the weld line tensile stresses than PWRT and has the added disadvantage of introducing significant compressive stresses in the HAZ as well.[25]

PWRT directly along the weld line on the other hand clearly has a marked effect on the longitudinal residual stresses largely in broad agreement with the predictions of Wen *et al.* made by finite element modelling.[25] Before roller tensioning, the shape free misfit (eigenstrain) between weld and parent plate corresponds to the weld metal being too 'short' longitudinally to match the unaffected plate material. PWRT introduces compression in the plate normal direction, thereby elongating the material in the longitudinal direction (and possibly also in the transverse direction) across the roller contact area.

The relatively slight change in weld hardness with increasing down force might suggest that the introduced plastic strains are relatively small but can be sufficient to reverse the misfit, thereby introducing compressive weld line stresses.

It should be noted that, in principle this method for reducing weld stresses, is not just applicable to the weld stresses introduced by FSW. Because the weld stress profile in the as welded condition is similar to that for many types of fusion welds, it is to be expected that this post-weld treatment could be of wide ranging utility for the reduction in weld stress and distortion. Furthermore, unlike GMT, it is easy to apply to linear as well as non-linear welds provided the weld can be supported firmly below the weld root.

Acknowledgements

The authors would like to thank Dr T. Buslaps (ID15A, ESRF, France), Dr T. Pirling, Dr D. J. Hughes and Ms E. Koukovini (SALSA, ILL, France) for the support during the beam time, the ESRF for the beam time through proposal ME1165 and the ILL for beam time through proposal 7-01-175. AIRBUS UK is acknowledged for providing the samples. J. Altenkirch would like to thank the ILL and the EPSRC Light Alloys Portfolio for financially supporting his PhD thesis.

References

1. M. N. James, D. J. Hughes, Z. Chen, H. Lombard, D. G. Hattingh, D. Asquith, J. R. Yates and P. J. Webster: *Eng. Fail. Anal.*, 2007, **14**, 384–395.
2. P. J. Withers: *Rep. Prog. Phys.*, 2007, **70**, 2211–2264.
3. R. S. Mishra and Z. Y. Ma: *Mater. Sci. Eng.: R, Rep*, 2005, **50R**, 1–78.
4. P. L. Threadgill, A. J. Leonard, H. R. Shercliff and P. J. Withers: *Int. Mater. Rev.*, 2008, to be published.
5. C. D. Donne, E. Lima, J. Wegener, A. Pyzalla and T. Buslaps: Proc. 3rd Int. Symp. on FSW, Kobe, Japan, September 2001, TWI. Published on CD-ROM.
6. L. D. Oosterkamp, P. J. Webster, P. A. Browne, G. B. M. Vaughan and P. J. Withers: *Mater. Sci. Forum*, 2000, **347**–**349**, 677–683.
7. M. J. Peel, A. Steuwer, M. Preuss and P. J. Withers: *Acta Mater.*, 2003, **51**, 4791–4801.
8. A. Steuwer, M. J. Peel and P. J. Withers: *Mater. Sci. Eng. A*, 2006, **A441**, 187–196.
9. M. A. Sutton, A. P. Reynolds, D. Q. Wang and C. R. Hubbard: *J. Eng. Mater. Technol.*, 2002, **124**, 215–221.
10. P. J. Webster, L. D. Oosterkamp, P. A. Browne, D. J. Hughes, W. P. Kang, P. J. Withers and G. B. M. Vaughan: *J. Strain Anal. Eng. Des.*, 2001, **36**, 61–70.
11. D. G. Richards, P. B. Prangnell, S. W. Williams and P. J. Withers: *Mater. Sci. Eng. A*, 2008, **A489**, 351–362.
12. K. Masubuchi: in 'Encyclopedia of materials: science and technology', 8121–8126; 2003, Oxford, Elsevier Science Ltd.
13. K. Masubuchi: 'Analysis of welded structures', 600; 1980, Oxford, Pergamon Press.
14. X. L. Wang, Z. Feng, S. A. David, S. Spooner and C. R. Hubbard: Proc. 6th Int. Conf. on 'Residual stress', Oxford, UK, July 2000, Institute of Materials, 1408–1414.
15. J. Altenkirch, A. Steuwer and P. J. Withers: 2008, to be published.
16. ASM: 'ASM handbook' Vol. 6, 'Welding, brazing and soldering', 1094–1103; 2001, Materials Park, OH, ASM.
17. D. G. Richards, P. B. Prangnell, P. J. Withers, S. W. Williams, T. Nagy and S. A. Morgan: Proc. 7th Int. Symp. on FSW, Awaji Island, Japan, 2008, TWI. Published on CD-ROM.
18. E. M. van der Aa, M. J. M. Hermans, I. M. Richardson, N. M. van der Pers and R. Delhez: in 'Residual stresses VII', 479–484; 2006, Uetikon-Zuerich: Trans Tech Publications.
19. J. Altenkirch, A. Steuwer, M. Peel, D. G. Richards and P. J. Withers: *Mater. Sci. Eng. A*, 2008, **A488**, 16–24.
20. J. Altenkirch, A. Steuwer, M. J. Peel, P. J. Withers, S. W. Williams and M. Poad: *Metall. Trans. A*, 2008, **39**(13), 3246–3259.
21. D. A. Price, S. W. Williams, A. Wescott, C. J. C. Harrison, A. Rezai, A. Steuwer, M. Peel, P. Staron and M. Kocak: *Sci. Technol. Weld. Join.*, 2007, **12**, 620–633.
22. P. Staron, M. Kocak, S. W. Williams and A. Wescott: *Physica B*, 2004, **350B**, 491–493.
23. W. Liu, X. Tian and X. Zhang: *Weld. Res. Suppl.*, 1996, **75**, 297–304.
24. Y. P. Yang, P. Dong, X. Tian and Z. Zhang: Proc. 5th Int. Conf. on 'Trends in welding research', Pine Mountain, GA, USA, ASM, June 1998, 700–705.
25. S. W. Wen, S. W. Williams, S. A. Morgan, A. Wescott and M. Poad: submitted to *Sci. Technol. Weld. Join*.
26. ASM: 'ASM handbook', Vol. 2, 'Properties and selection: nonferrous alloys and special-purpose materials'; 2001, Materials Park, OH, ASM.
27. G. Khelifati, V. Guillaumin, L. Naze and N. Laurrain: Proc. Conf. Aluminium 2006, Essen, Germany, September 2006, Essen Exhibition Centre, 4.
28. A. C. Larson and R. B. von Dreele: 'General structure analysis system (GSAS)', LAUR 86-748, Los Alamos National Laboratory, Los Alamos, NM, USA, 1994.
29. A. Steuwer, M. Dumont, M. Peel, M. Preuss and P. J. Withers: *Acta Mater.*, 2007, **55**, 4111–4120.
30. ILL: 'LAMP, large array manipulation program', available at: http://www.ill.fr/data_treat/lamp/lamp.html, Grenoble.
31. V. Hauk: 'Structural and residual stress analysis by nondestructive methods', 640; 1997, Amsterdam, Elsevier.
32. ISO/TTA3: 'Polycristaline materials – determination of residual stress by neutron diffraction', Technology Trends Assessment; 2001, Geneva, ISO.
33. M. R. Daymond, M. A. M. Bourke, R. B. V. Dreele, B. Clausen and T. Lorentzen: *J. Appl. Phys.*, 1997, **82**, 1554–1562.
34. O. Frigaard, O. Grong and O. T. Midling: Proc. Conf. INALCO '98, 208–218; 1998, Cambridge, TWI.
35. M. J. Peel, A. Steuwer, P. J. Withers, T. Dickerson, Q. Shi and H. R. Shercliff: *Metall. Mater. Trans. A*, 2006, **37A**, 2183–2193.
36. A. Steuwer, M. Dumont, J. Altenkirch, A. Deschamps and P. J. Withers: 2008, to be published.
37. M. Hutchings, P. J. Withers, T. M. Holden and T. Lorentzen: 'Introduction to the characterisation of residual stress by neutron diffraction', 424; 2005, London, CRC Press/Taylor & Francis.

The extent of relaxation of weld residual stresses on cutting out cross-weld test-pieces

J. Altenkirch[a)]
School of Materials, Grosvenor Street, Manchester M1 7HS, United Kingdom and University of Karlsruhe, IWK I, Kaiserstr. 12, Karlsruhe 76131, Germany

A. Steuwer
ESS Scandinavia, Stora Algatan 4, 22350 Lund, Sweden and Nelson Mandela Metropolitan University, Port Elizabeth 6031, South Africa

M. J. Peel
European Synchrotron Radiation Facility, 6 rue J Horowitz, BP220, 38043 Grenoble, France

P. J. Withers
School of Materials, Grosvenor Street, Manchester M1 7HS, United Kingdom

(Received 30 September 2008; accepted 20 February 2009)

Weld residual stress (RS) measurements are often undertaken on test-pieces which have been cut out from large components, yet it remains unclear to what extent the RSs in test-pieces are representative of those present in the original component. Similarly weld mechanical performance tests are frequently undertaken on cross-weld test-pieces without a proper understanding of the level or influence of retained RS. We present a systematic study of the relaxation of longitudinal RS in thin-plate butt welds produced using different materials and welding methods (FSW, laser-MIG, and pulsed-MIG). In each case the RSs were measured repeatedly in the same location as the welds were progressively and symmetrically cut down. Although cutting inevitably leads to stress redistribution, significant relaxation of the longitudinal RS was only observed when the weld length or width was reduced to below a certain value. This critical value appears to correlate with the lateral width of the tensile zone local to the weld-line and may be considered to be the characteristic length as defined in St. Venant's principle. Further, it was found that the level of stress relaxation as a function of weld length for all the welds studied could be collapsed onto a single empirical curve using a simple approach based on the characteristic length scales of the weld. Given the range of materials and welding methods used, this relation appears to be of general use for thin-plate welds although further work is required to test the limits of its applicability. [DOI: 10.1154/1.3152580]

Key words: residual stress, stress relief, St. Venant's principle, guidelines

I. INTRODUCTION

Weld stresses were among the first types of residual stress (RS) to be measured by neutron and synchrotron X-ray diffraction (Allen *et al.*, 1984; Hutchings *et al.*, 2005). They are a major source of concern for structural integrity assessments today (Withers, 2007). In particular the longitudinal component of the RS can be a significant fraction of the yield stress in the weld and heat affected zone (Threadgill *et al.*, 2009). Several stress engineering techniques have been developed to control RS, such as thermal tensioning (Gabzdyl *et al.*, 2003; Aa, 2007), global mechanical tensioning (Altenkirch, Steuwer, Peel, Withers *et al.*, 2008; Price *et al.*, 2007; Williams *et al.*, 2008; Richards *et al.*, 2008), and roller tensioning (Altenkirch, Steuwer, Withers *et al.*, 2008). Investigating and optimizing the efficacy of these techniques require a detailed knowledge of the RS profile. In many cases the welds are too long or cumbersome to be investigated in their entirety and smaller cross-weld test-pieces are cut out either to measure the RS or for weld performance evaluation (Threadgill *et al.*, 2009). According to the size of the removed test-piece the RS will be partially relaxed, which may lead to the RS measured being significantly less than those present in the original component. As a result the effect of RS on the component life cycle performance may be seriously underestimated. Alternatively, failure to take account of the retained RS when undertaking cross-weld performance testing may result in a misleading impression of the weld properties. As a consequence some guidelines are required when excising samples in order to estimate the severity of this effect: the aim of this paper is to establish such guidelines based on experimental evidence.

The typical RS distribution in butt welds has been described by Masubuchi (1980). The longitudinal RSs, σ_L, along the weld-line [line A-A in Figure 1(b)] are tensile and comparatively high over the essentially steady-state central region but tend to decrease to zero towards the ends of the plate. The transverse RSs, σ_T, may also be tensile but are normally much smaller and equilibrate along the weld-line by becoming compressive towards the ends of the weld. In contrast, the RSs σ_L lateral to the weld-line [line B-B in Figure 1(c)] are tensile in the weld zone and balanced by compression towards the sides of the plate. The RSs σ_T on the other hand are only moderately tensile and tend to zero at the plate side edges. Cutting in the longitudinal or transverse

[a)]Author to whom correspondence should be addressed. Electronic mail: jens.altenkirch@iwk1.uni-karlsruhe.de

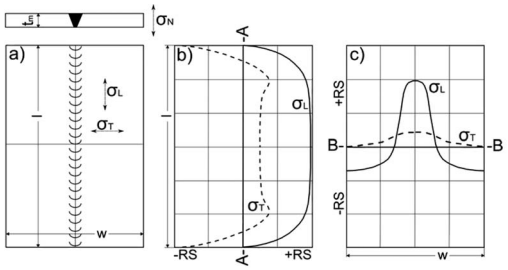

Figure 1. Schematic of typical longitudinal (solid) and transverse (dashed) RS distributions in a flat plate joined in a butt weld configuration: (a) illustration of the plate dimensions ($l \times w \times t_m$) and the RS directions, (b) σ_L and σ_T distributions along the weld-line (A-A), and (c) σ_L and σ_T distributions across the weld-line (B-B) (Masubuchi *et al.*, 1980).

direction leads to partial relaxation of these RSs requiring a redistribution of stress to maintain self-equilibrium. For an arbitrary point this redistribution will depend on its distance from the cut surface. It will be largely unaffected at large distances, as described qualitatively by St. Venant's principle for a static load on the free end of a beam (Timoshenko and Goodier, 1987). Toupin provided a mathematical interpretation of this principle for the stored elastic energy $U(s)$ per unit volume in a cylindrical beam of length l at a distance s from the end (Toupin, 1965),

$$U(s) \leq U(0)\exp\left\{-\left(\frac{s-l}{s_c(l)}\right)\right\}, \tag{1}$$

where $U(0)$ is the total stored energy and the dimensionless decay length constant $s_c(l)$ depends on the elastic properties of the material. This reflects the fact that the effect of self-equilibrating RS decays exponentially over a short distance (Toupin, 1965). St. Venant referred to the extent of notable relaxation as the *characteristic distance* (Timoshenko and Goodier, 1987), while Toupin (1965) referred to the *characteristic cross-section dimension*. However these dimensions have not been defined in the context of thin-plate butt welds.

In order to establish guidelines for the estimation of stress relaxation, the degree of longitudinal RS relaxation is quantified systematically upon sectioning welded plates in the longitudinal and transverse directions. Energy-dispersive diffraction using synchrotron X-rays has been used to determine the RS across the weld-line at midlength in five different types of butt welds as they are progressively shortened or narrowed. Welds were produced in aluminum plates (AA2098 and AA7449) using the friction stir welding (FSW) and steel plate (S355) using hybrid laser-MIG and pulsed-MIG techniques.

II. EXPERIMENTAL

A. Weld trials

Five butt welds were produced using different welding methods, materials, and weld geometries (Table I) aimed at representing a wide variety of welding conditions. The initial and intermediate lengths and widths of the samples are also given in Table I.

B. Residual stress determination

The longitudinal and transverse RS distributions were determined using synchrotron X-ray diffraction measurements performed in the energy-dispersive mode on the high-energy beamline ID15A at the European Synchrotron Radiation Facility (ESRF), France. A detailed description of the setup may be found elsewhere (Altenkirch, Steuwer, Peel, Richards *et al.*, 2008). In brief, it consists of two energy-discriminating detectors behind collimating slits each having a scattering angle of $5° = 2\theta$ and placed such that the in-plane scattering vectors, Q, are orthogonal to each other [see Figure 2(b)]. Measurements were made in transmission where the nominal gauge volume is set to $0.1 \times 0.1 \times 2.3$ mm^3. Whole pattern refinement was performed using GSAS (Larson and Von Dreele, 2004) and the unit cell parameter a was extracted directly from the structural model.

The variation in the unstrained unit cell parameter a_0 in the 12.2 mm thick butt weld 2 was determined using the comb method, while in the thin welds a biaxial stress state (ISO/TTA3, 2001; Hauk, 1997) was assumed and the re-

TABLE I. Welding details for the butt welds investigated.

No.	Technique/material	Details	Original dimensions	Intermediate dimensions
1	FSW/AA2098	8 kN down force, 1200 rpm, 500 mm/min, shoulder Ø 13 mm, tapered pin Ø 4.91 mm, and 3 mm length.	$880 \times 300 \times 3$ mm^3, weld path length of 880 mm	Lengths: 880, 800, 400, 200, 100, and 50 mm
2	FSW/AA7449	80 kN down force, 225 rpm, 250 mm/min Tri-flate™, shoulder Ø 30 mm, threaded pin Ø 17 mm, and 11.7 mm length.	$1000 \times 300 \times 12$ mm^3, weld path length of 800 mm	Lengths: 1000, 800, 400, 200, 100, and 50 mm
3	Hybrid Laser-MIG/S355	2.5 m/min, 4 kW laser power (27 V, 185 A), 11.43 m/min wire feed, 16 mm CTDW, 2 mm laser-arc distance, ar+20%CO_2+2%O_2 shielding gas, and 15l/min gas flow rate.	$500 \times 400 \times 4$ mm^3, weld path length of 500 mm	Lengths: 500, 400, 300, 200, 100, 70, and 40 mm
4	Pulsed MIG/S355	0.42 mm/min, 30.7 V, 193 A, 8.61 wire feed, 13 mm CTDW, Ar+20%CO_2+2%O_2 shielding gas, and 16l/min gas flow rate.	$500 \times 400 \times 4$ mm^3, weld path length of 500 mm	Lengths: 500, 400, 300, 200, 100, 70, and 40 mm
5	Pulsed MIG/S355	0.63 mm/min, 37.8 V, 220 A, 11.5 wire feed, 13 mm CTDW, Ar+20%CO_2+2%O_2 shielding gas, and 16l/min gas flow rate.	$500 \times 400 \times 4$ mm^3, weld path length of 500 mm	Widths: 400, 300, 200, 140, 100, and 60 mm

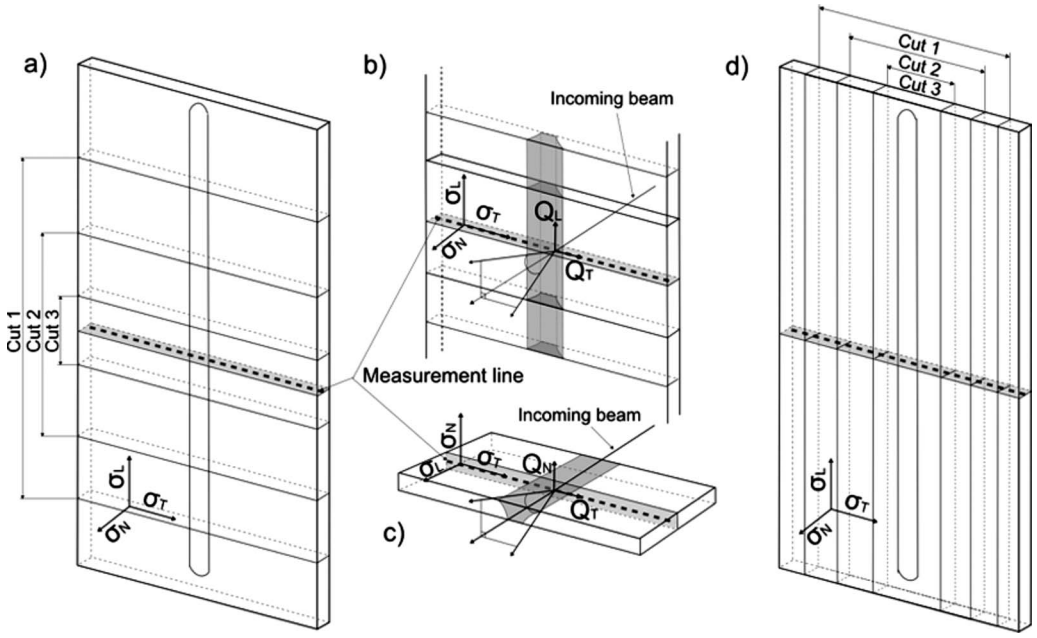

Figure 2. Illustration showing (a) the progressive reduction in test-piece length keeping the measurement line at midlength, (b) the sample orientation relative to the synchrotron X-ray beam for the measurement of the longitudinal and transverse strains, and (c) the sample orientation for the measurement of the normal strain at the final weld length. In (d) the progressive sectioning in the transverse direction is shown.

quired normal direction was measured with the shortest length specimen orientated as shown in Figure 2(c). However, a detailed description of both techniques is beyond the scope of this paper but may be found in Altenkirch, Steuwer, Peel, Withers *et al.*, 2008.

The transverse and longitudinal in-plane RSs were determined along a single scan running normal to the welding direction at the midlength and midthickness of the weld as shown in Figures 2(a) and 2(d). The strain and hence the RS for the longitudinal and transverse directions were calculated according to Altenkirch, Steuwer, Peel, Richards *et al.*, (2008). After measuring the initial RS distribution, the test-piece lengths and widths were progressively shortened (1–4) or narrowed (5) by removing an equal amount from each end/side thereby maintaining the measurement line at the midlength and middle of the plate, respectively, as shown in Figures 2(a) and 2(d).

III. RESULTS

A. Longitudinal sectioning

Figure 3 shows the measured RS σ_L for welds 1–4 as they were progressively reduced in length. The profiles are characteristic of welds with large tensile RS close to the weld-line balanced by low compressive RS in the parent material (Masubuchi, 1980). The precise form of the RS distribution naturally depends on the welding technique and parameters, but such details are beyond the scope of this paper. Upon progressive sectioning the longitudinal RSs start to decrease significantly below a certain length. On the other hand the transverse RSs do not appear to change significantly upon longitudinal sectioning and are therefore not shown here. It is noteworthy that the width of the tensile peak, w_t, as indicated by the horizontal arrows in Figure 3 for $\frac{1}{2}w_t$, remains approximately constant for varying weld lengths.

For simplicity in the following the degree of stress relaxation will be taken to be characterized solely in terms of the magnitude of the longitudinal weld-line RS rather than any changes in the shape of the stress distribution. The normalized weld-line RSs for each sample as a function of normalized plate length are shown in Figure 4. As noted above, the RSs are largely unaffected by material removal until a critical fraction of the weld length has been removed. Be-

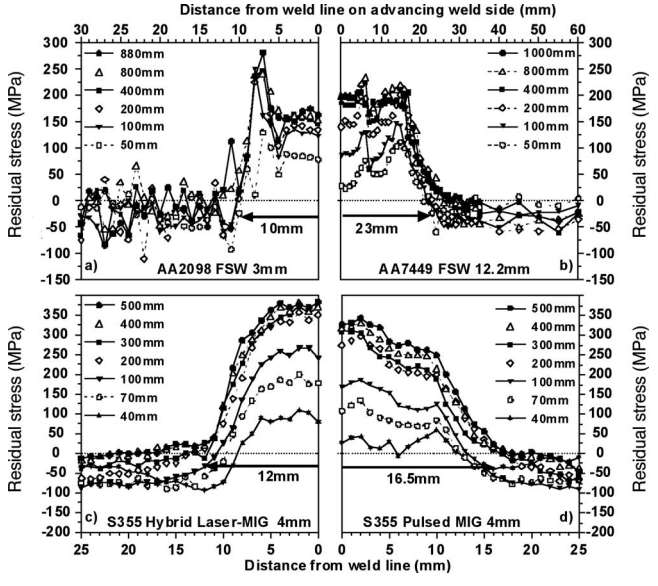

Figure 3. Longitudinal RS distributions of (a) weld 1, a FSW in AA2098, (b) weld 2, a FSW in AA7449 (Altenkirch, Steuwer, Peel, Richards *et al.*, 2008), (c) weld 3, a hybrid laser-MIG weld in S355, and (d) weld 4, a pulsed-MIG weld in S355 with progressive sectioning along the weld-line. The half-width of the tensile peak, $\frac{1}{2}w_t$, is shown for each sample. Though not evident from these central regions the RSs balance over the entire plate width.

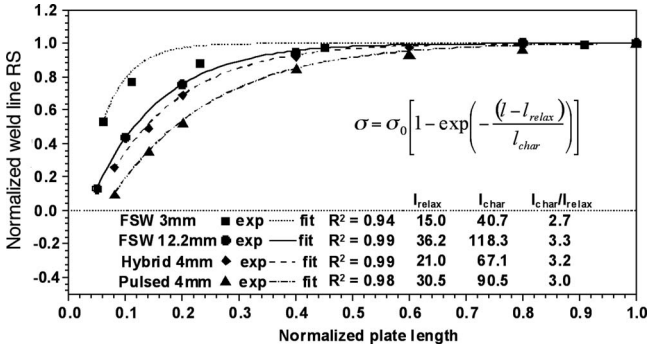

Figure 4. Normalized RS at the weld-line (σ/σ_0) vs normalized plate length (l/l_0). Markers represent the measured data; lines represent the best nonlinear fits achieved using Eq. (2) with the fitting parameters given in the figure.

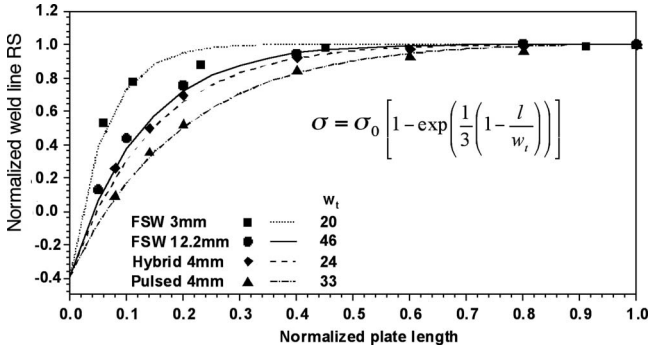

Figure 5. The normalized measured RS (markers) as a function of test-piece length [normalized to the length and stress in the original (long) weld] compared to the empirical relation described by Eq. (3) (lines) using the measured width of the stress peak, w_t, as taken from the RS distribution plots in Figure 3.

yond this point the reduction in RS follows an exponential decrease which can be described by a simple empirical parametric equation (Altenkirch, Steuwer, Peel, Richards *et al.*, 2008)

$$\sigma = \sigma_0\left[1-\exp\left(-\frac{(l-l_{relax})}{l_{char}}\right)\right], \quad (2)$$

where σ is the longitudinal weld-line RS for the current weld length l, σ_0 is the RS in a long (strictly infinite) weld, l_{relax} is the test-piece length at which there is essentially zero macroscopic RS, and l_{char} is the characteristic length. The latter may be reasonably compared to the characteristic distance of St. Venant's principle (i.e., stresses in a given location are unaffected by changes in loading if such changes occur beyond this distance from the area being measured) (Timoshenko and Goodier, 1987; Toupin, 1965; Ugural and Fenster, 1994; Berdichevsky and Foster, 2003). The concept of a characteristic length is poorly defined in the literature but essentially describes how the residual stresses change and redistribute upon the removal of material and it is this definition that is used here. It should be noted from the form of Eq. (2) that our expression is an essentially elastic relation in that the relaxed stress is linearly related to the initial stress. In this respect it might be anticipated that for most thin-plate welds the cutting does not introduce significant plastic deformation.

In the current case the respective l_{char} and l_{relax} parameters were determined by nonlinear fitting to the measured data (Figure 4). For instance for the 4 mm thick S355 pulsed-MIG weld (4), the fit to the data is consistent with values of 90 and 30 mm for l_{char} and l_{relax}, respectively, with a high quality of fit. That the RS approaches zero at l_{relax} (0.06 =30/500 in normalized units) is also clearly evident in Figure 4. It is noteworthy that in all welds l_{relax} corresponds closely to the width of the tensile peak, w_t, thus perhaps indicating that at this length the tensile region is no longer constrained to a meaningful degree by the surrounding material. Similarly empirical evidence suggests that l_{char} is approximately three times w_t although the reason for this is not clear at the present time. From these observations Eq. (2) may be simplified by taking $l_{relax}=w_t$ and $l_{char}=3w_t$,

$$\sigma = \sigma_0\left[1-\exp\left(\frac{1}{3}\left(1-\frac{l}{w_t}\right)\right)\right]. \quad (3)$$

This simplification reduces the number of variables and has the advantage that the remaining variable, w_t, can be determined directly from the RS distribution plot. The relaxation of stress expected on the basis of the empirical relation given by Eq. (3) using the w_t values obtained from the RS distributions in Figure 3 is shown in Figure 5 and compared to the experimental data.

The good agreement with Eq. (3) supports the hypothesis that the characteristic and relaxation lengths are both proportional to the width of the tensile region for these welds. It also means that the data can all be collapsed onto a single relaxation line using Eq. (3) when the weld length is normalized by the width of the stress peak w_t rather than the original weld length (l_o), as shown in Figure 6. Furthermore, the excellent agreement evident in Figure 6 suggests that it is possible to predict the amount of stress relaxation that would occur in a test-weld on cutting to a given length using a simple empirical relation without recourse to detailed finite element modeling as long as w_t is known or can be estimated.

For FSW, for example, the width of the tensile peak w_t appears to be largely controlled by the diameter of the tool shoulder ϕ_t. In the two FS welds investigated, w_t is approximately $1.5\phi_t$. The literature reveals that this value does

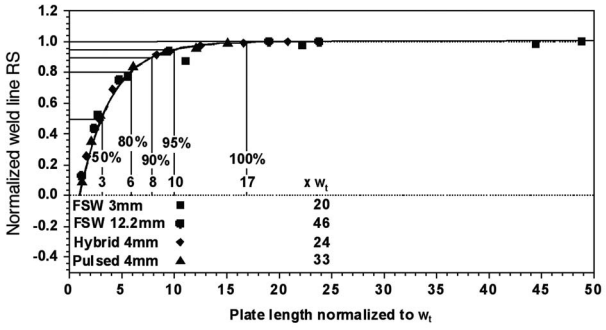

Figure 6. The experimental data normalized by the infinite weld stress, σ_0, and the w_t value for each weld compared to the empirical mother curve described by Eq. (3) describing the RS relaxation behavior upon progressive sectioning.

change somewhat as a function of alloy type, tool speed, and the down force applied (Altenkirch, Steuwer, Peel, Withers *et al.*, 2008; Peel *et al.*, 2003). Nevertheless a value for w_t estimated from the shoulder dimensions does provide a good indicator of the likely relaxation levels and suggests a guideline figure for the minimum size of test-pieces if little relaxation is required.

Finally, from Figure 6 it can be seen that relaxation is less than 10% if the retained section of the weld is eight times longer than the width of the tensile peak. Thus, Eq. (3) permits an evaluation of the minimum length of a weld retained for a cross-weld sample to have negligible stress relaxation compared to the original weld. Conversely, it is possible, if undertaken carefully, to infer the unrelaxed RS level for a long (infinite) weld on the basis of measurements made on shorter sections. However, care must be taken when choosing the value for w_t since, as noted above, it varies slightly as the retained weld length decreases (Figure 3). Finally in cases where cross-weld tests are used to extract mechanical performance metrics (Peel *et al.*, 2003; Mahoney *et al.*, 1998; Sutton *et al.*, 2004), it may be desirable to remove the effects of RS. In such a case it would be beneficial to choose a test-piece length less than the lateral width of the tensile zone w_t so that RSs are negligible.

B. Transverse sectioning

The magnitude of the longitudinal tensile RS σ_L might be expected to fall as the plate width containing the weld decreases. This is of concern because in many trials relatively narrow test plates are used either for convenience or economy; in other cases narrow regions must be cut out of wider welded plates or structures for the purposes of evaluation.

The extent of RS relaxation with decreasing plate width has been evaluated for test weld 5 and the results are summarized in Figure 7. While the transverse RSs σ_T are low and largely unaffected by progressive narrowing of the plate, the longitudinal RS decreases due to stress redistribution occurring so as to maintain stress balance within the plate. It is evident that while the shape of the longitudinal stress profile remains essentially constant as the plate is reduced in width, the profile begins to shift downwards when the plate becomes less than 300 mm wide. In fact, the weld-line RS (averaged over ±3 mm of the peak centre) falls from around ~480 to ~300 MPa as the width is reduced stepwise from 300 to 60 mm and the elastic strain from 2150×10^{-6} to 1300×10^{-6} [Figure 7(c)].

All residual stresses arise from an elastic accommodation of stress-free misfit (Withers and Bhadeshia, 2001), in this case between the near weld region which is longitudinally too small and the parent plate further from the weld that is relatively longer. RS can normally be relaxed either by reducing the misfit itself or by lessening the constraint offered by the surrounding material. In our case, the misfit can be reduced by plastic deformation of the weld or parent, while the constraint is clearly reduced by reducing the width of the plate. Figure 7(c) shows the difference in elastic strain between the edge and the centre of the plate which for a long weld is essentially equal to the stress-free misfit between weld and parent. For an infinitely wide plate all the misfit would be accommodated elastically in the weld region because of the large extent of the restraining parent. When the plate is 400 mm wide the difference in longitudinal elastic strain between the parent and the weld is $\sim2300\times10^{-6}$ with ~90% accommodated in the weld. As the width of the restraining parent plate is reduced the misfit is accommodated increasingly by compressive strain in the parent. When the plate is just 60 mm wide the misfit strain is accommodated approximately 40%:60% so that the parent plate experiences a compressive strain of approximately -700×10^{-6} (−150 MPa) and the weld 1300×10^{-6} (300 MPa). As a result the misfit is approximately 2000×10^{-6} as shown in Figure 7(c). In other words the stress-free misfit is decreased by only $\sim300\times10^{-6}$ by the cutting procedure indicating that the stresses have been relieved primarily elastically rather than by plastic deformation.

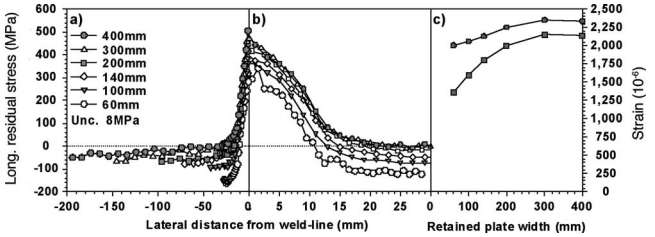

Figure 7. Longitudinal RS distribution across the *N-T* cross section for test weld 5 as a function of retained plate width. In (a) the stress profile across one half of the plate is shown, (b) displays a closeup of the stress profile local to the weld-line, while (c) plots the variation in the peak elastic strain (squares) with retained plate width alongside the difference in elastic strain between the centre of the plate and the edge (circles).

Assuming stress balance and simple downward shifting of the peak longitudinal RS σ, as the plate width, w, narrows, the remnant RS can be inferred by applying stress balance to the tensile (w_t) and compressive $(w-w_t)$ regions from the initial peak RS σ_0, which would arise in an infinitely wide plate, by using a simple parametric equation

$$\sigma = \sigma_0\left(1-\frac{w_t}{w}\right), \tag{4}$$

where w_t again is the width of the tensile stress peak as defined earlier from the RS profile. In the current case we can infer from Eq. (4) that the stresses in an infinite plate, σ_0, of ~500 MPa and 33 mm for w_t, a value very close to that of the actual width of the stress peak in Figure 7(b), result in a stress relaxation curve that fits the experimental data well as depicted in Figure 8. From these results it can be concluded that simple stress re-equilibrium described by

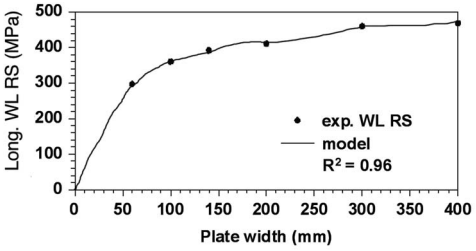

Figure 8. Longitudinal peak stress for weld 5 as measured (symbols) and as predicted (line) on the basis of the 400 mm data using Eq. (4) as a function of retained plate width.

Eq. (4) reflects the longitudinal stress reduction behavior for progressive reduction in the width of a welded plate surprisingly well.

IV. CONCLUSIONS

In this paper we have investigated the extent of elastic relaxation of RS in thin welded plates that are progressively cut down to form test-pieces of shorter and shorter length or narrower width. With regard to a reduction in retained weld length for cross-weld samples, the relaxation behavior for welds produced in different materials and with different welding methods was found to collapse onto a single empirical relaxation curve using just the width of the stress peak, w_t, as a governing parameter in a simple exponential equation. From this equation the minimum length of test-pieces needed when making stress measurements to maintain the RS at 90% of its unrelaxed value was found to be eight times the stress peak width. For shorter test-pieces the relation could be used to back calculate the unrelaxed stress state that would arise for a long weld. In order to attain a maximum steady-state welding RS the weld length should be some 17 times as long as the tensile zone is wide even neglecting start-up and stop issues. Conversely if the length of the weld in the test-piece is approximately equal to the width of the longitudinal stress peak, then the RSs are likely to be almost completely relaxed in the midlength of the test-piece. While the utility of this relationship has been investigated for a range of butt welds in thin plate, further work needs to be conducted to investigate whether it is also applicable to thicker welds. In this respect it should be borne in mind that thick welds can have high multiaxial stresses which may introduce plastic deformation on cutting or out of plane bending that may complicate the analysis.

With regard to the reduction in the width of the welded plate, the largest longitudinal tensile stresses would be expected in a plate of infinite width. It has been shown that reducing the plate width reduces the maximum longitudinal tensile stresses in the weld-line primarily by shifting the overall profile downwards in order to establish a balancing compressive stress in the parent material while the shape of the stress profile is maintained. In this case, the redistribution in order to achieve stress balance as the constraining effect of the parent plate is essentially achieved elastically with relatively little reduction in the stored misfit strain. Again a simple analytical equation based on stress balance for the derivation of the fall in peak tensile longitudinal stress was established allowing those stresses that would arise in a wide plate to be calculated from measurements of a narrow one. This effect should also be borne in mind when welding narrow plates to assess RS.

By contrast to the longitudinal stresses the transverse stresses were not affected neither when reducing the length nor the width of the test welds.

ACKNOWLEDGMENTS

The authors would like to thank Dr. T. Buslaps (ID15A, ESRF, France) for the support during the beam time and the ESRF for the beam time through Proposal No. ME1165. Further M. Poad (AIRBUS, UK) as well as W. Suder and Professor S. W. Williams (Cranfield University, UK) are acknowledged for supplying the sample welds. J.A. would like to thank the Institut Laue Langevin (Grenoble, France) and the EPSRC Light Alloys Portfolio, UK for financially supporting his Ph.D. thesis.

Aa, E. M. Van der (**2007**). "Local cooling during welding: Prediction and control of residual stresses and buckling distortion," Ph.D. thesis, Delft University of Technology, Delft, p. 231.

Allen, A. J., Andreani, C., Hutchings, M. T., Sayers, C. M., and Windsor, C. G. (**1984**). "Neutron diffraction studies of texture and residual stress in weldments," Proceedings of the Fifth International Symposium on Materials Science, Roskilde, Risø National Laboratory, Denmark.

Altenkirch, J., Steuwer, A., Peel, M., Richards, D. G., and Withers, P. J. (**2008**). "The effect of tensioning and sectioning on residual stresses in aluminium AA7749 friction stir welds," Mater. Sci. Eng., A **488**, 16–24.

Altenkirch, J., Steuwer, A., Peel, M. J., Withers, P. J., Williams, S. W., and Poad, M. (**2008**). "Mechanical tensioning of high-strength aluminum alloy friction stir welds," Metall. Mater. Trans. A **39**, 3246–3259.

Altenkirch, J., Steuwer, A., Withers, P. J., Williams, S., Poad, M., and Wen, S. (**2008**). "Residual stress engineering in friction stir welds by roller tensioning," Sci. Technol. Weld. Joining **14**, 185–192.

Berdichevsky, V. and Foster, D. J. (**2003**). "On Saint-Venant's principle in the dynamics of elastic beams," Int. J. Solids Struct. **40**, 3293–3310.

Gabzdyl, J., Johnson, A., Williams, S. W., and Price, D. (**2003**). "Laser weld distortion control by cryogenic cooling," Proceedings of the First International Symposium on High-Power Laser Macroprocessing, Osaka, Japan, Vol. 4831, pp. 269–275.

Hauk, V. (**1997**). *Structural and Residual Stress Analysis by Nondestructive Methods* (Elsevier, Amsterdam), p. 640.

Hutchings, M., Withers, P. J., Holden, T. M., and Lorentzen, T. (**2005**). *Introduction to the Characterization of Residual Stress by Neutron Diffraction* (Taylor & Francis, London), p. 424.

ISO/TTA3 (**2001**). "Polycrystalline Materials: Determination of residual stress by neutron diffraction," International Organization for Standardization, Geneva, Vol. 3, p. 48.

Larson, A. C. and Von Dreele, R. B. (**2004**). *General Structure Analysis System (GSAS) (Report LAUR 86-748)* (Los Alamos National Laboratory, Los Alamos, NM).

Mahoney, M. W., Rhodes, C. G., Flintoff, J. G., Spurling, R. A., and Bingel, W. H. (**1998**). "Properties of friction-stir-welded 7075 T651 aluminum," Metall. Mater. Trans., A **29**, 1955–1964.

Masubuchi, K. (**1980**). *Analysis of Welded Structures* (Pergamon, Oxford), p. 600.

Peel, M. J., Steuwer, A., Preuss, M., and Withers, P. J. (**2003**). "Microstructure, mechanical properties and residual stresses as a function of welding speed in aluminium AA5083 friction stir welds," Acta Mater. **51**, 4791–4801.

Price, D. A., Williams, S. W., Wescott, A., Harrison, C. J. C., Rezai, A., Steuwer, A., Peel, M., Staron, P., and Kocak, M. (**2007**). "Distortion control in welding by mechanical tensioning," Sci. Technol. Weld. Joining **12**, 620–633.

Richards, D. G., Prangnell, P. B., Williams, S. W., and Withers, P. J. (**2008**). "Global mechanical tensioning for the management of residual stresses in welds," Mater. Sci. Eng., A **489**, 351–362.

Sutton, M. A., Yang, B., Reynolds, A. P., and Yan, J. (**2004**). Mater. Sci. Eng., A **364**, 66–74.

Threadgill, P. L., Leonard, A. J., Shercliff, H. R., and Withers, P. J. (**2009**). "Friction stir welding of aluminium alloys," Int. Mater. Rev. **54**, 49–93.

Timoshenko, S. P. and Goodier, J. N. (**1987**). *Theory of Elastics* (McGraw-Hill, Singapore).

Toupin, R. A. (**1965**). "Saint-Venant's principle," Arch. Ration. Mech. Anal. **18**, 83–96.

Ugural, A. C. and Fenster, S. K. (**1994**). *Advanced Strength and Applied Elasticity* (Prentice-Hall, Englewood Cliffs).

Williams, S. W., Morgan, S. A., Wescott, A., Poad, M., and Wen, S. W. (**2008**). "Stress engineering: Control of residual stresses and distortion in welding," Proceedings of the Second International Workshop on Thermal Forming and Welding Distortion, Bremen, Germany, p. 9.

Withers, P. J. (**2007**). "Residual stress and its role in failure," Rep. Prog. Phys. **70**, 2211–2264.

Withers, P. J. and Bhadeshia, H. K. D. H. (**2001**). "Residual stress part 2: Nature and origins," Mater. Sci. Technol. **17**, 366–375.